



Universiteit
Leiden
The Netherlands

Translational symmetry breaking in holographic strange metals

Balm, F.A.

Citation

Balm, F. A. (2023, May 16). *Translational symmetry breaking in holographic strange metals. Casimir PhD Series*. Delft-Leiden. Retrieved from <https://hdl.handle.net/1887/3618303>

Version: Publisher's Version

License: [Licence agreement concerning inclusion of doctoral thesis in the Institutional Repository of the University of Leiden](#)

Downloaded from: <https://hdl.handle.net/1887/3618303>

Note: To cite this publication please use the final published version (if applicable).

Translational Symmetry Breaking in Holographic Strange Metals

PROEFSCHRIFT

**TER VERKRIJGING VAN
DE GRAAD VAN DOCTOR AAN DE UNIVERSITEIT LEIDEN,
OP GEZAG VAN RECTOR MAGNIFICUS PROF.DR.IR. H. BIJL,
VOLGENS BESLUIT VAN HET COLLEGE VOOR PROMOTIES
TE VERDEDIGEN OP DINSDAG 16 MEI 2023
KLOKKE 11:15 UUR**

DOOR

FLORIS ADRIAAN BALM
GEBOREN TE UTRECHT
IN 1994

Promotor: Prof.dr. J. Zaanen
Copromotor: Prof.dr. K.E. Schalm

Promotiecommissie: Dr. E. van Heumen (Universiteit van Amsterdam)
Prof.dr.ir. H.T.C. Stoof (Universiteit Utrecht)
Dr. M.P. Allan
Dr. S. Bhattacharyya
Prof.dr. S.F. Portegies Zwart
Prof.dr. J.M. van Ruitenbeek

Casimir PhD-series Delft-Leiden 2023-10

ISBN-13: 978.90.8593.558.2

This thesis can be found electronically at <https://openaccess.leidenuniv.nl/>.

The research that is presented in this thesis was funded through the NWO/FOM Strange Metal free program (167).

This thesis was typeset using LaTeX with the KOMAScript scrbook class in the font ‘EB Garamond’, size 10.

Cover: Simulation of a black hole’s accretion disk,
NASA’s Goddard Space Flight Center/Jeremy Schnittman/SVS Visualiser
overlaid with Matrix text, Jamie Zawinski, Wikimedia Commons

To my wife and son.

Contents

Contents	i
Foreword	v
1. Theory of Condensed Matter	I
1.1. Drude Transport	I
1.1.1. Thermopower	3
1.2. Beyond Classical Theory	5
1.2.1. A Better Electron Gas	5
1.2.2. Towards Field Theory	7
1.3. (Broken) Symmetry	8
1.3.1. Noether's Theorem	8
1.3.2. Landau Theory and Symmetry Breaking	8
1.3.3. Continuous Spontaneous Symmetry Breaking	10
1.4. Superconductivity	11
1.4.1. BCS Theory	11
1.4.2. Challenges in Superconductivity	12
1.4.3. Hole Doped Cuprates	12
1.5. Strange Metals	13
1.5.1. Strong Coupling Issues and the Fermion Sign Problem	15
1.6. New Territory	17
2. AdS/CFT: The Holographic Duality	19
2.1. History of AdS/CFT	19
2.1.1. A More General Statement of the Duality	19
2.1.2. Limits of the Duality	20
2.2. Renormalization Group and Geometry	21
2.2.1. Finite Temperature	22
2.3. GPKW Dictionary	23
2.3.1. Fields and Scaling Dimensions	23
2.3.2. Black Hole Thermodynamics	26
2.3.3. Top-Down vs Bottom-Up	27
2.4. Holographic Applications to Condensed Matter Physics	27
2.4.1. Hydrodynamics	28
2.4.2. Conductivities from Holography: Real-time Information	29

2.5.	Finite Density: The Reissner-Nordström Black Hole	31
2.5.1.	Scaling Properties of Reissner-Nordström	32
2.5.2.	Thermodynamics of Reissner-Nordström	33
2.6.	Einstein-Maxwell-Dilaton Theory	35
2.6.1.	The Gubser-Rocha Conformal-to-AdS ₂ Metal	37
2.6.2.	DC Conductivity in the Gubser-Rocha Model	39
2.7.	Breaking Translational Symmetry	40
3.	Numerical Holography and Lattices	41
3.1.	Spatial Modulation	41
3.1.1.	Bidirectional Lattices	41
3.1.2.	RN Lattice Model	42
3.1.3.	DeTurck Method	44
3.1.4.	Thermodynamics of the Lattices	45
3.2.	Solutions to the Unidirectional Lattice	46
3.2.1.	Numerical Convergence of Holographic Lattices	47
3.2.2.	Bidirectional Lattice	48
3.3.	Einstein-Maxwell-Dilaton lattices	49
3.4.	Computing Perturbations	50
3.4.1.	Optical Conductivities in the Homogeneous Reissner-Nordström Black Hole	51
3.4.2.	Finite Momentum Correlators	53
3.4.3.	Lattice Conductivities	54
3.4.4.	DC conductivities	56
3.5.	Outlook	57
4.	Holographic Lattice Fermions	59
4.1.	Attribution	59
4.2.	Introduction	59
4.3.	Umklapp Scattering and Fermi Pockets in Unidirectional Potential	62
4.4.	Holographic Fermi Surfaces and Zeros	65
4.5.	Fermionic Spectral Function in a Holographic Lattice	71
4.6.	Destruction of the Fermi Surface by the Zeros in the Green's Function	73
4.6.1.	Weak Lattice Potential	73
4.6.2.	Strong Lattice Potential	77
4.7.	Discussion	80
4.A.	Appendix A: Fermionic Equations of Motion in the RN Background	85
4.B.	Appendix B: Numerical Calculus and Precision Control for Gravity Background	86
4.C.	Appendix C: Numerical Calculus for Dirac Equation	87
4.D.	Appendix D: Green's Function in the Bloch Momentum Representation	89
5.	Quantization of the Gubser-Rocha Model	93
5.1.	Attribution	93
5.2.	Introduction	93

5.3.	Setup	94
5.4.	Regularization, boundary terms and choice of quantization	96
5.4.1.	Boundary action	96
5.4.2.	Choice of quantization and thermodynamics	99
5.5.	Deformed Gubser-Rocha black holes	103
5.5.1.	Numerically constructed solutions	103
5.5.2.	The holographic dual of the one-parameter family of solutions in different quantization choices	105
5.6.	Conclusion	108
5.7.	Validity of the boundary action	109
5.8.	Matching of metric gauge choices	III
6.	Planckian Transport for a Holographic Local Quantum Critical Metal in Periodic Potentials	113
6.1.	Attribution	113
6.2.	The Planckian Dissipation Mystery versus Computational Holography	113
6.2.1.	Main Observations and Summary of the Results	115
6.3.	Holographic Strange Metals, Transport and Translational Symmetry Breaking	122
6.4.	Umklapp Hydrodynamics for Weak Lattice Potentials	125
6.5.	The Applicability of Hydrodynamics and the Imprint of Local Quantum Criticality	130
6.6.	DC vs Optical conductivities in explicit lattice (holographic) strange metals from Umklapp	133
6.6.1.	Low Temperatures: Drude Transport	134
6.6.2.	Intermediate temperatures: a mid IR-peak in the optical response	137
6.6.3.	Intermediate Lattice Strength: Towards an Incoherent Metal	138
6.6.4.	On the Applicability of Umklapp Hydrodynamics	140
6.7.	Observations at Strong Lattice Potentials: Planckian Dissipation and Incoherent Metals	140
6.7.1.	The Remarkable Ubiquity of Planckian Dissipation	140
6.7.2.	An Incoherent Metal Explained with Microscopic Scrambling	143
6.7.3.	Saturating Behavior and Planckian Dissipation	148
6.8.	Discussion: Is it Relevant for Condensed Matter Physics?	149
6.A.	Appendix A: AdS RN and GR Black Holes	153
6.A.1.	Reissner-Nordström	153
6.A.2.	Einstein-Maxwell-Dilaton	154
6.A.3.	Lattice Backgrounds	155
6.A.4.	DC Conductivity	156
6.B.	Appendix B: Semi-local Criticality and an Induced IR Length Scale	157
6.C.	Appendix C: Four-Pole Fitting Formula	160
6.D.	Appendix D: Memory Matrix Formalism	160
6.E.	Appendix E: Scaling of Hydrodynamical Relaxation Rates	160
6.F.	Appendix F: Lorentz Oscillator Decoupling	162

7. Conclusion	165
List of Publications	167
Bibliography	167
Summary	187
Samenvatting	189
Curriculum Vitae	191
Acknowledgements	193

Foreword

In this thesis, I will discuss holographic strange metals and what happens in such a system when translational symmetry is broken. This thesis is split along the middle into two distinct parts. In chapters 1 through 3, I will give an overview of some of the theory and background as an introduction on the topic, as well as an opportunity to provide some clarity on the specific systems and conventions used. Chapters 4 through 6, comprise three papers on which I have been an author related to aspects of transport and linear response phenomena that can be computed numerically in holographic strange metals. Let the reader beware that due to the nature of the different projects, this means that some information might seem duplicated between these chapters and the introduction. This is mostly not the case, as progressive insights have refined and adapted our notations and conventions over the years, and these sections are therefore kept as explicit as possible for the sake of accuracy.

I. Theory of Condensed Matter

In the early 1900's, the advent of the quantum revolution shone a new light on many of the open problems of physics at the time. An especially relevant example for this thesis is the conduction of electrons in metals. With the discovery of the electron at the end of the 19th century, Drude proposed a simple model for the conduction of electrons through solids. In this model, resistivity originates from a classical ideal gas of electrons scattering off each other like pinballs[1, 2]. The success of this theory was remarkable: both DC and AC electrical conductivity at room temperature are well described. The failings of this theory on the other hand provided a great challenge to the physics community. For example, transport properties at low temperature as well as heat capacities do not agree with experimental results at all. The eventual resolution of these problems have earned it its place as a starting point for modern physics education, as exemplified by its status as the subject of the very first chapter of esteemed textbooks like Ashcroft & Mermin[3]. In itself, it serves as an example of how the theory condensed matter physics has evolved over the past century. In relation to this thesis it will form a convenient point of departure from which to develop some of the ideas and challenges faced in condensed matter physics today, and how the the work contained in this thesis attempts to tackle them. In particular, I will present the case for the use of the holographic duality to study condensed matter systems, since some recent remarkable results from our research should attract the attention of the theoretical physics community at large to investigate classes of problems that are largely out of reach of conventional condensed matter physics theory.

I.1. Drude Transport

The Drude model of transport is a very straightforward textbook system, with which any physics student should be familiar. The full theory, as well as the subtleties related to the Sommerfeld improvements to the model, have been described in detail in many excellent resources[3]. The Drude model departs from the assumption that in a piece of metal the current density of electrons \vec{J} flowing through it can be expressed by

$$\vec{J}(t) = n e \vec{v}(t), \quad (1.1)$$

where n is the number density of carriers, e is the charge per carrier and \vec{v} is the velocity of each of the carriers. Assume now that an electron is scattered at a time $t = 0$ somewhere in the metal under the influence of a constant uniform electric field \vec{E} . At that point in time, it acquires some randomized velocity \vec{v}_0 due to the collision. After the collision, the electric field acts with a constant force $\vec{F} = e\vec{E}$ on the electron, meaning that its velocity at a time t after the collision is given

by

$$\vec{v}(t) = \int_0^t \frac{\vec{F}(t')}{m} dt' = \vec{v}_0 + \frac{e\vec{E}t}{m}. \quad (1.2)$$

In order to get the macroscopic behaviour, we have to perform an average over all particles in the system. It is assumed that this initial velocity \vec{v}_0 is uniformly randomly distributed such that the average value vanishes

$$\langle \vec{v}_0 \rangle = 0. \quad (1.3)$$

Hence this term drops out when taking the average

$$\langle \vec{v}(t) \rangle = \frac{e\vec{E}\tau}{m} \quad (1.4)$$

The relaxation time τ here is defined as the average time since a collision $\langle t \rangle \equiv \tau$. The classical result for a constant (DC) electric field is then that

$$\vec{J} = \sigma_{DC} \vec{E} = \frac{ne^2\tau}{m} \vec{E}, \quad (1.5)$$

where σ_{DC} is the DC conductivity. At room temperature this prediction works well when putting in estimates for number density and electron charge and mass.

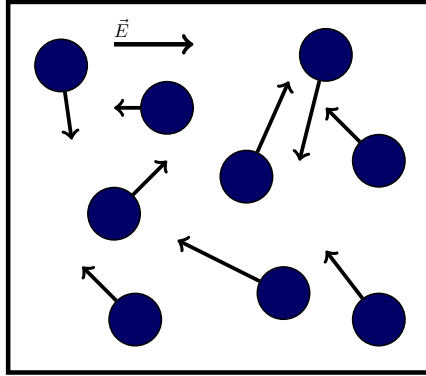


Figure 1.1.: The Drude model departs from considering classical pinballs moving randomly under the influence of an electric field.

We can generalise the applied electric field to a general time-dependent force. In this case, we first express the electrical current \vec{J} in terms of the momentum \vec{P} of the electrons by

$$\vec{J}(t) = \frac{ne\vec{P}(t)}{m}. \quad (1.6)$$

Under the assumption that the electrons have some average scattering rate τ and are subject to some average force $\vec{F}(t)$ due to oscillating fields, by considering the probability of scattering in a

small time window dt and the effect of the force during that time, the differential equation governing the average momentum of the electrons can be written as

$$\frac{d\vec{P}(t)}{dt} = -\frac{\vec{P}(t)}{\tau} + \vec{F}(t). \quad (1.7)$$

Important here is that in the absence of $\vec{F}(t)$, we get a damping of $P(t)$, as the solution will go like

$$\vec{P}(t) = \vec{P}(0)e^{-t/\tau}. \quad (1.8)$$

In other words, if the electrons are not being driven, their average momentum will decay exponentially in time. The rate of the momentum relaxation will be intricately linked to the conductivity. Assume for example that the field is being driven at a fixed frequency ω , and that we are in a late-time system where the momentum also oscillates with this same frequency. Going to frequency space in equation (1.7), we can deduce that the frequency-dependent conductivity is given by

$$\sigma(\omega) = \frac{ne^2\tau}{m} \frac{1}{1 - i\omega\tau}. \quad (1.9)$$

The real part of this forms a Lorentzian in frequency space centred at $\omega = 0$ with width $1/\tau$.

In general, the presence of a Drude-like conductivity requires there to be a mechanism for momentum to decay. If it does not decay, it would mean that it lives forever, and the relaxation time would become infinite. As a result the conductivity would be infinite: all particles keep moving at ever increasing speeds, forever accelerated by the electric field, as they are never scattered. That would for example be the situation in the limit of a dilute Fermi gas in the Galilean continuum. In the real world though, there are many mechanisms through which momentum can decay. This is for example possible through Umklapp scattering, where an electron can dump a specific amount of momentum into the lattice, as well as through interaction with disorder in the lattice. Overall linear momentum of the whole system is still conserved, but appears to decay in the purely electronic part of the system. This is illustrated in figure 1.2.

1.1.1. Thermopower

As mentioned above, there are some areas where Drude theory does not work well, the thermopower is one of these. Consider what happens when a temperature gradient is applied to an electronic system. From elementary thermal physics, we know that electrons start moving from the hot side towards the cold side as a result along the direction of heat flow. This creates an electric field, as electrons are removed on the hot side and are transported to the cold side. We can define the thermopower Q as the ratio of induced electric field to temperature gradient [3]

$$\vec{E} = Q\vec{\nabla}T. \quad (1.10)$$

If we assume for now to be in a one-dimensional wire with spatial coordinate x , we can find that the average thermal velocity \vec{v}_Q is given by [3]

$$v_Q = \frac{1}{2} (v(x - v\tau) - v(x + v\tau)), \quad (1.11)$$

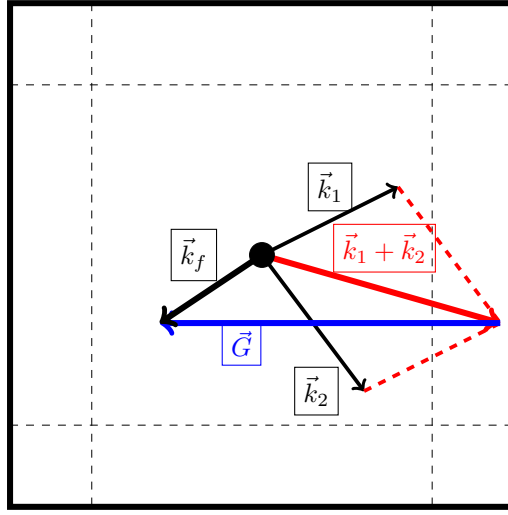


Figure 1.2.: Simple model showing Umklapp scattering for phonons. Through some process two phonons with momenta \vec{k}_1, \vec{k}_2 scatter to form a third phonon with $\vec{k}_1 + \vec{k}_2$, but as this is outside the first BZ this can be folded back by a lattice vector \vec{G} , such that $\vec{k}_f \neq \vec{k}_1 + \vec{k}_2$, meaning momentum gets lost.

or in other words, the average velocity that is induced by the temperature is given by the difference in velocities of electrons to the left and right of the point x . If there is a temperature gradient $\vec{\nabla}T$, these two velocities will be different, with the side with higher temperature having a greater velocity than the side of lower temperature. The factor $1/2$ comes in because roughly $1/2$ of the electrons will be moving in the $+x$ direction and the other half in the $-x$ direction. In a three-dimensional material, this will essentially apply equally in all three dimensions, where after some grinding of equations we can find that

$$\vec{v}_Q = \frac{\tau}{6} \frac{d(v^2)}{dT} \vec{\nabla}T. \quad (1.12)$$

From equation (1.4) above, we know that the electrons acquire an average velocity from the DC electric field which is given by

$$\vec{v}_E = -\frac{e\vec{E}\tau}{m}. \quad (1.13)$$

In a steady state the overall velocity which is a sum of the thermal and electrical velocity must be exactly zero, which means that

$$\vec{v}_E + \vec{v}_Q = 0. \quad (1.14)$$

Using the formulas above, the Drude model then predicts that Q is given by

$$Q = -\frac{c_v}{3ne}, \quad (1.15)$$

where c_v is the heat capacity at constant volume. This seems like a reasonable classical estimate, and one can wonder how this compares to real world physics. This is where the issues start: when one takes the classical kinetic theory result that $c_v = 3nk_B/2$, this goes enormously wrong: the value of the thermopower is overestimated by a factor 100 in electronic materials. The Drude model as it is presented here offers a clear picture of a classical view of conductivity, where resistivity can be phrased in terms of quantities like the collision time and the number density of charge carriers. As hinted at by the introduction, it is quantum physics that comes to the rescue here, and the resolutions of some of these issues are in a way a precursor to the issues that are faced in condensed matter physics today.

1.2. Beyond Classical Theory

With the knowledge of today, one can make the educated guess that it is the classical assumptions made in describing the electrons that are at the root of this problem. Instead, one should consider the electrons to be identical quantum mechanical particles. Furthermore, it is rash to ignore all the other interactions that are present in a real-world system, such as coulomb interactions between the conduction electrons for example.

1.2.1. A Better Electron Gas

In the time that Drude wrote down his theory, there was no clear picture of what had to be used as the distribution functions in the metals he was aiming to describe. Following arguments from kinetic theory, assuming an ideal classical gas of electrons would give rise to the Maxwell-Boltzmann distribution, which for a gas of particles moving in one dimension can be written as

$$f(v)dv = \sqrt{\frac{m}{2\pi k_B T}} e^{-mv^2/2k_B T}, \quad (1.16)$$

where k_B is Boltzmann's constant. At a fixed temperature, it is clear to see that the distribution has an $e^{-\alpha v^2}$ behaviour, which supposes that the vast majority of velocities drawn from this distribution will lie between $v^2 = 0$ and $v^2 = 4k_B T/m$. The shape of this distribution function has important consequences for some of the properties that we can compute about theoretical metals. In particular, as we saw before, when Drude calculated the thermopower, the specific heat that is found with this distribution is wrong by a very large factor. But if you suppose it must just be some wrong factor in the thermal transport, seeing that the electrical transport worked well, then it is all the more surprising that the Lorentz ratio between thermal and electrical conductivities as found in the Wiedemann-Franz law [4] matched rather closely to experimental results. This turns out to be a fortuitous coincidence, as we will soon see.

With the advent of quantum theory, it was realised that the Pauli exclusion principle must be applied to the electrons we are concerned with, as the underlying statistics that govern fermionic particles are antisymmetric in nature. This has far-reaching consequences: we cannot have multiple fermionic particles occupying the same state. Even in the ground state there are many fermions pushed to higher energy modes. Any undergraduate will have seen how this leads to characteristic

quantities that belong to a free electron gas, such as the Fermi energy and momentum and further derived quantities such as Fermi velocity and temperature. I will just highlight the Fermi velocity here: in a metal it turns out to be of the order of 1% the speed of light even at very low temperatures. This is in stark contrast to what is expected for the Maxwell-Boltzmann result, as that finds that the average thermal velocity would approach zero as the temperature approaches zero. At room temperature, the Fermi velocity is around two orders of magnitude greater than the velocity that Drude assumed in his original calculations.

For problems involving fermionic particles one should therefore not make use of the Maxwell-Boltzmann, but rather the Fermi-Dirac distribution

$$f(v)dv \propto \frac{1}{e^{\frac{\epsilon(v)-\mu_0}{k_B T}} + 1}, \quad (1.17)$$

where ϵ is the energy and v is the speed of the electron. This distribution has distinctly different features, especially the relationship with between v and μ_0 . For $\epsilon(v) \ll \mu_0$, this exponential is negligibly small and $f(v)dv \approx 1$. On the other side, when $\epsilon(v) \gg \mu_0$, the value of the exponential is large and therefore $f(v)dv$ is exponentially suppressed. The width of this transition is set by the temperature, T . For low temperature it is very abrupt, and for high temperature it becomes much more gradual. This is shown in figure 1.3. However, because the total integrated number of states that is described by the distribution must be the same at both low and high temperature, it must be spread out up to much higher velocities to account for all possible states.

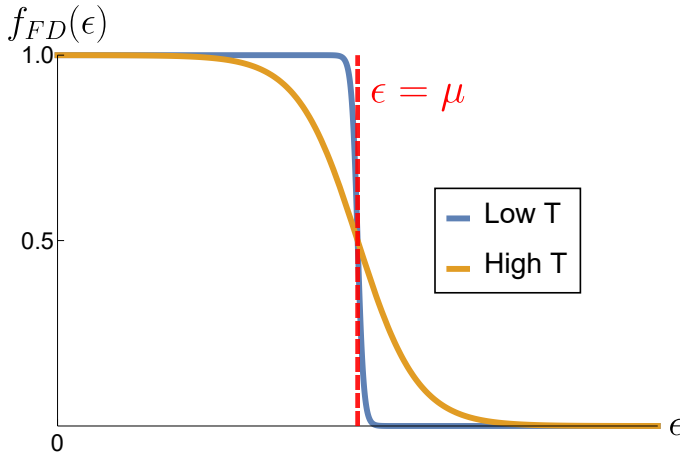


Figure 1.3.: Difference between the low and high temperature behaviour of the Fermi-Dirac distribution. At high temperature a significant number of states above the chemical potential are occupied, whereas in the zero-temperature limit the transition becomes a step function.

Let us now revisit the matter of the thermopower as a good example, making only the simple change of going from the Maxwell-Boltzmann distribution to the Fermi-Dirac distribution.¹The

resulting expression for the thermopower is now augmented by an extra factor $\frac{k_B T}{E_F}$, which in many ordinary metals is of order 10^{-2} , which accounts for the factor that was missing from the Drude calculation from before.[3] Regarding the Lorentz ratio, it turns out there was another factor 10^{-2} overestimation, namely in the specific heat, indeed coincidentally cancelling each other out.

1.2.2. Towards Field Theory

This simple, semiclassical fix is a step in the right direction. One can wonder what happens whether a full, honestly quantum-mechanical treatment of a free electron gas would be able to capture all of the physics that is present in real metals. This is of course not the case: the interactions that are neglected in the free electron gas play an important role. Even more so, at no point in this discussion has the ionic lattice that makes up the metal itself been taken into account. This adds even more complexity, not to mention the interplay between the dynamics of the two.

One of the first steps further is to go beyond the world of simple quantum mechanics, and enter into a realm where it is possible to address more than just single particles. For example, if you wish to write own a wave function in quantum mechanics to deal with more than one particle that obeys fermionic statistics, you have to deal with fully anti-symmetrized wave functions. For a small number of particles, say (a, b) in positions $(1, 2)$, this is still tractable:

$$|\Psi\rangle = \frac{1}{\sqrt{2}} \left(|a(1)\rangle |b(2)\rangle - |b(1)\rangle |a(2)\rangle \right). \quad (1.18)$$

Problems quickly arise when we need to deal with more particles: the number of terms will grow as 2^n particles. In a macroscopic piece of material there are on the order of $n \approx O(10^{23})$ atoms in the game. The resulting number of terms, $2^{10^{23}}$ is such an unimaginably huge number that it will consist of $O(10^{22})$ digits. In terms of computer bits, this corresponds to about as much digital data as exists in the entire world, and that is only to write down the number of states itself - let alone writing down any of the individual states. To say that it is not a number that can easily be handled is understating it. A further problem is that quantum mechanics is not often very well equipped to deal with a non-fixed number of particles. A different approach is clearly needed. The answer comes in terms of field theory, where instead of single-particle degrees of freedom, we are instead dealing with a continuum of degrees of freedom, where we can think of the elementary low-level excitations as ‘particles’. I will not discuss the beauty and many subtleties of (quantum) field theory here.[5]

¹This requires some justification. Modifying only the probability distribution is only a part of the story if you are to do a proper quantum treatment. Quantum mechanics itself needs to somehow be included: this is nothing more than ‘classical pinballs’ but with a different velocity distribution. This semiclassical approach does give some satisfying results, and is sometimes good enough to get a decent theoretical prediction. A more detailed discussion can be found in [3].

1.3. (Broken) Symmetry

One of the central tenets in the description of physical systems is the concept of symmetry and what happens when symmetries are broken. It is an immensely powerful principle, not merely simplifying some mathematical expressions, but allowing us to disentangle the physical characteristics of a system into distinct components that are governed by different principles, separated by their symmetries, and the (conserved) quantities that are associated with each of them.

1.3.1. Noether's Theorem

Noether's theorem is perhaps one of the most famous ways in which symmetry manifests itself. For a classical system, Noether's theorem states that continuous symmetries of the Lagrangian of a system correspond to conserved quantities. That is, if we can make a transformation in the system that leaves the Lagrangian unchanged, there must be some sort of conserved quantity associated with that transformation. This has some well-known results associated with it, such as time-translational invariance being responsible for conservation of energy, spatial translational invariance providing conservation of momentum, and rotational invariance corresponding to the conservation of angular momentum.[6]

In classical field theory, the idea is analogous, only instead of conserved quantities, we get conserved currents. If we consider a Lagrangian in 4 dimensions that does not explicitly depend on the space-time coordinates x^μ , then the symmetry is encoded in the conservation of the stress-energy tensor $T^{\mu\nu}$, which can be evaluated as

$$T_\mu{}^\nu = \left(\frac{\partial \mathcal{L}}{\partial (\partial_\nu \phi)} \right) \partial_\mu \phi - \delta_\mu^\nu \mathcal{L}. \quad (1.19)$$

The conservation of energy and momentum can then be expressed as

$$\partial_\nu T_\mu{}^\nu = 0. \quad (1.20)$$

For quantum field theories, the situation is again very similar, and the role of Noether's theorem is played by the Ward identities in the theory.[5]

1.3.2. Landau Theory and Symmetry Breaking

While it is important to be able to identify conserved quantities, it is when symmetries are broken that things get really interesting. This is clearly seen in Landau theory.[7] Without going into any microscopic details of any theory we are dealing with, not making any reference to what physics governs these microscopics, we will depart from a simple model with a free energy given some scalar order parameter φ . For the sake of simplicity, let us only take temperature as an external parameter.

$$\mathcal{F}(T, \varphi) = A(T)\varphi^2 + B(T)\varphi^4. \quad (1.21)$$

The coefficients A, B are the ones that now fully determine the behaviour of this system. The form of equation (1.21) dictates that there will always be a local extremum at $\mathcal{F}(0) = 0$. We will

always take $B > 0$ here, such that the free energy is at least bounded from below. The interesting part is fully dependent on A . Schematically, there are two distinct regimes for what this free energy may look like, see figure 1.4.

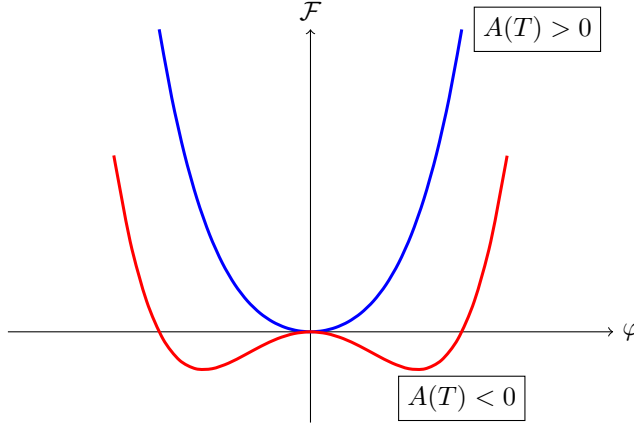


Figure 1.4.: The free energy for the two different scenarios for $A(T)$. For $A(T) < 0$, two minima are present away where $\varphi \neq 0$, while there is a local maximum at $\varphi = 0$.

If we depart from the phase where $A(T) > 0$, then $\varphi = 0$ is the minimum of the free energy and the system will have that as its ground state. Imagine now that lowering the temperature changes the sign of $A(T)$ to be negative. When $A(T) < 0$, there will always be some range of values of φ where

$$\mathcal{F}(\varphi \neq 0) < \mathcal{F}(0), \quad (1.22)$$

which means that a phase exists with a non-zero order parameter which is at a lower free energy compared to $\mathcal{F}(\varphi = 0)$. In this particular example, the minima exist at

$$\varphi_{\pm} = \pm \sqrt{\frac{-A}{2B}}. \quad (1.23)$$

Therefore, the system will undergo a phase transition to a new phase where the order parameter φ takes on the value that minimizes \mathcal{F} . But that is not the whole story. From the explicit form of the model, it is clear to see that there is a manifest symmetry under the transformation $\varphi \rightarrow -\varphi$. This means that there is a priori no preference for the system to end up the minimum at φ_+ over the one at φ_- and vice versa. In the end, the system will, by some process or another, pick one of the two spontaneously². This is the essence of spontaneous symmetry breaking: the free energy preserves in this case the \mathbb{Z}_2 symmetry of the order parameter $\varphi \rightarrow -\varphi$. Without imposing a preference of one over the other the system will nonetheless end up in a state that breaks this symmetry spontaneously.

²One could argue that no matter the system, at some point even Heisenberg's uncertainty principle will always bring the system out of the unstable maximum at $\varphi = 0$.

1.3.3. Continuous Spontaneous Symmetry Breaking

The example above is the prototypical example of discrete spontaneous symmetry breaking. The concept of spontaneous symmetry breaking becomes even more physically interesting if the symmetry that relates the equivalent states is continuous. The standard example for this is the complex order parameter ϕ , with a similar (real-valued) free energy to equation (1.21):

$$\mathcal{F}(\phi) = a|\phi|^2 + b|\phi|^4. \quad (1.24)$$

The system depends only on the magnitude of the scalar ϕ . Again we assume that the constant b in front of the highest-power term of ϕ is always positive. For $a > 0$ there is a stable minimum at $\phi = 0$, but for $a < 0$, the point at $\phi = 0$ becomes an unstable maximum, as illustrated in figure 1.5. We can take advantage of the symmetry and write the complex scalar in terms of its magnitude and phase

$$\phi = |\phi| \exp(i\theta). \quad (1.25)$$

We can see that the value of the free energy is independent of the phase θ of the scalar. In figure 1.5, this means that there is now a circle at finite magnitude of ϕ that minimizes the free energy, there is a continuous $U(1)$ symmetry between all these states.

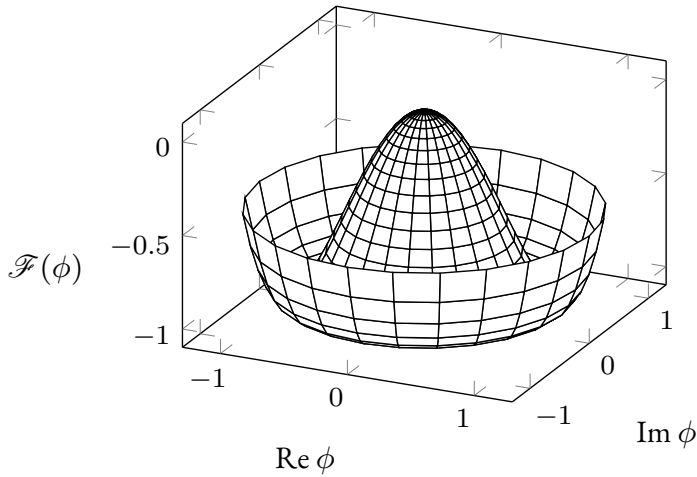


Figure 1.5.: Mexican hat potential for $a = -2, b = 1$.

The theory will have to pick some particular value of the phase θ to settle in, for which there is no particular preferential value. Here Goldstone's theorem comes into play. [8] This theorem states that for every generator of a continuous symmetry that is spontaneously broken, an extra massless scalar particle is added to the spectrum of the theory, the so-called Goldstone boson. These Goldstone bosons pop up in many places, the most important for our purposes is in crystalline solids. One can regard there the existence of the crystal lattice as a spontaneous symmetry breaking of

translationally invariant, isotropic, homogeneous space-time. The Goldstone bosons that pop up there we know more commonly as the phonons of the lattice.

Instead of spontaneous symmetry breaking, a theory can also be subject to explicit symmetry breaking. For example, one can start with a free-particle Hamiltonian, which is translationally invariant, and then add a periodic potential term to it. This modifies the theory, but now it is not only the states of the theory themselves that will break some symmetry: it is the Hamiltonian itself that is no longer translationally invariant. There is not such a neat theorem relating explicit symmetry breaking to appearing particles like there is for spontaneous symmetry breaking, but they can conspire and give rise to different effects.[9] For example, a symmetry is both spontaneously and explicitly broken, the boson that is generated by the spontaneous symmetry breaking now acquires a finite mass.

1.4. Superconductivity

All of the ideas discussed before come together in the theory describing superconductors. In superfluids, a global $U(1)$ symmetry is spontaneously broken. Superconductors are in a way similar, but there it is the $U(1)$ gauge redundancy that is broken³ spontaneously. The first superconductors were discovered by Heike Kamerlingh Onnes at Leiden at the start of the twentieth century, and the subject and its related puzzles continue to bring new and interesting questions more than a century later.[10] At first superconductivity had been observed only at temperatures very close to zero Kelvin. Advances towards the end of the 20th century saw the advent of the high- T_c superconductors, which in the 1980's and 1990's pushed the maximum temperature of the superconducting transition up from $O(10)$ Kelvin into the much more accessible cooling range of liquid nitrogen through ceramic compounds such as Lanthanum-Strontium-Copper-Oxides (LSCO) and Bismuth-Strontium-Calcium-Copper-Oxides (BSCCO).[11–15]

1.4.1. BCS Theory

In the first decades after the discovery of superconductivity, as it was found to be present in more and more materials, a theoretical explanation for the phenomenon was still sorely lacking. The very first microscopic theory came due to Bardeen, Cooper and Schrieffer.[16] Their insight was that an attractive interaction between fermions on other sides of the Fermi surface, no matter how small, has the effect of pair formation into what are now known as Cooper pairs.⁴ All manner of methods have since been developed to understand the physics of BCS theory, and for a concise introduction I will defer to reference [17].

³Which is again subtle and different from symmetry breaking as discussed before, as this generates massive bosons out of the photons rather than introduce new massless degrees of freedom. Regardless, symmetry breaking is still a key player here.

⁴The nature of the attractive interaction is one that for many intents and purposes can be left somewhat undetermined for quite a long time when considering BCS theory. One of the more conventional options is to consider the (screened) coulomb interaction in the solid in the presence of phonons. This can then be treated in perturbation theory to get to an effective interaction, which can be attractive. There is also the method of canonical transformations, which is described in detail in [18].

Another interesting aspect of BCS theory is the ground state that is assumed by the theory. In terms of creation, this is often written as

$$|\Psi_{\text{BCS}}\rangle \propto \prod_k \left(u_k + v_k c_{k\uparrow}^\dagger c_{-k\downarrow}^\dagger \right) |0\rangle. \quad (1.26)$$

Here u_k, v_k are some complex parameters, whose magnitudes must add to unity. This is a surprisingly simple waveform —instead of a complicated mixture of creation and annihilation operators concerning many different pairings on the Fermi surface, it turns out that the BCS state in momentum space is just a simple product state of pairs of created fermions. The importance of this statement will become clear later.

1.4.2. Challenges in Superconductivity

The BCS theory of superconductivity briefly displayed above works well for some compounds. Eliashberg theory, which in some sense can be seen as an extension of BCS theory in which retardation effects and dynamical interactions have been taken into account, works especially well for e.g. elemental superconductors.[19–21] One of the fundamental points of BCS superconductors is that the only symmetry that is broken is the $U(1)$ gauge symmetry, where the superconductor globally picks an (unobservable) phase spontaneously. The resulting order parameter is therefore highly symmetric. This preservation of symmetry is far from universal. In many systems of superconductors, additional symmetries are observed to be broken, and the symmetry of the pairing interaction can take the form of p -, d - or even f -wave symmetries. BCS theory is simply not equipped to deal with these more complicated symmetry breaking patterns. For example in the case of cuprate superconductors, iron pnictides, and many others, BCS theory simply fails.[21–23] These superconductors where the pairing interaction is not of BCS type are therefore known in general as unconventional superconductors.

Another commonly⁵ appearing characteristic in these unconventional superconductors is that it appears the correlations that appear in them are strong, much stronger than might be expected. Cuprate superconductors, especially those that are doped with holes, display this characteristic.[24] Some of these cuprate compounds have transition temperatures that exceed 100 Kelvin —much more than could ever be expected from a BCS superconductor.[25] One of the biggest outstanding questions in condensed matter theory exactly concerns describing the high temperature superconductors, and finding out why the temperature of their transition is so high. Many attempts have been made, but ultimately none so far have passed all the tests required in order to be accepted as ‘the’ theory of high-temperature superconductivity.[26, 27] But in spite of the attention it has received, it is perhaps not the most burning question in the cuprates from a fundamental physics point of view.

1.4.3. Hole Doped Cuprates

In the past decades, more than 200 different cuprate superconducting compounds have been identified.[28] What they have in common is their general crystal structure, which consists of one or

⁵But not necessarily.

more copper-oxide planes stacked on top of one another separated by layers of other atoms, such as Bismuth, Yttrium, Strontium, Calcium and more. In their undoped state, many of them fall into the category of Mott Insulators. In a quick-and-dirty classical way, Mott Insulators can be thought of as a material where the electrons in the conduction band get stopped in a ‘traffic jam’ due to strong lattice forces. The real story is of course rather more complex, but for present purposes it will suffice, and indeed strong potentials are the name of the game in the cuprates.[29] A whole world of phases opens up when these materials are doped, for example by changing the oxygen content, or by substitution of elements. Both the electron-doped and the hole-doped regions of the phase diagram are host to a plethora of interesting physical phenomena going on; we will be focused here solely on the hole-doped side.[28, 30]

While the details of all the different non-stoichiometric compounds created in this way are of course different, the phase diagram that can be mapped out of them follows some very general trends. This phase diagram, which is presented schematically in figure 1.6, contains much more than just Mott Insulators. In fact, although it is ‘unconventional’, the d-wave superconductor at the bottom is perhaps one of the least mysterious parts of this diagram, and it is rather the rest of the diagram that deserves much more attention. First of all, the Mott Insulator forms an anti-ferromagnetic state at small hole and electron doping, persisting up to a doping of a few percent. The superconductivity is only present at rather high doping, and is only truly ‘high T_c ’ in a somewhat small doping range around its maximum, the point of optimal doping. On the left of the superconducting dome is located the pseudogap phase.[31] This phase is rather mysterious and its transition temperature is rather hard to pin down exactly.[32] What can be said about it is that many of the different experimental techniques that are available, starting with nuclear magnetic resonance spectroscopy, have now confirmed that parts of the Fermi surface appear to become gapped far above the superconducting transition temperature.[21, 33] On the very highly doped side of the phase diagram, the situation becomes somewhat boring, and the materials return to being ordinary metals.

Many of the most interesting puzzles in the cuprates come together right in the centre wedge of the phase diagram, where strange metal phase resides.

1.5. Strange Metals

The strange metal has earned its name because it is quite literally a metal that behaving in a strange way. This normal-state region of the cuprate superconductors is really anything but that, and has several properties that display this general strangeness. The first and perhaps most striking characteristic is found in the in-plane resistivity⁶, which near optimal doping above the superconducting transition scales linearly with temperature [36–38]

$$\rho_{ab} \sim \rho_0 + bT. \quad (1.27)$$

⁶The residual resistivity at zero temperature, indicated by ρ_0 is not generically zero, but there are some systems where it does appear to vanish.[35] Rather, it is the constant linear slope that marks the linear-in- T behaviour.

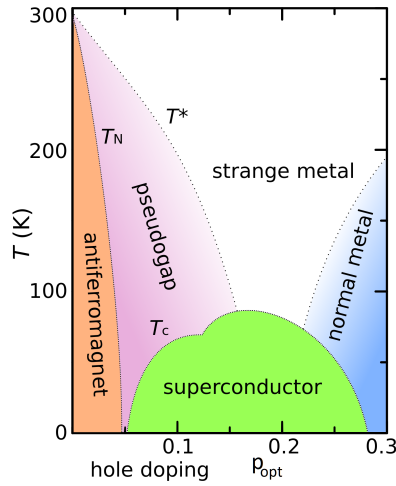


Figure 1.6.: Schematic phase diagram of cuprate superconductors on the hole-doped side. At zero doping the Mott insulator state is located. The pseudogap phase persists sometimes up to room temperature at low doping. When the doping is less than the optimal doping p_{opt} , this is referred to as underdoped, more doping is called overdoped. There is much that is not shown in this figure, such as possible charge density wave orderings and other phenomena.[34] T^* , T_c , T_N are the pseudogap, superconducting transition, and Néel temperatures respectively. This picture has been edited from https://commons.wikimedia.org/wiki/File:Cuprates_phasediagram_en.svg under the CC BY-SA 3.0 license.

This was seen already quite early on in the cuprate superconductors [39, 40].⁷ In some cases, this linear-in-temperature regime extends to far above room temperature. There are several reasons why this is interesting. First of all, the linear-in- T behaviour is not what is expected from a metallic phase: going by standard Landau Fermi Liquid theory, one expects the resistivity to instead scale as T^2 at low temperatures.[41] One typically expects the resistivity to saturate at a finite temperature, to what is called the Mott-Ioffe-Regel limit.[42] Another strange feature is that many of the cuprates blow right through that limit. The compound is still metallic, but conducts much worse than should be expected, hence this is often called ‘bad metallic’ behaviour.

This is only the start of the conundrum of the strange metal. This linear-in- T behaviour persisting over such a large range of temperature is an indication that there should be some very strong, universal principle underlying the physics of these systems. At the heart of this seems to be the hint that electronic interactions in the cuprates are strong, so strong that traditional perturbative methods are not able to capture the physics of these systems adequately. This is most sharply seen in the lack of quasiparticles, which seem to disappear in the strange metal, as well as the Hall angle,

⁷It is important to recognise that the ‘goodness’ of the linear-in- T resistivity does depend on doping, and it is very near optimal doping that the best linearity is often observed.[40]

does not behave as expected in a quasiparticle Fermi liquid.[43–47]

There is some evidence that right in the middle of the superconducting dome, at zero temperature, there is located a quantum critical point.[48] The scale invariance that is generated from the quantum phase transition, along with the suggestive characteristic wedge-shape of the strange metal region, seem to suggest that the strange metal might have some underlying quantum criticality. The nature of a possible quantum critical point is still a matter of debate in the physics community, as it is not sure what is actually happening at this point, and there is no good theory of what the order parameter might be that is undergoing the phase transition.[43, 49] The very high temperatures up to which the strange metal regime extends are also at odds with the idea of a single quantum critical point as the reason for all the strange behaviour.

Regardless of whether the quantum critical point actually exists, there are indications that there is some kind of quantum critical behaviour is going on. For example, measurements of the dynamic charge response $\chi''(q, \omega)$ seem to suggest that there is a special kind of quantum critical behaviour going on that completely decouples the spatial from the temporal dynamics.[50] The optical conductivity also shows interesting behaviour. Optical measurements show that there appears to be a very good Drude-like response at low frequency. One can describe a Drude response in terms of a width and a momentum relaxation rate. The Drude weight appears to be remarkably temperature-independent, but the Drude width appears to be set by some universal ‘Planckian’ time scale[51, 52]

$$\tau = A \frac{\hbar}{k_B T}, \quad (1.28)$$

where A is some $O(1)$ prefactor. In the typical Drude formula,

$$\sigma(\omega) = \frac{\omega_p^2 \tau}{1 - i\omega\tau}, \quad (1.29)$$

in the DC limit $\omega \rightarrow 0$, we recover that the resistivity goes as

$$\rho \sim \frac{1}{\omega_p^2 \tau}. \quad (1.30)$$

The Drude weight ω_p^2 , which is related to carrier density, is constant at low temperature and the relaxation time $\tau \sim T^{-1}$ (or equivalently, relaxation rate $\Gamma \sim T$). Together, this makes a very straightforward way to make the resistivity go linearly with temperature, $\rho \sim T$. This is just a set of observations though, and there is currently no good theory that unifies and explains all observations in a coherent way.

1.5.1. Strong Coupling Issues and the Fermion Sign Problem

The strange metal puts current state-of-the-art condensed matter theory on the spot. We require a theory where we do not think in that well-ingrained notion of quasiparticles that we as physicists are so familiar with, as the perturbative treatment that they are built on does not work in the presence of strong coupling. Common theories like the regular Fermi liquid, which works so well in normal metals, simply do not apply. The strange metal and in strongly correlated electron

systems are simply put obscured by their eponymous strong electronic couplings. If the couplings are weak, typically some kind of perturbation theory can be used, where the coupling strength λ is a small parameter. There are some ways of investigating strong coupling theories, and the strong interaction of hadrons has long provided a reason for high-energy theorists to try to explore it, but there is no good way of treating strongly coupled condensed matter systems in general. We will explain why.

So what can be done in order to describe the strange metal, if not analytically then at least numerically? One of the problems mentioned in section 1.2.2 was the size of the Hilbert space, which grows exponentially with the number of particles in the system. After all, Moore's Law predicts an exponential increase of our computing capabilities, and has been working well for decades now. One might hazard a guess that we are getting to a point of just letting the largest computers in the world loose on the problem and simply brute forcing an answer numerically.

Sadly, this is just a pipe dream. For example, the two-dimensional Hubbard model has often been proposed as the number one model that will with enough long-range hoppings be able to capture the relevant physics. In a Monte-Carlo setting at finite doping⁸, each of the configurations that needs to be considered carries with it an overall sign, depending on the exact realisation of the spins of the electrons in the system. The problem comes from the fact that to calculate an observable, one must average over a number of configurations. However, in order to get good statistics in a Monte-Carlo problem, observables need to be computed as an average of many configurations. The problem here is then that the number of configurations needed get to get acceptable error bars on the observables increases exponentially when going to lower temperature.[53] This growth is so fast, that it is simply impossible to make a large enough system.

Other approaches run into similar issues. Take for example the tensor networks, and DMRG in particular. [54, 55] Instead of having to deal with the entire Hilbert space, they rely on methods to somehow reduce the big $2^{10^{23}}$ Hilbert space down to the realm of what computers can handle. This is typically done by using some heuristic to decide on a number of states to keep. For some theories, this is easy. If the theory is gapped somewhere, it is safe to assume that the dynamics relevant to the ground state will not involve states above the gap scale.[54] This does not apply in the strange metal though. In the end, all numerical approaches always have to face that the number of states the Hilbert space needs to be reduced. In conventional, weakly coupled systems we can make some assumptions about entanglement for example, namely, that the ground state will take on some simple, product-state like form. This often works, and when thinking in terms of tensor networks this allows us to write the state as a product of complex matrices at different sites, each of which have some size χ called the bond dimension. It turns out the bond dimension can be interpreted to tell a lot about entanglement in the system. If a system has no entanglement at all, it is just a pure product of complex numbers (matrices of size $\chi = 1$) at the different sites, and it is only necessary to keep a minuscule part of the complete Hilbert space available for the lowest lying excited states. With increased entanglement, the size of the matrices that are needed to describe the entire state grows exponentially. Eventually, when the state is maximally entangled, we need again to take into account a large part of the Hilbert space. In the doped Hubbard model, it can be shown

⁸In the particle-hole symmetric case the problem is sign-free, however that is a well-known and well-studied case. This lucky simplification is not however true away from the exact symmetric point.

that one does need to keep a very large amount of states in the matrices in order to get reliable results - supporting the idea that dense entanglement can play a vital role in understanding the physics of this.[56] Therefore, it seems reasonable to want to be able to deal with densely entangled systems if one really wishes to describe the strange metal.

1.6. New Territory

The conclusions drawn from the previous section should all point in one direction. If we want to be able to describe the physics of the strange metal, we must deal with dense entanglement, strong correlations, strong lattice potentials, local quantum criticality and more, perhaps all at once, while not running into exponentially difficult computations.

From the unlikely realms of string theory and quantum gravity comes here a brilliant surprise: a duality that allows us to consider and compute theories at strong coupling, densely entangled, without running into fermion sign problems or exponentially large Hilbert spaces, where all the information is neatly encoded in black holes and curved space-times. This ‘holographic duality’ is at the very core of this thesis; it is using holography that all are computed and interpreted. In chapter 2, we will take a closer look at what this holographic duality encompasses and to what effect it has been used in this thesis. Chapter 3 will mainly focus on the definitions and conventions that are being used in the holographic lattices that are used throughout the thesis, and will outline the numerical procedures used to compute them.

The rest of the chapters will use and explore the holographic lattices in several different ways. Chapter 4 will deal with holographic probe fermions. By solving the Dirac equation in curved space-time, it is possible to compute the spectral function of strongly coupled fermions in the presence of very strong translational symmetry breaking. This indeed seems like it would have immediate connections to the properties of fermions in for example cuprate strange metals, where experiments like angle-resolved photoemission can measure this spectral function, however there are some important caveats, which will be discussed.

Chapter 5 is a rather technical chapter, but one that has played an important part, as it concerns a realisation that we had made that many groups that use the so-called Gubser-Rocha model misinterpret or overlook certain aspects of the model, especially in relation to the thermodynamical quantities that can be derived from this model. Furthermore, a correct interpretation of the model involving an exactly marginal scalar is convenient for use in the final chapter.

The most central paper of this thesis is chapter 6. In it, the Gubser-Rocha model for the holographic strange metal is subjected to both a 1D and 2D ionic lattices, with a wide range of lattice strengths. We then look at AC electrical and DC thermoelectrical conductivities to explore the precise mechanisms of transport in these lattices. Some highly intriguing results will be shown, including but not limited to a linear-in-temperature resistivity, the experimentally observed mid-infrared peaks in the optical conductivity, and a resistivity that appears to saturate to a relaxation rate set by a Planckian timescale.

Together, these chapters will form a succinct overview of uses of the holographic duality with an eye towards condensed matter physics and the strange metal.

2. AdS/CFT: The Holographic Duality

2.1. History of AdS/CFT

The AdS/CFT correspondence (also often called the holographic duality) has its roots in string theory and the search for a theory of quantum gravity. The holographic principle, formulated by 't Hooft and refined by Susskind, made the identification between the information¹ contained in a volume of space-time, and their encoding on its boundary.[57, 58] The big discovery that turned everybody's heads was the discovery of the AdS/CFT correspondence by Maldacena [59]. The correspondence was hinted at by the similarity in symmetry structure between certain string theory models and supersymmetric Yang-Mills (SYM) theories in one lower dimension. To be precise, Maldacena initially formulated the correspondence between a type IIB string theory living on an $AdS_5 \times S^5$ space-time and an $\mathcal{N} = 4$, $U(N)$ SYM theory living in one less dimension. That explains the reason for the name 'AdS-CFT': it is a duality between on one side string theory, which can have classical gravity as its low-energy limit, on a space-time with negative curvature, so-called Anti-De Sitter space, and on the other side a conformal field theory. I will not go into details of either string theory or conformal field theory in this work, but there are many resources out there that discuss both in considerable depth, ranging from pedagogical introductions to reference works.[60–64]

The discovery of the correspondence triggered a major response in the string theory community, and it is commonly included as part of the second revolution in the field of string theory. It unearthed a deep connection between gravitational theories and conformal field theory. Soon after the discovery, it was found that there were other examples of theories where there exists such a duality.[65, 66] These all have their own specific details, such as the geometry and type of string theory, as well as the type of conformal field theory, but they all follow a very similar spirit of duality.

2.1.1. A More General Statement of the Duality

The statement of the duality for a general holographic correspondence is deceptively simple, and was made precise by Gubser, Polyakov, Klebanov and Witten [67]. Imagine a pair of theories between which the duality applies. One is the 'gravitational' side, where the string theory lives on some form of space-time with negative curvature. A technical aspect of those space-times is that they all have a boundary. The other theory is a (conformal) quantum field theory with one less

¹This uses the very abstract notion of 'information' as used in the field of information theory. It can be thought of as essentially 'degrees of freedom' of some kind.

dimension than the gravitational theory. The conformal field theory, like all quantum field theories, has all of its information contained in its generating functional. In this generating functional, we have the operators \mathcal{O}_i that are present in the theory, coupled to their respective sources j_i . As such, the generating functional contains enough information to compute all n -point correlators in the theory by taking functional field derivatives with respect to the sources. We will denote this functional as $Z_{QFT}[j_i]$. On the other hand, we have a gravitational theory which is coupled to extra fields ϕ_i , with boundary values j_i , and an associated partition function $\mathcal{Z}[\phi_i]|_{\phi_i \rightarrow j_i}$. Then the duality states that

$$Z_{QFT}[j_i] = \mathcal{Z}[\phi_i]|_{\phi_i \rightarrow j_i}. \quad (2.1)$$

In other words, using the duality one way can encode for and compute operators in the quantum field theory by having fields in the gravitational theory with the correct boundary behaviour. Applying the duality the other way, which says we can understand the gravitational side by doing computations in conformal field theory, is less relevant for the purposes of this thesis. This statement is incredibly deep, and allows for investigation both ways. It is possible to learn more about the QFT side by doing computations in the string theory side, but also the other way around. However, we are now struck with the problem that the theories specified on either side are far from easy to work with. A good example is the fields in the field theory: in the canonical example of $\mathcal{N} = 4$ SYM, the number of fields in the theory N is very large. Making any computation can be difficult, and how do we know to couple fields for these into the gravitational theory? The duality luckily has a way to simplify this in a way that is also useful for the purposes of our condensed matter aspirations.

2.1.2. Limits of the Duality

Crucial in the simplification that we desire is the fact that this duality is a weak-strong duality. This is evident when computing exactly which limits can be taken in terms of coupling strengths and numbers of degrees of freedom.[62] Since the string theory on the AdS side is hard to formulate and even harder to compute anything with, we would like to make use of its low energy limit, which is simpler. Let us take here the canonical example of AdS/CFT, to be precise the one where $\mathcal{N} = 4$ SYM theory with gauge group $SU(N)$ and coupling g_{YM} . [59] This is dual to type IIB string theory with string length l_s and coupling g_s , which lives on $AdS_5 \times S^5$ with AdS radius L and N units of $F(5)$ flux on S^5 . [61, 62] There duality maps the parameters g_{YM} and N to the parameters g_s and L/l_s on the string theory side, via [62]

$$g_{YM}^2 = 2\pi g_s \quad 2g_{YM}^2 N \equiv 2\lambda = L^4/l_p^4, \quad (2.2)$$

where we have defined λ as the 't Hooft coupling $g_{YM}^2 N$. The way we want to use the duality is to be able to compute things on the gravity side, which we then want to be able to interpret on the CFT side through the duality. For this, we want to get rid of as much stringiness as possible, as loop corrections and string couplings make our lives difficult here. In order to accomplish this, we will want the string coupling $g_s \rightarrow 0$, while having the length of the strings to be inconsequential compared to the AdS radius, such that $L^4/l_p^4 \rightarrow \infty$. Equation (2.2) then tells us that here we want to take $g_{YM}^2 \rightarrow 0$, while simultaneously $\lambda = g_{YM}^2 N \rightarrow \infty$. In other words, for the gravity

to be classical² we need to be in the limit of infinitely strong 't Hooft coupling. This shows that the duality is of the weak-strong nature: in order to be weakly coupled on the gravitational side, we end up in the limit of matrix large- N in the CFT.[61] This will turn out to be both a blessing and a curse: by going to the classical limit on the gravitational side, we are able to actually perform the computations required to explore extremely strongly coupled systems that are normally far out of reach of ordinary perturbative treatments on classical (though high-power) computers. For condensed matter physics, the presence of large- N spoils a lot of the fun, because this is never physically realised in any real world system and any significant claims will always have to be taken with the grain of salt that there could be significant corrections stemming from an expansion in $1/N$. For the rest of this work, we will stay in the large- N limit. This is in a sense the 'weakest' form of the duality from the sense that we get the easiest to handle gravitational physics, at the cost of only being able access a very restricted parameter space in the conformal field theory.

2.2. Renormalization Group and Geometry

Perhaps of greatest interest from a condensed matter perspective is the way that the Renormalization Group (RG) flow manifests itself. Dating back to the 1950's, the idea of the RG and RG flow was formulated from the desire to look at the physics of systems at different energy scales.[68, 69] The canonical way of thinking about renormalization in field theory is through the idea of a beta function. One considers a coupling constant g and looks at the properties of that coupling constant at different energy scales μ . When the energy scale is decreased, and more and more of the higher-energy modes of the theory are thrown out, the effective coupling strength of the theory changes. This is what the beta function of the theory encodes, and this can be stated as

$$\mu \frac{\partial g(\mu)}{\partial \mu} = \beta(g(\mu)). \quad (2.3)$$

When $\beta(\mu) = 0$, the scale transformation has no effect on the coupling strength and the theory is said to be scale-invariant. The magic now happens when we take a certain theory, and consider a series of copies of this theory, each evaluated at a slightly different, ever lower energy scale μ . The parameter μ then tells us at each point along its evolution how the physics of the theory behaves. We can imagine this now as an extra dimension of the theory: in essence we are adding a new 'energy scale' coordinate to the space-time of our theory,³ and we can track how it evolves. The realisation was made that this maps neatly to holographic physics, where the boundary represents the original theory. The theory living at the boundary is commonly called the ultraviolet (UV) theory: no degrees of freedom have been integrated out yet, and it contains all the microscopics. Going deeper into the interior of this space-time, renormalization effects start to kick in, and the deeper you enter into the 'bulk' of the geometry, the more you let the RG flow continue into the infra-red (IR) of the theory. Taking the example of the CFT, we know that in a CFT we must have $\beta(\mu) = 0$, as conformal field theories by have scale invariance as one of their defining

²Here the low-energy limit is technically supergravity, but in the setups we use we only have classical Einstein gravity, without supersymmetry.

³This is not an exact 'energy' dimension, but thinking about it proves to be enlightening in many respects, e.g. in section 6.5.

properties. The bulk geometry must therefore reflect the same scale invariance, which turns out to be manifestly true for empty AdS space-time. The mathematics are of course more involved, but these statements together with the requirement of having a ‘boundary’ for the space-time quite naturally leads to an AdS-like space-time. This is schematically represented in figure 2.1.

This consideration of RG flow brings to light the important aspect that, in a sense, what the AdS/CFT correspondence is doing is geometrizing the RG flow of the quantum field theory into a dynamical gravitational bulk, which is sometimes abbreviated in the statement [61]

$$\text{RG} = \text{GR}. \quad (2.4)$$

This provides a compelling reason to use the holographic duality: in physics, we are often interested in low-energy excitations that come from some microscopically detailed theory. The details of how to map microscopics to low-energy excitations is highly non-trivial. RG is one of the canonical ways to get the low-energy physics. These can prove to be very complicated, and there are a lot of limiting factors to their applicability, such as strong coupling and dense entanglement in general.[70] Holography turns the game on its head here. The RG scale is a fundamental dimension of the space-time, and once a black hole solution has been found, we can interpret what the RG is doing in the field theory simply by looking to a different radial slice of the bulk space-time, overall a much more straightforward affair.

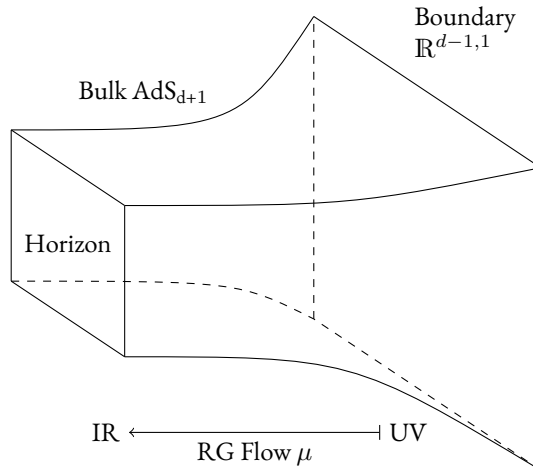


Figure 2.1.: The AdS space-time can be constructed by an RG flow, where each value of μ is a successive point in the flow.

2.2.1. Finite Temperature

Any real condensed matter system exists at finite temperature, simply by the third law of thermodynamics. This has to be taken into account when doing computations and one must be concerned with finite temperature field theory in order to make accurate predictions. This is in general quite

tricky again, and once more holography offers a convenient way out. In the bulk space-time, we can encode for a finite temperature field theory by placing a non-extremal black hole in the centre of the space time. This modifies things. For example, the bulk scale invariance that was present in the otherwise empty AdS space-time now no longer applies, as it is definitely possible to tell how close to the black hole you are. This results in some more non-trivial RG flow. The resulting flow is also rather pleasing: the black hole horizon turns out to correspond to a new infrared fixed point in the RG flow, where the physics of the original theory have indeed been changed from the ultraviolet scale invariant physics.[61] What is even more impressive is that these black holes can encode not only for temperature, but they can also carry different charges, such as electric and magnetic charge, which are crucial to condensed matter physics as they give rise to finite density and magnetic fields in the boundary theory. This thesis always operates at finite temperature, and therefore there will always be a non-extremal black hole of some type present in the centre of the bulk space-time that is being considered.

2.3. GPKW Dictionary

Now let us look at some specific examples, as the summary so far sounds intriguing, but it is not yet a useful apparatus that can be used for performing computations. The interpretation and use of many of the ingredients is expressed in what is commonly referred to as the dictionary, which translates quantities between the boundary field theory and gravity sides of the duality. This dictionary is named after Gubser, Polyakov, Klebanov and Witten.[67] Rather than just stating the results, some of the results deserve a bit more attention.

2.3.1. Fields and Scaling Dimensions

Suppose we are in the large- N limit, where we should be able to use classical gravity in the bulk geometry without quantum corrections as a dual to the field theory. If we have a single field ϕ that we want to have include in the holographic dual, we have to find the solution to the Einstein equations of motion of that field, under the condition that its boundary value

$$\phi|_{\text{Bdy}} \rightarrow j_i, \quad (2.5)$$

as described above in section 2.1.1. To set things up, let us first look at the space-time itself.[71, 72] We want to have a solution to Einstein's equations, which can be derived by doing a functional variation with respect to the curved metric from Einstein-Hilbert action

$$S = \int d^{d+2}x \sqrt{-g} (R - 2\Lambda), \quad 2\Lambda = -\frac{d(d+1)}{L^2} \quad (2.6)$$

where L is the AdS radius. Since we have $d+2$ dimensions in the bulk, the dual field theory will live in $d+1$ dimensions. A metric which is a solution to the Einstein equations with negative cosmological constant is the aforementioned anti-De Sitter space-time, which can be parameterised as

$$ds_{\text{AdS}}^2 = \frac{L^2}{z^2} \left(-dt^2 + dz^2 + d\vec{x}^2 \right), \quad (2.7)$$

where $d\vec{x}^2 = dx_1^2 + dx_2^2 + \dots$ runs over all purely spatial dimensions of the theory. The isometries of this AdS space-time turn out to be identical to those of a $d + 1$ dimensional conformal field theory – exactly what we expect from the way the duality was described in section 2.2.[60]

Let us assume now that the scalar field has a mass m , and that it is perturbatively coupled into the system, i.e., we assume a fixed background metric and we do not consider the back-reaction of the scalar onto the metric. The contribution to the action of the scalar field is given by

$$S_\phi = \int d^{d+2}x \sqrt{-g} \frac{1}{2} \left((\nabla\phi)^2 + m^2 \phi^2 \right), \quad (2.8)$$

from which we can deduce that the scalar then obeys the equation of motion

$$\left(\nabla^2 - m^2 \right) \phi(x) = 0. \quad (2.9)$$

We can use separation of variables to propose a plane-wave solution in the non-holographic direction, but leave the holographic direction as a general function of r . Under this assumption the equation of motion expands to

$$\partial_r^2 \phi - \frac{d}{r} \partial_r \phi + \left(\omega^2 - k^2 - \frac{(mL)^2}{r^2} \right) \phi = 0. \quad (2.10)$$

This equation has a solution in the form of Bessel functions.[73] When looking at the $r \rightarrow 0$ behaviour, which is the direction of the boundary, the series expansion at small r has two distinct sectors, namely

$$\phi \sim \phi_A r^{d+1-\Delta} (1 + \dots) + \phi_B r^\Delta (1 + \dots), \quad (2.11)$$

where \dots are higher powers of r and $\phi_{A,B}$ are integration constants. Δ are the solutions to

$$\Delta (\Delta - d - 1) = (mL)^2. \quad (2.12)$$

Depending on the value of Δ , one of these fields will be the dominant contribution in the region near the boundary, and the other one will be subdominant. The accepted terminology in the field for these terms is leading and subleading, respectively. Typically, the dominant term actually diverges near the boundary, and is called the non-normalisable mode.⁴

Let us now assume that ϕ_A is the leading component, and ϕ_B is the subleading one. It is exactly the leading component that is the one dual to the source of the operator in the side of the field theory. When evaluating the boundary action coming from equation 2.8, this will turn out to reduce to [74]

$$S_{\phi, r \rightarrow 0} \sim \int d^{d+1}x \sqrt{-\tilde{g}} (\phi_A \phi_B). \quad (2.13)$$

⁴I will not cover the subtleties such as the appearance of logarithmic terms in these expansions.

Making the identification of ϕ_A with its source j , we are still left wondering what the operator ϕ_B is.⁵ If we now remember the generating functional and the partition function, we know that we can use it in order to compute expectation values:

$$\langle O \rangle \sim \frac{\delta}{\delta j} Z[j] \Big|_{j=0}. \quad (2.14)$$

Comparing this to equation (2.13), this gives us the identification with the vacuum expectation value (VEV)

$$\langle O \rangle_{CFT} \sim \phi_B. \quad (2.15)$$

This example glosses over some of the more subtle points here. One is that in the case of for example the stress tensor, the expectation values might be naively divergent. This can be addressed by instead putting these sources at some $\epsilon > 0$ away from the boundary, and then adding counterterms which kill any divergent behaviour, after which we can safely send $\epsilon \rightarrow 0$ and recover the renormalised boundary values.[75]. Another is what might when both modes are normalisable. This turns out to allow for an admixture of boundary conditions into what we call the source and the response. This actually turned out to have important consequences in several parts of this thesis, for probe fermions in chapter 4 and for background space-time geometries and the thermodynamic interpretation thereof in chapter 5.

Subtleties aside, we can identify two-point functions in momentum space by[74]

$$G(k) = \frac{\phi_B(k)}{\phi_A(k)}. \quad (2.16)$$

From the point of view of condensed matter physics, we always prefer to use the retarded Green's function to study the two-point properties of our system. This can be achieved by imposing infalling boundary conditions on the scalar field, meaning that towards late times, the wave in the field theory will be travelling towards and eventually (partially) falling into the black hole horizon.

All this together gives us an entry in the dictionary, where we look to compute the solutions to the gravitational equations of motion, and then pull this through the duality to the boundary field theory by properly identifying source and response components. In this simple example we only looked at two-point functions, but one can look at any n -point function in general.

There are many more entries in the dictionary. Another interesting quality is how gauge fields and symmetries interact. The general identification here is that global symmetries in the boundary will correspond to local symmetries in the boundary. This is for example made explicit when considering a $U(1)$ gauge field in the boundary. The corresponding local $U(1)$ symmetry is dual to a global $U(1)$ symmetry in the boundary. In general, a gauge field will correspond to the conserved current that is associated with the related global symmetry. A more comprehensive, but by no means complete, overview can be found in table 2.1 below.[61]

⁵There are some exact factors of r to be taken into account, but these are not essential to the schematic discussion here.

Field Theory	Gravity
Large N	Classical gravity
Operator \mathcal{O} with dimension Δ	Field ϕ with mass m
Source of operator \mathcal{O}	Leading behaviour of ϕ
Vacuum expectation value $\langle \mathcal{O} \rangle$	Subleading behaviour of ϕ
Global symmetry	Local symmetry
Stress tensor	Gravitons
2-form current	2-form field
Finite temperature	Non-extremal black hole
Finite chemical potential	Charged black hole
Free energy	Value of Euclidean on-shell action
\vdots	\vdots

Table 2.1.: Some basic dictionary entries which feature in this thesis.

2.3.2. Black Hole Thermodynamics

Mentioned before was that black holes in the interior of the space-time are able to encode for finite temperature in the boundary CFT. This is actually tightly linked to discoveries by Bekenstein and Hawking in the 1970's that black holes carry entropy and can emit thermal radiation.[76, 77] The laws we are familiar with in our normal everyday thermodynamics have their own parallels in the form of the laws of black hole thermodynamics. Like the first, second, and third law of ordinary thermodynamics, there are laws of black hole thermodynamics where we can identify black hole quantities like surface area and surface gravity with entropy and temperature, respectively.

The black holes in these curved space-times allow for a wide variety of interesting phenomena, unlike their closely related cousins that live in flat space. The applicability of the 'no-hair' theorem is an example of this: in flat space, it is not possible for black holes to have any kind of structure on the horizon.[78] Instead, they are uniquely determined by the parameters charge, mass and angular momentum, which are just global quantum numbers, without any more structure. This no-go theorem does not hold in negatively curved space-time and therefore we can have all kinds of 'hair' on our black holes, such as scalars that can even acquire some spatial modulation.[79] Another example is black hole evaporation. Astrophysical black holes in flat space evaporate over time.⁶ A peculiar property of AdS space-time is that it takes only a finite time for massless objects, for example photons from Hawking radiation, to go from the centre of AdS space all the way to the boundary. This is in stark contrast to geodesics of massive particles, which will never reach the boundary in finite proper time. If one then assumes that any energy that these photons could carry is reflected back from the boundary into the interior of the space-time, eventually the reflected radiation will end up in thermal equilibrium with the radiation emitted by the black hole. As such the black holes can form an equilibrium state.[80] Therefore unlike in flat space, stationary

⁶For astrophysical black holes this happens extremely slowly, even on cosmological timescales.

black holes in AdS can exist and we can understand their dual to be some very late-time field theory in full local thermal equilibrium.[61]

2.3.3. Top-Down vs Bottom-Up

One of the open problems in the field of holography is that while it is conjectured that the AdS/CFT correspondence holds quite generally, we only have a limited number of examples where the duality is known to be exact. In order to understand fully what system we are describing and that the duality remains valid, we can start to play mathematical tricks with these known exact correspondences, such as dimensional Kaluza-Klein reductions. Together with convenient limits we can have a good idea what the conformal field theory is on the field theory side of the duality, while ending up in a gravitational theory that is more manageable than full-blown type IIB string theory, just to give an example. A side effect of this is that almost invariably, Kaluza-Klein reductions which get rid of some dimensions give rise to extra dilatonic scalar fields that get coupled into the gravitational side.[61] This general framework is known as the top-down approach to AdS/CFT. It is not always the most convenient approach to take, as the actions can either be difficult to deal with or in our case uninteresting from a condensed matter point of view. This is for example due to those extra scalars. The holographic dictionary in table 2.1 has some relevant entries such as the free energy and chemical potential, but these scalars have no good interpretation and they certainly do not turn up explicitly in real-world condensed matter systems. From the top-down approach, it can be very hard or impossible to get the exact ingredients in terms of fields and operators that you would like to describe on the condensed matter side.

The bottom-up approach attempts to remedy this problem by taking a different point of view of the duality. It treats the duality as a more phenomenological tool by simply choosing some elements that have in top-down models been shown to have a certain dual interpretation and building an action from that and trusting that the correspondence will still apply. The downside of this is that while we can compute quantities like retarded Green's functions and vacuum expectation values this way, there is no way of finding out what the exact Hamiltonian is of the theory dual to the gravitational action we have posed. As a result, the duality can now not be used to find the physics of a specific boundary theory, but it can give generalities about the physics of strongly coupled field theories. In this work, most of the models presented are of the bottom-up variety, as the translational symmetry breaking that we employ does not follow naturally from top-down constructions.

2.4. Holographic Applications to Condensed Matter Physics

The stage is now set, we have a way of posing our problem and a large number of questions that we would like to address. Let us see how the holographic duality can aid us in this. While the statement of the duality is clear, and the weak-strong nature of it is appealing for the purposes of performing computations, there is some more machinery to discuss.

2.4.1. Hydrodynamics

It turns out that the duality can encode for real-world physics in some surprising ways. What we are often interested in, as mentioned earlier, is the long-wavelength, low energy limit of the physics of the boundary theory. This can be achieved by doing what boils down to a gradient expansion, assuming that the only fluctuations that play a role are small and slow. Degrees of freedom are always slow when they correspond to conserved or nearly conserved quantities. Quantities that are not conserved for any perturbation in them will dissipate and thermally equilibrate quickly, without much of a chance to propagate over wavelengths. On the other hand, conserved quantities obey many continuity equations, which prevents them from doing exactly this, and instead perturbations will propagate for a long time or undergo some diffusion process in order to return to local equilibrium.[81] The gradient expansion of the theory into these slow modes is often synonymous with the hydrodynamics of the theory if they are the only slow modes in the theory. This is a more general consideration than what we would typically call hydrodynamics, after all it does not concern the flow of a real-world physical fluid like water flowing around in our field theory. Instead, the hydrodynamics we are concerned with would describe a relativistic fluid.⁷ This is a powerful machinery, and it is able to include relevant effects such as (perturbative) ionic lattices and external electric and magnetic fields.

The applications to holography are quite easy to state and is related to a by now somewhat famous result. For a relativistic fluid, the stress tensor is given by

$$T^{\mu\nu} = (E + P)u^\mu u^\nu + Pg^{\mu\nu} + \Pi^{\mu\nu} \quad (2.17)$$

where E , P are the internal energy and pressure and u^μ is the fluid velocity.[81] The first two terms describe ideal hydrodynamics. $\Pi^{\mu\nu}$ is the interesting part, the part where the derivative expansion comes into play. This can be a complicated term, but crucially it contains a set of constants that are known as transport coefficients such as the shear viscosity and bulk modulus of the fluid we are considering. However, these are a priori just a set of coefficients without a particular value: they represent the microscopic behaviour of the theory, and while their presence may be universal, their values are anything but that.[81]

This is where we can again use holography. In the gravitational dual, it is possible to compute some of these transport coefficients directly. This is one of the ways in which we can learn a lot about the field theory by looking at the gravitational side. While we will be considering only linear fluctuations in hydrodynamics, the mapping between gravity and hydrodynamics goes much deeper, showing that the Navier-Stokes equations can actually be found from the Einstein equations.[83, 84]

A particularly famous result that is related to this is the computation of the shear viscosity.[85, 86] The first-order terms in the gradient expansion of equation (2.17) will for example contain the shear viscosity, η . For example, to first order, the hydrodynamic constitutive relations in the

⁷There are other ways of constructing hydrodynamics, for example in a non-boost invariant setting, which do not feature in this work.[82]

Landau frame are given by [81]

$$T^{\mu\nu} = E u^\mu u^\nu + P \Delta^{\mu\nu} - \eta \sigma^{\mu\nu} - \zeta \Delta^{\mu\nu} \partial_\lambda u^\lambda + O(\partial^2), \quad (2.18)$$

where Δ is a projector with the flat space metric

$$\Delta = \eta^{\mu\nu} + u^\mu u^\nu, \quad (2.19)$$

ζ is the bulk viscosity and $\sigma^{\mu\nu}$ is the transverse traceless symmetric tensor [81]

$$\sigma^{\mu\nu} = \Delta^{\mu\alpha} \Delta^{\nu\beta} \left(\partial_\alpha u_\beta + \partial_\beta u_\alpha - \frac{2}{d} \eta_{\alpha\beta} \partial_\mu u^\mu \right). \quad (2.20)$$

For AdS black holes at zero density, it actually turns out that this shear viscosity is related to the zero-frequency scattering cross-section of the black hole. This in turn can be expressed in terms of the area and volume of the black hole and therefore also the entropy of the black hole by the laws of black hole thermodynamics. When including geometric factors, this yields the ratio

$$\frac{\eta}{s} = \frac{1}{4\pi} \frac{\hbar}{k_B}. \quad (2.21)$$

This ratio of viscosity to entropy is known as the minimal viscosity, as it is conjectured to be a lower bound on the viscosity of a strongly interacting field theory.[85] Remarkably, this bound also seems to hold at finite density. Most strongly interacting materials found in nature are nowhere near this bound though. Only the quark-gluon plasma, which was studied in detail around the same time as the minimal viscosity was discovered, has a surprisingly small value for this ratio, even though it does not have ingredients like the large- N of holography.[87] A charitable interpretation can see this as a hint that holography can indeed tell us useful things about the real world.

2.4.2. Conductivities from Holography: Real-time Information

Holography is not only limited to computing hydrodynamic transport coefficients. One of the more technically useful aspects of holography is that it gives access to real-time information about the dual system. This is in stark contrast to typical field theoretical results, where it is often necessary to work in imaginary time to make computations feasible. Finite temperature is then encoded in the radius of the time circle in imaginary time. That in itself is not a problem, but the difficulties come when trying to translate back into real time, as that is what we observe. The Wick rotation that has to take place is technically very challenging, and often means that it is impossible to get anything but the most general scaling dimensions out.[88] Holography is in this aspect very different. Since temperature is already encoded in the thermodynamics of the black hole⁸, it turns out that computing real-time properties of field theory involve driving the holographic system out of

⁸The temperature equals radius in imaginary time still shows up in black hole physics too. For the Schwarzschild solution in flat space for example, one can rotate to a Euclidean space-time, where the temperature is found from the radius of the time circle is fixed in order to avoid a conical singularity in this space-time. This is a more ad-hoc argument than the original derivation of black hole temperatures, but it is an interesting connection.

equilibrium, and looking at the real-time evolution. This gets us real-time field theory observables without having to resort to any Wick rotations.[71]

For the sake of illustration, let us consider the electrical AC conductivity of the field theory. We can choose to take a static black hole in equilibrium and apply a time-dependent electric field $E(t)$ to it. This will in general drive the black hole out of equilibrium. Let us assume that this field is oscillating at some finite real frequency ω . This electric field is assumed to be a small perturbation, which does not back-react on the initial black hole background. The electric field E is then induces a current response J , and their proportionality is the conductivity σ :

$$J(\omega) = \sigma(\omega)E(\omega). \quad (2.22)$$

In a conformal field theory at zero density, on dimensional grounds this conductivity takes the form

$$\sigma(\omega) \sim \omega^{d-2}, \quad (2.23)$$

where d are the number of transverse spatial dimensions. Since we typically consider AdS_4 , our boundary will have $d = 2$ transverse dimensions and hence σ becomes exactly frequency independent.[61]

That is a fairly trivial result, and we do not need to rely on any holographic computation to find this out. At finite temperature, one can no longer rely on dimensional analysis. Nevertheless, the holographic computation of this result at finite temperature is rather straightforward at zero chemical potential and it is a good starting point to show the power of holography. In order to compute the conductivity, we will make use of linear response theory.[88] In linear response, we know that we can find the conductivity from the retarded Green's function via

$$\sigma(\omega) = \frac{1}{i\omega} G_{JJ}^R(\omega). \quad (2.24)$$

The retarded Green's function is that of the current operator, which is defined by

$$G_{JJ}^R(\omega) = -i \int dt dx e^{i\omega t} \Theta(t) \left\langle [J(t, x), J(0, x)] \right\rangle. \quad (2.25)$$

$\Theta(t)$ is the step function that takes care of the time ordering here such that $t > 0$. In a previous chapter, we encountered exactly how to compute Green's functions by considering leading and subleading behaviours of a field theory. In this case, we now need to consider a black hole in order to do the computation at finite temperature. As we are at zero density, this will be the AdS -Schwarzschild black hole, which can be parameterised by only its horizon radius which sets its temperature after scaling out some other parameters such as the AdS radius and Newton's constant. In order to find the conductivity, we need the bulk dual of the current. What we now need to do is find the Green's function that is related to turning on a perturbative electric field $E_x = F_{tx}$. For a spatially homogeneous electric field, in terms of the gauge field this will correspond to turning on a component $A_x dx$ which in Fourier space will have behaviour like $A_x = a_x(r)e^{-i\omega t}$. The

exact boundary behaviour can be extracted by carefully looking at the near-boundary expansion,⁹ which will find that the expansion for A_x goes as [61]

$$A_x \propto a_x^0 + \frac{a_x^1}{r} + \dots, \quad (2.26)$$

where $a_x^{0,1}$ are the leading and subleading behaviours near the boundary, respectively. One can solve for the equations of motion, and the condition for the retarded Green's function is fixed by choosing the infalling boundary conditions.[71] The solution¹⁰ will have

$$a_x^0 = c, \quad a_x^1 = i\omega c \quad (2.27)$$

for some constant c . Using the dictionary to extract the Green's function from holography, we can find that for any temperature

$$\sigma(\omega) = \frac{1}{i\omega} G_{JJ}^R(\omega) = \frac{1}{i\omega} \frac{a_x^1}{a_x^0} = 1. \quad (2.28)$$

This is exactly the result is found for the zero-density CFT, since it has no dependence on frequency.[64] More importantly though, there is no dependence on temperature either, which one might not have expected. At zero temperature, there is no scale in the CFT, so there cannot be any identifiable features at some ω , as this would indeed be an indication of some scale. However, temperature is a scale in the theory, as it can be combined with k_B for example to create an energy scale. It is then surprising that the introduction of this scale does not appear to have any effects. [61]

2.5. Finite Density: The Reissner-Nordström Black Hole

Zero density is not the most interesting system though. Apart from some very fine-tuned systems, such as graphene at exact charge neutrality, this is not a system we are likely to see appear in experiments.[89] Luckily going to finite chemical potential in holography is a rather simple affair, and it does not require the development of a lot of new machinery. The star player in respect has long been the Reissner-Nordström black hole. This black hole can be constructed as a compactification of some 11-dimensional M -theory, which we will not go into the details of.[90, 91] For our purposes, the starting point will be the Einstein-Maxwell action

$$S = \int d^4x \sqrt{-g} \left(\frac{1}{2\kappa^2} \left[R - 2\frac{\Lambda}{L^2} \right] - \frac{1}{4e^2} F_{\mu\nu} F^{\mu\nu} \right), \quad (2.29)$$

where $F = dA$ is the field strength for the $U(1)$ gauge field A . We will always use the units where $2\kappa^2 = 16\pi G = 1$, $e = 1$, $\Lambda = -3$, $L = 1$. Note that here, in contrast to the scalar example that was discussed in the section above, this gauge field is coupled in to gravitation action in the

⁹For the gauge field no holographic renormalisation is necessary/

¹⁰See box 7.3 [61]

full action, as such the back-reaction of the gauge field on the metric is taken into account. The equations of motion that arise can with some manipulation be written as

$$\begin{aligned} R_{\mu\nu} + 3g_{\mu\nu} &= \frac{1}{2} \left(F_{\mu\rho} F_{\nu}{}^{\rho} - \frac{1}{4} g_{\mu\nu} F_{\rho\sigma} F^{\rho\sigma} \right), \\ \nabla_{\mu} F^{\mu\nu} &= 0. \end{aligned} \quad (2.30)$$

This set of equations admits a black hole solution with a finite charge with AdS_4 asymptotics. The black hole can be written using a metric

$$\begin{aligned} ds_{RN}^2 &= \frac{z_+^2}{z^2} \left(-f(z) dt^2 + \frac{1}{f(z)} dz^2 + dx^2 + dy^2 \right) \\ A &= A_t dt = \mu \left(1 - \frac{z}{z_+} \right) dt \end{aligned} \quad (2.31)$$

The emblackening factor $f(z)$ for Reissner-Nordström is given by [90, 92]

$$f(z) = \left(1 - \frac{z}{z_h} \right) \left(1 + \frac{z}{z_h} + \frac{z^2}{z_h^2} - \frac{\mu^2 z^3}{4z_h^3} \right). \quad (2.32)$$

The emblackening factor has two roots at z_+, z_- , which are the locations of the outer and inner horizon at finite temperature respectively. At zero temperature these collapse to a double root. We will only be considering finite temperature here, and therefore we will treat our space-time as if it ends at $z_h \equiv z_+$. We will always be able to rescale the horizon radius such that $z_h = 1$, for both ease of notation and later numerical convenience.

However, there are some scenarios where keeping the horizon radius explicit is useful, for example when computing thermodynamic susceptibilities, as was done in section 6.7. Most observables that are directly computed are typically given or found in units of horizon radius as that is often a free parameter in the solutions. This has a deeper root in the diffeomorphism invariance that is encountered in the gravity side. For practical purposes, that means that all the parameters we referring to, whether they are radii, expectation values, or other objects, have to be phrased with reference to some scale. In the dual boundary, z_h has no natural meaning, but there we can express all dimensionfull quantities in terms of the chemical potential.¹¹ When we state for example that we take the parameter $\mu = 2$, that is shorthand for $\mu = 2z_h$. The boundary of the AdS space-time is located at $z = 0$ in this parametrization.

2.5.1. Scaling Properties of Reissner-Nordström

Another key property of the RN black hole is its particular near-horizon geometry. If we depart from the metric as presented in equation (2.31), we can take the horizon to be located at $z = 1$. In

¹¹In relevant condensed matter systems, such as the cuprates, the typical size of μ is about 1 eV. In natural units, this corresponds to a temperature of about $10^4 K$. Room temperature would be on the order of $T = 3 \times 10^{-2} \mu$, to give a sense of scale.

a series expansion around $z = 1$, the emblackening factor will expand as

$$f(z) \approx f'(1)(z-1) + \frac{1}{2}f''(1)(z-1)^2 + \dots, \quad (2.33)$$

where black hole thermodynamics tells us (see equation (2.40) below) that $f'(1) \propto T$. At $T = 0$ then, we can find after a rescaling of the radial coordinate that the near-horizon geometry up to some constant factors can be written as

$$ds^2 = \frac{1}{\xi^2} \left(-dt^2 + d\xi^2 \right) + dx^2 + dy^2. \quad (2.34)$$

This geometry is now no longer AdS_4 , but rather $\text{AdS}_2 \times \mathbb{R}^2$ in coordinates $(t, \xi) \times (x, y)$.¹² A similar metric can still be found by making the right choices of coordinate substitutions in a series expansion in T for $T/\mu \ll 1$. [71, 93] What is interesting here is the symmetries of this $\text{AdS}_2 \times \mathbb{R}^2$ space-time. In empty AdS_4 , there is a global scaling symmetry

$$(t, x, y, z) \rightarrow \lambda(t, x, y, z). \quad (2.35)$$

In this $\text{AdS}_2 \times \mathbb{R}^2$ case there is a symmetry that goes as

$$(t, \xi) \rightarrow \lambda(t, \xi), \quad (x, y) \rightarrow (x, y). \quad (2.36)$$

When writing this in terms of a dynamical critical exponent z , which is associated with a scaling

$$t \rightarrow \lambda t, \quad x \rightarrow \lambda^{\frac{1}{z}} x, \quad (2.37)$$

it can be seen that this $\text{AdS}_2 \times \mathbb{R}^2$ near-horizon geometry corresponds to a $z \rightarrow \infty$ system. In other words, the spatial dimensions completely decouple from the temporal and radial dynamics. This is exactly the local quantum criticality that is seen in the strange metal. [50, 90] This local quantum criticality is a feature of the near-horizon geometry, and therefore only of the lowest energy scales that enter in the problem, near the end of the RG flow. In the UV of the theory this symmetry is not present, and therefore this is an emergent property of the system. This peculiar fact, that the RN black hole turns out to have an emergent quantum critical sector, is one of the reasons that the string theory community has been looking to it as a point of departure for looking at interesting condensed matter systems such as the strange metal. This emergent quantum critical sector is unique and not found in any conventional condensed matter theory, however it turns out to be one of the most natural and simple to find things when doing holography. [61]

2.5.2. Thermodynamics of Reissner-Nordström

The RN black hole is dual to a quantum field theory at both finite temperature and chemical potential. For this solution, it is possible to evaluate the Euclidean on-shell action I_E , which according to the dictionary in table 2.1 yields the thermodynamic potential

$$\Omega = T I_E. \quad (2.38)$$

¹²Or, in general, $\text{AdS}_2 \times \mathbb{R}^d$ when starting from AdS_{d+2} .

From this it is possible to compute all thermodynamical quantities such as entropy and compressibilities in terms of derivatives of this free energy.[94–96] As luck would have it, in the Reissner-Nordström black hole some of these quantities can actually be evaluated directly from the near boundary behaviour or horizon integrals through standard dictionary entries without having to compute the entire free energy and compute derivatives. This is especially useful in numerical settings, where computing and finding the derivatives of the free energy by integrating the on-shell action can be very challenging. Rescaling all observables to the chemical potential μ ¹³ and one can find out that there is also a finite charge density

$$\frac{\rho}{\mu^2} = -\partial_z A_t \Big|_{z=0} = \frac{1}{\mu}. \quad (2.39)$$

The temperature of the black hole can be evaluated by evaluating the surface gravity of the black hole and is given by [76, 77]

$$\frac{T}{\mu} = \frac{|f'(1)|}{4\pi} = \frac{12 - \mu^2}{16\pi\mu}. \quad (2.40)$$

The black hole entropy, which via black hole thermodynamics can be related to black hole surface area, is given by

$$s = \frac{S}{\mu^2} = \frac{4\pi}{\mu^2}. \quad (2.41)$$

This formula for the entropy may seem innocuous, but there is some important physics in it. As can be deduced from equation (2.40), the zero-temperature limit corresponds to $\mu \rightarrow \sqrt{12}$. One of the characteristics of the RN black hole is that the zero temperature limit has a finite horizon area.[92] Since the entropy is proportional to the horizon area, this means that the entropy is still finite even at zero temperature. For condensed matter systems, which we are interested in, this is a large complication, as they have no entropy at $T = 0$.¹⁴ Naturally, one should feel sceptic of the results coming out of RN for this very reason. This does not mean though that everything coming out of this model is useless. In reality, what it means is that we should be keeping an eye open to places where this might become an important factor and either adapt our interpretations accordingly, or alternatively switch to other types of black hole solutions where this issue does not appear. The more cynical view is that this is a fundamental sickness of the AdS-Reissner-Nordström black hole for the purposes of condensed matter physics and a strong argument for the use of other black hole solutions such as the Gubser-Rocha black hole of section 2.6, which is why it has been used for the majority of chapters 5 and 6.[98, 99]

Regarding the energy density and pressure, we can compute these via the expectation value of the stress-energy tensor $\langle T_{\mu\nu} \rangle$ of the field theory by standard holographic renormalization techniques. In this particular case, that is done by constructing

$$\tilde{T}_{\mu\nu} = 2(K_{\mu\nu} - Kh_{\mu\nu}) - 4h_{\mu\nu}, \quad (2.42)$$

¹³For the sake of simplicity, I have not written down the black hole in terms of its charge Q , which is the more usual starting point, but rather already in terms of μ . These two quantities are of course related, and can be expressed in terms of each other.

¹⁴Zero-temperature entropy does arise sometimes, for example in frustrated systems, but these are not in the scope of this thesis.[97]

where $h_{\mu\nu}$ is the induced metric at a slice at a constant radial $z = \epsilon$ away from the boundary, $K_{\mu\nu}$ and K are extrinsic curvature and its trace, respectively, and μ, ν run over the non-radial indices (t, x, y) . The constant -4 arises from the Gibbons-Hawking-York counterterm.[75, 100] When appropriate counterterms are taken into consideration, in the limit $\epsilon \rightarrow 0$ the following expression becomes finite, yielding us the stress tensor

$$\langle T_{\mu\nu} \rangle = \lim_{\epsilon \rightarrow 0} \frac{1}{\epsilon} \tilde{T}_{\mu\nu}. \quad (2.43)$$

Evaluating this in the homogeneous Reissner-Nordström black hole this gives

$$-T^t_t = 2T^x_x = 2T^y_y = 2 + \frac{\mu^2}{2}. \quad (2.44)$$

This means that the corresponding internal energy and pressure are given by

$$\frac{E}{\mu^3} = \frac{2P}{\mu^3} = \frac{1}{\mu^3} \left(2 + \frac{\mu^2}{2} \right). \quad (2.45)$$

Note from this that this is a conformal system as the trace of the stress tensor vanishes

$$\langle T^\mu_\mu \rangle = E - 2P = 0. \quad (2.46)$$

2.6. Einstein-Maxwell-Dilaton Theory

The Reissner-Norström black holes that have been discussed so far are ubiquitous in AdS/CFT, as they are just about the simplest system that can provide a finite chemical potential. The ease of computations in the system has been the main driver for its popularity. The thermodynamics of the RN states are however rather problematic, as there is no condensed matter system we could want to describe that has the property of finite ground-state entropy. In this sense, the RN black hole is only one of a much larger family of black holes which can have different types of near-IR scaling behaviours.

A part of this family of black holes can conveniently be explored by coupling a dilatonic field into the theory.[61, 101, 102] Dilatons are rather general in holography, as mentioned above in section 2.3.3. These dilatonic fields are dynamical and back-react onto the geometry, but more important is the way in which they couple to the Maxwell sector. A generic EMD Lagrangian where a single dilaton field ϕ is coupled in can be written as

$$\mathcal{L}_{\text{EMD}} = R - \frac{Z(\phi)}{4} F_{\mu\nu} F^{\mu\nu} - \frac{1}{2} \nabla_\mu \phi \nabla^\mu \phi - V(\phi). \quad (2.47)$$

There are here two coupling functions, $Z(\phi)$ and $V(\phi)$. V is the potential for the scalar, which also includes the cosmological constant in its series expansion, $V(0) = 2\Lambda$.

Often, $V(\phi)$ can take the form of a sum of exponentials, sometimes balanced to form hyperbolic geometric functions. The coupling function $Z(\phi)$ presents a modification of the coupling constant of the Maxwell sector in the theory. This changes the effective value of the charge density in the system, as through the holographic dictionary

$$\rho_{CFT} = Z(\phi) F^{tz} \Big|_{z=0}. \quad (2.48)$$

Compare this to the Einstein-Maxwell setup that was used for the RN black holes, where $Z(\phi) = 1$. A crucial difference with the RN black hole is in the low-temperature IR geometry. Where for RN we are left with a finite-size extremal black hole that carries a large amount of zero-temperature entropy, the general EMD black holes can have horizons that keep shrinking all the way to zero temperature, giving the entropy a temperature dependence

$$S \sim T^\alpha, \quad \alpha > 0. \quad (2.49)$$

The form of the potentials V, Z is generically what determines the scaling properties of the solutions.[101, 102] The dilaton takes on a large value at the horizon, and therefore in order to understand the horizon scaling we only need to consider what the leading near-horizon behaviours of the potentials are.[102] In typical top-down cases, the exponentials scale near the horizon like

$$Z \sim e^\phi, \quad V \sim e^{-\phi}. \quad (2.50)$$

But, as we have seen before, in holography we are not bound by only exact top-down constructions, and we are able to take other values for the parameters. The potentials are typically parametrized by the factors γ, δ as

$$Z = e^{\gamma\phi}, \quad V = V_0 e^{-\delta\phi}. \quad (2.51)$$

The scaling analysis in these theories is a bit more complicated than in the Reissner-Nordström case. In standard coordinates, the metric of the deep IR at zero temperature can be described as

$$ds^2 \sim r^{-2\theta/d} \left(-r^{2z} dt^2 + r^2 d\vec{x}^2 + \frac{1}{r^2} dr^2 \right). \quad (2.52)$$

Here the coordinate r ranges from the interior $r = 0$ to the boundary $r = \infty$. The parameter z is one we have encountered above – this is the same dynamical critical exponent as before. The parameter θ is the hyperscaling violation exponent.[103–105] In a very rough description, a theory with parameters (z, θ) will display scaling of the thermodynamical observables as if the theory has dynamical critical exponent z but lives in $d - \theta$ dimensions.[104] The choices made for the coupling exponents γ, δ can be mapped onto resulting values of z, θ . [102] It is important that in the presence of $\theta \neq 0$, the near-IR theory is no longer scale-invariant, but rather it is scale-covariant, with under the scale transformation[104]

$$t \rightarrow \lambda^z t, \quad \vec{x} \rightarrow \lambda \vec{x}, \quad r \rightarrow \lambda r. \quad (2.53)$$

The metric then transforms as

$$ds^2 \rightarrow \lambda^{2\theta/d} ds^2. \quad (2.54)$$

There are several interesting ideas that we can consider for θ, z . For example, $\theta = d - 1$ can be thought of as describing the physics of a system near its Fermi surface, which is always has a lower dimensionality than the dimensionality of the theory.[104] For reasons that will become clear soon, the most interesting value in relation to the strange metal is the rather peculiar choice of $z, -\theta \rightarrow \infty$.

2.6.1. The Gubser-Rocha Conformal-to-AdS₂ Metal

When considering the thermodynamics of these EMD systems, we can find that the entropy will scale with temperature as

$$S \sim T^{(d-\theta)/z}. \quad (2.55)$$

If we wish to describe a strange metal, we would ideally like to consider an entropy that scales as temperature like

$$S \sim T^1. \quad (2.56)$$

This is the well-known Sommerfeld entropy, also experimentally observed in strange metals.[52] To take full advantage of the power of holography we would want to do this in a setting where we are locally quantum critical.[50] In other words, that means $z \rightarrow \infty$. These two ideas can only both be satisfied in the limit

$$z, -\theta \rightarrow \infty, \text{ such that } \frac{-\theta}{z} = 1. \quad (2.57)$$

A hyperscaling violation exponent of minus infinity is rather strange, and definitely is hard to think about in terms of an effective dimensionality of a problem. Nevertheless, it is a well-defined limit.[101, 102] It has been shown that these models can reproduce the linear-in- T resistivity of strange metals as well.[106] To be more exact, these systems correspond to the choice $\gamma = -\delta = 1/\sqrt{3}$ in term of the coupling exponents. That means we have that the following couplings

$$Z(\phi) = e^{\phi/\sqrt{3}}, \quad V(\phi) = 2\Lambda \cosh\left(\frac{\phi}{\sqrt{3}}\right). \quad (2.58)$$

This choice of potential is consistent with what was discussed earlier, as it is only the leading exponential behaviour that is relevant in the IR, so only one of the exponential terms in the hyperbolic cosine will be of relevance there. This potential has the added benefit of having the property that

$$V'(\phi) \Big|_{\phi=0} = 0, \quad (2.59)$$

which allows for proper AdS asymptotics.[102] This system turns out to have an analytical solution in the form of a black-brane solution.[98, 107] The metric, scalar and gauge profiles of this solution can be parametrized in terms of the charge Q of the black hole for a horizon radius of $z_H = 1$

as

$$\begin{aligned} ds^2 &= \frac{1}{z^2} \left(-f(z)dt^2 + \frac{1}{f(z)}dz^2 + g(z)(dx^2 + dy^2) \right), \\ \phi &= \frac{\sqrt{3}}{2} \log(1 + Qz), \\ A &= \sqrt{3Q(1+Q)} \frac{1-z}{1+Qz} dt. \end{aligned} \tag{2.60}$$

The two functions f, g are given by

$$\begin{aligned} f(z) &= \frac{(1-z)}{g(z)} \left(1 + (1+3Q)z + (1+3Q(1+Q))z^2 \right) \\ g(z) &= (1+Qz)^{3/2}. \end{aligned} \tag{2.61}$$

The chemical potential is given by $\mu = \sqrt{3Q(1+Q)}$. In contrast to the RN solution, from a simplicity standpoint the preferred parameter for this theory is Q , as the expressions in terms of the chemical potential, though equally valid, are simply horrible to read. Nonetheless, in a similar fashion to RN we will prefer to think of observables and parameters in units of chemical potential, as that is a scale we can make reference to when looking at physical experiment. Black hole charge itself does not have a physically relevant measure. The thermodynamics of this state are given by

$$T = \frac{3\sqrt{1+Q}}{4\pi} \Rightarrow \frac{T}{\mu} = \frac{\sqrt{3}}{4\pi\sqrt{Q}}. \tag{2.62}$$

The entropy is again given by the horizon area

$$S = 4\pi \int \sqrt{h} = 4\pi (1+Q)^{3/2} \Rightarrow \frac{S}{\mu^2} = 4\pi \frac{\sqrt{1+Q}}{3Q}, \tag{2.63}$$

and the charge density is ¹⁵

$$\rho = \mu(1+Q) \Rightarrow \rho/\mu^2 = \frac{\sqrt{1+Q}}{\sqrt{3Q}} \tag{2.64}$$

As can be expected, the temperature dependence of the thermodynamical observables is clearly different from those in the Reissner-Nordström black hole. It is easiest to think in the parameter Q . The temperature scales as

$$T/\mu \sim Q^{-1/2}, \tag{2.65}$$

so at low temperature Q is large. The entropy similarly scales as

$$S/\mu^2 \sim Q^{-1/2} \tag{2.66}$$

in the large- Q regime, so indeed we have that

$$\frac{S}{\mu^2} \sim \frac{T}{\mu} \tag{2.67}$$

¹⁵The factor $Z(\phi)$ mentioned earlier in equation (2.52) is absent, as $Z(\phi(z=0)) = Z(0) = 1$.

at low temperatures $T/\mu \ll 1$. The scaling at large T is different, as for large T we have that the parameter Q is small, and therefore

$$S/\mu^2 = \frac{4\pi\sqrt{1+Q}}{3Q} \sim 1/Q \sim T^2. \quad (2.68)$$

The charge density also shows two different regimes. For large Q the charge density scales as

$$\rho/\mu^2 \sim Q^0 \sim T^0, \quad (2.69)$$

while for small Q the constant term dominates in the numerator, meaning that

$$\rho/\mu^2 \sim Q^{-1/2} \sim T^1. \quad (2.70)$$

The stress tensor in this system requires a bit more consideration. The full discussion of this has been the subject of one of the papers that make up this thesis, as given in chapter 5. Other references that have dealt with this topic have overlooked certain subtle points in relation to near-boundary expansions of the analytical solution when considering quantization choices.[108, 109] The resulting stress tensor including counterterms is now expressed as

$$T_{ij} = 2K_{ij} - 2({}^dR_{\gamma,ij}) - 2(K+2)\gamma_{ij} + \gamma_{ij} \left[c_\phi \phi N^z \partial_z \phi + \Lambda_\phi \phi^2/2 \right], \quad (2.71)$$

where N_μ is the outward-pointing unit normal vector. The coefficients are then fixed to be

$$\Lambda_\phi = 2c_\phi - 1, \quad c_\phi = \frac{1}{3}. \quad (2.72)$$

The first of these is easy to understand, as both terms can contribute to cancelling the lowest-order divergence. The argument for choosing $c_\phi = 1/3$ is more subtle, but essentially boils on choosing the scalar to be a marginal operator in the theory. The resulting thermodynamics are that of a one-charge theory, rather than the generic two-charge that would arise from coupling in a scalar to the boundary theory. The full details can be found in chapter 5. The resulting expressions for the stress energy tensor are rather simple,

$$-T_t^t = 2T_x^x = 2T_y^y = 2(1+Q)^3. \quad (2.73)$$

Hence the energy and pressure can be expressed as

$$\frac{E}{\mu^3} = \frac{2P}{\mu^3} = \frac{2}{\mu^3} (1+Q)^3 = \frac{2}{3\sqrt{3}} \left(1 + \frac{1}{Q}\right)^{3/2}. \quad (2.74)$$

where again we recover a conformal theory.

2.6.2. DC Conductivity in the Gubser-Rocha Model

The DC conductivity of this system is formally divergent. The system is translationally invariant, so momentum is conserved and there is no resistance in the system to a DC perturbation. There is

a large amount of spectral weight contained in a δ -peak located at the origin. An important result was found in massive gravity variations on the RN and GR model where momentum is no longer conserved.[106, 110–112] Massive gravity is a slightly peculiar construction, where a frame-fixing occurs due to the introduction of a reference metric. This breaks diffeomorphism invariance, and as a result the graviton acquires a mass. Massive modes propagating in the bulk space-time now only have a finite lifetime, so this causes linear momentum to be able to decay in the system. Since momentum is now no longer conserved, this renders the DC conductivity finite. Spectacularly, in the GR model when momentum is indeed not conserved, the resistivity acquires a dependence

$$\rho_{DC} \propto T + O(T^2). \quad (2.75)$$

This is a phenomenal result, and we might expect to be able to find this in other systems where conservation of momentum is removed through more realistic methods, as massive gravity, though holographically a sound theory, has little bearing on the physics in the lab. In particular, one could break translations into an (ionic) lattice, which has indeed been shown to have similar effects in terms of breaking momentum conservation.[110, 111] This is the theme of this thesis.

2.7. Breaking Translational Symmetry

The allusion to massive gravity models just made aside, all results so far have got one thing in common, and that is that all models are perfectly translationally invariant, momentum is still perfectly conserved. The two transverse directions (x, y) do not contain any structure at all. Of course in actual physical systems, this is not the case. For Drude-like transport, which is observed in even the strange metals at low frequency, the source of momentum dissipation is not something as holographic and weird as a ‘massive gravity’ construction. Instead, we know very well that translational and rotational symmetries of space-time are broken into some crystal lattice.[113] There are several ways to break translational symmetry in holography. The computationally more straightforward ones are models that break translational symmetry in a homogeneous way, which means that the differential equations that describe the systems are only dependent on the radial coordinate and any dependence on the transverse coordinates is engineered to be absent.[114–117] This again is a very particular construction, and if we are to do an honest job using holography to model physical systems in the presence of a crystal lattice we should have an actual lattice present. This requires a periodic modulation that captures both the rotational and translational properties of a crystal lattice. The way to really achieve that is to let go of the simple radial-only models and turn the problem of solving for the bulk geometry into a set of partial differential equations, that now can also depend explicitly on the transverse coordinates as well as the radial coordinate. This type of symmetry breaking is often called inhomogeneous symmetry breaking, and it is of this type that the remainder of this thesis explores the intriguing consequences.

3. Numerical Holography and Lattices

The effort of breaking translational symmetry inhomogeneously in holographic condensed matter systems goes back over a decade. The basic idea rather simple. Translational symmetry breaking is introduced explicitly by modulating one of the source terms of the field theory. There are different setups with different fields being sourced, and there are many things that can be computed, but first let us focus on the generics, how the translational symmetry is broken and what the general improvements in the works related to this thesis have been to various existing setups in order to get more accurate results. [107, III, 114, 118–124]

Now let us finally break the translational symmetry, but keep the setup static, without any time dependence. While we can in principle use holography to compute non-stationary, time-dependent black holes, this is technically extremely challenging, not to mention in the presence of translational symmetry breaking.[125] As mentioned before, the static solution is thought to describe late-time locally thermally equilibrated states.

3.1. Spatial Modulation

The first real calculations using holographic lattices were done by Horowitz, Santos and Tong, where they took Reissner-Nordström and imposed a lattice in two different ways, first by modulating the the source term of an extra backreacted scalar field, and also by modulating the chemical potential.[118, 120] The modulation of the chemical potential is what comes closest to reproducing an actual ‘ionic lattice’, where regions of high and low chemical potential are spatially distributed, and have regions of low and high charge density associated with them, without the need for extra scalar fields.

The procedure to do this increases in complexity the more dimensions get their translational symmetry broken. I will first state the most general ansatz that is used for two-dimensional lattices. After this, I will show an example computation for a one-dimensional lattice in RN without extra scalars, as this simplifies the setup considerably and allows for the highlighting of some important points.

3.1.1. Bidirectional Lattices

The lattices presented in this thesis have translational symmetry broken in either one or two directions in the boundary. The mechanism by which this was imposed is general in both RN and GR black holes. It is possible to have a wide variety of extra phenomena take place, for example pseudoscalars that spontaneously break translational symmetry.[119, 121, 126] However, research

projects started in these directions were never brought to a satisfying conclusion, and are therefore not included in this thesis. In this work, only the chemical potential, set by $A_t(z = 0)$, is modulated explicitly.

3.1.2. RN Lattice Model

The action and equations of motion for the full Reissner-Nordström setup are given by

$$S = \int d^4x \sqrt{-g} \left(R - 2\Lambda - \frac{1}{4} F_{\mu\nu} F^{\mu\nu} \right). \quad (3.1)$$

with associated Einstein and Maxwell equations

$$\begin{aligned} R_{\mu\nu} + 3g_{\mu\nu} &= \frac{1}{2} \left(F_{\mu\rho} F_{\nu}{}^{\rho} - \frac{1}{4} g_{\mu\nu} F_{\rho\sigma} F^{\rho\sigma} \right), \\ \nabla_{\mu} F^{\mu\nu} &= 0. \end{aligned} \quad (3.2)$$

Since time-reversal symmetry is not broken, it is possible to find solutions to the equations of motion where 8 fields are coupled together: the time component of the gauge field, the diagonal metric terms, and the spatial-radial off-diagonal metric terms. Other terms, such as the spatial terms of the gauge field, do not couple in as these would present themselves as effective magnetic fields in the electromagnetic field strength tensor. We do not break time reversal symmetry in our lattice, which means that these modes decouple. There is still some gauge freedom stemming from diffeomorphism invariance, which expresses itself in the Einstein equations by yielding constraint equations rather than dynamical equations for some of its components. These gauge freedoms will need to be fixed, more on which will follow in section 3.1.3. In general then we need to therefore solve for all 8 fields non-linearly simultaneously in order to obtain a fully back-reacted solution.

The metric is most conveniently parameterized via

$$\begin{aligned} ds^2 &= \frac{1}{z^2} \left(-Q_{tt} f(z) \eta_t^2 + Q_{xx} \eta_x^2 + Q_{yy} \eta_y^2 + \frac{1}{f(z)} Q_{zz} dz^2 \right), \\ \eta_t &= dt, \\ \eta_x &= dx + Q_{xy} dy + Q_{xz} dz, \\ \eta_y &= dy + Q_{yz} dz, \end{aligned} \quad (3.3)$$

accompanied by the gauge field

$$A = \bar{\mu}(1 - z) a_t dt \quad (3.4)$$

The function $f(z)$ is kept fixed here to be equal to that in equation (2.32)

$$f(z) = (1 - z) \left(1 + z + z^2 - \frac{\mu^2 z^3}{4} \right). \quad (3.5)$$

In principle, these functions Q_{ij} , a_μ , φ can be functions of x , y and z , where we do not allow time dependence in order to maintain the static black hole. Translational symmetry breaking is wired in as follows. We will always restrict to rectangular lattice setups¹, where we assume that there are two independent periodicities going on in both of the transverse directions where we identify the coordinates

$$x \sim x + L_x, \quad y \sim y + L_y. \quad (3.6)$$

All of the functions Q_{ij} , a_μ , φ will therefore be assumed to have the same periodicity. For purely spontaneous translational symmetry breaking considerations this is all that is done, although one must be careful to pick a period which is compatible with the preferred wave vector of the instability. In the case of explicit modulation we choose the chemical potential to be also some periodic function with the same period, however we can choose freely how to fill this in. In practice, we always use a single harmonic potential in one or two directions to fill the periodic domain, but it is possible to have multiple periods of the explicit potential in the domain. This means that the time component of the gauge field can go like

$$a_t(x, y, z = 0) = \bar{\mu} \left(1 + \mathcal{A}_x \cos(G_x x) + \mathcal{A}_y \cos(G_y y) \right). \quad (3.7)$$

In order to satisfy periodic boundary conditions, this must mean that

$$L_{x,y} = \frac{2\pi N_{x,y}}{G_{x,y}}. \quad (3.8)$$

The resulting Einstein equations, when the ansatz is plugged in, is to not mince words a complete mess. There are many hundreds or thousands of terms following from all the different combinations of derivatives and non-linearities.² In the presence of any kind of translational symmetry breaking there is no analytical non-perturbative solution, and therefore the equations of motion (3.2) have to be evaluated numerically. In order to properly numerically evaluate this problem, we want to be able to phrase this as a boundary value problem. Two of the boundaries, namely in the x and y directions are straightforward, as periodic boundary conditions will impose conditions on the fields and their derivatives at the points of identification over the entire range of z . The boundary conditions on both ends of the radial direction require a bit more thought. At the boundary we want to impose AdS asymptotics —we are doing AdS/CFT after all—possibly supplemented by our explicit translational symmetry breaking term. At the horizon it is regularity of the fields, as well as the requirement of constant temperature across the black hole horizon that yields enough boundary conditions for a well-posed boundary value problem.

To give a quick summary, at the boundary we can impose that only the diagonal metric fields are equal to 1, which recovers AdS asymptotics

$$Q_{ij,i=j}|_{z=0} = 1, \quad Q_{ij,i \neq j}|_{z=0} = 0. \quad (3.9)$$

¹Note that the ansatz presented above is slightly less general than the one presented in [127], but is much more straightforward to deal with in the case of rectangular lattices. The reduced complexity of the ansatz also makes it easier for computer algebra software to handle the very large equations that come out when the equations of motion are applied to this ansatz.

²Anecdotally, these equations can become so big that when compiled into C-code, simply cannot handle the sheer size and errors out.

along with a gauge field

$$\bar{\mu} a_t|_{z=0} = \mu(x, y) \quad (3.10)$$

The chemical potential $\mu(x, y)$ is what can set our explicit ionic lattice, via

$$\mu(x, y) = \bar{\mu} a_t(x, y) = \bar{\mu} \left(1 + \mathcal{A}_x \cos(G_x x) + \mathcal{A}_y \cos(G_y y) \right). \quad (3.11)$$

The boundary conditions at the horizon at $z = 1$ follow from regularity and can be found imposing a series expansion on the equation of motion after gauge fixing³ in powers of $z - 1$ and requiring that each of the terms in the series expansions vanish. This will give a set of in general non-linear boundary equations of the form

$$\partial_z F_i|_{z=1} = g \left(\{F_j, \partial_x F_j, \partial_y F_j\} \right), \quad (3.12)$$

or in other words, boundary conditions can be found for the radial derivatives of all the fields F in the ansatz in terms of all the other fields and their tangential derivatives on the horizon. This is then supplemented by the condition

$$Q_{tt}|_{z=1} = Q_{zz}|_{z=1} \quad (3.13)$$

which encodes for the surface gravity and therefore temperature to be constant across the black hole horizon.

3.1.3. DeTurck Method

There is one major thing missing from the equations before they can be solved. The Einstein equations are hyperbolic-elliptical, which poses problems for any numerical effort.[128, 129] The problem that has been posed throughout section 3.1 so far ostensibly has the form of a boundary value problem. This type of problem, especially in a non-linear setting, lends itself very well to numerical approaches when the problem is elliptic. This is due to the fact that the eigenvalues of the principal symbol of an elliptic problem all have the same sign, and therefore it is possible to use relaxation-like approaches, where we start from an initial guess and let the system ‘settle’ into the true solution. The Einstein equations as we posed them are not elliptic.[128] Instead, due to gauge freedom, it is only elliptic for the physical degrees of freedom. The way this problem is phrased leaves some room for gauge freedom, which presents itself as an invariance under coordinate reparametrization. The exact phrasing and solution to this problem have been described in great detail.[129] The main message to take away is that we want to fix this gauge invariance in our equations, which would render the equations for all fields elliptic. This is one by using the DeTurck method, also known as the DeTurck trick.[130] The equation of motion for the gauge field in the explicit lattice does not require a gauge fix, as typically radial gauge $a_z = 0$ is chosen.

The problem is in essence that we can decompose any perturbation to a solution to the equations of motion into a pure gauge and a transverse part. The principal symbol acting on the pure gauge mode actually annihilates it. This makes the equations for the gauge degrees of freedom into some

³See sections 3.1.3.

kind of lower-order constraint equations in this system. The fix comes by picking a particular vector ξ^μ , the DeTurck vector, which is defined by

$$\xi^\lambda = g^{\mu\nu} \left(\Gamma_{\mu\nu}^\lambda - \bar{\Gamma}_{\mu\nu}^\lambda \right). \quad (3.14)$$

Here $\bar{\Gamma}_{\mu\nu}^\lambda$ is the Christoffel symbol for some reference metric, which is a known solution to the Einstein equations. Choosing a gauge then can be done by for example choosing $\xi^\mu = 0$. This is still a constraint equation. However, we can be even smarter about this, and generate what is called the Harmonic Einstein equations. First we define the harmonic Ricci tensor as

$$R_{\mu\nu}^H = R_{\mu\nu} - \nabla_{(\mu} \xi_{\nu)}, \quad (3.15)$$

which we insert into the equations of motion by simply taking $R_{\mu\nu} \rightarrow R_{\mu\nu}^H$. This turns the set of equations into a manifestly elliptic one. It turns out that finding a solution to the harmonicized equations of motion will then simultaneously take care of solving the original equations of motion as well as the gauge condition. Additionally, finding a solution and showing that its DeTurck vector vanishes guarantees that the solution is not a Ricci soliton.[128]

3.1.4. Thermodynamics of the Lattices

Assuming that a solution to the equations of motion has been found, the first thing that is possible to do is to evaluate the thermodynamics of the phase. The procedure is essentially the same as outlined in section 2.5. The difference now is that the components of the metric and gauge field are now not analytically known, but instead we have to work with numerical values and their numerical derivatives. We can perform a near-boundary expansion up to order z^3 , and use the equations of motion to constrain several of the terms that appear in the boundary expansion. Using the expansions we can find the expressions that are summarized in table 3.1. The field theory

$$\begin{aligned} \langle T_t^t \rangle / \bar{\mu}^3 &= \left(-2 - \frac{\bar{\mu}^2}{2} + \frac{1}{2} \partial_z^3 Q_{tt} \right) \Big|_{z=0}, \\ \langle T_x^x \rangle / \bar{\mu}^3 &= \left(1 + \frac{\bar{\mu}^2}{4} + \frac{1}{2} \partial_z^3 Q_{xx} \right) \Big|_{z=0}, \\ \langle T_y^y \rangle / \bar{\mu}^3 &= \left(1 + \frac{\bar{\mu}^2}{4} + \frac{1}{2} \partial_z^3 Q_{yy} \right) \Big|_{z=0}, \\ \rho / \bar{\mu}^2 &= (a_t - \partial_z a_t) / \bar{\mu} \Big|_{z=0}, \\ \mu / \bar{\mu} &= a_t \Big|_{z=0}, \\ S / \bar{\mu}^2 &= 4\pi \sqrt{Q_{xx} Q_{yy}} / \bar{\mu}^2 \Big|_{z=1}. \end{aligned}$$

Table 3.1.: Observables in the RN Lattice in terms of the UV expansions of the fields in the ansatz, where values per unit cell can be obtained by averaging over the unit cell in the transverse directions.

is still conformal, provided one uses the correct prescription in GR models explained in chapter 5, as the trace of the stress tensor still vanishes:

$$\left\langle T_t^t + T_x^x + T_y^y \right\rangle \propto \left(\partial_z^3 Q_{tt} + \partial_z^3 Q_{xx} + \partial_z^3 Q_{yy} \right) \Big|_{z=0} = 0, \quad (3.16)$$

which can be found as a constraint for the third-order components from the near-boundary expansion of the equations of motion. The accuracy to which this holds can be used as a convergence check, since a well-converged solution will have equation (3.16) vanish to some good accuracy.

3.2. Solutions to the Unidirectional Lattice

Numerical solutions to this differential equation problem need to deal with another problem: the equations are not well defined at the horizon and boundary, as some coefficients of the equations scale as z^{-4} as $z \rightarrow 0$. Therefore, simply putting it in a black-box algorithm like Mathematica's `NDSolve` is unlikely to provide useful results, as it will attempt to evaluate the equations of motion so close to the boundary that this results in an incredibly stiff problem. One option is to make an explicit series expansion to some finite cut-off and integrating from there.[131] This method was used in many early constructions of numerical holography, and can be improved by going either to a high order in series expansion or making the cut-off very small. This has some disadvantages, as explicitly constructing the power expansion required to get high accuracy becomes quite cumbersome especially when the boundary starts to have one or two transverse spatial dimensions. Due to the nature of the Einstein equations these are simply big expansions, and take a long time to compute even with modern computer algebra systems.

The alternative is to discretise the problem on a structured grid, where there is one set of grid points located at the boundary, and another some finite δz away from it. On this grid, we can then solve the problem with finite-difference methods. On the boundary and horizon, we will then only evaluate the boundary conditions. The Dirichlet and Robin boundary conditions presented in section 3.1 are finite on those points. Using a high-enough order in the finite difference scheme makes the divergence at δz not too extremely high, not as divergent as required for (adaptive) black-box routines.

The iterative scheme used needs to depart from some ansatz for the solution. It does not necessarily need to be a solution to the equations of motion in some way, but it needs to be ‘close enough’ to the true solution we are trying to arrive at. The parameters in this scenario are the chemical potential, μ , lattice vector G_x and lattice strength \mathcal{A}_x . As I have set the horizon radius $z_h = 1$, the temperature is then set by the chemical potential to be

$$\frac{T}{\bar{\mu}} = \frac{12 - \bar{\mu}^2}{16\pi\bar{\mu}}. \quad (3.17)$$

Convenient as a starting point for the iterative scheme is often to pick the Reissner-Nordström background at the temperature we desire, or otherwise a known numerical solution at parameters close to the ones we desire. Note that in the translationally invariant RN solution, the parameter

G_x does not have any significance.⁴ The solutions for small lattice strength \mathcal{A}_x will be close to the analytical Reissner-Nordström solution. The resulting lattices are shown in figure 3.1

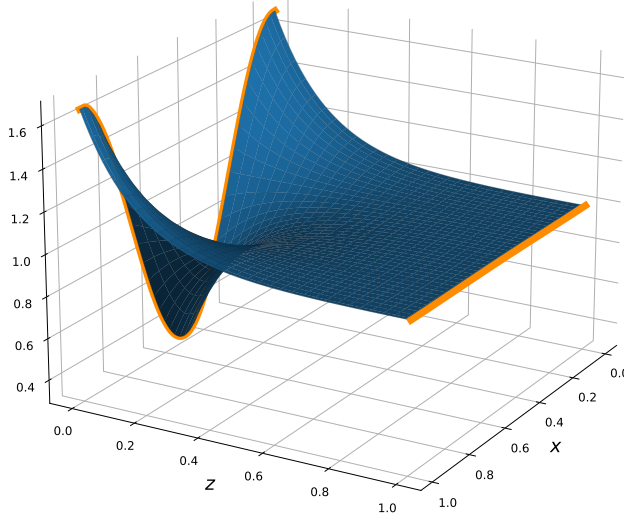


Figure 3.1.: This is an example of a bulk picture of the unidirectional lattice. This particular profile is of the bulk electric field $F_{tz} = -\partial_z A_t$. The parameters here are $T = 0.15\mu$, $G = 4\mu$, $\mathcal{A}_x = 0.1$.

3.2.1. Numerical Convergence of Holographic Lattices

Testing the validity of an ansatz and the code used to compute the numerical solutions is often one of the most important and yet one of the most easy to overlook parts of writing code. This is especially true in an academic setting, where the desire to get results sometimes outweighs the ‘proper’ procedure of testing the code thoroughly before using it in production. Furthermore, it can be possible for the code, even if it is not wrong, to give answers that reach unsatisfactory levels of precision at certain parameters. In the holographic lattices, this can for example be caused by low temperatures or large gradients in the problem. Therefore, it is crucial that there are tools available that can be used not only as sanity checks, but also to prove that a given solution to a problem is satisfactory. In this case there are several tools available. The most useful ones are the

⁴This makes for a good check to see if observables are correctly implemented, as the translationally invariant solution should have no mind of any finite G_x whatsoever.

trace of the stress-energy tensor and the DeTurck vector. In the case of the trace of the stress-energy tensor, it is good practice to have the trace vanish to a much greater accuracy than each of its individual components. The DeTurck vector can be shown to be a purely spatial quantity and therefore it is enough to check that its norm $\xi^2 = \xi^\mu \xi_\mu \geq 0$ vanishes, rather than having to compute whether each component vanishes independently. In order for precision to be under control, these will need to display some key properties, most importantly that it should show that the knobs we can tune that we expect to increase accuracy actually do so. The unidirectional lattice was the primary inspiration for the Python code, which was written to be a very general n -dimensional (non-)linear PDE solver. As it is written in Python it is not extremely fast, however what it lacks in speed it makes up for in flexibility. It is most suited to two-dimensional differential equations, so that is why the unidirectional lattice together with the radial direction is a good test for its performance. This convergence is shown in figure 3.2. Unsurprisingly, increasing the number of points in the lattice as well as the differentiation order increases the precision. The DeTurck vector shows a similar picture in figure 3.3. The difference between the lowest and higher-order finite difference approximations is large, and the diminishing returns between difference order 6 and higher becomes even more apparent, to the point that beyond 40×80 points there is no benefit to the higher-order differentiations any more.

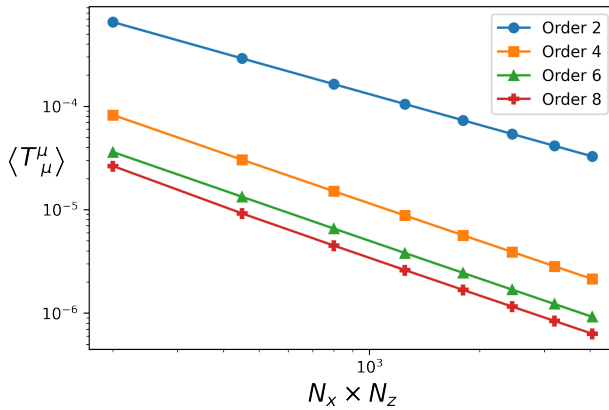


Figure 3.2.: Convergence of the trace of the boundary stress energy tensor as a function of total number of grid points in the problem. For this particular case, the convergence is done at a fixed low temperature and lattice vector as $T = 0.01\mu$, $G = 0.05\mu$, $\mathcal{A}_x = 0.2$, and $N_z = 1.5 \times N_x$. The individual components of T^μ_ν are $O(1)$.

3.2.2. Bidirectional Lattice

The bidirectional lattice has a lot more degrees of freedom to solve for, as there are now N_y times more points in the grid, as well as 15 functions up from 6. In order to tackle this problem, it was necessary to write code in a compiled language. We opted for C, where we were able to use the

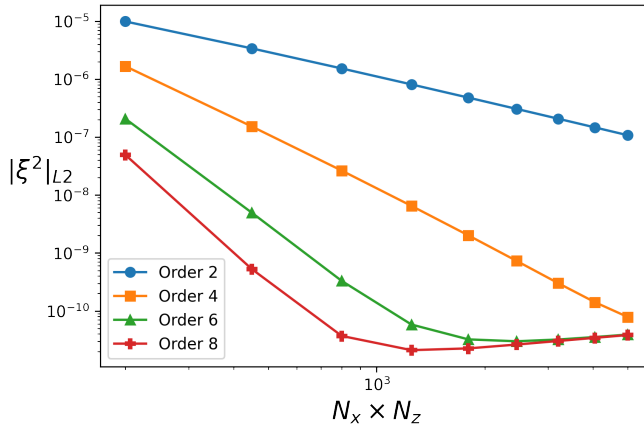


Figure 3.3.: Convergence of the L^2 norm of the ξ^2 over the whole grid. The rate of convergence changes from approximately N^{-1} to N^{-6} when increasing the differentiation order from 2 to 6. Again, this is done at a fixed low temperature and lattice vector as $T = 0.01\mu$, $G = 0.05\mu$, $\mathcal{A}_x = 0.2$, and $N_z = 1.5 \times N_x$.

PETSc library which is suited to run on computing clusters and supercomputers. We can still perform the same convergence checks, however the flexibility of the code is now more limited. In practice, this means that switching differentiation order, which was simply a parameter in the previous code, is now more complicated. The difficulty lies in constructing the Jacobian matrix. This matrix needs to not only couple many fields, but also be consistent in a distributed-memory scheme. While the positions where entries need to be placed is easy to describe symbolically calculate in a program like Mathematica, this is not easily done in pure C. Therefore, based on the 1D results, the order-4 derivatives seem like a good choice. They offer much higher accuracy, but do not increase memory usage by too much, as the number of entries of the matrix per row scales as differentiation order squared due to the mixed derivatives that appear in the expressions. This is clearly seen in figures 3.2 and 3.3. The extra cost in terms of memory use and time it takes to solve makes order 6 and above not worth the trouble.

3.3. Einstein-Maxwell-Dilaton lattices

The Gubser-Rocha black hole that was discussed before in section 2.6 can also be generalised to include translational symmetry breaking effects. The steps that have to be taken to go from the translationally invariant black branes to the EMD lattices is very reminiscent of those necessary to go from the RN black hole to its lattice counterparts.[107] The setup is very similar to the RN ansatz, albeit with one extra field, namely the scalar. In the Gubser-Rocha lattices, we only have access to explicit translational symmetry breaking through the chemical potential, and there are no spontaneous symmetry breaking transitions that we are aware of. The general bidirectional lattice

black hole will have a metric ansatz that looks like

$$\begin{aligned} ds^2 &= \frac{1}{z^2} \left(-Q_{tt} f(z) \eta_t^2 + g(z) (Q_{xx} \eta_x^2 + Q_{yy} \eta_y^2) + \frac{1}{f(z)} Q_{zz} dz^2 \right), \\ \eta_t &= dt \\ \eta_x &= dx + Q_{xy} dy + Q_{xz} dz, \\ \eta_y &= dy + Q_{yz} dz. \end{aligned} \tag{3.18}$$

The gauge field and scalar field will take the form

$$\begin{aligned} A &= A_t dt = \mu \frac{(1-z)}{1+Qz} a_t(x, y, z), \\ \phi &= \frac{\sqrt{3}}{2} \log(1 + Qz\varphi(x, y, z)). \end{aligned} \tag{3.19}$$

The rest of the argument goes much the same way. The boundary conditions are given by an asymptotically AdS boundary and the horizon boundary conditions again arise from a series expansion near the horizon. More tricky, as highlighted in chapter 5, is the boundary condition of the scalar. The boundary condition at $z = 0$ that has been employed here is

$$3Q\varphi + 4\partial_z\varphi - 3Q\varphi^2 = 0 \tag{3.20}$$

which corresponds to an unsourced scalar in mixed $c_\phi = 1/3$ quantisation. This is different from earlier approaches, where the boundary condition do not maintain key properties like conformality of the stress energy tensor in the presence of an explicit lattice.[99]

It will come as no surprise that the derivation of the stress energy tensor and other thermodynamic observables goes in much the same way as the RN black holes the entropy and charge density are easy, as they are given by

$$\begin{aligned} S/\bar{\mu}^2 &= 4\pi \sqrt{(1+Q)^3 Q_{xx} Q_{yy} / \bar{\mu}^2} \Big|_{z=1}, \\ \rho/\bar{\mu}^2 &= ((1+Q)a_t - \partial_z a_t) / \bar{\mu} \Big|_{z=0}. \end{aligned} \tag{3.21}$$

The stress tensor now acquires components not only from the third derivative of the metric fields, but also from the source and VEV of the scalar field through the ϕ -dependent terms in equation (2.71). The full expressions are too long to be included here, but the general structure follows that of table 3.1. Using the near-boundary expansions we can deduce that the trace of this does indeed vanish, giving us always conformal matter, as in the homogeneous case.

3.4. Computing Perturbations

Thermodynamics of the black hole states are good first observables, as they can readily be evaluated from black hole backgrounds by simply reading off certain components. As mentioned before, it is quantities like (thermo)electrical conductivities that we really would like to be able to work with.

In general, many of the quantities that are relevant to physical experiment, such as momentum susceptibilities, conductivities, viscosities and much more can be expressed in terms of two-point functions in the field theory. The procedure to do this is fairly standard, but nonetheless requires a great deal of numerical effort in order to extract worthwhile information at physically interesting parameters. The principle is again the same as in section 2.4.2. Some of the components of the metric and gauge field are perturbed without back-reaction. The equations of motion are then expanded to linear order which gives access to two-point functions in the field theory. The difficulty comes mainly because of the nature of the problem. Not only are the fields at finite frequency and momentum complex-valued, which generally restricts the number of useful numerical solvers and preconditioning routines that exist for the problem⁵, but the problem is also a linear rather than non-linear one. While this removes the need to make many solutions and updates, it does mean that to get a good solution the differential equation we need to solve with higher accuracy, as we cannot rely on the guarantee that if we make a ‘good enough’ update step we still get to a good solution as is the case in the non-linear case. Instead, we need to make sure that we get the solution correct directly. This is in general a tricky thing, and here I present only the overview to show how these techniques are all connected. Many of the results in this section only make sense in the context of a particular lattice setup but the methods will carry over onto other setups too.

3.4.1. Optical Conductivities in the Homogeneous Reissner-Nordström Black Hole

The translationally invariant RN black hole forms a good starting point for these considerations. The quintessential example is the electrical conductivity, which is why it featured prominently for pure AdS in section 2.4.2. What is new here is that at finite chemical potential, there are multiple modes that start to couple in to the electrical conductivity. In particular, if we perturb the gauge field by

$$A_x = \delta A_x(z) e^{-i\omega t} \quad (3.22)$$

we can see that this couples to metric perturbations

$$g_{xt} = \delta h_{xt}(z) e^{-i\omega t}, \quad g_{xz}(z) = \delta h_{xz}(z) e^{-i\omega t}. \quad (3.23)$$

There is a lucky coincidence here as it is possible to make a gauge choice to be in radial gauge to make h_{xz} vanish, and by combining the other two equations of motion the problem can be reduced to a single second order ordinary differential equation for $A_x(z)$. The resulting equation in terms of the chemical potential μ , the emblackening factor $f(z)$ and the parameter γ as [132]

$$(f\delta A'_x)' + \frac{\omega^2}{f}\delta A_x - \frac{4\mu^2 z^2}{\gamma^2}\delta A_x = 0. \quad (3.24)$$

This equation does not have a simple analytical solution, and is only able to be solved numerically. Boundary conditions come from sourcing the (perturbative) electric field $f_{tx} = \partial_t A_x$ along with

⁵It is possible to phrase the problem in terms of coupling of real fields by expanding the real and imaginary parts separately, but that doubles the number of fields and equations in the problem which severely hinders performance.

insisting on computing the retarded Green's function, as this is the physically most relevant one. If we take out an oscillating factor

$$A_x(z) = f(z)^{-4\pi i\omega/T} \tilde{A}_x(z), \quad (3.25)$$

then infalling boundary conditions can be imposed by requiring \tilde{A}_x to be a series expansion in $(z - 1)$. This gives us the retarded Green's function. In general setups, this then gives the same kind of boundary condition expansions as in the lattice, where we can fix the first-order expansion coefficient at the horizon in terms of the horizon values. The conductivity is given by

$$\sigma(\omega) = \frac{A'_x}{i\omega A_x} \Big|_{z=0}. \quad (3.26)$$

Since the equation is linear, we can then fix the boundary condition at the boundary to simply be $A_x(z = 0) = 1$, as we only fix the ratio of coefficients in the expansion at the horizon, and not the value itself.⁶ Equation (3.26) then takes care that only the ratio of subleading to leading component is read off, not the actual value of the solution which is rather arbitrary.

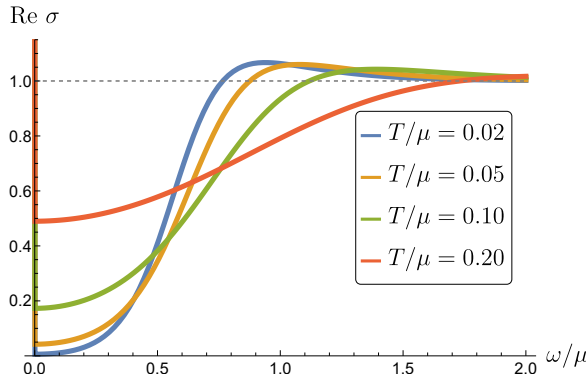


Figure 3.4.: AC conductivity of the RN black hole at finite frequency for different temperatures. Notice how in the high-frequency limit $\omega \gtrsim \mu$, the optical conductivity approaches the zero-density CFT limit $\sigma(\omega) = 1$.

The resulting conductivity can be seen at different temperatures in figure 3.4. Spectral weight is transferred from $\omega < 1$ to $\omega \gtrsim 1$ when temperature is lowered, and a depletion of the conductivity appears to happen for low frequency. The intensity of this depletion increases for lower temperature. Note that the $\omega = 0$ value is divergent due to translational symmetry of the solution. This can also be checked in Kramers-Kronig consistency, which indeed produces a $1/\omega$

⁶There are many other methods of computing conductivities, such as shooting methods and other bulk matching procedures. However, since we have access to a general way of computing partial differential equations through the solver I have developed, it is much more convenient to phrase this in the same framework as the earlier backgrounds and the lattice conductivities as well.

behaviour for $\omega \rightarrow 0$. [133, 134] This kind of result can actually be seen in real condensed matter systems, for example in graphene, which also has a dip below $\omega = \mu$ but recovers a constant $\sigma(\omega) = 1$ at high frequency, as expected for a $2 + 1$ dimensional CFT.

3.4.2. Finite Momentum Correlators

Of course, there is more to transport than just computing the electrical conductivity. Maintaining the fluid analogy, the current-current correlator should be governed by several poles, for example a sound mode in the longitudinal sector and a shear mode in the transverse sector. However, it is not possible to identify these in the homogeneous model unless we go to finite momentum of the correlator, as we require the vector momentum in order to define transverse and longitudinal directions. At $k = 0$, only modes in the spin zero-sector can appear. The general ansatz for the perturbation at finite frequency and momentum is

$$\begin{aligned} g_{\mu\nu} &= g_{\mu\nu}^{(0)} + \varepsilon h_{\mu\nu}(z) e^{-i(\omega t - k_x x - k_y y)} + O(\varepsilon)^2, \\ A_\mu &= A_\mu^{(0)} + \varepsilon b_\mu(z) e^{-i(\omega t - k_x x - k_y y)} + O(\varepsilon)^2. \end{aligned} \quad (3.27)$$

$g^{(0)}$ and $A^{(0)}$ are the background values of the metric and gauge field that have already been computed. If we enter this ansatz into the equation of motions (3.2), at first order in ε we will get a linear set of coupled differential equations for the perturbations in the presence of a fixed background. Using the translationally invariant Reissner-Nordström background, the perturbations will not in general have any more dependence on the transverse directions x, y other than in the oscillating exponential. As the background is rotationally invariant, we can freely pick $\vec{k} = k\hat{x}, k_y = 0$. In this case now, the modes $h_{ty}, h_{xy}, h_{zy}, b_y$ are odd under parity $y \rightarrow -y$ and will therefore decouple from the rest of the perturbations which are even under parity. The even-parity modes will be the fields that couple in the longitudinal sector, and the odd-parity modes correspond to transverse sector. [135] There is a rather large amount of gauge freedom left in the equations at the moment, stemming from diffeomorphism invariance and $U(1)$ gauge symmetry of the Maxwell field. Common choices to fix the gauge are the radial gauge, which simply sets [135]

$$h_{\mu z} = b_z = 0. \quad (3.28)$$

Another popular gauge choice is DeDonder and Lorenz gauges, where [136]

$$\nabla^\mu (\bar{h}_{\mu\nu} = 0), \quad \nabla^\mu b_\mu = 0, \quad (3.29)$$

where \bar{h} is the trace-reversed perturbation metric

$$\bar{h}_{\mu\nu} = h_{\mu\nu} - \frac{1}{2} \text{Tr}(h) g_{\mu\nu}^{(0)}. \quad (3.30)$$

This is in principle a general ansatz for computing any perturbation we wish. When sourcing the correct components of $h_{\mu\nu}$, one can for example compute correlators

$$G_{T^{\mu\nu}T^{\mu\nu}}(\omega, k) \sim \langle h_{\mu\nu} h_{\mu\nu} \rangle. \quad (3.31)$$

In the case of the homogeneous RN black hole things simplify tremendously, and it is possible to make some clever combination of fields into what are called the master field equations.[135, 137, 138] This however is rather specific and does not apply whenever a lattice is in play. Therefore, I will not expand in great detail on this procedure in here. Instead, let us stay focused on electrical conductivity. The choice of transverse or longitudinal sector will come from our choice of electric field. The source of the electric field turns out to be the value of the $b_{x,y}$ perturbations at the boundary

$$E_x = f_{tx}|_{z=0}, \quad E_y = f_{ty}|_{z=0} \quad (3.32)$$

while the responses are

$$J_x = f_{zx}|_{z=0}, \quad J_y = f_{zy}|_{z=0} \quad (3.33)$$

where $f_{\mu\nu}$ is the field strength tensor at first order in the perturbation parameter ε . This corresponds to picking

$$E_x = i\omega b_x(z=0), \quad E_y = i\omega b_y(z=0). \quad (3.34)$$

For the electrical conductivity, the correlators are computed

$$G_{J^i J^j}(\omega, k) = \left. \frac{\partial_z b^i(\omega, k, z)}{b_j(\omega, k, z)} \right|_{z=0}. \quad (3.35)$$

The conductivity then we need to keep in mind that at finite momentum, we need to subtract the real part of the zero-frequency limit of the correlator in order to remove certain contact-like terms [81, 139]

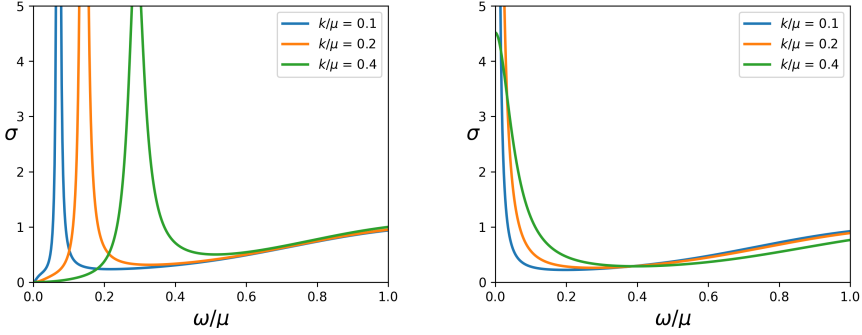
$$\sigma(\omega, k) = \frac{G(\omega, k) - \text{Re } G(\omega, k \rightarrow 0)}{i\omega}. \quad (3.36)$$

In the translationally invariant situation, we expect two things depending on the direction of k with respect to E . In the longitudinal channel, where $\vec{k} \parallel \vec{E}$, we expect to see a sound-like response, with a corresponding sound peak at some $\omega = v_s k$ where v_s is the sound velocity. This kind of response is shown in figure 3.5a. There is also a diffusion pole which causes some momentum dissipation near $\omega = 0$, but in the specific case of longitudinal conductivity this is suppressed by a factor ω^2/k^2 . In the transverse case, where $\vec{k} \perp \vec{E}$, we expect to see a diffusion pole appear. At low \vec{k}/μ this will form a weak source of momentum relaxation. As a result, we expect a small Drude peak to form in the low-frequency regime. This is shown in figure 3.5b.

3.4.3. Lattice Conductivities

In the presence of a lattice, either uni- or bidirectional, this story changes in essence very little. Again we can write the perturbations similar to equation (3.27), but now with the added modification that the perturbations also acquire a spatial modulation

$$\begin{aligned} h_{\mu\nu}(z)e^{-i(\omega t - \vec{k} \cdot \vec{x})} &\rightarrow h_{\mu\nu}(x, y, z)e^{-i(\omega t - \vec{k} \cdot \vec{x})}, \\ b_\mu(z)e^{-i(\omega t - \vec{k} \cdot \vec{x})} &\rightarrow b_\mu(x, y, z)e^{-i(\omega t - \vec{k} \cdot \vec{x})}. \end{aligned} \quad (3.37)$$



(a) Longitudinal optical conductivity. For the (b) Transverse optical conductivity. Note that for larger values of k , the sound peak moves to higher frequency and broadens, indicating increased attenuation. higher k , the Drude peak lowers and becomes wider.

Figure 3.5.: Optical conductivity at finite momentum in RN. We choose here a constant source E_x , and let $\vec{k} = k\hat{x}$ or $\vec{k} = k\hat{y}$ for longitudinal and transverse computations, respectively. In both cases, for large ω the CFT result $\sigma(\omega) \rightarrow 1$ is recovered.

The difference now is that the exponentials are not a periodic function on the domains L_x, L_y , while the perturbations are assumed to be. This is reminiscent of a Bloch wave expansion for perturbations that is common in condensed matter physics. The principle of solving the equations is still a relatively simple affair, as the principle is the same as in all the cases before. The main difference is that now this turns into a set of linear partial differential equations rather than a set of linear ordinary ones. The horizon boundary conditions are also given by requiring an order-by-order solution of the equations of motion near the horizon to the infalling waves. The argument that from symmetry k_y can be set to zero in general is lost, because the uni- and bidirectional lattices break rotational invariance badly. Another difference is that now the differential equation for the perturbations has to be computed on a given (numerical) background. The variable coefficients in the differential equations are then also dependent on a set of background fields instead of just the radial coordinate. The gauge fixing terms described in section 3.4.2 still apply, and will now in general depend on both spatial dimensions as well as background fields. This is mainly a practical challenge from a programming point of view, not from a conceptual one. The evaluation of the correlator is then the same as in equation (3.35), with the added point that we need to average over the spatial dimensions in order to get the proper response.⁷ The optical responses in several types of 1D holographic lattices have been extensively studied in other works.[107, 118, 120, 136, 140] The main result that can be highlighted here is that in the presence of a weak (ionic or other) lattice, there is also a small amount of momentum relaxation, as in the case of the transverse conductivity

⁷Since we always take the source to be spatially homogeneous, the average only needs to be done over the expectation value. It is possible to do both finite wave vector sourcing and responses, see the discussion on inverting the alternate quantization later in chapter 4.

in pure RN, but now also in the $k = 0$ channel. As a result, we again expect a finite Drude peak to appear.

3.4.4. DC conductivities

The limit $\omega \rightarrow 0$ in the definition of the conductivity as in equation (3.36) is problematic when we try to deal with conductivity at zero-frequency. Namely, the DC limit is well defined, but evaluating at exactly $\omega = 0$ contains a divide-by-zero, which is something that computers do not handle well. DC transport contains a lot of information about the system and therefore it is good to have access to it. Conveniently, there is an easier way to find these. In general, they are computed by taking particular combinations of time-independent perturbations to the metric and gauge field. This procedure has been investigated in great detail, with an interesting result at the end. It turns out that the DC conductivity in both Reissner-Nordström and dilatonic black holes can be evaluated by solving a Stokes flow-like problem at the black hole horizon.[114, 140–146]

In the most general setting, where we not only have the Einstein-Maxwell action but potentially also other scalar fields, it turns out that by perturbing the black hole just right and using the symmetries in the equation of motion the horizon equations that need to be solved becomes a system of four equations, where [142, 146]

$$\begin{aligned} \eta_H \left(-2\nabla^j \nabla_{(i} v_{j)} + v^j \nabla_j \phi^{(h)} \nabla_i \phi^{(h)} \right) - d\chi_{ij}^{(h)} Q^j - F_{ij}^{(h)} J^j - \\ \rho_H (E_i + \nabla_i w) - T s_H \left(\zeta_i - \nabla_i \frac{p}{4\pi T} \right) = 0, \\ \partial_j Q^j = 0, \quad \partial_j J^j = 0. \end{aligned} \quad (3.38)$$

These η_H, s_H, ρ_H are horizon quantities that play the role of shear viscosity, entropy and charge density in this Stokes-like problem for a fluid with velocity v_j , pressure p and forcing term w_j living on the black hole horizon. s_H is the same as the entropy we assign to the black hole when considering its thermodynamics, and $\eta_H \equiv s_H/4\pi$, akin to the famous result for minimal viscosity.[85] Additionally, one can find that $\nabla_j v^j = 0$ must also be satisfied, making this a Stokes-flow like incompressible flow problem. The thermal and electrical gradients are here sourced by ζ_i, E_i and can in principle depend on spatial position, although I will not consider that in this thesis. The unknowns here are the field v^j, w, p , while the rest of the quantities are given in terms of bulk fields evaluated at the horizon. Q_i, J_i are the resulting heat and electrical currents. These are defined on the horizon, but it can be shown that their unit cell averages \bar{Q}, \bar{J} are not renormalised from the horizon to the boundary, and are therefore equal to the averages of the DC currents we want to interpret in the boundary theory. The conductivities are then found with

$$\begin{pmatrix} \bar{J}^i \\ \bar{Q}^i \end{pmatrix} = \begin{pmatrix} \sigma^{ij} & T\alpha^{ij} \\ T\bar{\alpha}^{ij} & T\bar{\kappa}^{ij} \end{pmatrix} \begin{pmatrix} E_j \\ \zeta_j \end{pmatrix}. \quad (3.39)$$

Here $\alpha, \bar{\alpha}$ are the thermoelectric conductivities and $\bar{\kappa}$ is the thermal conductivity.

The exact forms of these depend on the exact setup that is being used.[142] What is the case is that this simplifies in certain scenarios. Specifically, if translational symmetry is broken in some

kind of homogeneous way, where there is no lattice, the thermoelectric conductivity can be evaluated by just evaluating certain horizon quantities. The case of the unidirectional lattice is simple too, where now thermoelectric currents can be expressed in terms of integrals over horizon quantities.[140] For the bidirectional lattice due to the lack of remaining symmetries there is no such simplification and one has to resort to actually solving the Stokes differential equations (3.38) numerically. This can be done rather simply, as this is just yet another modification of the code solving a perturbative problem in the presence of a background, like in the AC case, but now restricted to only the horizon.⁸

3.5. Outlook

All this together provides a lightning overview of the methods that have been used in the production of this thesis. The results of these endeavours will be presented in the following chapters, in papers on fermionic spectral functions in holographic lattices, optical and DC conductivities in Gubser-Rocha black holes, and thermodynamics and quantization considerations in the Gubser-Rocha model. All the numerics contained therein are based on the equations that have been presented here. Their practical efficient implementation into computer code is a story in and upon itself, which unfortunately could not be included in this thesis due to constraints of length. For this in-depth discussion on the numerical solutions of non-linear elliptic boundary value problems in two and three dimensions, there are more in-depth discussions available.[147]

⁸One thing to keep in mind for accuracy is that in the way the setup is currently phrased, there are zero modes present for the fields p , w , as they can be augmented by a constant shift $p \rightarrow p + c$, without changing the Stokes equations, as they only appear as derivatives in the Stokes equations. In order to get a correct linear solve, one should expect to have to fix the values of p , w at some point in the domain. This will remove the zero (or often numerically very small) pair of eigenvalues from the matrix that is used to solve the problem.

4. Holographic Lattice Fermions

4.1. Attribution

This paper was published under the title “Isolated Zeros Destroy Fermi Surface in Holographic Models with a Lattice” in the Journal of High Energy Physics (JHEP) 2020, article 151 [148], together with A. Krikun, A. Romero-Bermúdez, K. Schalm, and J. Zaanen. Relevant codes for this section will be published together with the publication of this thesis at [149, 150].

4.2. Introduction

The physics of strongly correlated electron systems remains a major puzzle in modern condensed matter theory. The possible deviations from conventional Fermi liquid behaviour are simultaneously extremely interesting and extremely hard to study. Nonetheless, evidence coming from experiments in high temperature superconductors and other strange metallic systems points out that such non-Fermi liquid systems do exist in nature and display many unconventional phenomena. The defining feature of non-Fermi liquid behavior is the absence of long lived quasiparticles anchored on a well-defined Fermi surface, which could be used as building blocks for Fermi liquid perturbation theory. Such signatures of a destruction of the quasiparticles are seen in the angle resolved photoemission (ARPES) studies of experimentally realized strange metals [151]. In high T_c superconductors in the normal phase, the spectral width, or the inverse lifetime, of the fermionic excitation at the Fermi level becomes unnaturally broad in the anti-nodal directions, whereas one still observes well defined quasiparticles at the nodes [152, 153] – the nodal-antinodal dichotomy. In the pseudogap phase the phenomenon of so-called Fermi arcs is even more striking: the sharp Fermi surface simply ends at a point in the Brillouin zone, which is topologically forbidden for a Fermi liquid-like system [154]. A careful theoretical understanding of these phenomena has been hampered by an absence of conceptually new approaches that do not rely on a stable quasiparticle description.

The holographic duality provides such a conceptually novel way to treat the strongly correlated systems without the need to postulate the quasiparticle description to begin with; for a review see [61]. It has been shown in the earlier works [93, 155, 156] that one can obtain a spectrum with or without the long lived fermionic quasiparticles depending on the parameters of the holographic model. The natural question arises of whether it is possible to achieve the transition between these regimes as a function of direction in the Brillouin zone, as it is observed in real materials. This is the question we address in the present work. Most of the earlier works in holography on single fermion spectral functions are restricted to isotropic setups, with the rare exceptions including

[115, 157–160]. In order to study anisotropy and the effects of the Brillouin zone boundary, we introduce a periodic modulation of the chemical potential, which mimics the ionic lattice, breaks the rotational symmetry down to a discrete group and introduces Bloch momenta.¹ A similar study has been performed recently in [158, 160] which also includes a spontaneous breaking of translational invariance. In our case we restrict ourselves to a simpler setup that includes only an explicit periodic lattice, without spontaneous striped order. This allows us to perform the analysis of our results in the cleanest possible way. Similarly, in order to isolate the effects of the periodic lattice, we don't consider any non-minimal interaction terms in the Lagrangian of fermions coupled to gravity in holographic dual description.

As expected, we observe the generic effects of a periodic potential: the fermionic dispersion relation becomes multivalued in the first Brillouin zone due to the presence of lattice copies from the neighbouring zones. Umklapp gaps appear from the interaction between these copies and results in the formation of Fermi pockets. These basic effects had already been observed before in various holographic models with periodic potentials [157–159]. It simply shows the universality of Umklapp at the boundary of the Brillouin zone in fermionic responses in periodic potentials. However, we report here that, for substantially strong lattice potentials (much stronger than considered previously in i.e. [157, 159]), a **novel physical effect** appears: the partial destruction of the Fermi surface due to the interaction of poles and zeros in the Green's function. A noticeable spectral weight suppression in strong holographic mixed spontaneous and explicit lattices was observed earlier in [158, 160]. However the effect which we observe is different: in our purposely simple tractable model we can completely identify that there is not just suppression, but that the Fermi surface is actually destroyed due to a collision of the defining pole with a zero in the Green's function.²

Zeros of the fermionic Green's function have been observed in holographic models in several contexts. One kind of zeros, the “alternative quantization zeros”, has been pointed out in the early works using bottom-up models [93, 155, 156] as well as in top-down constructions [161]. The existence of these zeros is understood straightforwardly within the holographic approach: they originate from the fact that, for a range of the parameters, a particular holographic theory can be treated as a dual to two distinct quantum theories on the boundary [74]. These two treatments are the “direct” and “alternate” quantization of the boundary operators and the simultaneous existence of both leads to the appearance of zeros in the Green's function of one theory, precisely at the point where the other one has poles. As we will see below, in the presence of a strong lattice potential these “alternative quantization zeros” approach the pole corresponding to the putative Fermi surface. This proximity kills the peak in the spectral response. The origin of this type of zeros is quite clear from the holographic point of view and universal in that context, but their interpretation in terms of conventional condensed matter theory remains elusive. We shall comment on possible interpretations in the discussion section. The phenomenon we observe is somewhat similar to the “pole-skipping” in holographic correlators for hydrodynamic energy-density modes, discussed recently in [162–166] and for fermionic modes in [167]. There one also observes the line of poles in the spectral density being cut by the line of zeros.

¹For the sake of technical simplicity we focus on a quasi-one-dimensional lattice, i.e. we only consider the modulation in one spatial direction.

²For a discussion on the possible origins of the anisotropic spectral weight suppression observed in [158, 160] see [115]

This holographic understanding of controlled zeros in the Green's function has already been exploited in attempts to describe the zeros in the spectrum arising from Mott physics [168–172]. One mechanism relies on an extra Pauli or dipole coupling present in the fermionic Lagrangian. It has been shown that in the particular case of massless bulk fermions this can partially convert the Fermi surface into the line of zeros. We intentionally do not include the extra coupling in our model, which allows us to distinguish the phenomenon we observe here from the one mentioned in those works. On the other hand, zeros in spectral functions can have several origins but true Mott physics is intrinsically linked to the presence of a lattice and translational symmetry breaking as studied here.

The spectral signature of zeros colliding with poles/peaks is a very identifiable characteristic and for that reason of high interest. More recently, a new zero-pole collision has been found [173] unrelated to holography. It was shown that in the presence of a quantum critical continuum coupled with two systems with discrete spectra, the spectrum of one such system has a characteristic zero at the resonance of the other. And this zero may collide with a pole. This effect is in the same class as the Fano resonance, where the spectrum of a continuum theory interacting with a discrete system has a zero at the resonance frequency of the latter. Alongside with our main finding we observe this new class of “resonant zeros” in our holographic model. The reason is that the near horizon geometry generically encodes a certain type of the quantum critical continuum and the periodic potential gives rise to the many copies of the discrete particle dispersion spectra within the first Brillouin zone. The fermion spectral function precisely probes a discrete sector coupled via continuum to other discrete spectra. The effect of these zeros is also interesting, but not so spectacular as the one from “alternative quantization” ones. These discrete-continuum-discrete resonant zeros cut through the Fermi surface and destroy the quasiparticle peak at a particular point, but they do not remove extended intervals from the Fermi surface.

Our finding that “alternative quantization” zeros interfere with Fermi-surface poles in holographic models with strong lattice potentials is theoretical and it is our thorough understanding of a peculiar aspect of holographic theories that allows us to unambiguously identify this mechanism. The result strikingly resembles the phenomenon of Fermi arcs, seen in the pseudogap. The creation of Fermi arcs was already the motivation for the holographic studies [168–172], but in our work they are directly tied to the presence of the lattice and anchored to the directional pattern of the Brillouin zone. Undoped Mott insulators are known to have zero responses in the single particle fermionic spectral function. In conventional condensed matter theory there are attempts to explain the formation of Fermi arcs in the pseudogap phase of the cuprates originating from these Mott zeros in the spectral density [174–178]. In these approaches, it is argued that, due to strong interactions, the self-energy of the quasiparticle diverges forcing the “dressed” Green's function to vanish at certain points in the phase space. These zeros do not violate the Luttinger count [179], but render the Fermi surface disconnected. It would be interesting to determine whether there is any connection between our results and this other approach, but as we shall discuss in the conclusion, there are a number of fundamental open questions that will require significant further study.

The paper is organized as follows, in the first two sections we give an overview of basic features of ordinary Fermi surfaces in a periodic potential (Sec. 4.3) as well as the holographic fermionic

response in the case of a simple isotropic background (Sec. 4.4). In Section 4.5, we describe the model and the method. The main result is presented in Section 4.6 and we draw our conclusions in Section 4.7. The appendices are devoted to the details of our treatment in the homogeneous black hole background (App. 4.A), the construction of periodic backgrounds (App. 4.B) and the analysis of the fermionic response (App. 4.C). We also explain the Brillouin zone representation of the Green's function in Appendix 4.D.

4.3. Umklapp Scattering and Fermi Pockets in Unidirectional Potential

We start by recalling the basic features of the fermionic spectral function in a periodic potential. We wish to illustrate that at strong lattice potentials there are several non-linear responses, that are normally not considered in linear analysis of Bloch wave physics and Umklapp. Nevertheless these non-linear responses follow from a straightforward calculation. We consider a non-interacting Dirac fermion $\bar{\psi}$ in 2+1 dimensions in the presence of a periodically modulated chemical potential $\mu(x) = \mu[1 + \lambda \sin(px)]$ along the x -direction only. In order to facilitate the analysis of our main results, we keep the y -direction homogeneous. The Dirac equation reads (here the bars denote a 2 + 1 dimensional toy-model in order to avoid confusion with our main treatment below)

$$\begin{aligned} [\bar{\gamma}^\mu \partial_\mu - i\mu(x)\bar{\gamma}^t] \bar{\psi}(x, y, t) &= 0, \\ \mu(x) &\sim \mu(x + 2n\pi/p) = \mu(1 + \lambda \sin(px)) \\ \bar{\gamma}^t &= i\sigma_1, \quad \bar{\gamma}^x = \sigma_2, \quad \bar{\gamma}^y = \sigma_3, \end{aligned} \tag{4.1} \tag{4.2}$$

where σ_i are the Pauli matrices. We introduce frequency, momentum in y -direction as well as the Bloch momentum in x -direction

$$\bar{\psi}(x, y, t) \equiv e^{i(k_x x + k_y y - \omega t)} \bar{\psi}_k(x), \quad \bar{\psi}_k(x) \sim \bar{\psi}_k(x + 2n\pi/p), n \in \mathbb{N}, \tag{4.3}$$

to get the equation on the Bloch wave function $\bar{\psi}_k(x)$, which is by construction periodic with the same period as the potential $\mu(x)$:

$$[-\sigma_1(\omega - \mu(x)) + i\sigma_2 k_x + i\sigma_3 k_y + \sigma_2 \partial_x] \bar{\psi}_k(x) = 0. \tag{4.4}$$

Here, the Bloch wave function $\bar{\psi}_k = \{\bar{\psi}_k^\uparrow, \bar{\psi}_k^\downarrow\}$ is a 2-component spinor and the Dirac operator is a 2×2 matrix differential operator. Since the Bloch wave function has the same period as the potential, it is convenient to expand it in the Fourier series:

$$\begin{pmatrix} \bar{\psi}_k^\uparrow(x) \\ \bar{\psi}_k^\downarrow(x) \end{pmatrix} = \sum_l \begin{pmatrix} a_{kl}^\uparrow \\ a_{kl}^\downarrow \end{pmatrix} e^{ilpx}. \tag{4.5}$$

In this representation, the Dirac equation (4.4) turns into a matrix equation for the vector wave function (let us drop the k index for now) $\vec{a} = \{\dots, a_l^\uparrow, a_l^\downarrow, a_{l+1}^\uparrow, a_{l+1}^\downarrow, \dots\}$

$$M \cdot \vec{a} = \vec{0} \quad (4.6)$$

$$M = \begin{pmatrix} \ddots & & & & \\ & -(k_x - 2p) - \delta\omega & -ik_y & -i\lambda\mu/2 & 0 \\ \vdots & ik_y & (k_x - 2p) - \delta\omega & 0 & -i\lambda\mu/2 \\ & i\lambda\mu/2 & 0 & -(k_x - p) - \delta\omega & -ik_y \\ 0 & & -i\lambda\mu/2 & ik_y & (k_x - p) - \delta\omega \\ & \ddots & & & \ddots \end{pmatrix}, \quad (4.7)$$

where $\delta\omega \equiv \omega - \mu$ for brevity. The Green's function in the Fourier mode representation is simply the inverse of the Dirac operator: $G_{lm} = (M^{-1})_{lm}$. In ARPES experiments, the most important element of the Green's function is the G_{00} component, which characterizes the projection of the fermionic linear response function in a crystal on the plane-wave states of the incident photon and photo-electron. Therefore, in what follows, we will be focusing on the spectral function associated with the G_{00} component of the fermionic Green's function

$$A(\omega, k) = \text{Im Tr} G_{00}(\omega, k), \quad (4.8)$$

where the trace is taken over the spin states. Throughout the paper we assume a practical definition of the Fermi surface as the locus of maxima of the spectral density in the momentum plane at the Fermi level.

In Fig. 4.1, we show various examples of the spectral density in the toy model (4.4) for various parameters of the background potential.³ In the left column we consider a weak periodic potential ($\lambda = 0.08$) for three values of the size of the Brillouin zone p . For a weak periodic potential all the results can be easily understood from linear analysis. When the BZ is large enough, the Fermi surface does not reach the BZ boundary and has the same isotropic shape as in the case without modulation with Fermi momentum k_f . For a smaller BZ (smaller p , middle panel), lattice copies of the Fermi surface from the neighbouring Brillouin zones are seen. These copies are visible in the G_{00} component due to the off-diagonal mixing terms $i\lambda\mu/2$ in Eq. (4.6). Therefore, the spectral density in these lattice copies is suppressed by a factor of λ and, in case of the weak potential, they are hardly visible. When the Brillouin zone size is further reduced ($p/2 < k_f$), the neighbouring Fermi surfaces start to overlap and Umklapp gaps are opened at the Brillouin zone boundary. From the point of view of the inversion of matrix (4.6), this is simply a linear eigenvalue repulsion effect due to non-zero off-diagonal terms $i\lambda\mu/2$. This occurs around the point when the eigenvalues of the top-left and bottom-right blocks of the matrix (4.6) become identical. In this case, the series

³The Green's function of the real equation (4.6) is real. In order to make the spectral function visible, we evaluate it at a slightly imaginary frequency $\omega = E_f + i10^{-4}$, $E_f = 0.4$.

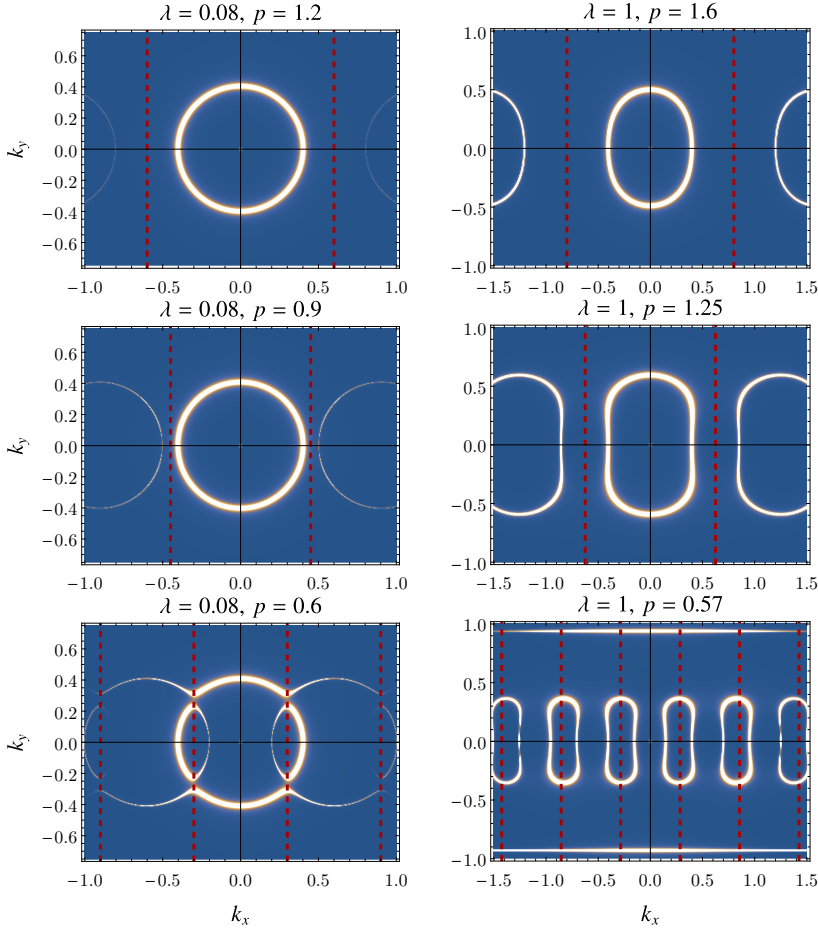


Figure 4.1.: **The shape of the Fermi surface of a non-interacting 2+1 dimensional Dirac toy model in a unidirectional periodic chemical potential.** Shown is the spectral density (4.8), which equals the 00 component of the inverse matrix M (4.6).

Left column: At weak modulation the shape of the Fermi surface appears circular as in the absence of a lattice. However, lattice copies appear in the neighbouring Brillouin zones (BZ). When the BZ (red dashed grid lines) becomes smaller than the Fermi momentum, these copies overlap and an Umklapp gap is opened at the intersection point, giving rise to Fermi pockets.

Right column: At strong modulation amplitude $\lambda = 1$ nonlinear effects are seen. The shape of the Fermi surface is now affected even far from the boundary of the BZ. When BZ gets smaller, the FS is first squeezed and then strong Umklapp gaps are opened, leading to the small dumbbell-like Fermi pockets near k_x axis and the nearly k_x independent flat “band” at finite k_y .

of circular Fermi surfaces turn into a series of Fermi pockets in addition to a an outer band parallel to x -axis. This “band” is an artefact of the unidirectional modulation of the potential, which we introduced for simplicity. In the case of a realistic crystal lattice in both x - and y - directions, Fermi

pockets would form in the y -direction as well.

For strong modulating potential $\lambda = 1$, right column of Fig. 4.1, the situation is more involved. Even though qualitatively the response is the same, quantitatively non-linear effects will now also affect the shape of the Fermi surface. Firstly, of course, the lattice copies of the Fermi surface acquire a larger spectral weight due to the stronger mixing and are visible already for large Brillouin zones (top row). As the BZ decreases, the strong interaction effects that change the shape of the Fermi surface are seen. It becomes “squeezed” as in the middle row of Fig. 4.1. Finally, once the Fermi surfaces overlap, the umklapp gap that opens is so large that the outer “band” gets pushed far away and is almost flat (independent of k_x), while the heavily deformed Fermi pockets are stretched along the BZ boundary, deforming in a dumbbell-like shape, see the bottom row of Fig. 4.1.

As we will see below, these different types of the Fermi surface geometries that we find in the toy model (4.4) with non-interacting electrons on top of the periodic potential will also appear in the fermionic response of the strongly coupled holographic model. This will aid us in distinguishing effects that are due to strong self-interactions from effects that are due to strong lattice potential.

4.4. Holographic Fermi Surfaces and Zeros

Next we recall the universal presence of zeros in the fermionic spectral response in a finite-density holographic model of a strongly interacting system of fermions. This is also so in the absence of a lattice and the simplest example of such a system – the homogeneous model at finite temperature and chemical potential – is described by a Reissner-Norström black hole in the $3+1$ dimensional curved AdS space [61]. The corresponding metric reads

$$\text{RN black hole} \quad ds^2 = \frac{1}{z^2} \left[-f(z)dt^2 + dx^2 + dy^2 + \frac{dz^2}{f(z)} \right] \quad (4.9)$$

with

$$f(z) = \left(1 - \frac{z}{z_h}\right) \left(1 + \frac{z}{z_h} + \frac{z^2}{z_h^2} - \frac{\mu^2 z_h^2}{4} \frac{z^3}{z_h^3}\right) \equiv \left(1 - \frac{z}{z_h}\right) P\left(\frac{z}{z_h}\right) \quad (4.10)$$

and z_h being the radius of the black hole horizon which is related to the temperature and chemical potential in the dual theory:

$$16\pi T z_h = 12 - \mu^2 z_h^2. \quad (4.11)$$

The gauge field potential of the charged black hole is simply

$$A_t = (z - z_h)\mu. \quad (4.12)$$

In what follows we will set $z_h = 1$ by choosing the appropriate measuring units.

In order to study the fermionic response in the holographic framework, one considers the Dirac equation on the curved space-time (4.9) [61, 93, 155–157, 180, 181]:

$$\left[\Gamma^f e_f^\mu \left(\partial_\mu + \frac{1}{4} \omega_{b\mu}^a \eta_{ac} \sigma^{cb} - iq A_\mu \right) - m \right] \Psi(t, x, y, z) = 0, \quad (4.13)$$

where $\Psi = (\psi^\uparrow, \psi^\downarrow)^T$ is a 4-component 3+1 dimensional Dirac spinor, which we break into two 2-component subparts corresponding to the different spin states on the boundary. Here e_μ^f are the tetrad vectors; $\omega_{b\mu}^a$ is the spin connection⁴; η_{ac} is the Minkowski $(-, +, +, +)$ metric; A_μ is the gauge field, and $\sigma^{ab} \equiv \frac{1}{2}[\Gamma^a, \Gamma^b]$ is the generator of Lorentz transformations, where we choose the Γ -matrices to be

$$\Gamma^t = i\mathbb{1} \otimes \sigma^1, \quad \Gamma^x = \sigma^3 \otimes \sigma^2, \quad \Gamma^y = \sigma^2 \otimes \sigma^2, \quad \Gamma^z = \mathbb{1} \otimes \sigma_3. \quad (4.14)$$

The tunable parameters here are q and m – the charge and mass of the bulk fermion field. In the homogeneous background (4.9) one can immediately expand in plane waves along $\{x, y\}$ directions. It is also convenient to rescale the spinor and introduce the new fields ζ^a :

$$\psi^a = (g/g_{zz})^{1/4} e^{ik_x x + ik_y y - i\omega t} \zeta^a(z), \quad a \in \{\uparrow, \downarrow\} \quad (4.15)$$

where $g_{\mu\nu}$ is the metric and g its determinant. After this redefinition, the equation for ζ^\uparrow reads

$$\left[\partial_z - \frac{m}{z\sqrt{f}} \sigma_3 + i \frac{\omega + qA}{f} \sigma_2 + \frac{k_x}{\sqrt{f}} \sigma_1 \right] \zeta^\uparrow(z) - ik_y \frac{1}{\sqrt{f}} \sigma_1 \zeta^\downarrow(z) = 0. \quad (4.16)$$

Taking advantage of the isotropy of the RN black hole, we choose the coordinates in such a way that $k_y = 0$ and the Weyl spinors ζ^\uparrow and ζ^\downarrow decouple. For ζ^\downarrow , the k_x momentum term has the opposite sign. Therefore, in the subsector $k_y = 0$ the two spinors describe left- and right-moving modes in the x -direction. This simplification generically doesn't happen in the presence of a lattice, however it still arises when the fermion propagates along the unidirectional potential, as we will see in the next section⁵.

The analysis near the AdS boundary $z \rightarrow 0$ shows the spinor components behave as

$$\zeta^\uparrow(z; \omega, k)|_{z \rightarrow 0} = \begin{pmatrix} b^\uparrow(\omega, k) z^m + a^\uparrow(\omega, k) \mathfrak{a}_r^0(\omega, k) z^{-m+1} + \dots \\ a^\uparrow(\omega, k) z^{-m} + b^\uparrow(\omega, k) \mathfrak{b}_s^0(\omega, k) z^{m+1} + \dots \end{pmatrix}, \quad (4.17)$$

where the constants $\mathfrak{a}_r^0, \mathfrak{b}_s^0$ can be fixed by solving the equations of motion, see Appendix 4.A, and can in principle depend on parameters (ω, k) . Given the expansion (4.17) of the bulk fermion

⁴Spin connection is defined as via $\partial_\mu e_\nu^a + \omega_{b\mu}^a e_\nu^b - \Gamma_{\mu\nu}^\tau e_\tau^a = 0$, where $\Gamma_{\mu\nu}^\tau$ is Christoffel symbol.

⁵This is a consequence of our choice of the Γ -matrices (4.14). Their reduction on the boundary, defined by the action of 2+1 dimensional Lorentz generator $\sigma^{\mu\nu}$, $\mu, \nu \in (t, x, y)$ on a positive subspace of Γ^z coincides with $\tilde{\gamma}^\mu$ in (4.4). The different spin states which we consider are the eigenstates of $\tilde{\gamma}^y$ and they decouple in case when the fermions propagate along x -axis, since in the corresponding 1+1 dimensional problem they possess different chiralities.

profile one identifies the independent coefficients a and b with respectively the source and the expectation value of the corresponding fermionic boundary operator Ψ of conformal dimension $\Delta = \frac{3}{2} + m$ [93, 155, 156, 180, 182–185]. This is called “direct quantization” (Direct Q). It is important to note however, that this identification is not unique: for $m \in [0, \frac{1}{2})$ one can consider an “alternative quantization” (Alt. Q, which we denote with tilde: $\tilde{\Psi}$) and consider b as the source and a as the expectation value of the operator $\tilde{\Psi}$ with conformal dimension $\tilde{\Delta} = \frac{3}{2} - m$. In this regime of $m \in [0, \frac{1}{2})$, a single bulk model can correspond to the two distinct boundary theories, depending on the type of quantization chosen. A useful way of studying alternative quantization is to consider the direct framework but to extend the range of m to negative values of $m \in (-\frac{1}{2}, 0]$. In this way the roles of a and b are switched in (4.17).

Within the linear response approximation, the holographic identification of source and response allows one to obtain the two-point function of the fermionic operator under consideration: the fermionic Green’s function $G = \langle \Psi^\dagger \Psi \rangle = (\text{response})/(\text{source})$. In general the Green’s function is a matrix, and to divide out the sources requires a few steps. In the notation of [180], given the relation between the sources and responses⁶

$$\begin{pmatrix} b^\uparrow \\ b^\downarrow \end{pmatrix} = \mathcal{S} \begin{pmatrix} a^\downarrow \\ a^\uparrow \end{pmatrix}, \quad (4.18)$$

the (retarded) fermionic Green’s function reads

$$G_R = -i\mathcal{S}\gamma^t, \quad (4.19)$$

where $\gamma^t = i\sigma_1$ with our choice of the Γ -matrices (4.14) [93, 155, 156, 180, 185–188]. Therefore, in direct quantization $G^{\uparrow\uparrow} = b^\uparrow/a^\uparrow$, while in alternative quantization $\tilde{G}^{\uparrow\uparrow} = a^\uparrow/b^\uparrow$. In other words, the two point functions in both quantizations are related by

$$G^{\uparrow\uparrow} = b^\uparrow/a^\uparrow = 1/\tilde{G}^{\uparrow\uparrow}. \quad (4.20)$$

In particular and importantly, this means that the poles of the Green’s function in the alternatively quantized boundary theory correspond to the zeros of the Green’s function in case of the direct quantization.

The final point is to determine which type of the Green’s function we are looking at. This is fixed by the boundary conditions at the black hole horizon, see Appendix 4.A. The retarded Green’s function corresponds to a purely infalling solution at the horizon:

$$\zeta^\uparrow(z) \Big|_{z \rightarrow z_h} \sim (z_h - z)^{-i\omega/4\pi T}. \quad (4.21)$$

In short, in order to evaluate the Green’s function, one has to solve the Dirac equation (4.16) in the full bulk geometry (4.9) and find the ratio between the a and b branches of the AdS boundary expansion (4.17) of the solution. The first-order ordinary differential equation (4.16) together with

⁶Note that in the boundary fermionic theory the a^\uparrow is a source to b^\downarrow and vice versa, see [186, 187].

the boundary condition (4.21) is solved with the numerical shooting method, as we explain in Appendix 4.A, and for given values of the background parameters $\{T, \mu\}$, fermionic parameters $\{q, m\}$, frequency and momentum $\{\omega, k_x = k\}$, the asymptotic form (4.17) is read off from the solution. This gives us the Green's function $G^{\uparrow\uparrow}(\omega, k)$ from Eq. (4.20). In complete analogy we can evaluate $G^{\downarrow\downarrow}$ by solving the appropriate equation, or simply use the symmetry mentioned above $G^{\downarrow\downarrow}(k) = G^{\uparrow\uparrow}(-k)$. Finally, we evaluate the fermionic spectral density as

$$A(\omega, k) = \text{Im Tr} G(\omega, k) = \text{Im}(G^{\uparrow\uparrow}(\omega, k) + G^{\downarrow\downarrow}(\omega, k)), \quad (4.22)$$

which is the central object of our study. In what follows we mostly focus on the features of the Fermi surface, defined as the locus of the spectral density peaks at zero frequency: $\omega(k_F) = 0$.

The fermionic spectral density (4.22) at zero frequency in the RN black hole (4.9) computed this way is shown on Fig. 4.2. We have chosen the fermionic bulk mass $m = 1/4$, the charge $q = 1$ and $T/\mu \approx 0.005$. The Fermi surface with direct quantization is shown on the left panel. Moreover, since $m < 1/2$ alternative quantization is also possible and the result is shown on the right. The Fermi surfaces are circular, as expected for fermionic excitations at finite chemical potential in an isotropic background. We also observe the specific holographic feature of the appearance of multiple nested Fermi surfaces [93]. This is a generic feature in holographic models: the number of the observed Fermi surfaces depends on the mass and the charge of the bulk fermion as well as on the background chemical potential, and in principle it can be arbitrary [61].

Here we wish to call attention to another interesting phenomenon which is evident when comparing the results of direct and alternative quantizations: each plot in Fig. 4.2 includes the position of the Fermi surface in the other quantization in dashed lines. We see that the Fermi surfaces in the direct and alternative quantization alternate. This effect is more clearly visible on the left panel of Fig. 4.3, where the $k_y = 0$ cut of the spectral density is shown. Indeed, the solid and dashed vertical grid lines, indicating the Fermi surfaces in the direct and alternative quantization, respectively, alternate: there is always an alternative quantization FS in between two direct ones.

At this point it is important to remember that, due to the inverse relation between the Green's function in Direct Q. and Alt. Q. (4.20), a pole in the alternative Green's function \tilde{G} always corresponds to a zero in the Direct Green's function G . While a pole near the real axis produces a discernible peak in the spectral density A , a zero is only reflected in a depletion of spectral density with a minimum set by the imaginary part of the position of zero in the complex plane, which is proportional to temperature. This depletion, unlike the peaks, is harder to spot in density plots like Fig. 4.2. The reason is simply that in order for the depletion in spectral density to be visible, the latter must have a finite background value. However, the spectral density at zero frequency is set by temperature itself and therefore the depletion is not seen. Therefore, the most direct way of detecting the zero in the Green's function is indeed to study the peaks in its alternatively quantized counterpart. This is how we will identify the zeroes of the Green's function in the remainder of this paper.

Another reason for the absence of detectable depletions of the spectral density is that the trace of the Green's function contains several additive terms, only one of which is suppressed. Indeed, in

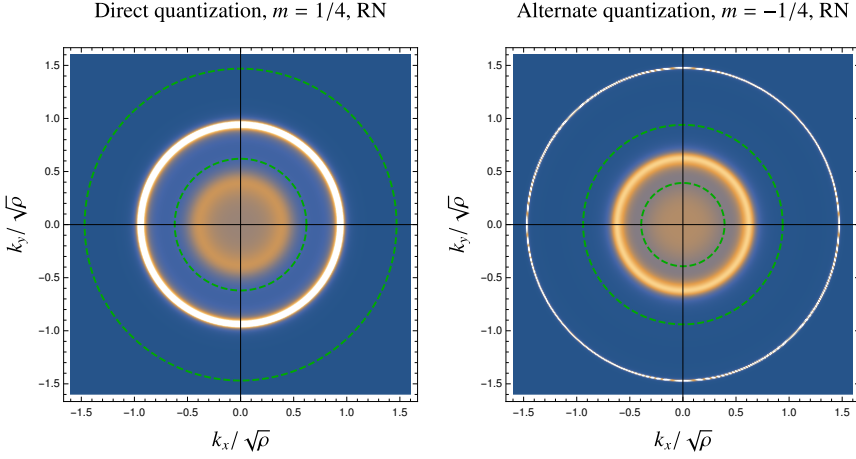


Figure 4.2.: **The fermionic spectral density at near the Fermi level ($\omega = 0.01\sqrt{\rho}$) in the isotropic Reissner Nordström background (4.9) for $m = 1/4$, $q = 1$.** The density plot shows the distribution of the spectral density in momentum plane k_x, k_y for the direct (left panel) and alternative (right panel) quantization picture. The circular Fermi surfaces are seen, which are expected for the isotropic background. In both cases there are two nested FS with different lifetime of the excitation. The positions of the FS in the other quantization picture are shown with the dashed lines on each panel, which makes apparent their alternating structure. $T/\sqrt{\rho} = 0.01$, $\mu^2/\rho \approx 3.329$

a particularly simple example with $k_y = 0$ the Green's function is diagonal in the spin representation

$$\text{Im Tr} G(\omega, k) = \text{Im} G^{\uparrow\uparrow} + \text{Im} G^{\downarrow\downarrow} = \text{Im} \left[\frac{1}{\tilde{G}^{\uparrow\uparrow}} \right] + \text{Im} \left[\frac{1}{\tilde{G}^{\downarrow\downarrow}} \right]. \quad (4.23)$$

Therefore, the peaks of a single component, shown in dashed in Fig. 4.3, are clearly seen in the total $\text{Im Tr} G$, while the depletion, if any, would be shaded with the finite value coming from the opposite-spin component. One could alternatively capture the position of zeros by looking at the real part of the Green's function at real ω , which changes sign at exactly this point. However this method suffers from the same problem: the contribution of the two spin components add together in the trace of the Green's function and one has to diagonalize it in the spin space in order to distill the position of zeros.

The Green's function zeros become particularly important in the case where the peaks in both direct and alternative quantization of the same spin component (shown with arrows in Fig. 4.3) come closer to each other. In this situation, the pole and the zero of the Green's function in the complex ω plane would recombine and the residue of the pole would vanish. In this way, a peak in the spectral density would be “eaten” by the approaching depletion producing a distinct observable phenomenon. This pattern is similar to what happens in a Fano resonance in a continuum coupled to a discrete system, but here it is manifested as a destruction of the Fermi surface at $\omega = 0$.

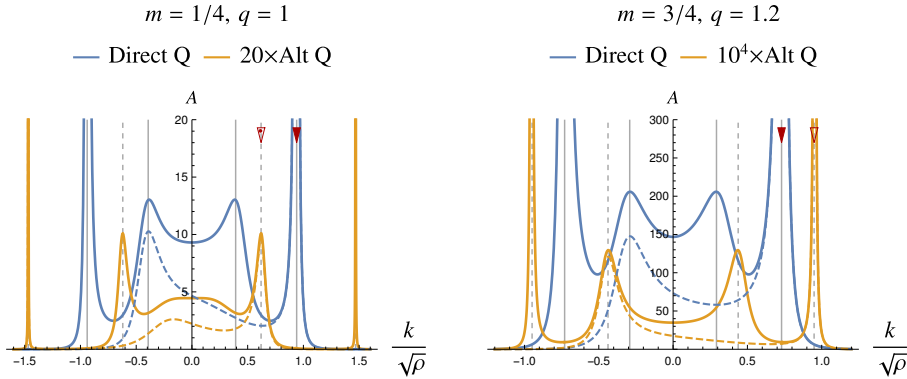


Figure 4.3.: **The fermionic spectral density near the Fermi level ($\omega = 0.01\sqrt{\rho}$) in the isotropic Reissner-Nordström background (4.9).** The $k_y = 0$ cuts in linear scale of the direct and alternative quantization pictures are shown. The left panel corresponds to the fermionic mass $m = 1/4 < 1/2$, where the alternatively quantized dual CFT is well defined, while the right panel corresponds to the case $m = 3/4 > 1/2$, where it does not exist. In both cases the clear peaks corresponding to the well defined Fermi surfaces are seen in both direct and alternative pictures (In case $m = 3/4$ one needs larger value of fermionic charge $q = 1.2$ in order for the FS to be formed). The dashed lines show the contribution of a single spin component to the spectral density. The red arrows point out the peaks which, if brought close to each other, may be destroyed due to the proximity of the zero and a pole in the given spin Green's function. In all cases $T/\sqrt{\rho} = 0.01$, which matches the parameters we will use later on.

In the simple isotropic model described above this does not happen since the poles and zeros are always separated. In what follows we will show that the situation changes when a strong periodic background chemical potential is considered.

Before moving forward, another comment regarding the existence of the zeros in the Green's function is in order. On the right panel of Fig. 4.3 we show the results obtained for a different mass $m = 3/4$ for which only a single quantization in the dual CFT is possible [155, 183]. In other words, one cannot prescribe a physical meaning to the Alt. Q Green's function. Formally, however, we can still evaluate the Alt. Q expression by inverting the Direct Q result. The artificially computed Alt. Q spectral density clearly exhibits the peaks even in this case, which therefore correspond to the zeros of the Direct Q Green's function. Therefore, we conclude that the general mechanism of appearance of the zeros, is independent of whether or not the alternatively quantized picture is well defined.

4.5. Fermionic Spectral Function in a Holographic Lattice

We now turn to the study on how the fermionic spectral function discussed in Sec. 4.4 is affected by the periodic chemical potential, and in particular when the strength of the lattice potential is strong. The bulk model with periodically modulated chemical potential – the holographic ionic lattice – has been introduced in [118] and studied in great detail in [136, 140]. In what follows we will adhere to the framework used previously by some of us in [79, 189] [190]. We consider the holographic model with Einstein-Maxwell action

$$S = \int d^4x \sqrt{-g} \left(R - \frac{1}{4} F^2 - 2\Lambda \right), \quad \Lambda = -3, \quad (4.24)$$

where $F = dA$ is the gauge field strength tensor, R is the Ricci scalar and Λ – the cosmological constant. We introduce the spatially modulated chemical potential (c.f. (4.2))

$$A_t(x, z) \Big|_{z=0} = \mu(x) = \mu_0 [1 + \lambda \sin(px)]. \quad (4.25)$$

The non-isotropic black hole solution can now no longer be constructed analytically, but must be found numerically. In order to find the gravitational background solution it is sufficient to consider the following metric ansatz

$$ds^2 = \frac{1}{z^2} \left(-\mathcal{T}^2 f(z) dt^2 + \mathcal{Z}^2 \frac{dz^2}{f(z)} + \mathcal{X}^2 (dx + Q_{zx} dz)^2 + \mathcal{Y}^2 dy^2 \right), \quad (4.26)$$

$$\mathcal{A} = A_t dt.$$

The blackening factor $f(z)$ is that of the RN black hole (4.9) and all the other ansatz functions depend on both z and x coordinates. Given that, at the horizon

$$\left(\mathcal{Z}^2 - \mathcal{T}^2 \right) \Big|_{z=1} = 0, \quad (4.27)$$

the temperature is still given by (4.11). Using the DeTurck trick [128, 129, 191] and the numerical methods for solving partial differential equations (PDEs) developed in [79, 147, 189] we obtain the background gravitational solutions for a given temperature T at a fixed chemical potential. The lattice wave-vector is p and λ is the amplitude of the chemical potential modulation in units of μ_0 . The details of the numerical procedure and precision control are discussed in Appendix 4.B. With the gravitational background solution at hand we proceed to solve the Dirac equation (4.13). The co-frame is now less trivial than for the isotropic case:

$$e_{\underline{t}} = \frac{\sqrt{f}\mathcal{T}}{z} dt, \quad e_{\underline{x}} = \frac{\mathcal{X}}{z} (dx + Q_{zx} dz), \quad e_{\underline{y}} = \frac{\mathcal{Y}}{z} dy, \quad e_{\underline{z}} = \frac{\mathcal{Z}}{\sqrt{f}z} dz, \quad (4.28)$$

but we can still follow the procedure outlined in Sec. 4.4. Since we are now working in a periodic background potential, we express the spinors in Bloch waves (4.4) instead of plane waves and therefore the rescaling of Eq. (4.15) is modified as

$$\psi^a(z, x) = (g/g_{zz})^{1/4} e^{ik_x x + ik_y y - i\omega t} \zeta^a(z, x), \quad (4.29)$$

$$\zeta^a(z, x + 2\pi/p) \equiv \zeta^a(z, x), \quad a \in \{\uparrow, \downarrow\},$$

where $\zeta^a(z, x)$ is now a position dependent periodic Bloch wave function. Substituting (4.28) and (4.29) into the Dirac equation (4.13), we obtain the fermionic equations of motion, which are now PDEs with $(2\pi/p)$ - periodic boundary conditions in x -direction (c.f. (4.16)):

$$\begin{aligned} & \left[\partial_z - \frac{m}{z\sqrt{f}} \mathcal{Z} \sigma_3 + i \frac{\omega + qA}{f} \frac{\mathcal{Z}}{\mathcal{T}} \sigma_2 + \frac{k_x}{\sqrt{f}} \frac{\mathcal{Z}}{\mathcal{X}} \sigma_1 \right] \zeta^\uparrow(x, z) \\ & - ik_y \frac{1}{\sqrt{f}} \frac{\mathcal{Z}}{\mathcal{Y}} \sigma_1 \zeta^\downarrow(x, z) \\ & - \left[i \frac{1}{\sqrt{f}} \frac{\mathcal{Z}}{\mathcal{X}} \left(\partial_x + \frac{1}{4} \partial_x \ln \frac{1}{\sqrt{f}} \frac{\mathcal{Z}}{\mathcal{X}} \right) \sigma_1 \right. \\ & \left. + Q_{zx} \left(\partial_x + \frac{1}{2} \partial_x \ln Q_{zx} + ik_x \right) \mathbf{1} \right] \zeta^\uparrow(x, z) = 0. \end{aligned} \quad (4.30)$$

The equation for the ζ^\downarrow component is obtained by a parity transformation: $k_i \rightarrow -k_i$, $\partial_i \rightarrow -\partial_i$ and $Q_{zi} \rightarrow -Q_{zi}$, for $i \in \{x, y\}$. The AdS boundary and horizon asymptotic behavior (4.17), (4.36), (4.21), (4.38) remain unchanged in the presence of the periodic potential, except that all the expansion coefficients are now periodic functions of the boundary coordinate x . The details of the numerical algorithm used to integrate these equations are given in Appendix 4.C.

Given a solution of (4.30) as a function of both z and x , we extract the near boundary coefficients $a(x)$ and $b(x)$ defined in Eq. (4.17). In order to obtain the linear response \mathcal{S} -matrix of Eq. (4.18), we expand these periodic expansion coefficients in Fourier series similarly to the method shown in Sec. 4.3:

$$a(x) = \sum a_l e^{ilpx}, \quad b(x) = \sum b_n e^{inpx}. \quad (4.31)$$

Therefore, the \mathcal{S} -matrix is a infinite matrix with both spin and Fourier indices (c.f. (4.6)).

$$\begin{pmatrix} b_n^\uparrow \\ b_n^\downarrow \end{pmatrix} = \sum_l \mathcal{S}_{nl} \begin{pmatrix} a_l^\downarrow \\ a_l^\uparrow \end{pmatrix}, \quad (4.32)$$

The Green's function is evaluated in the same way as in Eq. (4.19), except that it is now a matrix. It is worth mentioning that, since the Fourier basis exponents differ from each other by a shift with exactly one unit of the lattice wave vector p , the indices m, l can be interpreted as the Brillouin zone index. Therefore, the Green's function G_{ml} is simply a matrix in the Brillouin zone representation. We comment on some features of its structure in Appendix 4.D.

As it was discussed earlier in Sec. 4.3, the most interesting component of the Green's function for us is G_{00} , which measures the overlap between the response function in the material and the plane waves of the ARPES probe (4.8). In order to measure G_{00} and the associated spectral density, we consider a plane wave source $a(x) = 1$ as a boundary condition when solving the bulk equations of motion (4.30) and read off the homogeneous component of the response $b(x)$, see also Appendix 4.C.

In order to evaluate the Green's function in the alternative quantization picture, one has to invert the full infinite matrix and the simple formula (4.20) turns into

$$\tilde{G}_{00} = \left(G^{-1} \right)_{00}. \quad (4.33)$$

In order to perform this inversion one has to evaluate all the components of the Direct Q Green's function, which is hard in practice even when one truncates the Fourier series. Therefore, instead of using this method we evaluate the alternatively quantized Green's function by solving the Dirac equation with the negative fermionic mass parameter (see Appendix 4.A). As explained above, this switches the roles of $a(x)$ and $b(x)$ in the linear response calculation. In Appendix 4.D we check that the two approaches give identical results.

4.6. Destruction of the Fermi Surface by the Zeros in the Green's Function

Let us now analyze the results which we get for the fermionic spectral function in the holographic model described in Sec. 4.5. In what follows we study a series of the background gravitational solutions for various Brillouin zone sizes p , but with fixed charge density ρ . We also fix the temperature $T/\sqrt{\rho}$,⁷ and the amplitude of the chemical potential modulation λ (4.25). We consider two cases with weak and strong potential modulation, in direct analogy with the toy model study performed in Sec. 4.3. We use the same temperature and parameters for the bulk fermion as in the homogeneous RN-black hole case addressed in Sec. 4.4:

$$\frac{T}{\sqrt{\rho}} = 0.01, \quad m = 1/4, \quad q = 1. \quad (4.34)$$

As seen in Fig. 4.2, the size of the Fermi surface in the absence of the periodic potential for these parameters is $k_f \approx 0.94\sqrt{\rho}$.

4.6.1. Weak Lattice Potential

We start with a weakly modulating lattice with strength $\lambda = 0.1$. On Fig. 4.4, we show the momentum distribution of the spectral density, which in this case displays the circular Fermi surface with exactly the same size as the homogeneous one (c.f. Fig. 4.2). The weak lattice potential does not affect the shape of the Fermi surface. We choose the size of the Brillouin zone to be smaller than the Fermi momentum $p < 2k_f$, therefore the umklapp copies of the FS overlap and, in perfect agreement with the observations in toy-model of Sec. 4.3, we see umklapp gaps opening at the BZ boundaries. Another feature which is expected is the suppression of the spectral density in the neighboring Fermi surfaces. Indeed, these are almost invisible in the linear scale plot on top of Fig. 4.4. However, the bottom panel shows the logarithm of the spectral density, which makes the λ -suppressed lattice copies of the Fermi surface clearly visible. In a nut shell, the results obtained

⁷In practice we have control over the mean chemical potential μ_0 , which is set by the boundary condition, but we can tune it in such a way that the mean charge density, which can be read out for a given background solution stay fixed when we change the lattice wave-vector p .

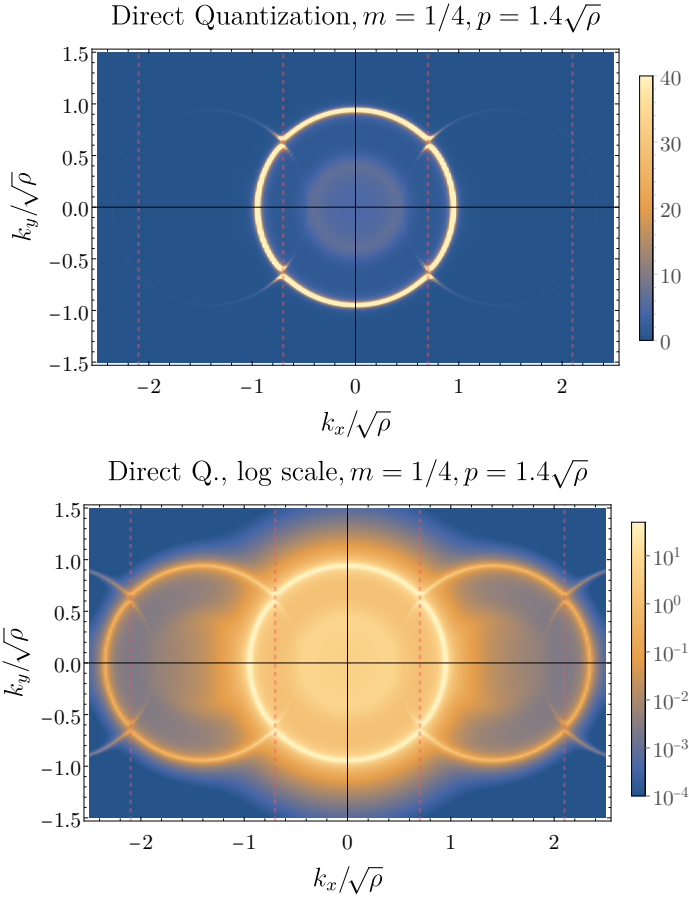


Figure 4.4.: **The fermionic spectral density in the holographic model with weak unidirectional periodic potential ($\lambda = 0.1$).**

The density plots at small ($\omega = 0.01\sqrt{\rho}$) show the effects of introducing the periodic potential. The two plots represent the same data on linear (upper) and logarithmic (lower) scales. Near the Brillouin zone boundary, indicated by the dashed lines, the umklapp gap is starting to open. The weak nature of the potential suppresses the intensity of the copies in neighbouring Brillouin zones, to the extent that they are hardly visible in the upper plot. The lower plot shows that the copies are clearly visible on a logarithmic scale.

The background parameters are: $p = 1.4\sqrt{\rho}$, $\lambda = 0.1$, $T = 0.01\sqrt{\rho}$, $\mu^2 \approx \rho/0.3$.

in the holographic model with a weak periodic potential are in perfect agreement with both the standard logic of fermion physics in a periodic potential, and the shape and size of the holographic

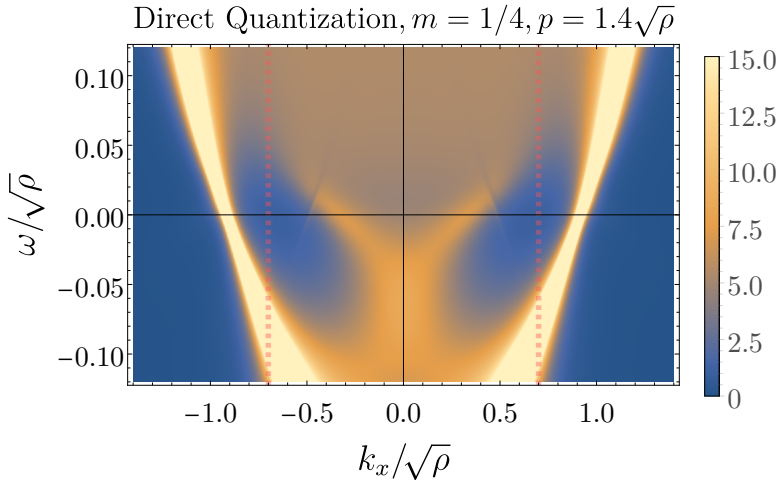


Figure 4.5.: **The frequency resolved fermionic spectral density in the holographic model with weak unidirectional periodic potential ($\lambda = 0.1$).**

The density plot shows a cut through the same data as Fig. 4.4 in the k_x, ω plane, at $k_y = 0.001\sqrt{\rho}$. Around $(k_x, \omega) \approx (\pm 0.4, 0.02)$, the dark lines crossing through the inner Dirac cone arise from the “resonant” type zeroes [173] discussed in Sec. 4.2.

Fermi surface in the homogeneous background. This serves as a consistency check of our approach and numerical techniques.

Similarly, a familiar pattern is also seen on the energy-momentum resolved spectral function shown on Fig. 4.5. As expected, the usual holographic dispersion relation for fermionic excitations is recovered. In this case, it consists of the two nested Dirac cones in the vicinity of the Fermi level. The spectral lines quickly broaden due to the quantum critical self energy $\Sigma(\omega) \sim \omega^{2\nu_{k_F}}$ [61, 93, 155, 156]. However, there is one distinctive new feature due to the presence of the holographic lattice. There is a localized depletion of the spectral weight along the lines which correspond to the dispersion bands of the neighbouring Brillouin zones. This feature is a consequence of a general effect pointed out earlier in [173]. Namely, when multiple systems with discrete spectra interact with each other by means of the quantum critical continuum, the spectral function of one of the systems develops isolated zeros, or depletions, at the positions of the energy levels of the other systems. In the case of the holographic model with a lattice, the discrete systems are the umklapp copies of the fermionic dispersion while the quantum critical continuum originates from the near horizon geometry [93]. This interesting effect may, in principle, also lead to a destruction of the Fermi surface at an isolated point, however it will not be relevant in the present study.

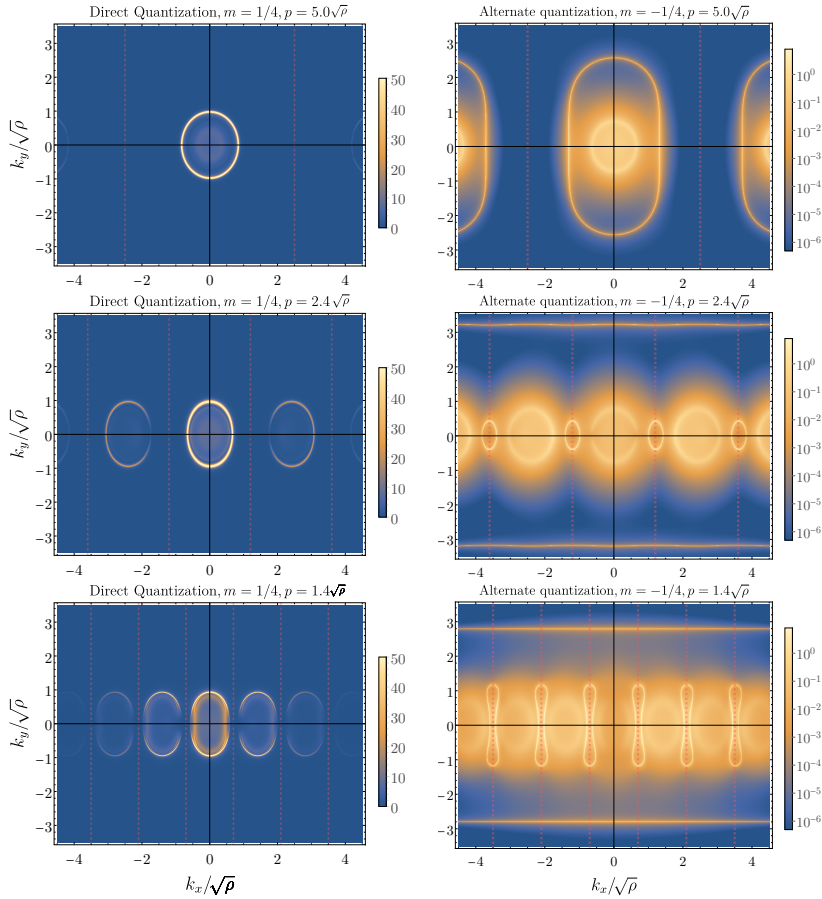


Figure 4.6.: **The fermionic spectral density in the holographic model with strong unidirectional periodic potential ($\lambda = 8.0$), in direct and alternate quantizations near the Fermi level ($\omega = 0.01\sqrt{\rho}$).** The squeezing of the outer Fermi surface happens like in the toy model on Fig. 4.1. In the Alt. quantization, where the Fermi surfaces are larger, the outer FS breaks apart in a band at $k_y \approx \pm 3$, and a pocket at the BZ boundary due to Umklapp. When the BZ boundary is brought closer, to $p = 1.4\sqrt{\rho}$, the spectral density appears to be drastically reduced in the direct quantization near the Umklapp surface. In the alternate quantization, dumbbell shapes similar to the non-interaction model in Fig. 4.1 appear. The background parameters are $T = 0.01\sqrt{\rho}$ and $p = 5\sqrt{\rho}$, $\mu^2 = \rho/0.54$ (top); $p = 2.4\sqrt{\rho}$, $\mu^2 = \rho/1.22$ (middle); $p = 1.4\sqrt{\rho}$, $\mu^2 = \rho/2.04$ (bottom).

4.6.2. Strong Lattice Potential

Let us now turn to the analysis of the case of strong potential modulation $\lambda = 8$, depicted in Fig. 4.6. Similarly to the toy model study of Sec. 4.3, we consider a series of backgrounds with different potential wave-vector p which sets the sizes of the Brillouin zone. The parameters considered allow to access the alternative quantization, which has an inverse Green's function $\tilde{G} = G^{-1}$. In order to analyze the spectral density in Alt. Q, we solve the Dirac equations (4.30) on top of the same gravitational background lattice, but taking the negative sign for the bulk fermion mass $m = -1/4$ (see Appendix 4.D for the details of obtaining the Alt. Q fermionic response). We show the results of the direct and alternative quantizations side by side on Fig. 4.6. Note, however, that we choose logarithmic scale for the Alt. Q results in order to resolve all the features of the FS.

On the first row of Fig. 4.6, the BZ is much larger than the Fermi surface in direct quantization (top left, $p = 5\sqrt{\rho} \approx 5k_f$). Therefore, since the umklapp surfaces are far away, the FS is not deformed even in this regime of strong lattice potential. This is expected; when momentum is much smaller than the BZ, i.e. in the long wave length limit, the periodic structure of the potential becomes irrelevant and only the mean value of the chemical potential μ_0 plays a role in the formation of the Fermi surface.⁸ On the other hand, the outer FS in the alternate quantization is larger ($k_f \approx 1.5\sqrt{\rho}$, see Fig. 4.2). Therefore, on the top right panel of Fig. 4.6, we see that, in this case, the FS is already deformed by the BZ boundaries, similar to the non-interacting toy model in Sec. 4.3.

When the BZ becomes smaller, $p \approx 3k_f$, second row of Fig. 4.6, the neighbouring Fermi surfaces come close to each other and get deformed due to the strong lattice potential in direct quantization. This is exactly the same situation observed in the toy model of Sec. 4.3. For Alt. Q (right panel), we readily observe the formation of Fermi pockets and the flat outer band. This is again similar to the toy model at strong lattice potential.

The novel interesting phenomenon arises when the Brillouin zone is squeezed even further. On the bottom row of Fig. 4.6 we show the situation with $p = 1.4\sqrt{\rho}$. Quite strikingly, we see that as the FS is squeezed further more, the sharp spectral density peaks indicating the shape of the Fermi surface disappear along the boundary of the BZ in direct quantization. A more detailed view in Fig. 4.7 shows this explicitly. On the other hand, the alternative quantization plot displays heavily squeezed dumbbell-like Fermi pockets, which are centered at the BZ boundaries.

As discussed in Sec. 4.4, we have a thorough understanding of some of the peculiar features of the holographic fermionic spectral response. This allows us to figure out the origin of the depletion of spectral function. The zeros of the direct quantization are the corresponding poles of the alternative quantization Green's function. In Fig. 4.8, we show high resolution results of the FS for Direct and Alternative quantizations. In each plot, we show with the dashed green lines the positions of the poles in the other quantization scheme. Most strikingly, the position of the secondary Fermi surface in the Alt. Q overlaps with the primary Fermi surface in the Direct Q, as seen on the left panel of Fig. 4.8. Therefore, there are *zeros* in Direct Q that get pushed towards the poles

⁸As is well known by now, this logic can be violated in other holographic models involving homogeneous lattices [115, 192] or the periodic scalar lattice [193].

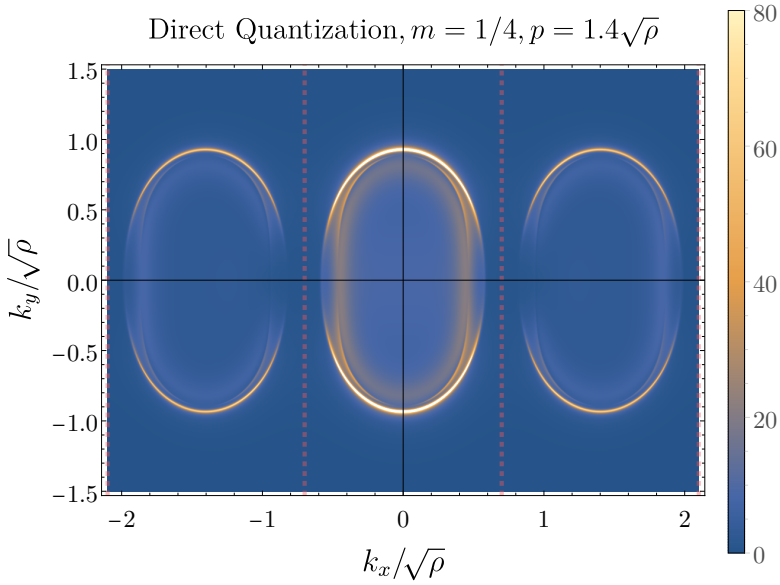


Figure 4.7.: **The destruction of the Fermi surface in strong unidirectional holographic lattice potentials** ($\lambda = 8.0$). Zooming on the picture shown on the bottom left in figure 4.6, it is clearly seen that the Fermi surface loses its sharpness and even disappears around $k_y = 0$.

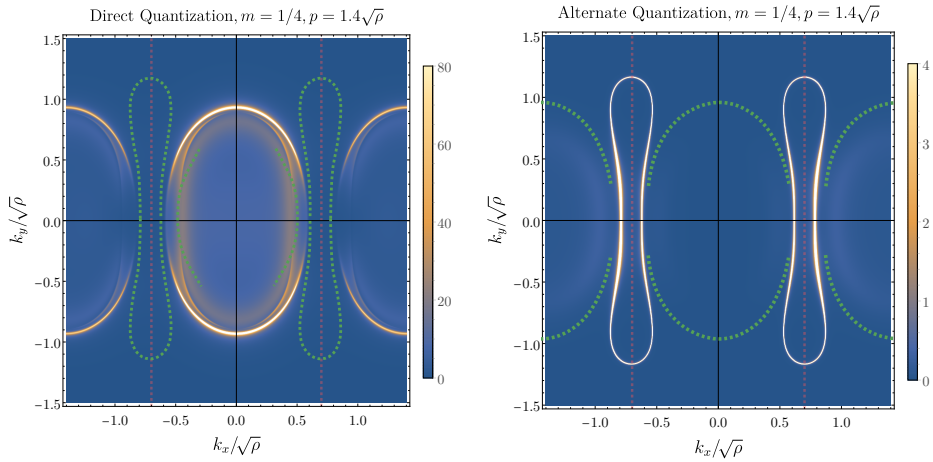


Figure 4.8.: **Poles and zeros of the fermionic response in strong holographic lattices** ($\lambda = 8.0$). Looking more closely at the spectral densities for large lattices and small BZ ($p = 1.4\sqrt{\rho}$), for the direct quantization in the left figure the spectral density broadens and disappears near the Umklapp surfaces $k_x \pm 0.7\sqrt{\rho}$. When tracing out the Fermi surfaces in direct and alternate quantizations and overlaying them on top of each other, it becomes apparent that when the Fermi surfaces of the two different quantization would lie at the same point, they both experience a reduction and broadening of the spectral weight near the FS. The secondary Fermi surface of the alternate quantization is also shown as a trace on the left. This is not visible on the right-hand picture due to the choice of color scheme (see the log-scale Fig. 4.6 instead).

defining the FS. This effect destroys the Fermi surface in an extended region near the BZ boundary. This cancellation of poles and zeros is the fundamental reason for the novel phenomenon we observe.

We can expose the “zero-eats-pole” effect in more detail by analysing cuts along the k_x -axis of the spectral density. These Momentum Distribution Curves (MDC) are shown in Fig. 4.9, where we plot the Direct and Alternative quantizations, in exactly the same fashion as we did in Fig. 4.3. A clear depletion is observed in the Direct Q MDC corresponding to the secondary FS peak in the Alt. Q scheme. As the size of the Brillouin zone (red dashed grid line) is decreased as shown in bottom left plot of Fig. 4.9, this depletion approaches the peak shown by filled red pointer and absorbs it completely at $p = 1.4\sqrt{\rho}$ as shown in the bottom right plot of Fig. 4.9. Therefore, we conclude that for strong lattices, the Fermi surfaces in both direct and alternative quantizations are deformed in such a way that the poles and zeros overlap and cancel each other.

This destruction has a dramatic effect on the very existence of the quasiparticle excitations in part of the kinematic region. This is best seen on Energy Distribution Curves (EDCs), which we show on Fig. 4.10. Here, we plot the frequency dependence of the spectral weight at two perpendicular directions in the Fermi surface: $k_x = k_f^{(x)}, k_y = 0$ and $k_x = 0, k_y = k_f^{(y)}$. When the BZ boundary is far away (top panel of Fig. 4.10), the EDCs are practically identical in both directions, confirming that the FS is almost isotropic. In the bottom left panel, the anisotropy is now manifest, since the FS is deformed by the lattice. Finally, the most drastic effect is seen on the bottom right panel of Fig. 4.10. On the one hand, in the k_y -direction, there is still a sharp peak corresponding to a quasiparticle excitation. However, the spectral density in the k_x direction (red line) is totally incoherent – there is no excitation with definite energy which propagates along the k_x -direction.

4.7. Discussion

In this work we have studied the fermionic spectral function in a holographic model with periodic ionic lattices. Our most important finding is a novel phenomenon which appears as a destruction of coherent spectral weight peaks of the Fermi surface along the directions of the lattice vector. We have shown that the origin of this phenomenon is the interaction between poles and zeros of the fermionic Green’s function. More precisely, due to non-linear effects from the strong background lattice potential, these are pushed together and suppress each other. What is tantalizing, is that the patterns of the spectral density observed here look very similar to the results of ARPES experiments in strongly correlated materials in which nodal-antinodal dichotomy and Fermi arcs are observed. There one also observes the destruction of the coherent spectral weight in certain directions. It is therefore very interesting to further investigate whether our results can clarify these unconventional phenomena.

A warning is in order however; one should handle the results of holographic models with great care. As we discussed in Sec. 4.4, the presence of zeros in our holographic treatment follows from the simple logic relying on the existence of two possible choices for the dual CFT operators corresponding to each quantization, and the existence of a Fermi surface in the alternate quantization. However, as we noted on Fig. 4.3, when only one quantization is allowed, zeros are still present

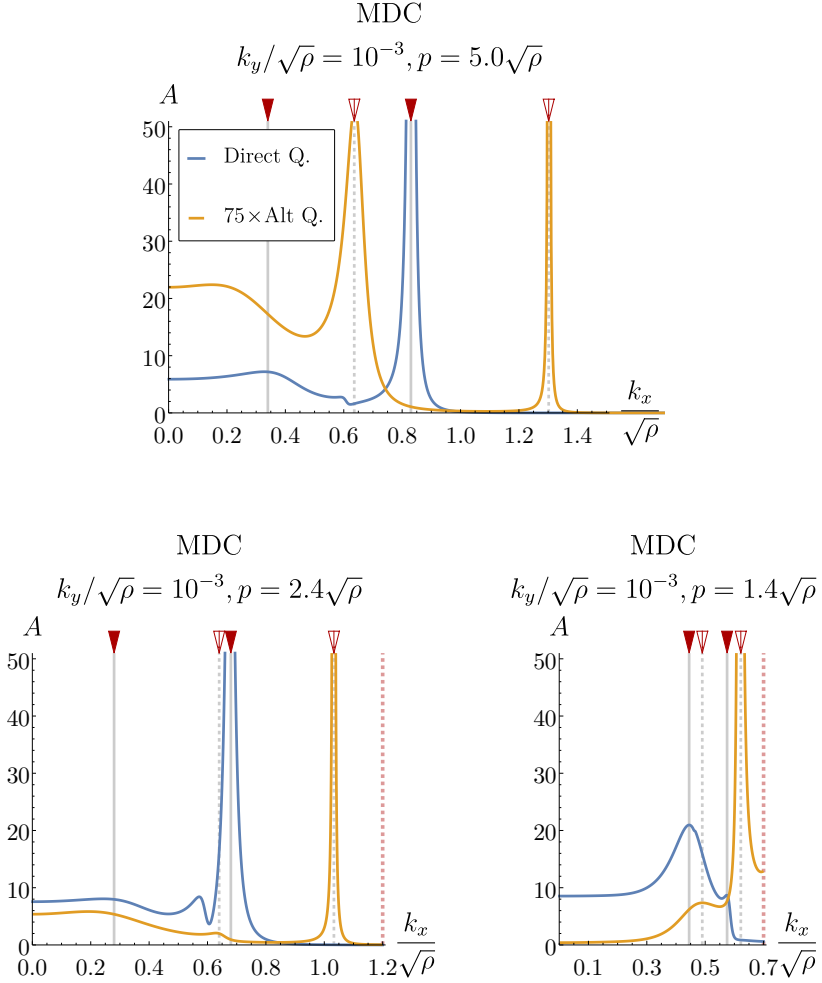


Figure 4.9.: **Momentum distribution curves in strong unidirectional holographic lattices ($\lambda = 8.0$) in direct and alternate quantizations.**

At large lattice momentum, when the BZ boundary is far away from the FS, the the peaks in direct and alternate quantization alternate along the MDCs (c.f. Fig. 4.3). The positions of Direct Q peaks and Alt Q dips are correlated. When the BZ boundary is brought closer, the peaks and zeroes seem to absorb each other. For $p = 1.4\sqrt{\rho}$, the quasiparticle peak is eaten by the zero completely.

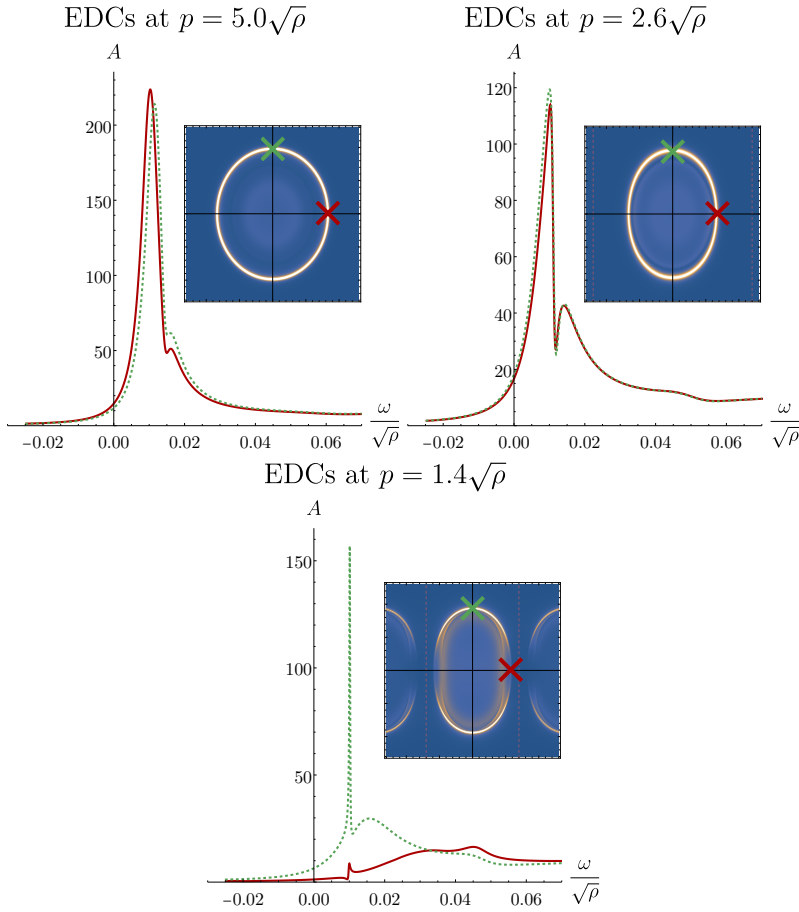


Figure 4.10.: **Energy distribution curves in for strong unidirectional holographic lattices ($\lambda = 8.0$) in direct quantization near and far from the Umklapp surfaces.**

When the BZ boundaries are far away, as in the top picture, the EDCs look very similar: they both show a well-defined, sharp peak. The dip on the right shoulder of the peak corresponds to the alternate quantization zero. When the BZ boundary is brought closer, first some asymmetry in the sharpness of the peaks appears. When the BZ boundaries are brought very close, the peak for the EDC near the BZ boundary gets destroyed by the zero completely.

and perhaps their existence is a more fundamental feature, which is yet to be explored. The fact that the zeros and (the multiple) poles of the fermionic Green's function appear in simple models as alternating series suggests that, as we drive some parameter (chemical potential or temperature) to zero, they might coalesce and form a branch cut in the complex plane. This signals the truly unparticle shape of the Green's function characteristic of the ultraviolet CFT of the holographic duality. This idea is rather at odds with the physics of experimentally realized strange metals, because the UV CFT of a holographic model is clearly not the UV theory governing the behaviour of electrons in real materials. Moreover, the multiple pole features of the fermionic response in the holographic model arguably rely on the large- N approximation, which may or may not be efficient in reality.

However, one can regard our results with a larger perspective; we observe that the destruction between zeros and poles requires the two fundamental ingredients: the very existence of zeros in the fermionic Green's function and strong lattice potentials, which influences the position of poles and zeros by bringing them closer together so that eventually they annihilate each other. Even though the understood origin of the zeros in our particular holographic model cannot be directly mapped to known condensed matter systems, there are models in condensed matter theory, which display similar features, in particular Mott insulators [174, 179]. Our finding suggests that, if upon doping the insulating Mott zeros of the Green's function remain present, their proximity to the quasi-particle poles may indeed be the origin of this spectacular experimental phenomenon. Doped Mott insulators are exactly the systems where the real Fermi arcs are observed. In this regard holographic studies certainly confirm its use as a convenient theoretical laboratory for studying the phenomenology of the strongly correlated systems which goes far beyond the applicability of the Fermi liquid theory.

Acknowledgements

We thank Nikolay Gnezdilov, Andrei Bagrov, Askar Iliasov, Li Li, Sera Cremonini, Saso Grozdanov and Richard Davison for fruitful discussions. We appreciate the useful comments we've got from Michael Norman, Philip Phillips, Robert Leigh and Blaise Gouteraux. We acknowledge the contribution of Stefan Vandoren and Simon Gentle who participated at the early stages of this project.

This work is a part of the Strange metal consortium, funded by Foundation for Research into Fundamental Matter (FOM) in the Netherlands.

This research was supported in part by Koenraad Schalm's VICI award of the Netherlands Organization for Scientific Research (NWO), by the Netherlands Organization for Scientific Research/Ministry of Science and Education (NWO/OCW), and by the Foundation for Research into Fundamental Matter (FOM).

A.K. appreciates the opportunity to deliver and discuss the preliminary results of this study, during the conference "Gauge/Gravity Duality 2018" that took place at the University of Würzburg and the workshop "Bringing Holography to the Lab" at Lorentz Center, Leiden. A.K. acknowledges the hospitality of CPHT group of École Polytechnique, Paris and the useful feedback they provided.

The numerical calculations were performed on the Maris Cluster of Instituut Lorentz.

4.A. Appendix A: Fermionic Equations of Motion in the RN Background

Here, we discuss in detail the algorithm to numerically solve the Dirac equation in the RN background (4.16) for two cases depending on the bulk fermion mass:

- $m = \frac{1}{4}$: The case $|m| < 1/2$, when the alternative quantization is allowed.
- $m = \frac{3}{4}$: The case $|m| > 1/2$, when the alternatively quantized CFT on the boundary side is ill-defined (non-renormalizable) [155, 183].

In both cases on top of the direct approach we will also formally evaluate the response in the alternative quantization (setting $m \rightarrow -m$), which can be done in the bulk even in case of $m = 3/4$, despite the fact that the boundary dual theory is ill defined.

In order to eliminate divergences at the UV boundary (4.17) and the oscillations due to the ingoing boundary conditions at the horizon (4.21), we redefine the components of the wave function in (4.16)

$$\zeta(z) \rightarrow z^{-m}(1-z)^{-i\frac{\omega}{4\pi T}}\xi(z), \quad (4.35)$$

and solve for $\xi(z) \equiv (\xi_r, \xi_s)^T$ in what follows.

For our choices of the bulk mass, the rescaling of Eq. (4.35) leads to one of the components approaching a constant at the boundary $z \rightarrow 0$, and the other component scaling as a positive half-integer power of z . The terms in the equations of motion contain only integer powers of z at the boundary, therefore one can expand the solution as series (see (4.17))

$$m = \frac{1}{4} : \quad \begin{cases} \xi_r &= bz^{1/2} (1 + \mathfrak{b}_r^1 z + \dots) + az (\mathfrak{a}_r^0 + \mathfrak{a}_r^1 z + \dots) \\ \xi_s &= a (1 + \mathfrak{a}_s^1 z + \dots) + bz^{3/2} (\mathfrak{b}_s^0 + \mathfrak{b}_s^1 z + \dots), \end{cases} \quad (4.36)$$

$$m = \frac{3}{4} : \quad \begin{cases} \xi_r &= bz^{3/2} (1 + \mathfrak{b}_r^1 z + \dots) + az (\mathfrak{a}_r^0 + \mathfrak{a}_r^1 z + \dots) \\ \xi_s &= a (1 + \mathfrak{a}_s^1 z + \dots) + bz^{5/2} (\mathfrak{b}_s^0 + \mathfrak{b}_s^1 z + \dots), \end{cases} \quad (4.37)$$

where the coefficients $\mathfrak{a}_a^l, \mathfrak{b}_a^l$ are fixed by the near boundary expansions of the equations of motion while a, b are the integration constants describing the source and response, respectively. Importantly, we see that because the expansion is in half-integer powers of z , the series proportional to a and b never overlap and therefore there are no logarithmic terms appearing in the expansion [75, 194].

Near the horizon, both spinor components approach constants for any value of mass. However, the equation coefficients include the factors of $\sqrt{f} \sim \sqrt{1-z}$, therefore the expansion near horizon goes in half-integer powers of $(1-z)$

$$z \rightarrow 1 : \quad \begin{aligned} \xi_r &= h(1 + \mathfrak{h}_1^1 \sqrt{1-z} + \mathfrak{h}_1^2 (1-z) \dots) \\ \xi_s &= -ih(1 + \mathfrak{h}_2^1 \sqrt{1-z} + \mathfrak{h}_2^2 (1-z) + \dots), \end{aligned} \quad (4.38)$$

where h is an arbitrary integration constant and the coefficients h_a^l , including the “ $-i$ ” factor in front of ξ_s come from the expansion of the equations of motion near horizon.

In order to render the solutions regular on both ends of the integration interval it is therefore convenient to rescale the coordinate as well. More specifically, we define

$$z \equiv \left(1 - (1 - r)^2\right)^2, \quad r \Big|_{z \rightarrow 0} \sim \sqrt{z}/2, \quad (1 - r) \Big|_{z \rightarrow 1} \sim \sqrt{(z - 1)/2}. \quad (4.39)$$

With these modifications, the problem reduces to solving two coupled first-order linear ODEs (4.16) on the interval $r \in [0, 1]$ subject to the boundary conditions (4.36), (4.38). There are 3 integration constants a, b and h , one of which can be set to unity due to the linearity. The remaining two are fixed by the two boundary conditions giving a unique solution for fixed ω, k_x, k_y . We use the numerical shooting method to obtain this solution. We shoot from both ends of the interval, using the expansion series (4.36) and (4.38) as the initial conditions, and look for the values of free constants b, h for which the solutions match in the arbitrary point in the interior of the interval. The advantage of this method is that we have a direct control over the response constant b and do not need to extract it from subleading terms in the near boundary expansions of the solution as it is usually done when shooting from horizon only.

4.B. Appendix B: Numerical Calculus and Precision Control for Gravity Background

In order to obtain the non-homogeneous gravitational background with a periodic boundary condition for the gauge field (4.25), we have to solve the full set of the Einstein equations. These follow from Eq. (4.24), which gives a set of 6 coupled non-linear partial differential equations (PDEs) in coordinates (x, z) , which are not elliptic. In practice we solve for functions $\hat{Q}_{\mu\nu}, \hat{A}_\mu$ defined as

$$A_t = \bar{\mu}(1 - z)\hat{A}_t, \quad \mathcal{T}^2 = 1 + z\hat{Q}_{tt}, \quad \mathcal{X}^2 = 1 + z\hat{Q}_{xx} \quad (4.40)$$

$$\mathcal{Y}^2 = 1 + z\hat{Q}_{yy}, \quad \mathcal{Z}^2 = 1 + z\hat{Q}_{zz}, \quad Q_{xz} = z\hat{Q}_{xz}, \quad (4.41)$$

such that the RN black hole solution corresponds to the choice $\hat{Q}_{\mu\nu}(x, z) = 0, \hat{A}_t(x, z) = 1$.

We use the DeTurck trick, outlined in [128, 129, 191] and used for this type of holographic models in [118, 136]. It allows to recast the Einstein’s equations as a boundary value problem for a set of nonlinear elliptic equations. We choose the RN black hole as a reference metric, which allows us to use for the non-homogeneous background the same expression of temperature as a function of chemical potential as that of the RN black hole (4.11).

The boundary conditions in x -direction are periodic, as dictated by the symmetry of the background lattice potential. It is convenient to rescale the spatial coordinate $x \rightarrow (2\pi/p)\hat{x}$ in order to fix the integration interval to unity: $\hat{x} \in [0, 1]$. At the $z \rightarrow 0$ boundary we require the metric to be asymptotically AdS with a nontrivial inhomogeneous source for the gauge field (c.f. (4.25))

$$z \rightarrow 0 : \quad \hat{Q}_{\mu\nu}(x, 0) = 0, \quad \hat{A}_t(x, 0) = 1 + \lambda \cos(2\pi\hat{x}). \quad (4.42)$$

The horizon boundary conditions follow from the asymptotic expansion of the Einstein equations near the horizon $f(1) = 0$. We expand the unknown functions in the Taylor series down to the first derivative order and substitute these expansions into the Einstein equations. This gives us 5 equations in the subleading order which relate the derivatives of the fields to their horizon values, i.e. generalized Robin boundary conditions. On top of that we get one algebraic equation $\hat{Q}_{tt}(x, 1) = \hat{Q}_{zz}(x, 1)$ at the leading order, which guarantees the solution to be static [118, 136, 140].

The numeric algorithm follows closely the treatment of our earlier works [79, 147, 189] with several technical improvements. We used a finite difference discretization of the equations on a homogeneously spaced grid and realized a Newton-Raphson procedure to solve the nonlinear boundary value problem. While supplementary procedures were implemented, including a relaxation scheme with Orszag regularization, no other methods matched the speed and accuracy of the direct Newton-Raphson method [195, 196], see also [147].

We ran a comprehensive series of precision and accuracy tests to make a judicious choice of computational parameters. We employed the norm of the DeTurck vector and the value of the trace of the Einstein tensor as measures of convergence. The thermodynamic potential was used as a physical observable, from which we could estimate the relative precision of our calculations. From this analysis, we were able to conclude that the configuration which gives us the best balance between speed and accuracy of computations for both the backgrounds and the fermions is a grid of $n_x \times n_y = 34 \times 80$ points, where we use 8th-order accuracy central finite difference derivatives in our finite difference scheme. This achieved relative errors of less than 10^{-5} in the thermodynamic potential, while still allowing for the fermionic equations to be computed quickly and accurately enough. In order to make sensible comparisons, we work in the canonical ensemble with a constant charge density. Since this is not a parameter in our equations, but rather an observable we can only extract after solving the background, we employed a root-finding algorithm with a relative tolerance of 10^{-3} to fix the charge density.

We implement our numerical routines in Python 3.6 using a set of packages that can be found in the standard SciPy stack [197]. Under the hood, these use the SuperLU [198] package for solving the sparse linear equations. We have performed several cross checks with a similar code in Mathematica [199], which was used earlier in [79, 189, 190], in order to prove the reliability of the package. The code was designed such that it could run a large number of small instances in parallel on any number of machines. This technique was suitable for running on the Lorentz Institute Maris cluster

4.C. Appendix C: Numerical Calculus for Dirac Equation

There are few subtleties which one encounters when solving the Dirac equation on the non-homogeneous background (4.30) numerically. First, in order to make the fermionic solutions regular on both horizon and asymptotic boundary we perform the same set of redefinitions of the wave-functions (4.35) and holographic coordinate (4.39) as it was done in the homogeneous case discussed in Appendix 4.A.

Moreover, there are several strategies which one can use in order to solve the set of first order differential equations numerically. One of them is to solve a Cauchy problem, integrate the equations starting from horizon and read off the boundary asymptotes. This is somewhat similar to the shooting method we discussed above and it was used in the early work [159]. However, when dealing with PDEs, one has to consider solving for all possible Fourier modes on the horizon and tracing out all the components of the response matrix \mathcal{S}_{nl} (4.18) before one gets access to the single \mathcal{S}_{00} component, which we are mostly interested in. Therefore we find this approach not suitable. Instead, we consider the boundary value problem, imposing the (position dependent) infalling boundary conditions (4.38) at the horizon as well as setting the source $a(x)$ on the asymptotic boundary $z \rightarrow 0$ to a desired Fourier mode. In this way, setting for instance $a(x) = e^{ip_l x}$ with fixed l and measuring the full profile of $b(x) = \sum_n e^{ip_n x}$, we get the information on all components of the response matrix in a row $\mathcal{S}_{ln}, n \in [-N/2, N/2]$, where N is the size of the grid in the x -direction. This boundary value approach is more useful since we can obtain the desired value \mathcal{S}_{00} in a single iteration by considering simply $a(x) = 1$ as boundary condition.

However, a problem arises when one tries to implement the boundary value PDE solving code in the case of a Dirac equation. The boundary value problem requires setting the boundary conditions for each field on both ends of the integration interval. For a first order differential equation, like the Dirac equation, this over determines the problem. We avoid this obstacle by formally setting a trivial boundary conditions of the form ‘0 = 0’ for half of the fields on the boundary. Indeed, after performing the rescaling of the fields (4.35) we guarantee that the sub-leading spinor component will behave as $\xi_r \sim z^{2m}$ at the boundary. Therefore, setting $\xi_r(0) = 0$ does not impose any extra constraint in the problem. This precise trick does not work however in case of alternative quantization, when we formally take $m < 0$ and the “response” branch $\sim z^{2m}$ diverges on the boundary. In the particular case of $m = -1/4$ studied here, this divergence is mild enough and we simply get rid of it by further redefining the “response” fermion component with an extra factor of z . More precisely, in case of $m = -1/4$ instead of (4.35) we use $\zeta_r \rightarrow z^{-m-1}(1-z)^{-i\frac{\omega}{4\pi T}}\xi_r$. This changes the near boundary behavior of the ξ_r component to $\xi_r \sim z^{1/2}$. As before, the Dirichlet boundary condition $\xi_r = 0$ is trivial and does not over constrain the problem.

We use a similar logic on the horizon; in addition to the leading behaviour $\xi_r(x) = i\xi_s(x)$, Eq. (4.38), following from the ingoing boundary condition, we include the sub-leading terms in the expansion of the equations of motion,. These, relate the derivatives of the functions to their boundary values. Since these relations are obtained from the equations of motion themselves, they do not introduce extra constraints and we are left with the correct amount of boundary conditions.

Another problem with the first order differential equations is that the matrix which represents the discretized problem on a lattice does not have a positively defined spectrum of eigenvalues typical of elliptic problems. Therefore, one can not rely on the iterative methods, because these are not guaranteed to converge. In our case, the Dirac equation is linear and one does not require to use iterations of any kind: the problem is solved “in one shot” by inverting the master matrix once. Even though we managed to make use of this approach, it may not always be applicable, especially in cases where the pseudospectral collocation is used and hence the matrix is dense, or simply if the grid is dense and inversion of the huge matrix is not feasible. In this case one can improve

the situation by substituting the first order equations (4.30) with the second order elliptic ones. Indeed, if we represent the equations (4.30) for ξ^\uparrow and their P-transformed counterparts for ξ^\downarrow as

$$\text{Dirac}^\uparrow \equiv \mathcal{D}_x[\xi^\uparrow] + \mathcal{K}_y \xi^\downarrow, \quad \text{Dirac}^\downarrow \equiv \mathcal{D}_{-x}[\xi^\downarrow] - \mathcal{K}_y \xi^\uparrow, \quad (4.43)$$

we can apply to one of the equations the differential operator of the other equation, and vice versa, to get the following second order system

$$\begin{aligned} (\text{Dirac}^\uparrow)^2 &= \mathcal{D}_{-x}[\mathcal{D}_x[\xi^\uparrow]] + \mathcal{D}_{-x}[\mathcal{K}_y] \xi^\downarrow + \mathcal{K}_y^2 \xi^\uparrow, \\ (\text{Dirac}^\downarrow)^2 &= \mathcal{D}_x[\mathcal{D}_{-x}[\xi^\downarrow]] - \mathcal{D}_x[\mathcal{K}_y] \xi^\uparrow + \mathcal{K}_y^2 \xi^\downarrow. \end{aligned} \quad (4.44)$$

In this form, the second order differential operator for each spinor component is the Laplacian in curved space. This representation allows us to use the full power of the iterative numerical techniques designed for elliptic equations. We have observed that the direct inversion of the master matrix, similar to the one we used in the first order case, becomes numerically less demanding due to improved features of the differential operators. When using the second order equations (4.44) one has to take care that no ghost solutions are obtained which do not solve the original problem. We can guarantee this by using the expanded first order Dirac equations as the boundary condition on the horizon. Unlike the first order case, these boundary conditions are not trivial, but they rather impose the constraint that the first order equations are satisfied at the horizon, and this constraint is further propagated in the bulk by the second order system. We checked in our numerical calculations that the two approaches, with the first and the second order differential equations, give identical results and this cross-check serves as a good confirmation of the validity of our numerical treatment.

4.D. Appendix D: Green's Function in the Bloch Momentum Representation

Here, we study spatial features of the Green's function in the Bloch momentum representation and the way the poles in the alternative quantization manifest themselves as zeroes in direct quantization. We focus on the response matrix (4.32). In practice, by representing the Dirac equation as a boundary value problem, as outlined in Appendix 4.C, we have a direct control over $a(x)$ and can, for instance, source any given harmonic mode. In most cases we just switch on $a_0 = 1$, corresponding to the constant source and obtain $b(x)$ as the series

$$b^{(0)}(x) = \sum_n e^{inpx} \mathcal{S}_{n0}. \quad (4.45)$$

Then, we extract the b_0 homogeneous component, which gives $\mathcal{S}_{00} = b_0/1$ (note that we normalized $a_0 = 1$ here).

In principle, we can go further and study a full rectangular sector of a (formally infinite) \mathcal{S} -matrix. In order to do so, we consider several harmonic sources $a^{(l)}(x) = e^{ilpx}$ and evaluate the responses for these cases

$$b^{(l)}(x) = \sum_n e^{inpx} \mathcal{S}_{nl}. \quad (4.46)$$

It is now clear that by extracting N Fourier modes of the response profiles $b^{(l)}(x)$ for a set of L harmonic sources we get access to the full $N \times L$ patch of the \mathcal{S} -matrix. Formally, in order to treat the alternative quantization as exchanging the roles between $b(x)$ and $a(x)$ and obtain the $\tilde{\mathcal{S}}_{00}$ component of the Alt. Q response matrix, we have to guess what kind of the boundary “response” condition $a(x)$ would lead to a constant “source” $b(x) = b_0$. In other words, our goal in this case is to find a set of coefficients a_l , such that

$$\sum_l a_l b^{(l)}(x) = \sum_{l,n} \mathcal{S}_{nl} a_l e^{inpx} = b_0. \quad (4.47)$$

In a vector notation this has a simple form

$$\mathcal{S} \cdot \vec{a} = b_0 \vec{e}_0, \quad (4.48)$$

where $\vec{a} = (\dots, a_{-1}, a_0, a_1, \dots)$ and \vec{e}_n is the unit basis vector with the only nonzero component at n -th position. Clearly, the result is

$$\vec{a} = b_0 \mathcal{S}^{-1} \cdot \vec{e}_0 \quad (4.49)$$

And after taking the a_0 component we arrive at the expression: $\tilde{\mathcal{S}}_{00} \equiv b_0/a_0 = (\mathcal{S}^{-1})_{00}$, from which the equation (4.33) of the main text follows. As we see here, if \mathcal{S}_{00} has a diverging value, it will enter the determinant of \mathcal{S} and therefore force the $(\mathcal{S}^{-1})_{00}$ component to vanish in complete analogy to the simpler homogeneous case we studied in Sec. 4.4. Given that using the harmonic sources we can evaluate a large enough sector of the \mathcal{S} -matrix, we can invert it approximately and obtain a required value of $(\mathcal{S}^{-1})_{00}$. However this treatment is not feasible in practice. The other way of obtaining the alternative quantization picture is by directly setting the boundary condition for $b(x) = 1$ and read out the profile of $a(x)$. In this way we directly measure the $\tilde{\mathcal{S}}_{00}$ component and no matrix inversion is needed. This approach is equivalent to setting the bulk fermion mass to its negative value (4.17), as we discussed above and it is much less demanding, therefore we predominantly use it in this work. Nonetheless, the rescaling of the fermionic wave function discussed in Appendix 4.C is different in this case. Consequently, the equations differ from the direct quantization ones. We find it important to check whether the two approaches do indeed lead to the equivalent results. On Fig. 4.11 we show that indeed the result obtained from inverting the \mathcal{S} -matrix for a set of 34 harmonic sources (left panel) coincides with the one which we get by changing the sign of the bulk fermion mass (right panel).

One extra comment on the structure of the \mathcal{S} -matrix is in order. This clarifies the relation between the shifts in parameter k and the values of the spectral function in the different Brillouin zones. It is useful to recall that the k -parameter is a part of the definition of the Bloch wave-function (4.29). The actual solution to the equations of motion near the boundary is

$$\psi(x, z) = e^{ikx} [a(x)(1 + \dots) + b(x)z^\alpha(1 + \dots)]. \quad (4.50)$$

From this solution we infer that $\vec{b} = \mathcal{S}[k] \cdot \vec{a}$. However, one can represent the same wave-function in a different way

$$\psi(x, z) = e^{i(k-p)x} [\tilde{a}(x)(1 + \dots) + \tilde{b}(x)z^\alpha(1 + \dots)], \quad (4.51)$$

$$\tilde{a}(x) \equiv e^{ipx} a(x), \quad \tilde{b}(x) \equiv e^{ipx} b(x). \quad (4.52)$$

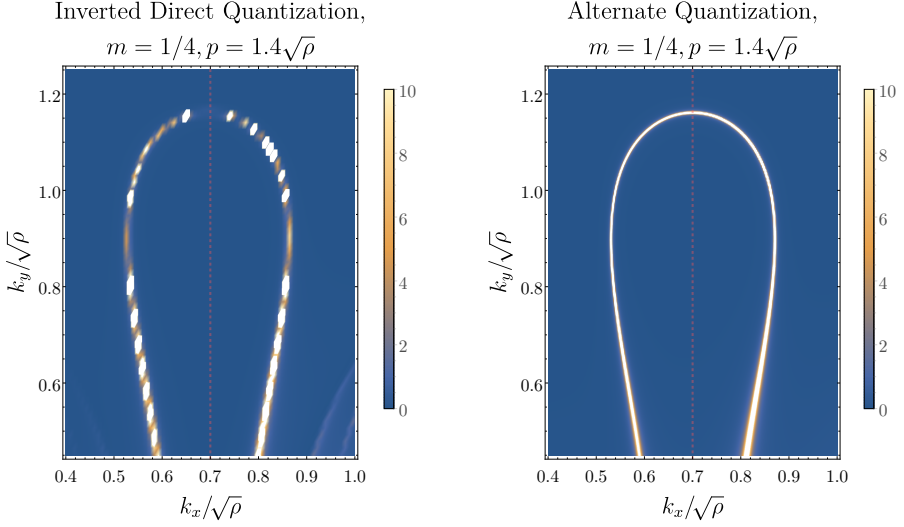


Figure 4.II.: **Comparison of the two treatments of the alternative quantization picture** The comparison between computation in alternate quantization and doing the inversion procedure from the direct quantization data. The main features (sharpness, shape, and the reduction of spectral weight near $(k_x, k_y) = (0.65, 0.40)\sqrt{\rho}$) are demonstrably reproduced. The inversion procedure does suffer from limited numerical precision, as the contributions from all the different Green's function components range over many orders of magnitude. The non-smoothness of the left-hand side arises because the width of the FS is smaller than the density of data points, causing the computation to not quite hit the peak. This can be improved in principle, however due to the prohibitive computational cost of this procedure we don't show it here.

The $\tilde{a}(x)$ and $\tilde{b}(x)$ functions are still periodic in the unit cell, therefore (4.51) is a perfectly valid Bloch wave representation as well. However, the Bloch momentum is now different and the relation between $\tilde{b}(x)$ and $\tilde{a}(x)$ reads

$$\vec{\tilde{b}} = \mathcal{S}[k - p] \cdot \vec{\tilde{a}} \quad (4.53)$$

Recalling the definition (4.52) we can relate the Fourier component of $a(x)$ and $\tilde{a}(x)$:

$$a_l = \tilde{a}_{l+1}, \quad b_n = \tilde{b}_{n+1}, \quad (4.54)$$

and together with (4.53) it allows us to relate the components of $\mathcal{S}[k]$ from the different Brillouin zones

$$\mathcal{S}[k - p]_{nl} = \mathcal{S}[k]_{n-1, l-1}. \quad (4.55)$$

This identity serves as another useful check of our numerical procedures and our results are in agreement with it.

5. Quantization of the Gubser-Rocha Model

5.1. Attribution

This paper has been previously published as a preprint on arXiv and has been submitted to JHEP for publication, and is currently under editorial review, under the title ‘Quantization and variational problem of the Gubser-Rocha Einstein-Maxwell-Dilaton model, conformal and non-conformal deformations, and its proper thermodynamics.’, together with N. Chagnet and K.Schalm.[99]

5.2. Introduction

One of the main insights holography has provided into the physics of strongly correlated systems is the existence of previously unknown (large N) non-trivial IR fixed points. These fixed points are characterized by an emergent scaling symmetry of the Lifshitz form categorized by a dynamical critical exponent z , a hyperscaling exponent θ , and a charge anomalous dimension ζ .

$$x \rightarrow \lambda^{1/z} x, t \rightarrow \lambda t, F \rightarrow \lambda^{\frac{d-\theta}{z}} F, \rho \rightarrow \lambda^{\frac{d-\theta+\zeta}{z}} \rho. \quad (5.1)$$

Here F is the free energy density and ρ the charge density [93, 102, 200, 201]. Within these Lifshitz fixed points those with $z = \infty$ are special. Such theories have energy/temperature scaling with no corresponding spatial rescaling. These are therefore systems with exact *local quantum criticality*. Phenomenologically this energy/temperature scaling without a corresponding spatial part is observed in high T_c cuprates, heavy fermions and other strange metals, where this nomenclature originates (see e.g. [202]). In holography $z = \infty$ IR fixed points correspond to an emergent AdS₂ symmetry near the horizon of the extremal black hole. The two most well-known such solutions are the plain extremal RN black hole and the extremal GR black hole [98]. The RN solution of AdS-Einstein-Maxwell theory has been studied extensively primarily because it is the simplest such model. Its simplicity also means it is too constrained to be realistic as a model of observed locally quantum critical metals. Notably the RN has a non-vanishing ground-state entropy and emerges from a $d > 2$ -dimensional conformal field theory. The more realistic GR model arises from a non-conformal strongly correlated theory, where one isolates the leading irrelevant deformation from the IR fixed point. This “universal” subsector gives it a chance to be applicable to observed local quantum critical systems. Moreover the groundstate now has vanishing entropy (to leading order). In the gravitational description this leading (scalar) (IR)-irrelevant operator is encoded in

a dilaton field that couples non-minimally to both the Einstein-Hilbert action and the Maxwell action. Even with its more realistic appeal, the more complex nature of the GR dynamics means it has been studied less; some examples are [106–108, 203, 204].

In the course of these studies of non-minimally coupled EMD theories, it was noted in particular that the proper holographic interpretation of the analytical Gubser Rocha (aGR) black hole solution depends sensitively on the particular quantization [108, 204]. Within holography, relevant and marginally relevant scalars allow for different quantization schemes. A relevant operator of dimension $\frac{d}{2} < \Delta < d$ always has a conjugate operator of dimension¹ $\frac{d}{2} - 1 < \Delta_{\text{conj}} = d - \Delta < \frac{d}{2}$, and one can choose whether one considers the original operator as the dynamical variable (standard quantization) or the conjugate operator (alternate quantization) or any intermediate linear combination through a double-trace deformation [205, 206].

An additional complication results from the fact that the (static and isotropic) aGR solution is a two-parameter solution depending on T and μ , whereas one expects a third independent parameter encoding the asymptotic source value of the dilaton field. A low-energy scalar can have a sourced (or unsourced) vacuum-expectation value; this changes the energy of the ground-state and hence should contribute to the thermodynamics. For minimally coupled scalars this was recently elucidated in [207].

In this paper we will show that the correct way to interpret the aGR solution is as a two-parameter subset of solutions within the three-parameter thermodynamic phase diagram. For essentially all quantization schemes this constrains the source of the dilaton field in terms of the temperature and chemical potential of the solution. Crucially this implies that derivatives of thermodynamic potentials mix the canonical contribution with an additional contribution from the scalar response. We will show this explicitly in Section 5.4.2. A proper understanding of the solution requires one to carefully separate out this contribution.

It also turns out, however, that there is a specific quantization scheme where the dilaton corresponds to an exactly marginal operator in the theory. This was previously noted for another set of the EMD actions [204].² In this special quantization choice the aGR solution corresponds to a solution with no explicit source for the dilaton field. Within this special quantization scheme one can deform the analytical solution to a nearby solution with a finite scalar source. We do so in Section 5.5. We conclude with a brief discussion on the meaning of this newly discovered exactly marginal deformation.

5.3. Setup

The GR black hole is a solution to the EMD action

$$S_{\text{bulk}} = \frac{1}{2\kappa^2} \int d^4x \sqrt{-g} \left[R - \frac{Z(\phi)}{4} F^2 - \frac{1}{2} (\partial\phi)^2 - V(\phi) \right], \quad (5.2)$$

¹The upper bound of Δ would suggest $\Delta_{\text{conj}} > 0$ but requiring unitarity of the conjugate theory leads to a higher bound.

²We thank Blaise Gout  raux for bringing this paper to our attention.

where the potentials are given by $Z(\phi) = e^{\phi/\sqrt{3}}$ and $V(\phi) = -6 \cosh(\phi/\sqrt{3})$.³ This action is a consistent truncation of $d = 11$ supergravity compactified on $AdS_4 \times S_7$ [98]. The equations of motion for this system are

$$\begin{aligned} R_{\mu\nu} &= \frac{Z(\phi)}{2} \left[F_{\mu}{}^{\rho} F_{\nu\rho} - \frac{1}{4} g_{\mu\nu} F^2 \right] + \frac{1}{2} \partial_{\mu} \phi \partial_{\nu} \phi + \frac{1}{2} g_{\mu\nu} V(\phi), \\ \nabla_{\mu} [Z(\phi) F^{\mu\nu}] &= 0, \\ \square \phi &= V'(\phi) + \frac{Z'(\phi)}{4} F^2, \end{aligned} \quad (5.3)$$

where we used that, on-shell, $R = 2V(\phi) + \frac{1}{2}(\partial\phi)^2$. The static and isotropic metric ansatz that is asymptotically AdS is

$$ds^2 = g_{\mu\nu} dx^{\mu} dx^{\nu} = \frac{1}{z^2} \left[-f(z) dt^2 + g(z) (dx^2 + dy^2) + \frac{dz^2}{f(z)} \right], \quad (5.4)$$

where the coordinate z is the radial direction with $z = 0$ the AdS boundary (UV). The aGR solution [98] is then given by

$$\begin{aligned} g(z) &= (1 + Qz)^{3/2}, \\ f(z) &= \frac{1 - z/z_h}{g(z)} \left[1 + (1 + 3Qz_h) \frac{z}{z_h} + \left(1 + 3Qz_h + 3Q^2 z_h^2 \right) \left(\frac{z}{z_h} \right)^2 \right], \\ A_t(z) &= \mu j(z) = \frac{\sqrt{3Qz_h(1 + Qz_h)}}{z_h} \frac{1 - z/z_h}{1 + Qz}, \\ \phi(z) &= \frac{\sqrt{3}}{2} \log [1 + Qz], \end{aligned} \quad (5.5)$$

where z_h is the horizon of this non-extremal black hole. From hereon we choose units where $2\kappa^2 = 16\pi G = 1$, such that the temperature, chemical potential and entropy-density of the GR-black hole are

$$\begin{aligned} T &= -\frac{f'(z)}{4\pi} \Big|_{z=z_h} = \frac{3\sqrt{1 + Qz_h}}{4\pi z_h}, \quad s = 4\pi a_h = 4\pi \frac{(1 + Qz_h)^{3/2}}{z_h^2}, \\ \mu &= A_t(z = 0) = \sqrt{3Qz_h(1 + Qz_h)}/z_h, \end{aligned} \quad (5.6)$$

where $a_h = \sqrt{g_{xx}(z_h)g_{yy}(z_h)}$ is the area density of the horizon. Expressed in terms of the temperature, it is easy to see that the entropy vanishes linearly $s = \frac{16\pi^2}{3\sqrt{3}} \mu T + \dots$ at low temperatures with no remnant ground state entropy. Important in the remainder is (i) to recall that both the temperature and the entropy can be read off from the near-horizon behavior of the metric alone.

³Note that the dilaton has dimension zero.

As local properties of the black hole they do not depend on the boundary conditions. (2) The analytic solution depends on two parameters Q and z_h . And (3) note that the metric gauge choice is not of the Fefferman-Graham (FG) type in that the change in metric functions starts at order z and not z^3 .

5.4. Regularization, boundary terms and choice of quantization

5.4.1. Boundary action

We must add to the gravitational action (5.2) a boundary action. This is to regularize its on-shell value as well as to make the variational principle well-defined. In the case of the scalar it also prescribes the quantization of the scalar field. We will be using in this work a standard multi-trace deformation of the Neumann boundary theory, which were generally described in [205, 206, 208] and more specifically in EMD theories [204], with a boundary action of the form

$$S_{\text{bdy}} = - \int_{z=\epsilon} d^3x \sqrt{-\gamma} \left[2K + 4 + {}^{(3)}R_\gamma \right] + S_{\text{bdy},\phi}, \quad (5.7)$$

Here $N^\mu = -\sqrt{g^{zz}}(0, 0, 0, 1)$ is an outward pointing spacelike unit normal vector defining the hypersurface $z = \epsilon \ll z_h$ and $\gamma_{\mu\nu} = g_{\mu\nu} - N_\mu N_\nu$ is the induced metric on the surface. Furthermore $K \equiv \gamma^{ij} K_{ij}$ is the trace of the extrinsic curvature $K_{ij} \equiv -\gamma_i^\mu \gamma_j^\nu \nabla_{(\mu} N_{\nu)}$ and ${}^{(3)}R_\gamma$ the Ricci scalar curvature of the hypersurface (Latin symbols correspond to coordinates on the hypersurface while the greek symbols are those of the original manifold). The first three terms correspond to the usual Gibbons-Hawking-York counterterms necessary to make the variational principle for the metric well-defined and also to regularize the Einstein-Hilbert-Cosmological Constant part of the action on shell. In our coordinatization Eq. (5.4) the induced metric is flat on-shell. The scalar part of the boundary term $S_{\text{bdy},\phi}$ can take two forms depending on whether we consider the standard quantization boundary theory where only the ϕ^2 regularization term appears

$$S_{\text{bdy},\phi}^{(\text{SQ})} = \int_{z=\epsilon} d^3x \sqrt{-\gamma} \frac{\Lambda_\phi}{2} \phi^2, \quad \Lambda_\phi = -1, \quad (5.8)$$

— here the value of Λ_ϕ is set to regularize the boundary term arising from varying the bulk action — or whether we consider a multi-trace deformation of the alternate quantization boundary theory

$$S_{\text{bdy},\phi}^{(\text{MT})} = \int_{z=\epsilon} d^3x \sqrt{-\gamma} \left[\frac{\Lambda_\phi}{2} \phi^2 + \phi N^\mu \partial_\mu \phi \right] + S_F, \quad \Lambda_\phi = 1. \quad (5.9)$$

The $\phi N^\mu \partial_\mu \phi$ is a Legendre transform from Dirichlet to Neumann boundary conditions, which also diverges at leading order and is the reason for the shift in Λ_ϕ as we will see.⁴ The multi-trace deformation S_F is a finite contribution to the boundary action and will be described when

⁴Strictly speaking $\phi N^\mu \partial_\mu \phi$ is a combination of a true Legendre transform $J\mathcal{O} = z^{\lambda_- - \lambda_+ - 1} \phi \partial_n z^{-\lambda_-} \phi$ (see Eq. (5.13)) and counterterms.

the asymptotics of the solution are analysed. We will continue the derivation with the choice $S_{\text{bdy},\phi} = S_{\text{bdy},\phi}^{(\text{MT})}$ while keeping in mind that a similar derivation can easily be done using instead $S_{\text{bdy},\phi} = S_{\text{bdy},\phi}^{(\text{SQ})}$, and we will invoke those results when necessary.

Varying the total action $S = S_{\text{bulk}} + S_{\text{bdy}}$ to first order, a proper holographic interpretation demands that one obtains a variation of the form [100]

$$\delta S = \int_{z=\epsilon} d^3x \sqrt{-\gamma} \left[\frac{1}{2} T_{\mu\nu} \delta \gamma^{\mu\nu} + J^\mu \delta A_\mu + \mathcal{O}_\varphi \delta \varphi \right], \quad (5.10)$$

where the terms multiplying the EMD fields are interpreted as the operators in the boundary CFT where $T_{\mu\nu}$ is the boundary stress tensor, J_μ the boundary current associated with the U(1) charge, and \mathcal{O}_φ the operator dual to a scalar which may be a non-linear function of the dilaton field. The important point is that the action evaluated on the black hole solution is equated with (minus) its Gibbs free energy density. The variation of the action (restricted to preserve isotropy) thus includes thermodynamic variations. The expression above makes clear that in addition to the temperature and the chemical potential there ought to be a dependence of the Gibbs free energy on an external (source) variation of (the boundary value of) the scalar field [207].

Performing this variation on Eqs (5.2) plus (5.7), we can write it as a bulk integral of an integrand proportional to the equations of motion (5.3), that vanishes on-shell, and a remaining boundary part. In the boundary part the normal derivatives of $\delta \gamma_{\mu\nu}$ cancel due to the Gibbons-Hawking-York term; there are no normal derivatives in A_μ . Restricting to boundary indices we have⁵

$$\begin{aligned} T_{ij} &= 2K_{ij} - 2({}^d R_{\gamma,ij}) - 2(K+2)\gamma_{ij} + \gamma_{ij} \left[\phi N^z \partial_z \phi + \Lambda_\phi \phi^2/2 \right] + T_{ij}^F, \\ J_i &= -Z(\phi) N^z F_{zi}, \end{aligned} \quad (5.11)$$

where T_{ij}^F is the contribution from S_F . The expression for \mathcal{O}_φ requires a more detailed discussion. Focusing on the variation in the dilaton ϕ in (5.10), we have

$$\delta S_\phi = \int_{z=\epsilon} d^3x \sqrt{-\gamma} \left[\Lambda_\phi \phi \delta \phi + \phi N^z \partial_z \delta \phi \right] + \delta S_F. \quad (5.12)$$

From its linearized equation of motion the dilaton has the following expansion in the near-boundary region

$$\phi(z) = \alpha z^{\lambda_-} + \beta z^{\lambda_+} + \mathcal{O}(z^3), \quad (5.13)$$

where $\lambda_\pm = \frac{3}{2} \pm \frac{1}{2} \sqrt{9+4m^2}$ and m is the effective mass. In the GR model the effective mass equals

$$m^2 = \frac{\partial}{\partial \phi^2} \left[V(\phi) + \frac{Z(\phi)}{4} F^2 \right] \bigg|_{\phi=0, z \rightarrow 0} = -2. \quad (5.14)$$

This value of the mass $-\frac{9}{4} < m^2 < 1 - \frac{9}{4} = -\frac{5}{4}$ is in the regime where two different quantizations are allowed, i.e. for this value of m both $\lambda_\pm > 0$ and either α (standard) or β (alternate)

⁵The radial components of $T_{\mu\nu}$ and J_μ vanish due to the projection on the hypersurface.

can be chosen as the source for the dual CFT operator with the other the response. One can also choose a mixture of the two, corresponding to a multi trace deformation, as we shall elucidate below.

The proper holographic normalization is most conveniently performed in a FG ansatz for the metric

$$ds^2 = \frac{1}{z^2} \left[-H_{tt}(z)dt^2 + H_{xx}(z)dx^2 + H_{yy}(z)dy^2 + dz^2 \right], \quad (5.15)$$

where we require Anti-deSitter (AdS) asymptotics $H_{\mu\nu}(z \rightarrow 0) = 1$ and use the equations of motion (5.3) to constrain the near-boundary expansion of $H_{\mu\nu}$ in terms of a small subset of degrees of freedom. We will use this ansatz for the remainder of this section. Using that $N^z(z) = -z$, and substituting (5.13) into (5.12), we can expand the variation w.r.t. the dilaton as

$$\delta S_\phi = \int_{z=\epsilon} d^3x \left[\frac{\Lambda_\phi - 1}{\epsilon} \alpha \delta\alpha + \alpha \delta\beta (\Lambda_\phi - 2) + \beta \delta\alpha (\Lambda_\phi - 1) + \mathcal{O}(\epsilon) \right] + \delta S_F. \quad (5.16)$$

As we claimed in (5.9), we must remove the leading divergence by imposing $\Lambda_\phi = 1$, leaving a finite contribution

$$\delta S_\phi = \int_{z=\epsilon} d^3x \left[-\alpha \delta\beta + \mathcal{O}(\epsilon) \right] + \delta S_F. \quad (5.17)$$

For the standard quantization term (5.8), it is easy to see that a similar derivation leads to $\Lambda_\phi = -1$.

One can modify the quantization by the addition of a multitrace deformation. This can in general be encoded in the boundary action S_F . Following [204, 208, 209], we choose $S_F = \int d^3x \sqrt{-\gamma} \epsilon^d \mathcal{F}(\alpha)$ such that, ignoring the metric variation, $\delta S_F = \int d^3x \sqrt{-\gamma} \epsilon^d \mathcal{F}'(\alpha) \delta\alpha$. Without loss of generality we choose \mathcal{F} of the form $\mathcal{F}(\alpha) = \frac{a}{2}\alpha^2 + \frac{b}{3}\alpha^3$ from here on. The variation of the boundary action then becomes

$$\delta S_\phi = \int_{z=\epsilon} d^3x \alpha \left[-\delta\beta + (a + b\alpha) \delta\alpha \right]. \quad (5.18)$$

We can therefore identify the VEV of the boundary scalar operator as $\mathcal{O}_\phi = \alpha$ while the source of the operator is

$$J_{\text{MT}} = -\beta + a\alpha + \frac{b}{2}\alpha^2. \quad (5.19)$$

Once again, had we chosen the standard quantization boundary term, then we would have $\delta S_\phi = \int d^3x \beta \delta\alpha$ such that $\mathcal{O}_\phi = \beta$ and $\varphi = \alpha$ leading to the boundary condition $J_{\text{SQ}} = \alpha$.

We have now almost all the ingredients to compute the scalar contribution to the stress tensor, but we still need to derive the variation of S_F w.r.t. the leading order of the boundary metric in order to compute the term T_{ij}^F , as was done before in [204]. Doing so, one simply finds $T_{ij}^F = \gamma_{ij} \epsilon^d \mathcal{F}(\alpha)$. It is interesting to note that the contribution S_F can also be absorbed into corrections to the ϕ^2 term as well as a ϕ^3 term as

$$S_{\text{bdy}} = \int_{z=\epsilon} d^3x \sqrt{-\gamma} \left[-(2K + 4 + {}^{(3)}R_\gamma) + \frac{\Lambda_\phi + \epsilon a}{2} \phi^2 + \phi N^\mu \partial_\mu \phi + \frac{b}{3} \phi^3 \right], \quad (5.20)$$

where $\Lambda_\phi + \epsilon a$ is a renormalized ϕ^2 coupling which will reproduce the α^2 contribution of \mathcal{F} , as was done in e.g. [205, 210]. The ϕ^3 coupling on the other end will reproduce the α^3 contribution of \mathcal{F} . This way of writing the boundary action highlights why we concentrated on \mathcal{F} of the form $\mathcal{F}(\alpha) = \frac{a}{2}\alpha^2 + \frac{b}{3}\alpha^3$. Lower order in α terms are constant shifts variationally and can be absorbed in a field redefinition – they are tadpoles. Any term α^n for $n > d$ would lead to vanishing contributions ϵ^{n-d} in the action – they are irrelevant deformations. The equality $\Lambda_\phi = 1$ remains true in order to regularize δS .

In the presence of such a boundary action, the contribution T_{ij}^F in the expression (5.11) simply includes the ϕ^2, ϕ^3 contributions and leads to

$$T_{ij} = 2K_{ij} - 2({}^d R_{\gamma, ij}) - 2(K + 2)\gamma_{ij} + \gamma_{ij} \left[\phi N^z \partial_z \phi + \frac{\Lambda_\phi + \epsilon a}{2} \phi^2 + \frac{b}{3} \phi^3 \right]. \quad (5.21)$$

We recognize the \mathcal{F} -dependent part of the stress tensor which agrees with the direct method. It is then immediate to compute the trace of the stress tensor

$$T_i^i = \frac{\alpha}{2} (3a\alpha + 2b\alpha^2 - 4\beta) = -\frac{\alpha}{2} (a\alpha - 4J_{\text{MT}}), \quad (5.22)$$

where in the last equality we used the boundary condition (5.19). This result points to the existence of a line of critical points with $a = 0$ where the sourceless ($J_{\text{MT}} = 0$ equivalent to the boundary condition $-\beta + a\alpha + \frac{b}{2}\alpha^2 = 0$) deformation \mathcal{F} is just marginal. This is equivalent to only deforming the boundary theory through a ϕ^3 term which indeed has dimension d and should therefore be marginal.

For completeness we mention that in the case of the standard quantization the trace of the stress tensor is simply $T_i^i = \alpha\beta = \beta J_{\text{SQ}}$.

5.4.2. Choice of quantization and thermodynamics

In this subsection, we will derive the thermodynamics of a black hole solution in a general compatible quantization choice. This goes beyond the analyses in [108, 204] where only the thermodynamics of a marginal scalar were considered, i.e. the case of alternate quantization with a multitrace deformation such that the stress tensor remains traceless. In view of extending the choice of possible theories to non-marginal ones, we will show that the thermodynamics space is extended from a 2-parameter to a 3-parameter space, as also emphasized for Einstein-Scalar theory in [207].

Let us start with the constraint that a choice of solution imposes on the possible quantization schemes. Indeed, while the choice of boundary terms in the action and therefore of the boundary deformation is a priori agnostic of a given solution to the bulk equations of motion, we have seen that the multi-trace deformation leads to a specific choice of boundary condition on the scalar (5.19). Not every solution to the bulk equations of motion (5.3) are compatible with every possible boundary condition, as was noted in [204, 211]. In the case of the metric corresponding to the aGR solution (5.5), the scalar ϕ has the following falloffs

$$\phi \sim \alpha z + (\beta - f'(0)\alpha/2)z^2 = \alpha z + (\beta - 3Q\alpha/4)z^2, \quad (5.23)$$

where we have related the values of $\phi'(0)$, $\phi''(0)$ to the falloffs α, β in the FG ansatz (5.15). This matching is made explicit in Section 5.8. Comparing with the full solution (5.5), we can therefore equate $\alpha = \sqrt{3}Q/2$ and $\beta = \sqrt{3}Q^2/8$. Consider then alternate quantization deformed by an arbitrary (relevant and marginal) multitrace deformation. In that case the source equals

$$J_{\text{MT}}(Q) = \frac{\sqrt{3}Q}{8} \left(4a + (\sqrt{3}b - 1)Q \right). \quad (5.24)$$

From this equation, we see there are a few distinct cases to consider

1. $a = 0, b = b_{\text{aGR}} \equiv 1/\sqrt{3}$: every instance of the 2-parameter aGR solution (5.5) is compatible with this choice and is sourceless $J = 0$. This is the sourceless marginal deformation we previously mentioned and which was studied in [108, 204, 211]. From Eq. (5.22), we see that this boundary theory has $T_i^i = 0$.
2. $a = 0, b = 0$: the quantization procedure is conventional alternate quantization. In this case, since the solution (5.5) is not sourceless, we must impose a Neumann boundary condition $\beta = -J$ with fine-tuned source $J(Q) = -\sqrt{3}Q^2/8$. The explicit source leads to an explicitly broken conformal symmetry in the boundary. (A similar argument holds for standard quantization with a Dirichlet boundary condition $\alpha = J$. One would then need to consider the boundary term $S_{\text{bdy},\phi} = S_{\text{bdy},\phi}^{(\text{SQ})}$ instead, and a fine-tuned source $J(Q) = \sqrt{3}Q/2$. Also here the explicit source leads to an explicitly broken conformal symmetry in the boundary.)
3. For all the other cases, one can look for explicitly sourced solutions $J = J(Q, a, b)$ defined in Eq. (5.24).⁶ This case is fundamentally similar to the case 2, with the explicit sourcing leading to a non-zero trace of the boundary stress-tensor.

In the end, we see that the only natural sourceless description we have of the solutions (5.5) corresponds to the marginal multi-trace deformation, case 1. The other cases, 2 and 3, are better understood as explicitly sourced deformations where the source is fine-tuned to select a certain subset of solutions at a fixed Q .

An important aspect is that even though a bulk solution may have different interpretations depending on the quantization choices set out above, the thermodynamics does know about the quantization choice. Let us consider the free energy of the solutions (5.5). Substituting the solution into the action, the free energy density Ω of the aGR black hole solution with compatible boundary condition is given by

$$S_{\text{on-shell}}^{\text{regularized}} = - \int d^3x \Omega, \quad \text{so} \quad \Omega = - \left(\frac{1}{z_h} + Q \right)^3 + \frac{Q^2}{8} \left(Q(1 - \sqrt{3}b) - 3a \right). \quad (5.25)$$

⁶If we insist on looking for solutions with $J = 0$, one of the couplings a or b must be fine-tuned e.g., $b(Q) = \frac{1}{\sqrt{3}}(1 - 4a/Q)$. As it was noted in [211], this means that fixing a, b to some constant will restrict the space of solutions to those for which $Q = \frac{4a}{1 - \sqrt{3}b}$. Allowing for a finite, albeit fine-tuned, source $J = J(Q)$ leads to the same result and we will choose this more natural point of view.

Furthermore, the holographic dictionary tells us that the chemical potential and the temperature of the boundary theory are given by (5.6). One might be inclined to use this to deduce a variation of Ω in the 2-parameter grand canonical ensemble $d\Omega = -s_1 dT - \rho_1 d\mu$ and derive from it the thermodynamic entropy and charge density of the theory

$$s_1 = - \left(\frac{\partial \Omega}{\partial T} \right)_\mu, \quad \rho_1 = - \left(\frac{\partial \Omega}{\partial \mu} \right)_T. \quad (5.26)$$

However, we have seen from Eq. (5.10) that the free energy variation in the presence of an explicit source should be corrected by a scalar contribution of the form (see also [207])

$$d\Omega = -s_2 dT - \rho_2 d\mu - \mathcal{O}_\varphi dJ. \quad (5.27)$$

This is the full 3-parameter thermodynamics of the system. The fact that the free energy (5.25) of the aGR solution only depends on T and μ , and not on the value of the scalar source means that the aGR solution should be seen as a 2-parameter constrained solution within this 3-parameter space. This family of solutions is only a subset of all the possible ones for *any* given compatible quantization scheme. A direct corollary is that to explore only this analytical set of solutions, variations of J, T, μ are not independent. Denoting J as the dependent variable, i.e. it is not independent but is a function of both T and μ , then the grand canonical potential varies as

$$d\Omega = - \left(s_2 + \mathcal{O}_\varphi \frac{\partial J(T, \mu)}{\partial T} \right) dT - \left(\rho_2 + \mathcal{O}_\varphi \frac{\partial J(T, \mu)}{\partial \mu} \right) d\mu \quad (5.28)$$

if one constrains one's considerations to aGR solutions only.

The precise relation of the VEV \mathcal{O}_φ and the source J to the fall-off of the dilaton depends on the quantization scheme as we have just reviewed. A choice of quantization is not a canonical transformation, as shown by [207] in the standard quantization case for Einstein-Scalar theories. Therefore the value of the free energy will depend on this choice. This is evident in the dependence on a, b in Eq. (5.25). In the full 3-parameter space of solutions this quantization choice dependence would only appear in the dilaton contribution part. In the constrained 2-parameter space of solutions, it would appear to imply that now also the thermodynamic entropy s_1 and charge density ρ_1 deduced from Eq. (5.26) depend on the quantization, as

$$\begin{aligned} s_1 &= 4\pi \frac{(1 + Qz_h)^{3/2}}{z_h^2} \left[1 + \frac{Q^2 z_h^3}{8(1 + Qz_h)^3} (Q(1 - \sqrt{3}b) - 2a) \right], \\ \rho_1 &= \mu \frac{1 + Qz_h}{z_h} \left[1 - \frac{Qz_h^2(2 + Qz_h)}{8(1 + Qz_h)^3} (Q(1 - \sqrt{3}b) - 2a) \right]. \end{aligned} \quad (5.29)$$

This is strange, as the Bekenstein-Hawking entropy and the charge density – the VEV of the sourced gauged field – are properties of the black hole solution and do not depend on the boundary action which sets the quantization. Indeed they can be read off directly from the geometry

as

$$s_2 = 4\pi \sqrt{g_{xx}(z_h)g_{yy}(z_h)} = \frac{4\pi(1 + Qz_h)^{3/2}}{z_h^2} \quad \text{the area of the horizon of the black hole,}$$

$$\rho_2 = -\partial_z A_t(z \rightarrow 0) = \mu \frac{(1 + Qz_h)}{z_h} \quad \text{the global U(1) charge.}$$

(5.30)

The solution is of course that in the constrained system s_1 and ρ_1 are not the true entropy and charge density, as they include the artificial contribution from varying $J(T, \mu)$ following from the constraint to stay within the 2-parameter aGR solution space. It is then a rather straightforward computation to connect Eqs. (5.29) and (5.30) through the variation of J expressed in Eq. (5.27). To that end, we can remember that the source J is constrained by the boundary condition (5.24) and that in our choice of quantization, we always have $\mathcal{O}_\varphi = \alpha$. In summary, the geometric expressions for the entropy and charge of the aGR solution are always the correct ones. The difference from the quantities computed from the Gibbs potential can be attributed to the fact that one considers a constrained system: the expression $s_1 = -\left(\frac{\partial \Omega}{\partial T}\right)_\mu = -\left(\frac{\partial \Omega}{\partial T}\right)_\mu - \mathcal{O}_\varphi \left(\frac{\partial J}{\partial T}\right)_\mu$ contains a term that is absent in the correct definition of the entropy $s_2 = -\left(\frac{\partial \Omega}{\partial T}\right)_{\mu, J}$, and similarly for ρ .

There is, however, the special case 1. When the deformation is purely marginal and sourceless – $a = 0$ and $b = \frac{1}{\sqrt{3}}$ – we can immediately infer that the variations of $J = 0$ will be trivial. In that case, we will have $s_1 = s_2$ and $\rho_1 = \rho_2$. The way to understand this is that within the 3-parameter space of possible solutions quantified by (T, μ, J) the 2-parameter aGR solution spans a different subspace depending on the quantization choice for the dual boundary theory. Figure 5.1, illustrates how this difference of boundary interpretation between the alternate quantization with sourceless marginal deformation of case 1 and the standard quantization of case 2 changes the shape of the aGR solution manifold inside the thermodynamic space of sources $\{T, \mu, J\}$. This visualization allows us to see at a glance how the sourceless marginal deformation reduces to a 2-charge thermodynamic space where 2-parameters of the solution naturally coincide with T, μ while the standard quantization interpretation of the aGR solution induces some non-trivial projection when varying the Gibbs free energy w.r.t. T, μ . For the sourceless marginal deformation the thermodynamics of the boundary thus simplifies greatly and will behave in a similar fashion to the conformal fluid dual to the RN black hole solution.

To complete the argument above we shall construct numerical solutions to the equations of motion (5.3) in the next section that differ from the aGR solution in that they explore the third direction orthogonal to T, μ and analyse their various boundary interpretations.

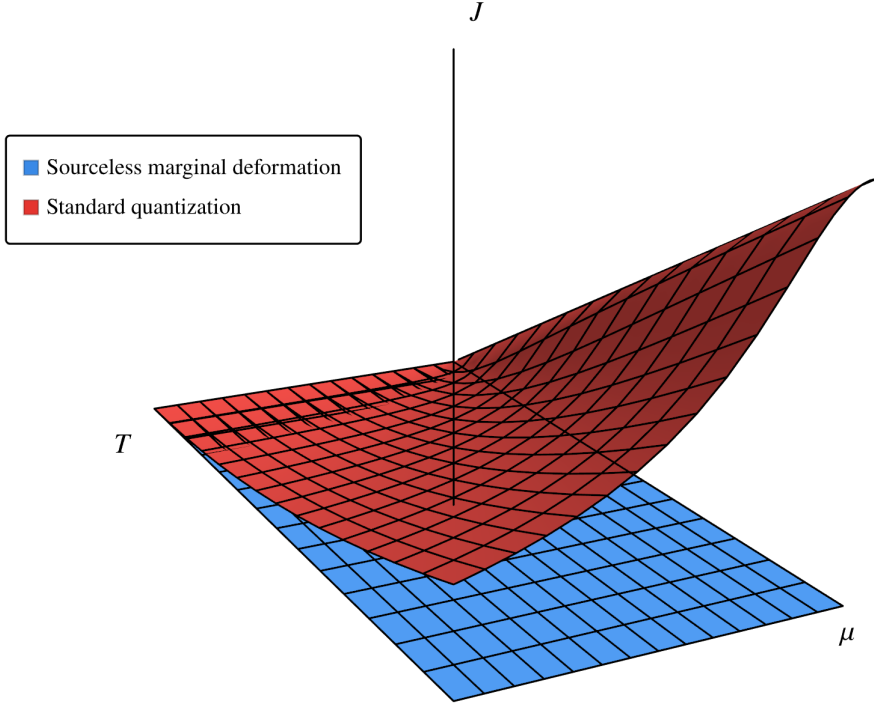


Figure 5.1.: aGR solution manifold in the thermodynamic parameter space of source $\{T, \mu, J\}$ for two specific choices of boundary interpretations (cases 1 and 2). The sourceless marginal case has trivial source and is by itself a 2-charge submanifold while the standard quantization case has a constrained source which leads to the non-trivial corrections in s_1, ρ_1 .

5.5. Deformed Gubser-Rocha black holes

5.5.1. Numerically constructed solutions

The solutions that generically differ from (5.5) correspond to setting different boundary conditions for the dilaton field. However, for each such new solution, its interpretation depends on the quantization one considers, i.e. what the on-shell value of the action including boundary terms reads.

We will solve the GR equations of motion (5.3) numerically using the following parametrization

$$\phi = \frac{\sqrt{3}}{2} z \psi(z), \quad A_t(z) = \mu j(z) a_t(z), \quad (5.31)$$

and with metric ansatz

$$ds^2 = \frac{1}{z^2} \left[-f(z) G_{tt}(z) dt^2 + \frac{dz^2}{f(z)} G_{zz}(z) + g(z) G(z) (dx^2 + dy^2) \right], \quad (5.32)$$

where $f(z), g(z), j(z)$ are held fixed to their expressions in the aGR solution (5.5) and $\psi, a_t, G_{tt}, G_{zz}, G$ are the dynamical fields. The radial coordinate z spans the range from the boundary at $z = 0$ to the outer horizon at $z = z_h$. The IR boundary conditions are chosen to have a single zero horizon corresponding to a non-extremal black hole and to impose regularity at the horizon for other fields (see e.g., [118]).⁷ The UV boundary conditions are chosen to impose AdS asymptotics for the metric components and $A_t(0) = \mu$. Parametrizing $\mu = \sqrt{3} Q z_h (1 + Q z_h) / z_h$ as in the aGR solution, the scalar boundary condition (5.19) can be rewritten in terms of the falloffs of ψ as

$$\psi'(0) = -\frac{2J}{\sqrt{3}} + \left(a - \frac{3Q}{4} \right) \psi(0) + \frac{\sqrt{3}b}{4} \psi(0)^2. \quad (5.33)$$

For simplicity, we will choose $z_h = 1$ and the temperature of the solutions will therefore be encoded by $Q = \frac{3\mu^2}{16\pi^2 T^2}$. In holography, we would usually first fix the boundary theory of interest by choosing a, b . Then every solution to the equations of motion would be labeled by (T, μ, J) imposed through the boundary conditions. However in this section, we will be interested in how a given set of solutions, labeled by $(T, \mu, \psi(0))$, behaves in the various compatible boundary theories. This is possible because the boundary condition we impose on the scalar is simply a way to parametrize how we choose a bulk solution constrained to have a black hole in the interior. Every boundary theory determined by a, b and the value of sourcing J compatible with the condition (5.33) will provide a valid boundary description. We will focus on the boundary interpretations in the next subsection. In many holographic studies $\psi(0)$ is often used interchangeably with the source J , but this is of course only true in standard quantization. We shall, however, be careful to distinguish between the boundary value $\psi(0)$ of the AdS scalar field and the source J of the operator in the quantization choice dependent dual field theory.

Let us now briefly describe the effect of changing $\psi(0)$ without referring to any specific boundary theory. By looking at the aGR solution (5.5), we see that $\psi(0) = Q \sim (T/\mu)^{-2}$ for this family. Therefore, increasing $\psi(0)$ is akin to lowering the temperature and vice versa. To confirm our intuition, we can compare solutions at fixed $Q_0 \sim (T_0/\mu)^{-2}$, and varying $\psi(0)$, to aGR solutions with $\psi(0) = Q \neq Q_0$ i.e., at different $T/\mu \neq T_0/\mu$. We will choose to focus on the gauge field $A_t(z)$ and more specifically the component $a_t(z)$ defined in (5.31). Formally, $a_t(z) = A_t(z)/(\mu j(z, T_0/\mu))$ for a fixed T_0/μ . Since the aGR solution at a differ-

⁷The boundary conditions from regularity imply in particular that $G_{tt}(z_h) = G_{zz}(z_h)$. This conveniently allows us to set the temperature with the parameters Q and z_h just like in the aGR solution in Eq. (5.6), as the temperature of this generalised model is given by $T = T_{\text{GR}} \sqrt{G_{tt}(z_h)/G_{zz}(z_h)} = 3\sqrt{1 + Q z_h}/4\pi z_h$.

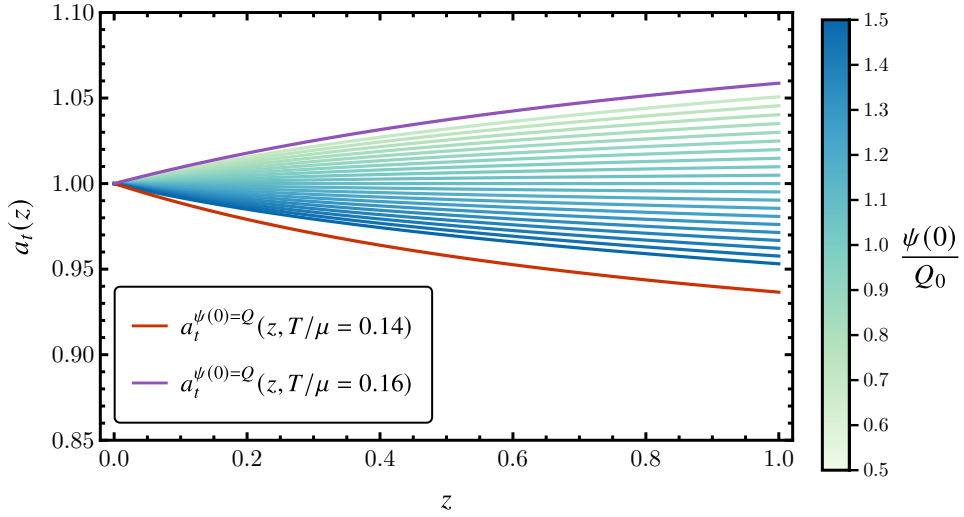


Figure 5.2.: Gauge field component $a_t(z)$ as defined in (5.31) at $T_0/\mu = 0.15$ and for various values of $\psi(0)$. We compare with the equivalent function $a_t^{\psi(0)=Q}$ of the aGR solution at different temperatures $T/\mu = 0.16$ (purple) and $T/\mu = 0.14$ (red). This illustrates that qualitatively the effect of changing the dilaton boundary value has similarities to changing the ratio T/μ .

ent temperature T/μ will have a gauge field $A_t(z) = \mu j(z, T/\mu)$, the correct field to compare with will be $a_t^{\psi(0)=Q}(z, T/\mu \neq T_0/\mu) = j(z, T/\mu)/j(z, T_0/\mu)$. We plot the profiles $a_t^{\psi(0) \neq Q_0}(z, T_0/\mu)$ in figure 5.2 and compare these to $a_t^{\psi(0)=Q}(z, T/\mu > T_0/\mu)$ (purple) and $a_t^{\psi(0)=Q}(z, T/\mu < T_0/\mu)$ (red). We see that indeed, starting from $\psi(0) = Q_0$, as we increase (decrease) $\psi(0)$ with Q_0 fixed, the solution becomes similar to the aGR solution at lower (higher) T/μ .

5.5.2. The holographic dual of the one-parameter family of solutions in different quantization choices

Having numerically constructed instances of this one-parameter deformation of fixed T/μ GR black holes, *each* instance in turn has multiple holographic dual interpretations depending on the quantization scheme. These are constrained by the compatibility condition (5.33). We will focus on three specific choices:

1. the conformal symmetry preserving quantization a , $J = 0$ boundary theory for which we can then label our solutions by $b(\psi(0)) = \frac{4}{\sqrt{3}\psi(0)^2} \left(\psi'(0) + \frac{3Q}{4}\psi(0) \right)$,
2. the standard quantization boundary theory with the label $J = \alpha = \frac{3}{2}\psi(0)$,

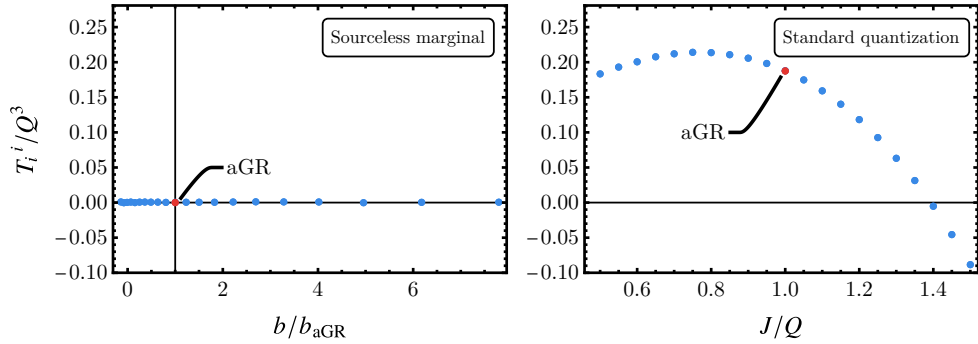


Figure 5.3.: Trace of the boundary stress tensor when varying the Dirichlet boundary condition $\psi(0)$. This can be interpreted as exploring boundaries with $a = 0$, $J = 0$ and varying marginal coupling b (left) or as changing the source $J = \alpha$ in standard quantization (right). aGR denotes the analytically known GR solution. (Left) We see that in this case, T_{ij} remains traceless regardless of b which is consistent with a marginal deformation and the result (5.22). (Right) In standard quantization, the trace is generically not zero, but this can happen for specific boundary theories: sourceless $J = 0$ – not visible on the graph – and when $\mathcal{O}_\varphi = 0$ – which happens at $J/Q \simeq 1.4$.

3. the alternate quantization boundary theory with $a, b = 0$ for which the label is now $J = -\beta = -\frac{3}{2}\psi'(0) - \frac{3\sqrt{3}Q}{8}\psi(0)$.

Using Eq. (5.11) we can compute the energy and the pressure of a solution in a specific quantization scheme and construct the trace of the stress tensor $T_i^i = -\epsilon + 2P$ for each of these solutions. For the choice 1, as we can see in Figure 5.3, the stress tensor remains traceless for any value of $b(\psi(0))$, confirming the analytic result Eq. (5.22). This is what we expect from a CFT deformed by a marginal operator. On the other hand, for the choice 2, we see that generically conformality is broken and the stress tensor acquires a non zero trace. In this quantization scheme, this is also true for the aGR solution, as we described in the case 2. There are two exceptions: the first one is when $J = 0$ (but $\mathcal{O}_\varphi \neq 0$) – which is reminiscent of a \mathbb{Z}_2 spontaneously symmetry breaking solution but here, the finite charge of the black hole actually always leads to an explicitly symmetry broken (ESB) solution $\phi(z) \neq 0$. This case is outside the range of the plot Figure 5.3. The second solution would happen around $J/Q \approx 1.4$ such that $\mathcal{O}_\varphi = 0$. These are consistent with what we would have expected from $T_i^i = \alpha\beta$.

Each one of these new black hole solutions has a different thermodynamics compared to the aGR solution.

A clean way to exhibit this is to show the boundary charge density ρ_2 , which for the choice 1 is the same as the variation of the Gibbs free energy w.r.t. the chemical potential, i.e. in that case $\rho_2 = \rho_1$. In Figure 5.4, we plot the charge density as a function of temperature for various values of the marginal coupling b . It is clear from this figure that the charge density as a function of T/μ

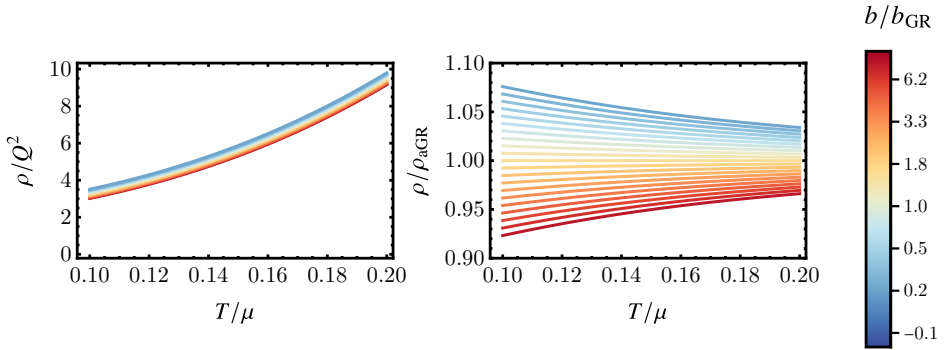


Figure 5.4.: Boundary charge density as a function of the temperature T/μ when imposing Dirichlet boundary conditions, which we interpret as varying the boundary theory through b . The charge density is normalized by Q^2 in the left-hand plot and by its aGR value defined in (5.30) in the right-hand plot. The qualitative behaviour of all these theories is extremely similar to the aGR solution (left) but quantitatively differs as a function of T/μ (right), showing the theories described are different.

is dependent on the choice of boundary theory and the deformed solution describes a different state, even if the change is small.

To reiterate this last point, let us remember that a priori, the true charge density of the theory ρ_2 , as well as the true entropy of the theory s_2 , only depend on the bulk solution – they are geometric quantities. Yet we now argue that different boundary theories have different thermodynamics. The resolution of this apparent contradiction is that while the entropy and charge density of a black hole solution only really depend on the bulk solution, how we explore the space of solutions is dependent on the choice of quantization. As we mentioned in Section 5.5, the holographic interpretation of black hole thermodynamics shows that we should label solutions by their sources $\{T, \mu, J\}$ – and in the case of the sourceless solutions of the choice 1, b plays the role of the label J . But different boundary theories have different notion of source J such that varying T and μ at fixed J will mean different path in the space of bulk solutions labeled by $\{T, \mu, \psi(0)\}$. In Figure 5.5, we illustrate this point by looking at the Bekenstein-Hawking entropy s_2 as a function of T/μ – all solutions are normalized by the aGR entropy defined in (5.30). Both choices 1 and 3 are used to label the solutions when varying the temperature, which can be done by imposing the boundary condition (5.33) for each of the choices. The values of $b(\psi(0))$ and $J = -\beta$ are chosen such that solutions meet in pair at $T/\mu = 0.2$. Upon lowering the temperature, we see that these pairs split indicating that the bulk solutions they belong to are not the same anymore. A path at fixed $J = -\beta$ is therefore generically different than a path at fixed $J = \alpha$ or fixed $b(\psi(0))$.

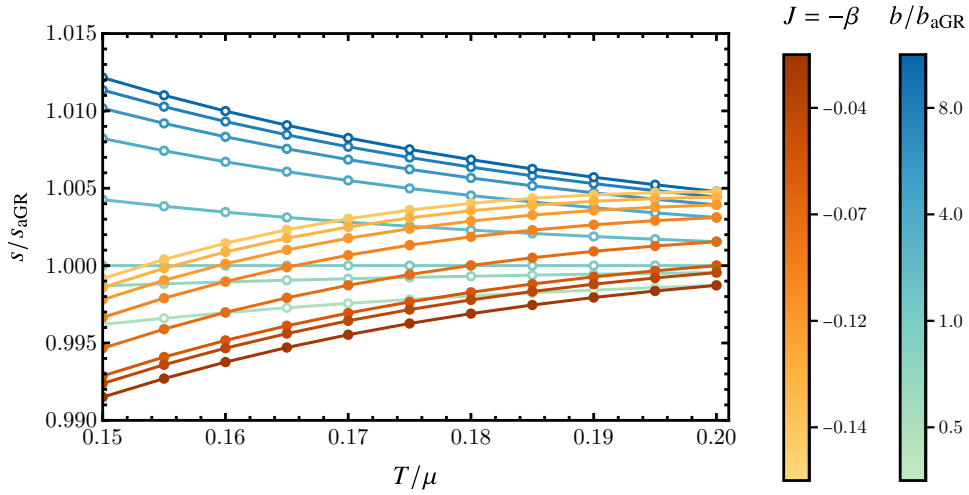


Figure 5.5.: Black hole entropy as a function of T/μ when keeping either the alternate quantization source $J = -\beta$ fixed (choice 3, orange gradient curves) or when keeping the label $b(\psi(0))$ fixed (choice 1, blue gradient curves). The curves meet in pairs at T/μ – indicating identical bulk solutions – and separate for other temperatures – indicating different black hole solutions.

5.6. Conclusion

In this paper, we have clarified how the GR black hole thermodynamics works in the context of holography and the appropriate quantization thereof. The well-known analytical solution (5.5) of [98] covers only a 2-parameter subspace of the full 3-parameter thermodynamics of black hole solutions to the action (5.2). The 2-parameter aGR black hole solution has been used widely as a physically sound version of the $z = \infty$ AdS₂ IR critical point that preserves the quantum critical properties but does so with a vanishing zero temperature entropy. It was already pointed out [108] that an unusual quantization choice could preserve conformal thermodynamics and hence stay within the analytically known 2-parameter family. This indicates the existence of a marginal operator in this specific quantization scheme [204] and we have recovered this in our analysis. For other quantization choices, the analytic solution has a fine tuned value for the source. To prove this point we have numerically computed the solutions corresponding to different boundary values of the dilaton. This fills out the full 3-parameter thermodynamic phase space. The filled out phase-space therefore elucidates that other quantization choices are just as valid as the one we chose to focus on. This had to be so, but the trade-off that one must make is to properly account for various scalar contributions to the general thermodynamics of the theory in line with the findings in [207].

Because the GR action is a consistent truncation of $d = 11$ supergravity compactified on $\text{AdS}_4 \times S_7$ and has ABJM theory as its known holographically dual CFT, in principle one should be able to identify this marginal operator in the CFT. The fact that marginality is associated with a multitrace deformation makes this not as straightforward as may seem. In particular as it originates naturally in alternate quantization, it is likely that it is an operator which is only marginal in the large N limit where the classical gravity description applies. We leave this for future research.

Our focus and interest is the use of the GR and other EMD models as phenomenological descriptions of AdS_2 fixed points, especially due to its resemblance to the experimental phenomenology of strange metals. In this comparison, thermodynamic susceptibilities and (hydrodynamic) transport play an important role. Our result here shows that in EMD models one must be precise in the choice of boundary conditions and scalar quantization as they will directly affect the long-wavelength regime of the dual boundary theory as well as correct the thermodynamics of any extension of the GR model. This is especially true for any boundary interpretation differing from the pure marginal case of [108, 204], as was shown by [207] for Einstein-Scalar models and we have shown here for the GR model. A proper understanding of the boundary conditions is necessary both for the thermodynamics of the background and the hydrodynamic fluctuations on top of that background.

5.7. Validity of the boundary action

In a previous version of this paper, we considered the boundary term introduced by [108] which is of the form

$$S_{\text{bdy},\phi}^{(c_\phi)} = \int_{z=\epsilon} d^3x \sqrt{-\gamma} \left[\frac{\Lambda_\phi}{2} \phi^2 + c_\phi \phi N^z \partial_z \phi \right], \quad \Lambda_\phi = 2c_\phi - 1, \quad (5.34)$$

which matches our boundary terms for specific values $S_{\text{bdy},\phi}^{(c_\phi=0)} = S_{\text{bdy},\phi}^{(\text{SQ})}$ and $S_{\text{bdy},\phi}^{(c_\phi=1)} = S_{\text{bdy},\phi}^{(\text{MT})}$ for $a = 0, b = 0$. The claim of [108] is that more general values of c_ϕ are also possible, which from a renormalization point of view is an acceptable assumption. The only prescription one has for boundary terms is to choose relevant and marginal ones (the irrelevant boundary terms contribute as corrections in the cutoff ϵ and can be truncated) which respect the symmetries of the action. However, choosing the boundary term (5.34) leads to

$$\begin{aligned} \delta \left(S_{\text{bulk}} + S_{\text{bdy},\phi}^{(c_\phi)} \right) &= \int_{z=\epsilon} d^3x \sqrt{-\gamma} \left[(1 - c_\phi) \beta \delta \alpha - c_\phi \alpha \delta \beta \right] \\ &= \int_{z=\epsilon} d^3x \sqrt{-\gamma} \left(-c_\phi \alpha^{1/c_\phi} \right) \delta \left(\beta \alpha^{1-1/c_\phi} \right) \end{aligned} \quad (5.35)$$

which generically differs from our result for the standard quantization or multi-trace deformation where $\mathcal{O}_\varphi = \alpha$ or β .

The question of the validity of such variational problem as Eq. (5.35) was raised before in e.g. [212] for the simple case of a non-relativistic particle. Consider a particle with action $S_1 = \int_{t_1}^{t_2} dt (-\dot{q}^2/2)$ to which one adds the total derivative term $S_2 = [\frac{1}{2} q \dot{q}]_{t_1}^{t_2}$. The variation of the

total action on-shell $\delta(S_1 + S_2) = [\frac{1}{2}q\delta\dot{q} - \frac{1}{2}\dot{q}\delta q]_{t_1}^{t_2}$ is of a similar form as the variation (5.35) for $c_\phi = 1/2$. The boundary condition required to make the boundary variation well-defined is then to fix $\dot{q}/q = C$ at $t = t_1$ and $t = t_2$. However, in the case of S_1 , this is not a correct boundary condition to impose. Since the bulk equation of motion is $\ddot{q} = 0$ with solutions $q(t) = At + B$ and $\dot{q}(t) = A$, the quantity to fix is $\frac{\dot{q}}{q} = \frac{A}{At+B} = \frac{1}{t+B/A}$ which only depends on the ratio B/A . Therefore, fixing it at t_1 leaves no freedom to also fix it at t_2 . At the same time the two boundary conditions at t_1 and t_2 do not select a unique solution. A direct check one can do is whether for other values of the analogous c_ϕ , this problem remains. Taking for example $S_2 = [\frac{1}{3}q\dot{q}]_{t_1}^{t_2}$, the boundary condition to impose is now to fix $\dot{q}/q^2 = \frac{A}{(At+B)^2}$. Solving this condition at the boundaries for values $C_{1,2}$ now does lead to fully determined solutions, unlike the previous case. However, the solutions are not unique, because the boundary conditions itself have arbitrary constants $C_{1,2}$. There are therefore multiple branches to the system of equations $AC_{1,2} = (At_{1,2} + B)^2$.

In holography only the UV boundary conditions are imposed in the exact same manner. The IR boundary condition in a black hole spacetime is different. We simply require regularity of the scalar at the event horizon. For $c_\phi = 1/n$, $n \in \mathbb{N}^*$, the question of whether the variational problem is well-defined is then whether the UV boundary condition of fixing $\frac{\beta}{\alpha^{n-1}} = C$ is sufficient to pick a unique solution once the IR boundary conditions are taken into account. It is quite straightforward to show that these are the same boundary conditions as the usual multi-trace deformation boundary condition (5.24), for $J = 0$ and specific choices of monomial $\mathcal{F}_n = \frac{a_n}{n}\alpha^n$. From (5.19), we see that for $n > 1$, the sourceless boundary condition for the deformation associated with \mathcal{F}_n is $\frac{\beta}{\alpha^{n-1}} = \frac{a_n}{n-1}$ so the matching between boundary theories occurs for $C = \frac{a_n}{n-1}$. Interestingly, choosing the boundary value C is equivalent to choosing a deformation coupling constant with (single-trace) scalar source $J = 0$. This is because the coupling constant a_n is really the same as a source for the multi-trace operator \mathcal{O}^n .

In Table 5.1 we look at $n = 1, 2, 3, \infty$ and what type of multi-trace deformation they match. For $n \geq 4$ the higher order terms in \mathcal{F} represent irrelevant operators and we shall not consider them. The special cases $n = 1$ and $n = \infty$ i.e. $c_\phi = 1$ and $c_\phi = 0$ are the alternate and standard quantization case of fixing $\alpha = J$ and $\beta = -J$. In the previous version of this article we argued that the aGR solution quantized with boundary term (5.34) and $c_\phi = 1/3$ could be viewed as a marginal deformation with $n = 3$ and $\beta/\alpha^2 = \frac{1}{2\sqrt{3}}$ which according to our mapping is equivalent to the case 1, as expected.

Moreover, and importantly, the on-shell values of the boundary actions (5.9) with monomial multi-trace deformations $\mathcal{F} = \mathcal{F}_n$ and (5.34) are also equivalent through the mapping described in Table 5.1. Indeed, we see that the difference between the boundary terms is

$$S_{\text{bdy},\phi}^{(\text{MT})}(\mathcal{F} = \mathcal{F}_n) - S_{\text{bdy},\phi}^{(c_\phi)} = \int_{z=\epsilon} \left[\frac{a_n}{n}\alpha^n - (1 - c_\phi)\alpha\beta \right] = \int_{z=\epsilon} [a_n - C(n-1)] \frac{\alpha^n}{n}, \quad (5.36)$$

where we injected the expansion $\phi \sim \alpha z + \beta z^2$ and in the second equality, we used the boundary condition $\beta = C\alpha^{n-1}$ with $c_\phi = 1/n$. We see that the difference (5.36) vanishes for the choice

n	Boundary condition	Analog multi-trace choice
$n = 1$	$\beta = C$	$a = 0, \quad b = 0, \quad J = -C$
$n = 2$	$\frac{\beta}{\alpha} = C$	$a = C, \quad b = 0, \quad J = 0$
$n = 3$	$\frac{\beta}{\alpha^2} = C$	$a = 0, \quad b = 2C, \quad J = 0$
$n = \infty$	$\alpha = C$	$a = 0, \quad b = 0, \quad J = C$

Table 5.1.: Matching between the boundary conditions obtained from the multi-trace deformation boundary action (5.9) and those obtained from the boundary term (5.34).

$C = \frac{a_n}{n-1}$ and thus the actions are the same through the mapping described in Table 5.1. We can conclude that as far the two roles of the boundary terms go – setting the boundary conditions of the variational problem and specifying an on-shell value for the action – these boundary terms yield the same answer for specific choices of the boundary theory. This explains how our previous derivation based on (5.34) yielded the same results as the derivation based on (5.9) for sourceless solutions. The on-shell action equivalence does not hold in generality, however. The boundary term (5.34) fails to account for polynomial deformations \mathcal{F} and therefore would miss out on the most general theories of case 3.

5.8. Matching of metric gauge choices

In Eq. (5.13) we have expressed our scalar field UV expansion in the FG gauge choice for the metric (5.15). In this section we will use r to denote this choice of radial coordinate. However, the aGR solution (5.5) uses a different metric gauge choice (5.4). This means that the expansion of the scalar field $\phi = \hat{\alpha}z + \hat{\beta}z^2 + \dots$ in the (5.4) coordinates is not directly identical to that given in Eq. (5.13). They are related by solving $\frac{dr^2}{r^2} = \frac{dz^2}{z^2 f(z)}$. This relation is formally given by

$$\log r(z) - \log \epsilon = \int_{\epsilon}^z \frac{dx}{x \sqrt{f(x)}}, \quad \text{with } \epsilon \rightarrow 0. \quad (5.37)$$

In the near-boundary regime, we will only be interested in the leading and subleading orders of this relation – since we only want to see how the leading and subleading orders in the scalar expansion mix – and we therefore expand $f(z) = 1 + f'(0)z + \dots$, where the analytical value of f is given in Eq. (5.5). Doing so, we find

$$r(z) \sim z - \frac{3Qz^2}{4} + \mathcal{O}(z^3). \quad (5.38)$$

It is then straightforward to input this in the FG UV expansion

$$\phi \sim \alpha r + \beta r^2 \sim \alpha z + \left(\beta - \frac{3Q}{4} \alpha \right) z^2, \quad (5.39)$$

as was claimed in Eq. (5.23).

6. Planckian Transport for a Holographic Local Quantum Critical Metal in Periodic Potentials

6.1. Attribution

This paper is to be published under the name *T-linear resistivity, optical conductivity and Planckian transport for a holographic local quantum critical metal in a periodic potential*. and has been submitted to arXiv, number 2211.05492.[213] Other contributing others to this paper are N. Chagnat, S. Arend, J. Aretz, K. Grosvenor, M. Janse, O. Moors, J. Post, V. Ohanesjan, D. Rodriguez-Fernandez, K. Schalm and J. Zaanen.

6.2. The Planckian Dissipation Mystery versus Computational Holography

Are there states of matter that are governed by physical principles of a different kind from those identified in the 20th century? This question arose in the study of strongly interacting electron systems realized in condensed matter, starting with the discovery of superconductivity at a high temperature in copper oxides. Their metallic states exhibit properties that appear to be impossible to explain with the established paradigm explaining normal metals – the Fermi-liquid theory – and these were accordingly called “strange metals” [43, 214].

An iconic signature is the linear-in-temperature electrical resistivity [42], an exceedingly simple behavior that is at odds with transport due to the quasiparticle physics of normal metals. A linear temperature dependence of the resistivity does occur naturally in conventional metals due to scattering of the quasiparticles against thermal disorder of the lattice above the Debye temperature. The problem in the cuprates and related systems is that the resistivity is linear all the way from the lowest to the highest temperatures where it has been measured. One anticipates some powerful principle of a new kind to be at work protecting this unreasonable simplicity.

The measured optical conductivities reveal at lower temperatures a Drude response [215–218], signaling that the electrical conduction is controlled by a current relaxation time. Intriguingly, this time is very close to the “Planckian dissipation” time scale $\tau_{\hbar} = \hbar/(k_B T)$. Planck’s constant \hbar plays a special role in dimensional analysis, as for instance the Planck scale of quantum gravity. Since \hbar carries the dimension of action, τ_{\hbar} is a time scale associated with the thermal physics

property of dissipation, the conversion of work into heat [51, 219]. The case was made based on DC data that this Planckian time is remarkably universal also involving a variety of non-cuprate unconventional metals exhibiting the linear resistivity [38, 71, 220].

However, upon raising temperature further, in the “bad metal” regime above the Mott-Ioffe-Regel bound optical conductivity studies show that the dynamical response changes drastically. Instead of a Drude response, a mid-infrared resonance develops with a characteristic energy that appears to increase with temperature, leaving a rather incoherent response at low energy [221]. Remarkably, there is no sign of this radical reconfiguration of the dynamical response in the DC resistivity that continues to be a perfectly straight line, seemingly controlled by τ_{\hbar} .

The occurrence of this universality of electrical conduction poses quite a problem of principle. On the one hand, considerable progress has been made in the understanding of dissipative phenomena in terms of quantum thermalization, explaining it in terms of unitary time evolution and the collapse of the wave function (e.g. [222]). An early result is the identification of τ_{\hbar} as the characteristic universal dimension for the dissipation time of non-conserved quantities associated with densely many-body entangled quantum critical states [223] realized at strongly interacting bosonic quantum phase transitions [48, 224].

This was very recently further clarified using both holographic duality (AdS/CFT correspondence) as well as studies in the closely related SYK models that connect macroscopic transport in such strange metals to microscopic quantum chaos. The central issue is that thermalization leading to local equilibrium may proceed very rapidly in densely entangled systems compared to quasiparticle systems. Using out-of-time-order correlators (OTOC’s) one can identify a quantum Lyapunov time τ_{λ} characterizing the microscopic time associated with the onset of quantum chaos that turns out to be bounded from below by τ_{\hbar} . In strongly correlated strange metals this microscopic time scale together with the chaos propagation “butterfly” velocity v_B can set the natural scale for the charge/heat and momentum diffusivities controlling the dissipative properties of the macroscopic finite temperature hydrodynamical fluid [225–227].

However, in ordinary metals electrical conduction is controlled by total momentum conservation, as a ramification of translational invariance: any finite density system in the Galilean continuum *has* to be a perfect conductor. A finite resistivity is therefore rooted in the breaking of translation invariance. But how can this ever give rise to a universal resistivity controlled by τ_{\hbar} ? This is the core of the mystery – all explanations we are aware of rely on accidental, fine tuning circumstances, e.g. [52, 71, 228].

Holographic duality is now widely appreciated as a mathematical machinery that has a remarkable capacity to shed light on general principles associated with densely entangled matter [61, 62, 71, 223], the “scrambling” that we just discussed being a case in point. It achieves this by dualizing the densely entangled quantum physics into a gravitational problem in one higher dimension that is computable with (semi-)classical General Relativity. However, this is only a relatively easy mathematical affair for a homogeneous translationally invariant space. When one breaks the spatial translation symmetry the Einstein equations become a system of highly non-linear partial differential equations. If one wishes to have a full view on what holography has to say about transport in the laboratory systems one has to confront this challenge. Invariably a very strong effective

potential due to the background of ions is present in the laboratory strange metals, and it is even believed to be a *necessary* condition to obtain strongly correlated electron behavior [174, 229, 230]. But what has holography to tell about the effects of strong lattice potentials on strange metal transport?

This can only be accomplished numerically. Although relatively efficient numerical relativity algorithms are available, the computations are demanding. Proof of principle was delivered that it can be done [118–120, 140, 231] and we set out to explore this more systematically. We focused specifically on the so-called Gubser-Rocha holographic strange metal [98]. This is unique in the regard that it is characterized by “local quantum criticality” (a dynamical critical exponent $z \rightarrow \infty$) as well as a Sommerfeld entropy $s \sim T$ in the regime $T \ll \mu$, generic properties that appear to be realized by the cuprate strange metals [223]. For comparison we also include results for the elementary Reissner-Nordström holographic strange metal. This also exhibits local quantum criticality, but it has a (pathological) finite zero temperature entropy.

6.2.1. Main Observations and Summary of the Results

We consider a 2+1 dimensional strongly interacting strange metal holographically dual to the Gubser-Rocha model in the presence of a harmonic square ionic lattice background encoded in the chemical potential

$$\mu(x, y) = \mu_0 \left(1 + \frac{A}{2} (\cos(Gx) + \cos(Gy)) \right) \quad (6.1)$$

We numerically compute the full set of DC thermo-electrical transport coefficients — electrical conductivity σ , thermal conductivity $\bar{\kappa}$, the thermo-electrical coefficient α — up to very large potentials ($A \simeq 8$) and temperatures as low as $T \simeq 0.005\mu$. For stronger potentials we sometimes resort to uni-directional 1D potentials to maintain numerical control. In addition, we also compute the optical conductivities. Because of numerical difficulties we encountered this is limited to intermediate potential strength ($A \lesssim 1 - 2$) and 1D lattices.

From this computational experiment we make three remarkable observations:

1. The DC electrical resistivity of the Gubser-Rocha metal becomes to good approximation linear in temperature at low temperatures, see the upper left panel in Fig. 6.1. Strikingly, we find the slope of this linear resistivity to saturate for an increasing potential strength after correcting for a spectral weight shift. This suggests a connection with the universal Planckian dissipation bound: using the optical conductivity to deconvolve this in a total spectral weight and a current life time, the saturation value for the latter is close to $\tau_{GR} = \frac{1}{2\pi} \hbar / (k_B T)$ (see Fig. 6.13).

The electrical conductivity of the RN metal also saturates for large potential strength at a roughly temperature independent value, although less perfect. The gross differences in temperature dependencies of the GR and RN metals between the electrical conductivity appear to reflect the different temperature dependencies of the entropies. We will discuss below why this is not so. Despite first appearances, the thermoelectric (α) and heat ($\bar{\kappa}$) conductivities do not saturate at larger lattice potentials, but vanish as $1/A$ (see Fig. 6.12).

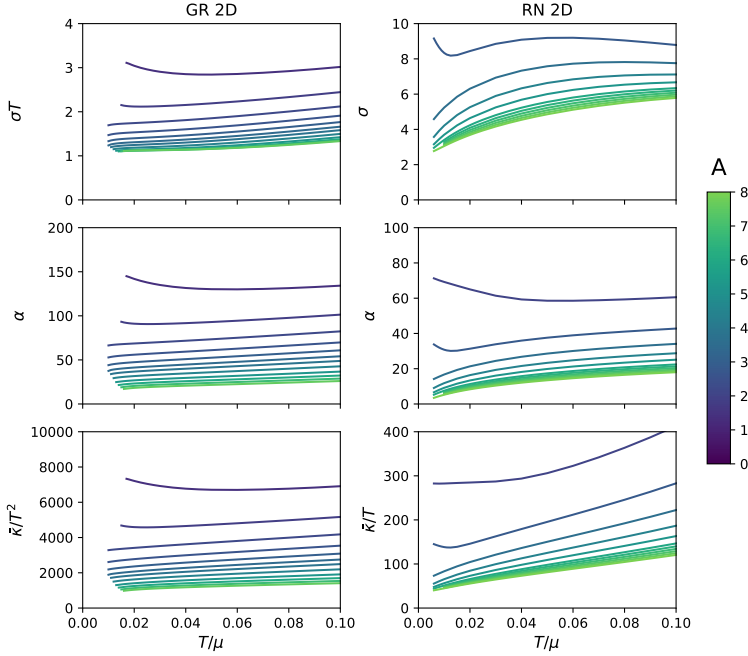


Figure 6.1.: The thermoelectrical DC transport coefficients as functions of temperature T in units of the chemical potential μ for the Gubser-Rocha (GR, left column) and Reissner-Nordström (RN, right column) metals in a 2D square lattice harmonic background potential with wave vector $G = 0.1\sqrt{2}\mu$ and a strength $0 < A < 8$. σ , α and $\bar{\kappa}$ are the electrical conductivity, thermo-electrical cross conductivity and the overall thermal conductivity respectively. The electrical conductivity of the GR metal (top-left panel) shows for all potentials a nearly linear in temperature resistivity ($\rho = 1/\sigma \sim T$) with a slope that shows saturating behavior for large potentials.

2. We can separate out the convective overall transport from more microscopic diffusive transport by considering the heat conductivity with zero electrical current $\kappa = \bar{\kappa} - T\alpha^2/\sigma$, also known as the open boundary heat conductivity. Similarly, one can define an electrical conductivity without heat transport $\sigma_{Q=0} = \sigma - T\alpha^2/\bar{\kappa}$ that is a (non-perfect) proxy for transport anchored in charge diffusion — it is proportional to charge diffusion, but its thermodynamic scaling is also determined by crossterms with the convective part. These are shown in Fig. 6.2. The $\sigma_{Q=0}$ is also (nearly) inversely proportional to temperature up to the largest potentials, similar to the overall σ . Most importantly, however, we see that for large potentials this diffusion-anchored contribution to the conductivity dominates the transport (middle panels): up to $\sim 80\%$ of the electrical currents is anchored in the diffusive sector. Similarly, the diffusion-anchored open boundary thermal conductivity (κ , lowest panels) accounts for almost the full heat conductivity $\bar{\kappa}$ of Fig. 6.1 in the large po-

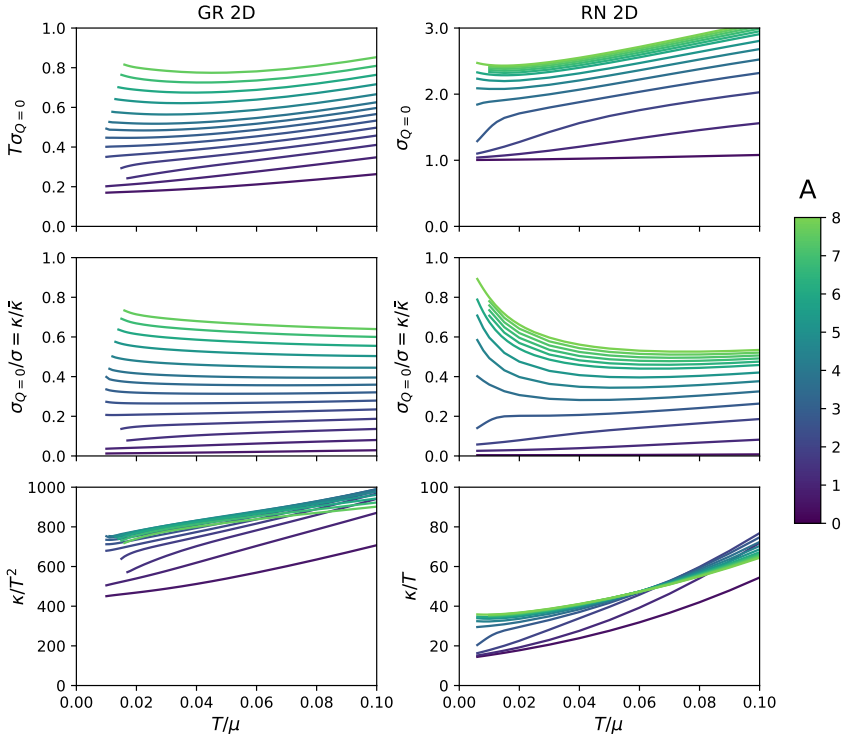


Figure 6.2.: The electrical conductivity at zero heat current $\sigma_{Q=0}$ shows that as the lattice strength is increased the non-convective current anchored in charge diffusion becomes the dominating conduction channel. At the largest lattice strength where $A = 8$, the ratio of non-convective to convective transport $\sigma_{Q=0}/\sigma$ reaches up to 80%, signalling that momentum conservation is nearly completely destroyed. By definition, the fraction $\sigma_{Q=0}/\sigma$ is equal to the ratio $\kappa/\bar{\kappa}$. The open boundary thermal conductivity κ anchored in thermal diffusion is rather independent of the lattice strength, barely changing after a moderate value of $A = 1$ has been reached. Parameters are the same as in Fig. 6.1.

tential regime. This signals that for the strongest potentials the system approaches closely the incoherent metal regime addressed by Hartnoll [219] where there is no longer a sense of momentum conservation; It is governed instead by a “hydrodynamics” that only relies on energy- and charge conservation. A key observation is that this is the regime which displays the “Planckian saturation” of the electrical resistivity highlighted above in Fig. 6.1. In other words, this is the regime that should contain the clue behind the saturation phenomenon.

3. Computing the optical conductivities, we find for small lattice potential at the lowest temperature a perfect Drude peak (left panel Fig. 6.3). Strikingly, upon raising temperature this

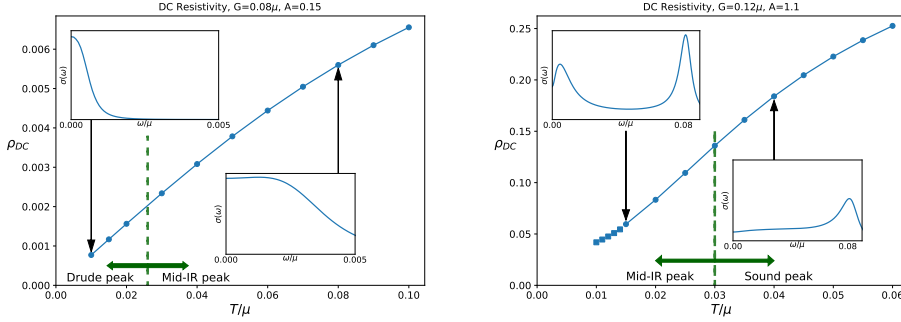


Figure 6.3.: The DC resistivities for the small- ($A = 0.15$, left panel) and intermediate ($A = 1.1$, right panel) lattice potential of the Gubser-Rocha metal are in both cases (nearly) linear in temperature. However, in both cases the optical conductivity (insets) undergoes radical changes when temperature increases. At the lowest temperatures in the small potential case (left panel) this consists of a simple Drude peak that gradually turns into an incoherent “flat top” low frequency response terminating at a developing “mid IR peak”. The characteristic temperature where this happens decreases for increasing potential strength. In the right panel, a full fledged mid IR peak has already developed at a low temperature $T \sim 0.015\mu$ (left inset), while it is accompanied by a high energy peak at $\omega = c_s G = \frac{1}{\sqrt{2}}G$ that is identified to be the “Umklapped sound peak”. Upon further raising temperature, the mid IR peak moves up in energy to eventually merge with the sound peak (right inset).

evolves into a mid IR peak, reminiscent of what is seen in experiment. Although the dynamical response shows such drastic changes, these remarkably do not imprint on the linearity in temperature of the DC resistivity *at all*. This finding is repeated in the intermediate potential case. There, the electrical DC resistivity can even stay linear-in- T through a second change in relaxational dynamics from the mid-IR-peak regime to a fully incoherent metal. Just within reach of our numerics, the spectrum at the lowest temperature (left inset) now already displays the mid-IR peak, and we have good reasons to expect that at even lower temperatures, outside of our numerical reach, a Drude response should still be present. There is also a second peak at higher frequencies that can be identified with the “Umklapp copy” of the sound mode at an energy $\omega = c_s G$ where c_s is the speed of sound and G the lattice wavevector (Section 6.6). Upon raising temperature the mid-IR peak moves to higher frequency to eventually merge with the “Umklapped sound” peak, transitioning to a fully bad incoherent metal regime (right inset), while the DC resistivity stays essentially linear-in- T throughout.

These observations are reminiscent of the experimental observation that the linear-in- T DC resistivity appears to be completely insensitive to the change from “good metal” to “bad metal” behavior when temperature increases. This transition can be defined using the ab-

solute value of the resistivity crossing the Mott-Ioffe-Regel limit but perhaps a better way is to identify it through the dynamical response, associating the good metal regime with a Drude response while the bad metal has the incoherent “mid IR peak” type of behavior as in our computations.

To dissect these numerical results is an intensive exercise. We therefore provide an executive summary of the paper here. The reader interested in the details may proceed directly to Section 6.3 and skip the remainder of this Introduction.

The Local Quantum Critical Strange Metals of Holography and Hydrodynamical Transport

Transport in holographic strange metals is governed by hydrodynamics (Section 6.3). Holographic strange metals originate in the quantum critical state of a non-trivial IR fixed point and the GR metal is singled out as the one with the right scaling properties to reproduce both the local quantum criticality and Sommerfeld entropy of the cuprate strange metals. The non-trivial fixed point is of a special kind in that it still has an intrinsic correlation length $\xi \sim 1/\mu$ ([232] and Appendix 6.B). Hydrodynamics has long been utilized to describe transport in such densely entangled critical states, and holography is no different. In the Galilean continuum hydrodynamics is governed by (near) *momentum conservation* captured by the Navier-Stokes equations describing *convective* currents, also called “coherent” in the condensed matter- and holographic communities. However, there are also transport channels that are controlled by only *diffusive* (or “incoherent”) transport. The overall electrical (σ) thermoelectric (α) and thermal ($\bar{\kappa}$) transport coefficients are set by the sum of both convective and diffusive transport channels. The open boundary thermal conductivity $\kappa = \bar{\kappa} - T\alpha^2/\sigma$ and the charge-without-heat transport $\sigma_{Q=0} = \sigma - T\alpha^2/\bar{\kappa}$ can be used to disentangle these. These zero out the dominant convective contribution. If Planckian dissipation occurs, the natural channel is this diffusive channel which can reflect universal microscopic dynamics. The convective channel is controlled by the way translational symmetry is broken and therefore unlikely to be universal. However, the convective channel dominates when translational symmetry is only broken weakly, and Planckian dissipation is therefore most natural in systems with strong translational symmetry breaking.

Convective Hydrodynamics in the Presence of a Weak Lattice Potential

The presence of a lattice potential plays an important role in cuprate strange metals and this is the obvious way translational symmetry is broken. Placing the holographic strange metals in a background lattice with a perturbatively small potential strength the nature of the linear response of hydrodynamical transport is in fact familiar (Section 6.4). Hydrodynamic fluctuations must be decomposed in Bloch modes that Umklapp at Brillouin zone boundaries. This holds for purely diffusive as well as propagating modes. Well known is that the translational symmetry breaking by the lattice makes momentum relax due to shear drag with a life time $\Gamma_{\text{shear}} = \eta G^2/(\varepsilon + P)$ (ε and P being the energy density and pressure and η the shear viscosity). However, a careful analysis reveals that the Umklapp potential gives rise to a mode coupling between this relaxational mode and the Umklapped charge diffusion mode characterized by a relaxation rate $\Gamma_{\text{charge}} = D_c G^2$,

where D_c is the charge diffusivity. For weak lattices $A \ll 1$ the result of this generic mode coupling problem is an optical conductivity of the form (cf. Eq. (6.19) & Eq. (6.32)),

$$\sigma(\omega) \sim \frac{\Omega - i\omega}{(\Gamma - i\omega)(\Omega - i\omega) + \omega_0^2} \quad (6.2)$$

where ω_0 is related to the strength of the mode coupling and Γ and Ω are combinations of Γ_{shear} and Γ_{charge} . Taking the DC limit gives an overall current relaxation rate $\Gamma_{\text{DC}} = \Gamma + \omega_0^2/\Omega$ controlled by two separate dissipative channels.

The above hydrodynamic analysis is only valid for lattice sizes $a = G^{-1}$ greater than the earlier emphasized retained correlation length $\xi \simeq 1/\mu$ of the IR fixed point or equivalently $G \ll \mu$ (Section 6.5). This length $\xi \simeq 1/\mu$ where hydrodynamics provides the better perspective on transport than the quantum critical power law response set by the near horizon geometry as elucidated by Hartnoll and Hofman [233]. In a lattice background this reflects itself in a strong change in the transport properties when the lattice momentum G crosses this scale. The results in the above are all associated with the hydrodynamical regime ($G \ll \mu$); for large lattice momenta ($G \gtrsim \mu$) the additional Umklapp contribution to the dissipation of the currents is strongly suppressed (Fig. 6.11).

This Umklapp hydrodynamics can explain our observations at weak lattice potential (Section 6.6). When $|\Gamma - \Omega| > 2\omega_0$ the AC conductivity displays a single peak, explaining the low temperature Drude-like result of Fig. 6.3. Only for the lowest temperatures is this a pure Drude peak controlled by a single pole, however. In detail it originates in two diffusive poles, the Drude $k = 0$ sound pole and the Umklapped charge diffusion pole; for each we fully understand their temperature dynamics from the underlying hydrodynamic computation and the thermodynamical properties of the holographic strange metal.

At higher temperatures (and/or at stronger lattices) generically $|\Gamma - \Omega| < 2\omega_0$ and a *real*, propagating part develops in modes controlling the AC conductivity. This pole collision explains the emergence of the mid-IR-peak in the dynamical response – the numerical results are perfectly fitted by this form.

The same two-relaxational-current response was identified in the context of a hydrodynamical fluid coupled to the fluctuations of a damped pinned charge density wave [234]. Our discovery is that Umklapp hydrodynamics gives the right temperature evolution necessary to have a mid-IR-peak appear as temperatures increase.

As emphasized, the DC resistivity can remain linear throughout this transition. This can be explained by the fact that the scaling properties of the hydrodynamic parameters are inherited from the underlying non-trivial quantum critical IR fixed point. For the GR strange metal both relaxation rates scale as T , whereas for the RN metal one scales as T^0 and the other as T^2 . This manifestation of the differing detailed expressions for both relaxation rates shows that a simple interpretation of the scaling of the resistivity in terms of the entropy fails. Instead their scaling is determined at a deeper level by the quantum critical IR fixed point.

At intermediate lattice strengths a similar scenario can take place. Now the transport response is determined by four modes, the two modes above and two Umklapped sound modes at $\text{Re } \omega = \pm c_s G$. Upon raising temperature the pole responsible for the mid-IR peak moves up with temperature to approach close to the Umklapped sound pole, such that it gets obscured and only one peak remains in the AC conductivity (right inset of Fig. 6.3). From this temperature onward the low frequency AC spectrum becomes roughly temperature independent. We can track this in terms of the quasinormal modes (Fig. 6.9) although we can no longer rely on the perturbative expansion to enumerate it. For a large part of this intermediate lattice regime, the DC resistivity is still effectively captured by the expression $\sigma_{DC} = \omega_p^2 / (\Gamma + \omega_0^2 / \Omega)$, though one needs a careful AC-fit to extract the values. Again, its temperature scaling is set by the non-trivial IR fixed point and can remain unaffected by the change in dissipative dynamics in the AC conductivity.

The Incoherent Hydrodynamics at Large Lattice Potential

At large lattice potentials momentum is strongly broken and we enter in a qualitatively different regime (Section 6.7). Observationally this is where the numerically extracted relaxation rate of the DC conductivity of the GR metal saturates at about the Planckian value $\Gamma_{\text{corrected}} \simeq 2\pi T$ (Fig. 6.13). Because momentum is strongly broken, the framework to understand whether this can be verified is the one where transport is governed by only two conserved quantities, energy and momentum [219]. Their fluctuations consist of two coupled diffusive modes with diffusion constants that are not the same as they are in the homogeneous system. At strict $T = 0$, charge and energy transport formally decouple and the electrical conductivity is governed by one of these modes $\sigma = \chi D_+$ with χ the charge susceptibility, while the thermal conductivity $\kappa = c_n D_-$ is governed by the other with c_n is the specific heat at constant charge density. At low but finite temperature they mix perturbatively, but are still dominated by their $T = 0$ scaling. From our numerics we conclude that $D_+ \sim T^{-1}$ whereas $D_- \sim T$ for the GR metal; similar behavior has been established in homogeneous holographic strange metals with strong momentum relaxation (GR metal in a Q-lattice) where the homogeneous geometry allows analytical solutions [235]. It has been argued that the temperature dependence of the thermal diffusivity empirically defined as $D_T \equiv \kappa / c_n$ should be insensitive to the breaking of translations and reduces to one of the incoherent diffusivities D_- at low temperature and strong lattices. Moreover, it can be related to microscopic chaos through a butterfly velocity v_B^2 times a maximal Lyapunov rate $\lambda = 2\pi T$ that embodies Planckian dissipation $D_T = \frac{1}{2} v_B^2 / (2\pi T)$ [225–227]. Provided we can extrapolate from the homogeneous result that in the non-trivial IR fixed point of the GR metal in a strong lattice the butterfly velocity still scales as $v_B^2 \sim T^2$, this is consistent with our findings. The puzzle is the DC-conductivity and charge response. We conjecture that the Planckian relaxation set by the maximal Lyapunov rate should still govern charge transport as well. Given that on dimensional grounds $D_+ \sim (v_B^{\text{charged}})^2 / (2\pi T)$, this can be only so if the butterfly velocity is not universal but depends on the quantum numbers of the operators probing chaos; there are hints that this is true [236–239]. If it can be shown that $v_B^{\text{charged}} \sim T^0$ this could explain not only the observed linear-in- T resistivity at strong lattice potentials in the GR metal, but also its saturation to the Planckian value.

We will end with a short discussion in Section 6.8 of these results with a focus on the possible rele-

vance to experiment. We also include a number of Appendices where we discuss various technical details.

6.3. Holographic Strange Metals, Transport and Translational Symmetry Breaking

In the absence of a lattice, the homogeneous finite density strange metals [61, 62, 71, 223] of holography are characterized by a non-trivial IR fixed point. These are specified by a handful of anomalous scaling dimensions: the dynamical critical exponent z , the hyperscaling violation dimension θ and the charge exponent ζ , expressing the scaling of time with space, the scaling of the thermodynamically relevant degrees of freedom with volume, and the running of the charge, respectively. Experimental evidences suggest that the cuprates are “local quantum critical” [50, 240, 241], referring to $z \rightarrow \infty$, while electronic specific heat measurements in the high temperature strange metal regime exhibit a Sommerfeld entropy, $s \simeq k_B T/\mu$ (see e.g. [242]) where μ is the chemical potential taking the role of the Fermi energy. Though the notion that cuprate strange metals are explained by a non-trivial IR fixed point was put forth independently of holography, the fixed point that shares the rough qualitative characteristics was first discovered using AdS/CFT. Amongst the holographic strange metals this is the so-called Gubser-Rocha (GR) strange metal [98], being the only holographic strange metal in the general classification that reconciles $z \rightarrow \infty$ with Sommerfeld entropy. Within the larger class of holographic strange metals, the critical scaling at the IR fixed point insists that the entropy should scale as $s \sim T^{(d-\theta)/z}$. For $z \rightarrow \infty$ and $d - \theta$ finite the entropy should therefore be temperature independent, implying a zero temperature entropy. This is the case for the holographic strange metal dual to the Reissner-Nordström black hole and the closely related SYK systems. The GR metal is characterized by a double scaling limit such that $z, -\theta \rightarrow \infty$ while $-\theta/z = 1$. This reconciles a low temperature Sommerfeld entropy $s \sim T + \dots$ with local quantum criticality. For comparison we will also present results for the Reissner-Nordström (RN) strange metal [61, 71, 156]. For a qualitative understanding of our results nothing more than the thermodynamics of the fixed point are required (summarized in Table I). The precise details RN and GR holographic strange metal and the duality map are discussed in Appendix 6.A.

	Scaling	RN $\theta = 0, z = \infty$	GR $z, -\theta = \infty$
Entropy	$s/\mu^2 \sim (T/\mu)^{(d-\theta)/z}$	$s/\mu^2 \sim (T/\mu)^0$	$s/\mu^2 \sim (T/\mu)^1$
Charge Density	*	$n/\mu^2 \sim (T/\mu)^0$	$n/\mu^2 \sim (T/\mu)^0$

Table 6.1.: Scaling behavior in holographic strange metals of the entropy density s and the charge density n in terms of the chemical potential μ and the temperature T . The first column highlights the general formula of holographic scaling geometries. The last two columns focus on the two holographic models with local quantum criticality ($z \rightarrow \infty$) of interest in this paper: the Reissner-Nordström and the Gubser-Rocha model. (*): For a discussion on this, see section 4.2.4 of [71].

The motivation for this study is that all experimental strange metals are known to occur in the presence of an excessively strong effective ionic background potential felt by the electron system, the Mottness of the cuprates being case in point (see e.g., [174, 229, 230]). The commonality of this lattice potential suggests an importance in observed systems of which the effects on the holographic strange metals have not yet been systematically investigated. We shall study the GR and the RN AdS black holes dual to 2+1 dimensional strange metals where we break translations by either a one dimensional or two-dimensional explicit periodic square ionic lattice potential encoded in the local chemical potential

$$\begin{aligned}\mu_{1D}(x, y) &= \mu_0 (1 + A \cos(Gx)) \\ \mu_{2D}(x, y) &= \mu_0 \left(1 + \frac{A}{2} (\cos(Gx) + \cos(Gy)) \right)\end{aligned}\tag{6.3}$$

The parametrization is such that the maximal deviation from the average is $\pm A$ in both cases.

The above explicit lattice condition appears as boundary conditions in the dual holographic gravitational description of the strange metal system in question. The difficulty is that studying such explicit translational symmetry breaking is only possible numerically outside perturbation theory. We solve the full set of spatially dependent Einstein-Maxwell-Dilaton equations of motion for the GR and RN strange metals using the DeTurck gauge in a Newton-Raphson scheme [128, 129, 147]. A summary is given in Appendix 4.B. DC transport is computed by numerically solving for the Stokes flow problem at the horizon [142, 143, 146, 243]. All numerical computations employ a higher-order finite difference scheme where the radial coordinate is discretized on the Chebyshev-Lobatto nodes (Appendix 6.A.3).

We treat the numerical data obtained as the outcome of an experiment. However, the framework in which to analyze this data is known. As we already emphasized, the dense entanglement of the quantum many body system described holographically by its dual gravity theory drives a very rapid quantum thermalization. This implies that local equilibrium sets in very rapidly, which in turn implies that, in the homogeneous background with no lattice, transport at macroscopic times and lengths is governed by hydrodynamics. Different from the quasiparticles in Fermi-liquid metals, a strange metal flows like water. It is a general hydrodynamical principle that it can be decomposed in convective- (also called “coherent”) and diffusive (“incoherent”) flows. The former refers to the motion of the fluid as a whole as protected by the conservation of total momentum in the translationally invariant homogeneous background. When the translational symmetry is weakly broken, both are readily recognizable in the Drude model, which introduces by hand a momentum decay rate $\Gamma_{\text{mom.rel.}} = \tau_{\text{mom.rel.}}^{-1}$ as the largest relaxation time. For relativistic hydrodynamics appropriate to strange metals where a linear dispersion relation of charged constituents induces an emergent Lorentz symmetry the Drude conductivities are

$$\begin{aligned}\sigma(\omega) &= \frac{n^2}{\epsilon + P} \frac{1}{\Gamma_{\text{mom.rel.}}} + \sigma_{\text{inc}} \\ \alpha(\omega) &= \frac{ns}{\epsilon + P} \frac{1}{\Gamma_{\text{mom.rel.}}} + \alpha_{\text{inc}} \\ \bar{\kappa}(\omega) &= \frac{s^2 T}{\epsilon + P} \frac{1}{\Gamma_{\text{mom.rel.}}} + \bar{\kappa}_{\text{inc}}\end{aligned}\tag{6.4}$$

Here n, s, ϵ, P of the convective terms are the charge, entropy, energy, and pressure density respectively. The Lorentz symmetry also demands that the incoherent contributions are related to each other by $\sigma_{\text{inc}} = \sigma_Q$, $\alpha_{\text{inc}} = -\frac{\mu}{T}\sigma_Q$ and $\bar{\kappa}_{\text{inc}} = \frac{\mu^2}{T}\sigma_Q$ in terms of a transport coefficient σ_Q .¹

Writing $\sigma_{\text{inc}} = \frac{T}{\mu^2}\bar{\kappa}_{\text{inc}}$, $\alpha_{\text{inc}} = -\frac{1}{\mu}\bar{\kappa}_{\text{inc}}$ instead, this reveals that in a Galilean invariant system where both $c \rightarrow \infty$ and $\mu = m_e c^2 + \dots \rightarrow \infty$, only the incoherent heat contribution survives. It is a highlight of non-relativistic finite temperature Fermi-liquid theory that such a diffusive heat conduction is present even dealing with spin-less fermions, mediated by the Lindhard continuum. This $\bar{\kappa}_{\text{inc}} = c_n D_T$, where the specific heat at constant density (equal to the specific heat at constant volume) $c_n \sim T$, while the thermal diffusivity $D_T \simeq v_F^2 \tau_{\text{col}}$ where $\tau_{\text{col}} \simeq \frac{E_F}{k_B T} \tau_h$; therefore $\bar{\kappa}_{\text{inc}} \sim 1/T$ as verified e.g. in the ^3He Fermi liquid. In contrast in the non relativistic limit $\epsilon + P \rightarrow \mu n \sim n m c^2$ the electrical conductivity becomes purely convective and one recognizes the familiar Drude weight expressed in the plasma frequency as $\omega_p^2 = n e^2 / m$.

The incoherent contributions to transport are in principle measurable in the laboratory by zeroing out the coherent part. This can be done by measuring heat transport in the absence of charge transport (open boundary heat conductivity) κ or charge transport without heat, $\sigma_{Q=0}$ equal to

$$\begin{aligned}\kappa &= \bar{\kappa} - \frac{T\alpha^2}{\sigma}, \\ \sigma_{Q=0} &= \sigma - \frac{T\alpha^2}{\bar{\kappa}}.\end{aligned}\tag{6.5}$$

Note that in the Galilean limit when there is only an incoherent heat conductivity $\kappa = \bar{\kappa}_{\text{inc}}$.

These incoherent contributions are diffusive. The open boundary combinations Eq.(6.5) are therefore a mixture of diffusive and convective transport. Nevertheless, it is useful and conventional to define the charge and thermal diffusivities $D_c \equiv \sigma/\chi$ and $D_T \equiv \kappa/c_n$, where χ is the charge susceptibility, and c_n the heat capacity. In the remainder of this text, we will see that when translational symmetry is strongly broken and the convective part is strongly suppressed, these diffusivities are directly related to diffusion constants in transport. These “incoherent metal” diffusivities and diffusion constants should not be confused with the well-known diffusion of charge D_ρ and energy D_π in weak or vanishing translational symmetry breaking. As we shall see in the Gubser-Rocha metal the latter are both linear-in- T at low temperature while they are T -independent at low temperature in Reissner-Nordström. In the incoherent metal, in contrast, we will see that $D_T \sim T$ while $D_c \sim T^{-1}$.

Will the Real Planckian Dissipating Channel Make Itself Known?

The point of this brief hydrodynamical exposition is to highlight the fundamental issue we address in this article. The above illustrates that even in the simplest Drude hydrodynamics there are two

¹There is one exception. If the translational symmetry breaking happens in only one of the spatial dimensions α_{inc} and κ_{inc} vanish [139]. In that particular case a subleading term in the numerator of the convective term precisely cancels the incoherent term in the thermoelectric and heat conductivity.

dissipative channels: the convective coherent Drude term encoding the way translational symmetry is broken, and the incoherent term related to a diffusion of microscopic origin. For weak lattice potentials, or more generally for weak translational symmetry breaking, the convective Drude term is much larger than the incoherent term. With the conjecture that in strongly correlated critical points the shear viscosity is bounded by the entropy $\eta \geq s/4\pi$, two of us, together with R. Davison, proposed that in disordered strange metals the usual shear viscosity based momentum relaxation rate $\Gamma_{\text{mom.rel.}} \sim \eta \sim s$ can explain a linear-in-T resistivity for a system with Sommerfeld entropy [106]. The connection between the resistivity and the entropy would explain the universality and the minimal viscosity would be the encoding of Planckian dissipation. Moreover, this argument is also consistent with a Drude response in the optical conductivity. The counterargument is that this only holds in detail for marginal disorder. Relevant or irrelevant disorder would significantly limit the regime of applicability of this argument [244, 245].

Taking a step back, it actually is difficult to argue that a universal phenomenon such as Planckian dissipation should manifest itself through the convective channel, as this coherent channel will generically depend on the details of translational symmetry breaking [225, 246]. The far more natural channel for Planckian dissipation would be the incoherent diffusive channel. But if one takes this point of view, one can no longer use it to explain the universal linear-in-T DC resistivity in strange metals. These all show strong Drude behavior in the optical conductivity, and the DC conductivity is therefore set by the coherent response in the context of weak translational symmetry breaking. It appears to be a Catch-22. Either a Planckian dissipation can set the universally observed linear-in-T resistivity in strange metals, but then the AC conductivity ought to be Drude, or weak translational symmetry breaking sets the resistivity, but then it is hard to see how it can be universal.

We will resolve this conundrum by showing explicitly that in weak lattice near a non-trivial IR fixed point, the thermodynamics of the fixed point together with a fixed-point-controlled scaling of transport coefficients can set the DC resistivity in a universal sense, independent of the dissipative channel shown in the AC conductivity. Qualitatively this is an extension of the Davison-Schalm-Zaanen $\Gamma_{\text{mom.rel.}} \sim \eta \sim s$ result. At the same time, for large lattice strengths the incoherent part becomes dominant and indeed shows universal Planckian dissipation as surmised by Blake and others [225–227]. For good measure we state that there may still be a deeper way to also understand the weak lattice results in terms of Planckian dissipation. Even though they appear non-universal, the observed scaling, together with the way the Sommerfeld entropy is a natural bounding behavior at low temperatures, leaves this possibility open.

6.4. Umklapp Hydrodynamics for Weak Lattice Potentials

As we emphasized, in the low frequency limit at macroscopic long wavelengths holography reduces to hydrodynamics albeit with specific transport coefficients. A fundamental principle behind the theory of hydrodynamics is local equilibrium. The state of the fluid can be described by a slowly spatially varying energy-momentum tensor $T_{\mu\nu}(x)$ and in the presence of a $U(1)$ charge, a current $J^\mu(x)$. In turn the local equilibrium condition implies that one can also describe fluid behavior in the presence of a slowly spatially varying external potential whether temperature $T(x)$, pressure

$P(x)$, or chemical potential $\mu(x)$ [247–249], Suppose this background is periodic in the coordinate x . The hydrodynamical problem of relevance is nothing else than that of a hydrodynamical fluid like water that is flowing through a periodic “array” of obstacles weakly perturbing the flow, characterized by a microscopic “lattice constant”. This is a rather unusual circumstance in standard hydrodynamics and we are not aware of any literature addressing the role of Umklapp in the AC structure of the correlators, though a beginning was made in [250].

But it represents an elementary exercise, and the answer is readily understood. From elementary solid state physics it is well known that a quantum mechanical wave function in a periodic background experiences Umklapp. This is purely a wave phenomenon and the principle therefore also applies to classical waves as described by hydrodynamics. Both a quantum mechanical wave function and linearized hydrodynamic fluctuations around equilibrium are described by a differential equation of the form

$$(\partial_t + M(x))\phi(x) = 0 \quad (6.6)$$

If $M(x)$ is periodic $M(x + \frac{2\pi n}{G}) = M(x)$, then $\phi(x)$ can be decomposed in Bloch waves $\phi(x) = \frac{1}{2\pi G} \int_{-G/2}^{G/2} dk \sum_n \phi_n(k) e^{i(k+nG)x}$. Taking $M(x) = -M_0 \partial_x^2 + A \cos(Gx)$ as canonical example, one can solve Eq. (6.6) perturbatively in A . Defining $\phi_n(k) = \phi_n^{(0)}(k) + A\phi_n^{(1)}(k) + \frac{A^2}{2}\phi_n^{(2)}(k) + \dots$, the solution to first order A is

$$\phi_n(k) = \phi_n^{(0)}(k) + \frac{A}{2G(G-2k)M_0} \phi_{n-1}^{(0)}(k) - \frac{A}{2G(G+2k)M_0} \phi_{n+1}^{(0)}(k) + \dots \quad (6.7)$$

This mixing between the different Bloch waves is Umklapp. In hydrodynamics these Umklapped responses have already been observed several years ago in numerical computations of holographic metals in explicit periodic lattices in [107, 120, 140]. Fig.4 in the article [140] shows an Umklapped sound mode at $\omega = v_s G$ in the optical conductivity with G the lattice momentum. However, a full treatment has been lacking.

For $U(1)$ charged relativistic hydrodynamics the fluctuation equations in the longitudinal sector in a spatially constant background are the coupled equations [8i]

$$\begin{pmatrix} -i\omega & ik & 0 \\ ik\beta_1 & D_\pi k^2 - i\omega & ik\beta_2 \\ -D_{n_1} k^2 & ik\beta_3 & D_{n_2} k^2 - i\omega \end{pmatrix} \begin{pmatrix} \delta\epsilon \\ \delta\pi_x \\ \delta n \end{pmatrix} = 0 \quad (6.8)$$

Here $\delta\epsilon$, δn , $\delta\pi_x$ are the fluctuations in energy-, charge-, and longitudinal momentum density respectively. The upper two-by-two block is the sound sector with $\beta_1 = \left(\frac{\partial \bar{p}}{\partial \epsilon}\right)_n$. At finite density this interacts with a charge diffusion mode in the bottom one-by-one block through the interac-

tions $\beta_2 = \left(\frac{\partial \bar{p}}{\partial \bar{n}}\right)_\epsilon$, $\beta_3 = \frac{\bar{n}}{\bar{\epsilon} + \bar{p}}$ and the diffusion constant D_{n_1} . The diffusion constants equal

$$\begin{aligned} D_\pi &= \left(2 \left(1 - \frac{1}{d}\right) \eta + \zeta\right) \left(\frac{\partial v_x}{\partial \pi_x}\right)_\epsilon = \frac{2 \left(1 - \frac{1}{d}\right) \eta + \zeta}{\bar{\epsilon} + \bar{p}}, \\ D_{n_1} &= \sigma_Q \bar{T} \left(\frac{\partial(\bar{\mu}/\bar{T})}{\partial \bar{\epsilon}}\right)_{\bar{n}} = -\sigma_Q \frac{\left(\frac{\partial \bar{n}}{\partial \bar{T}}\right)_{\bar{\mu}} + \frac{\bar{\mu}}{\bar{T}} \left(\frac{\partial \bar{n}}{\partial \bar{\mu}}\right)_{\bar{T}}}{\left(\frac{\partial \bar{n}}{\partial \bar{\mu}}\right)_{\bar{T}} \left(\frac{\partial \bar{\epsilon}}{\partial \bar{T}}\right)_{\bar{\mu}} - \left(\frac{\partial \bar{n}}{\partial \bar{T}}\right)_{\bar{\mu}} \left(\frac{\partial \bar{\epsilon}}{\partial \bar{\mu}}\right)_{\bar{T}}}, \\ D_{n_2} &= \sigma_Q \bar{T} \left(\frac{\partial(\bar{\mu}/\bar{T})}{\partial \bar{n}}\right)_{\bar{\epsilon}} = \sigma_Q \frac{\left(\frac{\partial \bar{\epsilon}}{\partial \bar{T}}\right)_{\bar{\mu}} + \frac{\bar{\mu}}{\bar{T}} \left(\frac{\partial \bar{\epsilon}}{\partial \bar{\mu}}\right)_{\bar{T}}}{\left(\frac{\partial \bar{n}}{\partial \bar{\mu}}\right)_{\bar{T}} \left(\frac{\partial \bar{\epsilon}}{\partial \bar{T}}\right)_{\bar{\mu}} - \left(\frac{\partial \bar{n}}{\partial \bar{T}}\right)_{\bar{\mu}} \left(\frac{\partial \bar{\epsilon}}{\partial \bar{\mu}}\right)_{\bar{T}}}. \end{aligned} \quad (6.9)$$

In the last two equations, the last equality leads to a seemingly more complicated form, but each of these derivatives is much simpler to compute. Barred quantities denote the (spatially constant) equilibrium background, and η, ζ, σ_Q are the microscopic transport coefficients: the shear- and bulk-viscosity and the momentum-independent contribution to the conductivity. As discussed, the holographic models we consider have $d = 2$ with an underlying conformal symmetry for which the equation of state $\bar{\epsilon} = 2\bar{p}$ implies that $\zeta = 0, \beta_2 = 0$ and $\beta_1 = c_s^2 = 1/2$; we will limit our focus to conformal hydrodynamics in the remainder.

Placing such a system in a spatially varying chemical potential $\mu(x) = \bar{\mu} (1 + A \cos(Gx))$ the Umklapp interactions follow from a re-derivation of the fluctuation equations in this background. A detailed derivation for both conformal and non-conformal hydrodynamics and discussion with a natural generalization to a two-dimensional lattice $\mu(x) = \bar{\mu} \left(1 + \frac{A}{2} \cos(Gx) + \frac{A}{2} \cos(Gy)\right)$ is given in a companion article [251]. In summary, to maintain equilibrium with spatially constant temperature also requires a spatially varying charge density $n(x) = \bar{n} + \bar{\mu} A \left(\frac{\partial \bar{n}}{\partial \bar{\mu}}\right)_{\bar{T}} \cos(Gx) + \dots$ and pressure $p(x) = \bar{p} + A \bar{\mu} \bar{n} \cos(Gx) + \dots$ to leading order in A . The exact equation of state $\bar{\epsilon} = 2\bar{p}$ in a conformal fluid means the energy density follows the pressure. By viewing the lattice as a small perturbation on the thermal equilibrium, we can express the perturbations in terms of the chemical potential modulation and the thermodynamic susceptibilities of the background. These corrections to the background are responsible for the Bloch decomposition and Umklapp interactions mixing them. To first order in the lattice strength A the three modes of the longitudinal sector² mix with their six Umklapp copies. Our interest in this article is how this Umklapp affects the response at low frequencies $\omega \ll G$ and zero momentum $k = 0$. At $k = 0$ the un-Umklapped charge diffusion mode decouples, and the remaining eight modes decompose into four parity-odd-in- G ones and four parity-even modes. The latter include the $k = 0$ sound mode $\delta\pi^{(0)}$, two Umklapped sound modes built on $\delta\epsilon^{(S)} = \int dx \sin(Gx) \delta\epsilon(x)$, $\delta\pi^{(C)} = \int dx \cos(Gx) \delta\pi(x)$; and one Umklapped charge diffusion mode built on $\delta n^{(S)} = \int dx \sin(Gx) \delta n(x)$ that interact

²Substituting this spatially varying background into the defining conservation equations of hydrodynamics and expanding in fluctuations, they no longer decompose in a longitudinal and transverse sector. It can be shown, however, that in the presence of a orthogonal lattice the naively longitudinal sector along one of the lattice directions is self-contained.

as

$$(\partial_t + M) \cdot \delta\phi = R \quad (6.10)$$

with

$$M = \begin{pmatrix} 0 & \frac{1}{2}AG\bar{\mu} & \frac{1}{2}AG\bar{\mu} & -\frac{3}{2}i\omega A\bar{\mu}\beta_3 \\ -\frac{AG\bar{\mu}}{(\bar{\epsilon}+\bar{p})\alpha_n} & D_\rho G^2 & 0 & 0 \\ -2AG\bar{\mu}\beta_3^2 & 0 & 0 & -G\beta_3 \\ -3i\omega A\bar{\mu}\beta_3 & 0 & \frac{G}{2\beta_3} & D_\pi G^2 \end{pmatrix} \quad (6.11)$$

and

$$\delta\phi = \begin{pmatrix} \delta\pi_x^{(0)} \\ \delta n^{(S)} - \beta_3 \delta\epsilon^{(S)} \\ \beta_3 \delta\epsilon^{(S)} \\ \delta\pi_x^{(C)} \end{pmatrix}, \quad R = \begin{pmatrix} \bar{n} \\ \bar{\mu}A\beta_3 \frac{D_\rho G}{\bar{B}_\rho G} \\ -\bar{\mu}A\beta_3 \frac{\bar{B}_\rho G}{\alpha_n} \\ \bar{\mu}A \left(\alpha_n^{-1} + \frac{\bar{n}^2}{(\bar{\epsilon}+\bar{p})c_s^2} \right) \end{pmatrix} \delta\bar{E}_x \quad (6.12)$$

where we have defined $D_\rho = D_{n_2}$ the charge diffusion constant and where we used the coefficient $\alpha_n \equiv \bar{T} \left(\frac{\partial(\bar{\mu}/\bar{T})}{\partial\bar{n}} \right)_{\bar{\epsilon}}$ which entered the definition of D_{n_2} . It is purely thermodynamic and has a universal scaling behavior determined by the scaling of entropy, as we will later highlight. We have added to our system a perturbatively small time-varying electric field $\delta E_x(t) = -\delta\bar{E}_x e^{-i\omega t}$ which will externally source a longitudinal current δJ^x . This term will also enter the hydrodynamic system as an extra term in the current constitutive relation through $\partial_x \mu \rightarrow \partial_x \mu + \delta E_x(t)$.

We can now therefore linearize the constitutive relation

$$\delta J^x = n\delta v^x - \sigma_Q \left[\partial^x (\delta\mu - \frac{\mu}{T} \delta T) + \delta E_x \right] \quad (6.13)$$

for the current density defined as

$$\delta J^x(t) = \left(\frac{\partial J^x}{\partial \phi} \right)^\top \cdot \delta\phi(t) + \sigma_Q \delta\bar{E}_x e^{-i\omega t} \quad (6.14)$$

with $\left(\frac{\partial J^x}{\partial \phi} \right)^\top = \left(\beta_3, \quad -\bar{\mu}A \frac{D_\rho G}{2} \beta_3, \quad \bar{\mu}A \frac{D_\rho G}{4\bar{n}\alpha_n}, \quad \bar{\mu}A \left(\beta_3 + \frac{1}{2\bar{n}\alpha_n} \right) \right).$

We make use of the dynamical system (6.10), to obtain the time-evolution of the dynamical fields $\delta\phi(\omega) = (-i\omega I_4 + M(\omega))^{-1} \cdot (\delta\phi(t=0) + R\delta\bar{E}_x)$. Since we have turned on the external electric field, we are not interested in explicitly sourcing any of the hydrodynamical variables and therefore we set $\delta\phi(t=0)$ as an initial condition such that $\delta\phi(\omega) \propto \delta\bar{E}_x$ and by extension so will be δJ^x . Finally, the optical conductivity can be computed as [251]

$$\sigma(\omega) = \frac{\delta J^x}{\delta\bar{E}_x}. \quad (6.15)$$

The inverse $(-i\omega I_4 + M)^{-1}$ is dominated by the vanishing of its determinant. These zeroes show up as poles in the conductivity. Expanding the determinant to order A^2 , there are four poles at

$$\begin{aligned}\omega_1 &= -i(\Gamma_\eta + \Gamma_d) + \mathcal{O}(A^4), \\ \omega_2 &= -i(D_\rho G^2 - \Gamma_d) + \mathcal{O}(A^4), \\ \omega_\pm &= \pm \frac{G}{\sqrt{2}} \left[1 - \bar{\mu}^2 A^2 \beta_3^2 + \mathcal{O}(A^4) \right] - i \frac{1}{2} \left[D_\pi G^2 - \Gamma_\eta + \mathcal{O}(A^4) \right] + \mathcal{O}(G^3)\end{aligned}\quad (6.16)$$

with

$$\begin{aligned}\Gamma_d &\equiv A^2 \frac{\mu^2}{2(\bar{\epsilon} + \bar{p}) D_\rho \alpha_n}, \\ \Gamma_\eta &\equiv 2\bar{\mu}^2 A^2 \beta_3^2 D_\pi G^2 = 2A^2 \frac{\bar{\mu}^2 \bar{n}^2}{(\bar{\epsilon} + \bar{p})^2} D_\pi G^2\end{aligned}\quad (6.17)$$

At low frequency $\omega \ll c_s G$, the contribution from the two sound poles ω_\pm should be negligible in the conductivity. By expanding the expression (6.15) as a quadruple Laurent series

$$\sigma(\omega) = \sigma_0 + \sum_{i=1,2,\pm} \frac{Z_i}{\omega - \omega_i} \quad (6.18)$$

and truncating the two sound modes, one finds that it takes the form³

$$\sigma_{\text{no sound}}(\omega) = \sigma_0 + \frac{Z_1}{\omega - \omega_1} + \frac{Z_2}{\omega - \omega_2} = \sigma_0 + Z_{\text{eff}} \frac{\Omega - i\omega}{(\Gamma - i\omega)(\Omega - i\omega) + \omega_0^2} \quad (6.19)$$

with

$$\begin{aligned}\Omega &= \overbrace{D_\rho G^2}^{\mathcal{O}(1)} - \overbrace{2D_\rho^2 G^2 \Gamma_d + \mathcal{O}(G^3) + \mathcal{O}(A^4)}^{\mathcal{O}(A^2)}, \\ \Gamma &= 2D_\rho^2 G^2 \Gamma_d + \Gamma_\eta + \mathcal{O}(G^3) + \mathcal{O}(A^4), \\ \omega_0^2 &= D_\rho G^2 \Gamma_d \left[1 - 2D_\rho^2 G^2 + \mathcal{O}(G^3) \right] + \mathcal{O}(A^4), \\ Z_{\text{eff}}/\omega_p^2 &= 1 + 4\bar{\mu}^2 A^2 \beta_3^2 D_\pi^2 G^2 - D_\rho \Gamma_d \left[4 + D_\rho (D_\rho - 4D_\pi) G^2 \right] + \mathcal{O}(G^3, A^4), \\ \sigma_0 &= \sigma_Q + \mathcal{O}(A^4),\end{aligned}\quad (6.20)$$

where the plasmon frequency is $\omega_p^2 = \frac{\bar{n}^2}{\bar{\epsilon} + \bar{p}}$.

The form Eq. (6.19) is well known from studying the hydrodynamics of decaying charge density waves or other unstable superfluids [221, 234, 252–258]. This is not surprising as the underlying

³An attempt to formally decouple the sound modes by taking the limit $c_s^2 \rightarrow \infty$ requires that $\Gamma_\eta \sim \frac{1}{c_s^2}$ and will therefore shift the poles. The truncated Laurent expansion keeps the poles in the right location.

physics is that of two damped currents cross-coupled with an interaction ω_0 (see Appendix 6.F). Both a decaying (i.e. damped) pseudo-Goldstone boson, as well as an Umklapp hydrodynamics interaction belong to this class.

Given an appropriate temperature scaling of Γ , Ω , ω_0 or equivalently $Z_{1,2}$, $\omega_{1,2}$ it was already proposed that such a conductivity could explain the emerging mid-IR peak at high temperature in the cuprates. We will argue below that this Umklapp hydrodynamics in an holographic AdS₂ metal with Sommerfeld specific heat provides precisely the right scaling.

6.5. The Applicability of Hydrodynamics and the Imprint of Local Quantum Criticality

Despite the fact that the interplay between holography and hydrodynamics has been formidable, it is not a given that a hydrodynamical understanding as given above applies directly to holographic strange AdS₂ metals in explicit lattices. Even though holography describes strongly coupled systems which implies a large hydrodynamical regime, this regime is finite as has been emphasized in several recent articles [259–263], and bounded by $\omega = 2\pi\Delta T$ where Δ is the scaling dimension of the lowest irrelevant operator from the strange metal fixed point. This argument against hydrodynamics can be sharpened by the fact that momentum dependent longitudinal DC-conductivities at zero frequency $\sigma(\omega = 0, k \neq 0)$ vanish [264].⁴ This is an unavoidable consequence of $U(1)$ current conservation: $\omega \rightarrow 0$ implies $G \cdot J = 0$. Naively considering Umklapp as the mixing of the $\sigma(\omega, 0)$ and $\sigma(\omega, k = G)$, would argue that the amplitude of the mixed-in Umklapp wave is thus very small. This is illustrated by a memory matrix computation [233, 264]. The momentum-dependent density correlation function $G_{J^t J^t}$ in a homogeneous AdS₂ metal, which is the operator to consider for our choice of lattice, scales as a function of the temperature as

$$\text{Im } G_{J^t J^t}^{\text{homogeneous}}(\omega = 0, k) \sim T^{2\nu_k} + \dots, \quad \nu_k = \frac{1 + \hat{\eta}}{2\sqrt{2 + \hat{\eta}}} \sqrt{10 + \hat{\eta} + 4(2 + \hat{\eta})\bar{k}^2 - 8\sqrt{1 + (2 + \hat{\eta})\bar{k}^2}} \quad (6.21)$$

where $\hat{\eta} \equiv -\theta/z$ characterizes the near-AdS₂ region and $\bar{k} \equiv \frac{k}{\mu\lambda}$ is a wavevector renormalization that correctly rescales to the emergent near horizon AdS₂ geometry in a lattice [140, 264]. For GR $\hat{\eta} = 1$ and for RN, $\hat{\eta} = 0$ while in both cases, $\lambda = 1$. This scaling of $G_{J^t J^t}$ follows from a near-far matching method in the AdS₂ bulk which shows that a generic Green's function takes the form

$$G = \frac{A + B\mathcal{G}}{C + D\mathcal{G}} \quad (6.22)$$

⁴Recall that momentum-dependent conductivities at finite momentum need not be in the hydrodynamic regime. Within hydrodynamics, longitudinal diffusive conductivities obeying $\sigma(\omega, k) = \frac{i\omega D\chi}{i\omega - Dk^2}$ give an exactly vanishing DC conductivity at finite momentum, but a finite DC conductivity at zero momentum obeying Einstein's relation $\sigma = D\chi$.

with A, B, C, D purely real and \mathcal{G} the AdS₂ Green's function [93]

$$\mathcal{G}(\omega, k) \propto T^{2\nu_k} \frac{\Gamma(1 - \nu_k) \Gamma\left(\frac{1}{2} + \nu_k - \frac{i\omega}{2\pi T}\right)}{\Gamma(1 + \nu_k) \Gamma\left(\frac{1}{2} - \nu_k - \frac{i\omega}{2\pi T}\right)} \quad (6.23)$$

The imaginary part of the density correlator is proportional to the imaginary part of the AdS₂ correlator as $\text{Im } G_{J^t J^t} \sim \text{Im } \mathcal{G}$. Though this scaling as a function of the temperature is exact, it ignores the possibility that there can still be a large amplitude as a function of the other parameters. This is in fact what happens when one extrapolates the exact answer for the momentum-dependent transverse conductivity $\sigma_{\perp}(\omega, k)$ to the hydrodynamic regime $k \ll \mu$ [265]. The momentum dependent current-current correlation function in an AdS₂ metal behaves as

$$G_{J_{\perp} J_{\perp}}(\omega, k) = -\frac{k^2 \mathcal{G}(\omega)}{\omega^2 + \frac{k^2}{2r_0} \mathcal{G}(\omega)} \quad (6.24)$$

Although the scaling is indeed captured by the Hartnoll-Hofman result Eq. (6.21) one also sees that for small k the hydrodynamic pole at $\omega = -iDk^2$ becomes far more important than the $(\omega/T)^{2\nu}$ -suppression. For $k \leq \mu$ the hydrodynamic pole captures the physics far better than the AdS₂ power-law.

As is clear from the mathematical expressions this is not a sharp transition, but a smooth crossover. Nevertheless there is a clear transition between dominant physics regimes (AdS₂ vs hydrodynamics) that can be made visible through the holographic dynamics. A finite momentum conductivity is better viewed as the response when the system is placed in a fixed spatially oscillating but static electric field background. The spatial oscillation imprints a lattice structure in the finite density system. The conventional RG perspective is that this lattice is irrelevant in the RG. This is the physics behind the power-law dependence on temperature in Eq. (6.21). The AdS₂ fixed points of the holographic metals that we study, either RN or GR, are so-called semi-local quantum liquids [232], however. This means that while for $T < \mu$ the two-point correlation function displays power-law behavior between two time-like separated points, it is exponentially suppressed between two space-like separated points. This exponential suppression is so strong that two points separated spatially by a distance $|x| \gtrsim \frac{1}{\mu}$ have no causal contact [232]. In momentum space this implies that the coupling between modes with $k \lesssim \mu$ is exponentially small. This decoupling means that for modes $k \lesssim \mu$ or equivalently a spatially oscillating but static electric field with $G \leq \mu$ the RG-flow becomes strongly suppressed once T decreases below μ . One can think of it as that the d -dimensional RG-flow at $T = \mu$ decomposes into individual RG-flows for each momentum mode. Recalling that in holography the radial direction encodes the RG-flow, we can visualize this. In Fig. 6.4 we plot the charge/current density as a function of location for a modulated chemical potential. For a lattice momentum $G \gg \mu$ the lattice irrelevancy towards the IR is uninterrupted. However for an oscillating chemical potential with periodicity $G \ll \mu$, the RG flow “halts” around the AdS radius value $r \sim \mu$ corresponding to $T \sim \mu$. For such values of $G \ll \mu$ the lattice thus remains quite strong in the IR and certainly much stronger than one would naively expect. The way to understand this is that precisely in this regime it is the proximity of the

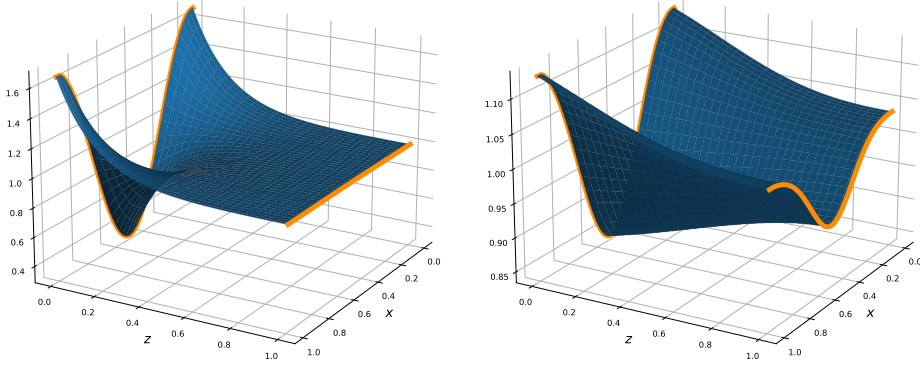


Figure 6.4.: A holographic visualization of the cross-over in response functions between $G > \mu$ (left) and $G < \mu$ (right). Plotted is the bulk electric field F_{tz} (whose boundary value is dual to the charge density) in the presence of a 1D spatially varying chemical potential $\mu(x) = \mu_0 + A \cos(Gx)$ as a function of position and the AdS radial direction z . For $G > \mu$ ($G = 4\mu$) one sees the lattice amplitude decrease smoothly as one moves from the AdS boundary to the horizon at $z = 1$. For $G < \mu$ ($G = 0.05\mu$) on the other hand, one sees that the RG flow is much slower and “halts” around $z \sim 0.5$. This is due to the exponential suppression of the coupling between different momentum modes at the AdS_2 IR fixed point. The results are for a RN black hole at $T/\mu = 0.15$.

hydrodynamic pole that dominates the response rather than the RG scaling suppression. Ultimately the RG wisdom does hold for any lattice perturbation and even for $G \ll \mu$ the lattice will eventually turn irrelevant in the IR (Sec 3.4 in [140]), and scaling again becomes the pre-eminent physical effect but this only happens at the lowest of temperatures.

For Umklapp hydrodynamics this is relevant because it implies that the regime where the hydrodynamics results capture the physics is appreciable. Below we shall verify that near an AdS_2 fixed point Umklapp hydrodynamics is the better way of understanding the physics for $G < \mu$, whereas AdS_2 Hartnoll-Hofman scaling is the better way for $G > \mu$. For the sake of clarity, we emphasize that strictly speaking at a mathematical level both can be, and often are, valid simultaneously as is evidenced by (6.24). However, the physical response is generically dominated by one or the other, and relying on only one of them is not sufficient.

There is a second reason why hydrodynamics is the more appropriate perspective for $G \ll \mu$. A more precise analysis of the momentum-dependent density correlator in an AdS_2 metal shows that it has multiple characteristic scaling contributions [264]

$$\text{Im } G_{J^t J^t}^{\text{homogeneous}}(\omega = 0, k) \sim c_- T^{2\nu_k} + c_0 T^{2\nu_k^0} + c_+ T^{2\nu_k^+} \quad (6.25)$$

with the additional scaling exponents

$$\begin{aligned}\nu_k^0 &= \frac{1 + \hat{\eta}}{2} \sqrt{1 + 4\hat{k}^2} \\ \nu_k^+ &= \frac{1 + \hat{\eta}}{2\sqrt{2 + \hat{\eta}}} \sqrt{10 + \hat{\eta} + 4(2 + \hat{\eta})\bar{k}^2 + 8\sqrt{1 + (2 + \hat{\eta})\bar{k}^2}}\end{aligned}\quad (6.26)$$

For $k = G \ll \mu$ as one needs for Umklapp between $\text{Im } G_{J^t J^t}^{\text{homogeneous}}(0, k')$ for $k' = 0, \pm G$, all these three exponents take values that are very close to each other. For such small differences in the exponents there is observationally no clean scaling regime. For low lattice strengths A this is the reason that the observed weak lattice DC conductivities in Fig. 6.3 do not scale exactly inversely-linear-in- T as noted in the Introduction. Through Umklapp, the lattice DC conductivity is related to the homogeneous density correlator (which we will review in more details in the next section)

$$\sigma_{\text{DC, lattice}} \sim \left(\lim_{\omega \rightarrow 0} \frac{\text{Im } G_{J^t J^t}^{\text{homogeneous}}(\omega, k)}{\omega} \right)^{-1} \sim \frac{1}{c_- T^{2\nu_k - 1} + c_0 T^{2\nu_k^0 - 1} + c_+ T^{2\nu_k^+ - 1}}. \quad (6.27)$$

Fig. 6.5 shows that the deviation from linearity is exactly due to the contribution of the additional exponents.

6.6. DC vs Optical conductivities in explicit lattice (holographic) strange metals from Umklapp

Having argued that hydrodynamics should dominate the response in holographic strange metals, we now exploit our ability to do computational experiments to confirm that Umklapp hydrodynamics applies when such holographic strange metals are placed in an explicit periodic lattice with a small amplitude A . Then we shall describe the surprising phenomenological conclusions for electrical DC and optical electrical conductivity.

To verify the applicability of Umklapp hydrodynamics in AdS_2 metals, we can study the location of the poles in linear response functions. Fig. 6.6 shows the poles in the optical conductivity $\sigma(\omega)$ in a GR strange metal in a 1D ionic lattice background $\mu(x) = \mu_0(1 + A \cos(Gx))$. There are multiple poles on the negative imaginary axis and two poles with real part at the location $\omega = \pm v_s G$. The latter are the ones already noted by [107, 120, 140] and identified as Umklapped sound modes [140]. That Umklapp is at work is confirmed by tracing the behavior of the poles as a function of temperature. Compare the behavior of the two poles on the negative imaginary axis closest to the origin to the analytically computed values Eqs. (6.16), we see that the match is very good; see Fig. 6.7. Moreover, if one also studies the response functions at finite momentum k , then one observes the characteristic Umklapp level repulsion at the edge of Brillouin zone $k = G/2$ (Fig. 6.6).

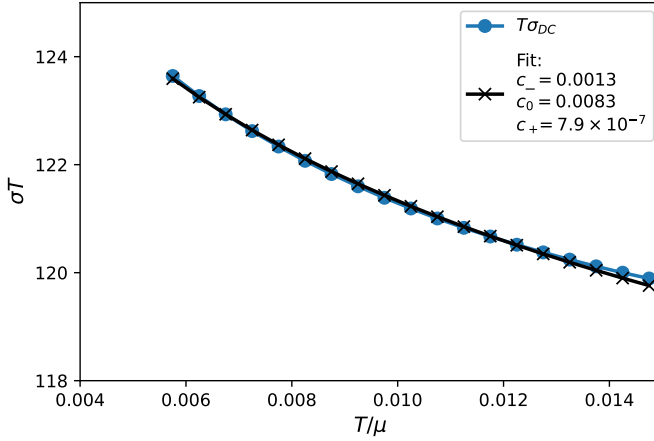


Figure 6.5.: The DC conductivity of the GR metal in a weak lattice potential $A = 0.05$ is not perfectly inversely linear-in- T . This is due to subleading scaling contributions computable from the AdS_2 fixed point. Shown is a three parameter fit of the DC conductivity for c_- , c_0 , c_+ to the functional form $\sigma_{DC} = 1 / \left(c_- T^{2\nu_G-1} + c_0 T^{2\nu_G^0-1} + c_+ T^{2\nu_G^+-1} \right)$ at low temperature with ν_G, ν_G^0, ν_G^+ given by Eq. (6.21) and Eq. (6.26), with $k = G$, for $G/\mu = 0.1$. The values of the exponents ν_G, ν_G^0, ν_G^+ at this wave vector are 1.00015, 1.0198 and 2.53, respectively. Therefore according to this fit, one expects the exponent ν_G to be the dominating one only at temperatures $T/\mu < \mathcal{O}(10^{-50})$.

6.6.1. Low Temperatures: Drude Transport

We have claimed Umklapp Hydrodynamics explains the remarkable finding summarized in Fig. 6.3 that the DC conductivity of a strange metal in a weak lattice remains linear-in-temperature while the mechanism governing the AC-response appears to change. We can now show this.

The DC conductivity from Umklapp Hydrodynamics to lowest order in the lattice strength A equals

$$\sigma_{DC} = \frac{Z_{\text{eff}}}{\Gamma + \frac{\omega_0^2}{\Omega}} + \sigma_Q = \underbrace{\frac{\omega_p^2}{\Gamma_\eta + \Gamma_d}}_{\mathcal{O}(A^{-2})} + \underbrace{\sigma_{\text{offset}} + \sigma_Q}_{\mathcal{O}(1)} + \mathcal{O}(A^2) \quad (6.28)$$

where, in the last equality, the first term is the leading order and the offset term σ_{offset} comes from the higher order terms in Eqs. (6.20). The first contribution in the DC from the sound part of the Laurent expansion (6.18) only comes at order $\mathcal{O}(A^2)$ and is therefore negligible here. These expressions already suggest that two physical mechanisms are at play in the DC result. At first sight this may appear contradictory to the conventional explanation of weak lattice DC conductivity in

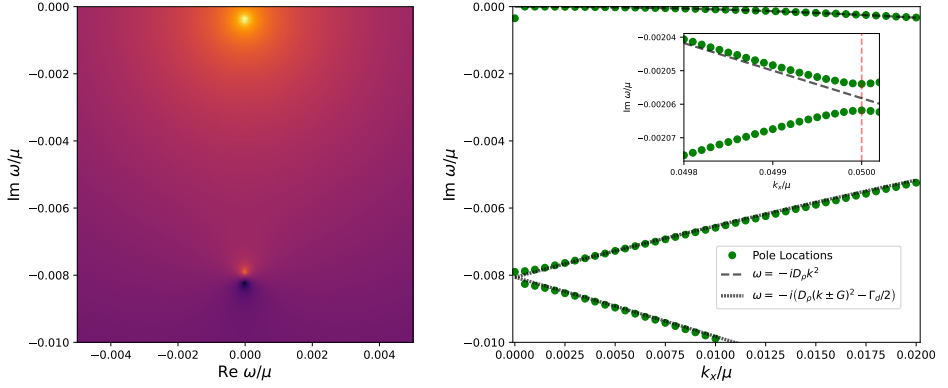


Figure 6.6.: Umklapp hydrodynamics. The left panel shows the presence of both the Drude (upper) pole and the Umklapped charge diffusion (lower) pole and associated zero in the complex frequency plane at $k_x = 0$. The right panel shows the motion of both poles as a function of longitudinal momentum k_x . The Umklapp is confirmed by matching this motion to the diffusion coefficients of the un-Umklapped hydrodynamics computed in Eqs. (6.24). The inset shows the level splitting near the Brillouin zone boundary at $k = G/2$. The results are computed in the GR black-hole lattice at $T/\mu = 0.1$, $G/\mu = 0.1$ with a 1D ionic lattice potential $\mu(x) = \mu(1 + 0.05 \cos(Gx))$. The deviation at low k finds its origin in the next order level splitting in umklapp which our formula does not account for, similar to the level splitting near the Brillouin zone.

terms of Drude momentum relaxation $\sigma = \frac{\omega_p^2}{\Gamma_{\text{mom.rel.}}}$. The momentum relaxation rate $\Gamma_{\text{mom.rel.}}$ can be computed in the memory matrix formalism [233, 266] to equal

$$\Gamma_{\text{mom.rel.}} = \frac{g^2 G^2}{(\bar{\epsilon} + \bar{p})} \lim_{\omega \rightarrow 0} \frac{\text{Im} \langle \mathcal{O} \mathcal{O} \rangle(\omega, k = G)}{\omega} \quad (6.29)$$

where $\mathcal{O}(G)$ is the operator that breaks translation invariance with coupling g . In the case of an ionic lattice with a cosine potential as we consider, there are two operators $\mathcal{O}(G) = J^t$, one inserted at wavevector G and one at $-G$ each with coupling strength $g = \bar{\mu}A/2$. Therefore the memory matrix momentum relaxation rate for the ionic lattice is

$$\Gamma_{\text{mom.rel.}} = \frac{\bar{\mu}^2 A^2 G^2}{2(\bar{\epsilon} + \bar{p})} \lim_{\omega \rightarrow 0} \frac{\text{Im} G_{J^t J^t}(\omega, k = G)}{\omega}. \quad (6.30)$$

Inserting its correlation function computed in a homogeneous background into (6.30) one in fact finds the exact same answer as computed by Umklapp hydrodynamics $\Gamma_{\text{mom.rel.}} = \Gamma_\eta + \Gamma_d$ (see Appendix 6.D for a derivation of this result). Theoretically this can be understood through the observation that there are two possible dissipative channels in hydrodynamics. There is sound

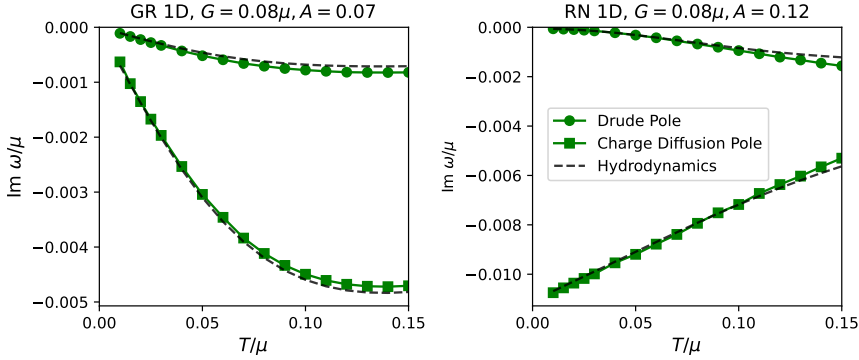


Figure 6.7.: The motion of the poles as one increases temperature. As the temperature is increased further the Drude pole eventually collides with the Umklapped charge diffusion pole and gains a real part. At low temperatures where a perturbative Umklapp analysis is valid the behavior of the poles can be understood from the un-Umklapped hydrodynamic analysis. Note that the imaginary part of the charge diffusion pole scales as T^1 in the GR lattice, while it scales as T^0 in RN. Results are in the GR and RN 1D lattices with $G/\mu = 0.08$ and potential strengths $A = 0.07$ and $A = 0.12$, respectively.

attenuation controlled by the shear viscosity η (and bulk viscosity ζ) and there is charge diffusion controlled by the microscopic conductivity σ_Q . Both are at the same order in the lattice strength $\Gamma_{d,\eta} \sim A^2$. This is the expansion parameter in the memory matrix computation and explains why they both show up.

The phenomenologically important characteristic is the temperature scaling of the DC resistivity. Implicitly the lattice scaling implies a scaling with temperature as the effective lattice strength should become irrelevant in the deep IR. This must be encoded explicitly in the scaling of both Γ_η and Γ_d , and not in the UV-strength A . However, there is a priori no requirement that both Γ_d and Γ_η will scale the *same* as a function of T . Generically they ought not. However, in holographic strange metals without a ground state entropy they do. For these systems at low temperatures

$$\begin{aligned} \Gamma_\eta &\sim \eta(T) \sim s \sim T^{(d-\theta)/z} \\ \Gamma_d &\sim \frac{T^2}{\sigma_Q(T)} \left(T \frac{\partial s}{\partial T} \right)^2 \sim \left(\frac{d-\theta}{z} \right)^2 T^{(d-\theta)/z} \end{aligned} \quad (6.31)$$

The derivation requires a mild assumption about the low temperature equation of state and is given in Appendix 6.E. Thus for the GR strange metal $\Gamma_\eta \sim T$ and $\Gamma_d \sim T$, whereas for the RN metal which has a ground state entropy $\Gamma_\eta \sim T^0$ but the first non-vanishing order for Γ_d is $\Gamma_d \sim T^2$. Over the range of validity, usually one of them will dominate, though it is conceivable that one dissipative momentum relaxation process switches dominance with the other. If this coincides with a change in scaling this would show up as a change of temperature scaling of the DC resistivity.

Two observations follow. The first is that despite the numerical results supporting the inference from disordered translational symmetry breaking that the momentum relaxation rate scales as the entropy, this is not true for the contribution from Γ_d .

The more important observation here and in the following is that which term dominates does not matter. In holographic strange metals the momentum-relaxation rate is set at a deeper level by the non-trivial locally quantum critical IR fixed point. As pointed out by Hartnoll-Hofman and briefly reviewed in the previous Section 6.5, in the regime where Eq. (6.30) holds, the frequency scaling enforced by local quantum criticality also sets the temperature scaling of the DC result. For the RN strange metal it is only Γ_η that is responsible for this, whereas in the Gubser-Rocha strange metal both obey the appropriate scaling. Since Γ_η also scales as G^2 , whereas Γ_d does not, one can tune the GR response to be dominated by Γ_d for $G \ll 2\mu$, and Γ_η to dominate for $G \gg 2\mu$. This coincides with the applicability of hydrodynamics as we discussed in the previous section, confirming a correlation with a physically observable change (see also section 6.6.4 below). This very difference between $\Gamma_\eta \sim G^2$ and $\Gamma_d \sim G^0$ actually causes the order of importance to be opposite in disordered systems. Because disorder can be viewed as an average over an infinite set of lattices, in the decay rate in a disorder system $\Gamma_{\text{disorder}} \sim \int G^{d-1} dG (\Gamma_d + \Gamma_\eta)$ the Γ_η term will generically dominate the integral [106]. Since $\Gamma_\eta \sim \eta \sim s$, this explains why in disordered systems entropy does directly control the dissipation time scale in contrast to a lattice with a fixed lattice momentum G_L as we explained above.

Independent of the dissipative mechanism, both leading in A momentum-relaxation rates Γ_η and Γ_d become vanishing small at low temperatures suggesting Drude transport. This is readily confirmed in the AC conductivity. Its real part displays a characteristic Drude peak. Mathematically, however, the peak is not exactly a (half-)Lorentzian, but follows from the two-pole expression Eq. (6.19).

6.6.2. Intermediate temperatures: a mid IR-peak in the optical response

We have just argued that the DC resistivity can remain the same while the physical regime controlling dissipation changes, because it is set at a deeper level by the underlying AdS_2 fixed point. Though we have just noted this fact by analyzing the analytic expressions, it is in fact dramatically made clear at an intermediate higher temperature, as we already summarized in the Introduction.

In the regime of interest the conductivity computed from Umklapp hydrodynamics is controlled by two poles. In the parametrization

$$\sigma(\omega) = \sigma_Q + Z \frac{\Omega - i\omega}{(\Gamma - i\omega)(\Omega - i\omega) + \omega_0^2} \quad (6.32)$$

these are the Drude and Umklapp charge diffusion poles at

$$\begin{aligned} \omega_{\text{Drude}} &= \frac{-i}{2}(\Gamma + \Omega) + \frac{i}{2}\sqrt{(\Gamma - \Omega)^2 - 4\omega_0^2} = -i(\Gamma_\eta + \Gamma_d) + \mathcal{O}(A^4), \\ \omega_{\text{Um.Ch.Diff.}} &= \frac{-i}{2}(\Gamma + \Omega) - \frac{i}{2}\sqrt{(\Gamma - \Omega)^2 - 4\omega_0^2} = -i(D_\rho G^2 - \Gamma_d) + \mathcal{O}(A^4). \end{aligned} \quad (6.33)$$

At low temperatures, the second pole (let alone the two already ignored Umklapp sound poles) has a small effect. Increasing the temperature changes this fundamentally, however. Both poles move as one increases the temperature. However, they do not move in unison. When the argument under the square root $(\Gamma - \Omega)^2 - 4\omega_0^2$ becomes negative, the poles collide. For temperatures higher than the pole-collision temperature, the poles can now acquire a real part and move off the imaginary axis symmetrically; see Fig. 6.8. Initially this “microscopic pole collision” has little effect on the optical conductivity. In a formal sense it slightly broadens the peak around $\omega = 0$ and without an insight into the complex frequency response it is essentially indistinguishable from a conventional Lorentzian Drude peak. However, as one increases temperature further and the poles move further away from the imaginary frequency axis, the peak will split into two, symmetrically arranged around $\omega = 0$. For the positive half-line $\omega > 0$ one would thus see a peak emerge in the near IR whereas the DC value at $\omega = 0$ continues to decrease.

This collision point is controlled by a combination of temperature, lattice strength and lattice periodicity. Already at moderate lattice strengths, this emergence of the mid-IR peak in the AC conductivity happens at temperatures $T < T_{\text{strange}}$ where the DC response is still set by the critical scaling behavior of the underlying AdS_2 strange metal. In other words, despite the qualitatively drastic change in the AC-vs- T conductivity, the DC-vs- T response is unaffected.

What is striking is that this emergence of mid-IR peak in the optical response as temperature increases while the DC-resistivity stays linear in T is precisely what is observed in high T_c cuprates and other strange metals as explained in the introduction. Given the earlier hypothesis reviewed there that transport in the high T_c -cuprates is hydrodynamical, it is conceivable that this is the explanation of this observed experimental finding.

The mechanism we just explained is tantalizing given its minimalistic nature. It is in fact *ubiquitous* for *any* hydrodynamical fluid exposed to a microscopic Umklapp potential where the effective potential strength is rising more rapidly than the momentum diffusivity. Notice that it does *not* apply to a Fermi liquid in metallic background potentials. The onset of equilibration is set by the quasiparticle collision time, but typically a substantial fraction of the centre of mass momentum is absorbed by the Umklapp impeding the total momentum conservation required for hydrodynamics including the mechanism in the above.

6.6.3. Intermediate Lattice Strength: Towards an Incoherent Metal

Our computational experiments on holographic strange metals can also provide us insight in what happens at larger lattice strengths beyond the applicability of perturbative Umklapp hydrodynamics. This is best quantified by tracking the behavior of the complex frequency poles in the AC conductivities. In Fig. 6.9 we show typical quasinormal mode spectrum computed for lattice strength $A = 0.15$. At low temperatures one finds that these are still dominated by the non-linear continuation of the same two-pole structure as we identified for small A , i.e. the Drude and Umklapp charge diffusion poles identified in Umklapp hydrodynamics.

What is notable, is that the pole collision has already happened at a lower temperature than for perturbatively small A . Qualitatively this is easy to understand in terms of the RG wisdom that the lattice becomes irrelevant in the IR. If one starts with a stronger A in the UV, one is at a relatively

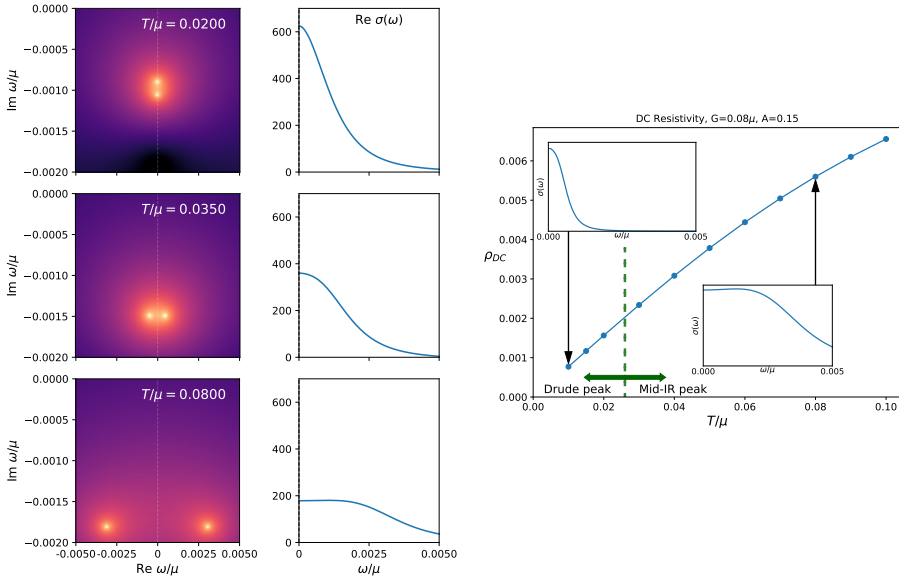


Figure 6.8.: Emergence of mid-IR peak in the optical conductivity $\sigma(\omega)$ from pole collision. At low temperatures the Umklapp has negligible consequences as the response is strongly dominated by the conventional Drude pole. At intermediate temperatures the Umklapp pole causes an additional broadening. When the temperature increases to the point where the poles collide and gain a real part the peak still looks Drude to the eye even though it arises from two poles symmetrically arranged on both sides of the real axis. At even higher temperatures these two poles move so far apart that the peaks separate and a mid IR peak at finite ω appears in the optical response. For this figure the parameters are $A = 0.15$, $G = 0.08\mu$, the same as in Fig. 6.3.

stronger strength at a temperature T or vice versa one is at a comparable strength at a lower temperature T . This may seem like semantics, but crucially the DC conductivity linear-in- T scaling remains set by the local quantum critical IR fixed point, which is less affected by an increase in A . As a result we can again observe in the AC conductivity a transition in the dissipative mechanism as one increases T during which the resistivity stays essentially linear (Fig. 6.3 in the Introduction). The transition in this case is that from the mid-IR-peak regime to an incoherent metal. The latter means that the low frequency AC response is no longer well described by the “two-coupled-relaxational-current” formula. Other poles now also influence the AC response, especially the two Umklapped sound modes. They feature prominently in the AC response; see Fig. 6.9.

Though the AC conductivity really shows the emergence of the incoherent metal regime at larger T and the “two-coupled-relaxational-current” expressions fails, for most of the temperature range

the DC limit $\omega \rightarrow 0$ is still well described by its asymptotic expression

$$\sigma_{DC} = \sigma_0 + \frac{Z}{\Gamma + \frac{\omega_0^2}{\Omega}} \quad (6.34)$$

With careful fitting of the optical conductivity as well as the complex location of the four poles, one can fit the parameters $Z, \sigma_0, \Gamma, \Omega, \omega_0^2$ as well as the parameters of the two first Umklapped sound poles as a function of A and T . For the full 4-pole ansatz, see Section 6.C. In Fig. 6.10 we show how the three parameters in the denominator Ω, Γ and ω_0 evolve as function of temperature for intermediate $0.1 < A < 0.8$. One sees how these explain the observed DC conductivity quite well. Given that the DC conductivity is so well captured by Eq. (6.34), one concludes that for these potentials the DC conductivity is still limited by the momentum life time.

6.6.4. On the Applicability of Umklapp Hydrodynamics

We end this section with a brief check on our earlier argument in Section 6.5 that Umklapp hydrodynamics is the relevant perspective to understand strange metal transport in a weak/intermediate lattice for $G \lesssim \mu$ rather than Hartnoll-Hofman scaling. The intuitive argument is that momentum dependent conductivities are strongly power-law suppressed as a function of T for $G \gtrsim \mu$ as the RG flow is not “halted”. Umklapping conductivities that have such marginal weight should have negligible observable effect. Fig. 6.11 shows that this insight is essentially correct. For a lattice with $G = 1.0\mu, T/\mu \lesssim 0.35$ and $A = 1.0$ the AC conductivity is Drude-like, and no transitions to a mid-IR-peak or incoherent metal are seen. An illustration that formally Umklapp hydrodynamics still applies is that one can still notice the now very highly suppressed Umklapped sound peak. Even so, for $G \gtrsim \mu$ the better perspective is Hartnoll-Hofman scaling. Since G/μ is large here, the various exponents in the resistivity described in Section 6.5 are not close and the lowest exponent ν_G of Eq. (6.21) alone is enough to describe the DC conductivity at low temperatures.

6.7. Observations at Strong Lattice Potentials: Planckian Dissipation and Incoherent Metals

6.7.1. The Remarkable Ubiquity of Planckian Dissipation

We now switch to analyzing our numerical results at large lattice potentials $A > 1$. As we reviewed in Section 6.3, for small lattice potentials $A < 1$, Planckian dissipation is unlikely to be universal as it will depend on the details of how translational symmetry is broken [226, 246]. At finite density one must be in a regime where translation is broken strongly and long time transport is controlled by another dissipative mechanism than translational symmetry breaking.

Performing this numerical experiment where we increase the lattice strength, one sees not only a beautiful sharper linear-in- T resistivity, but also a saturating behavior in that the resistivity appears to become independent of the lattice strength A , highlighted in the Introduction (Fig. 6.1). Though the thermoelectric and heat conductivity also appear to saturate, they do not. Replotting

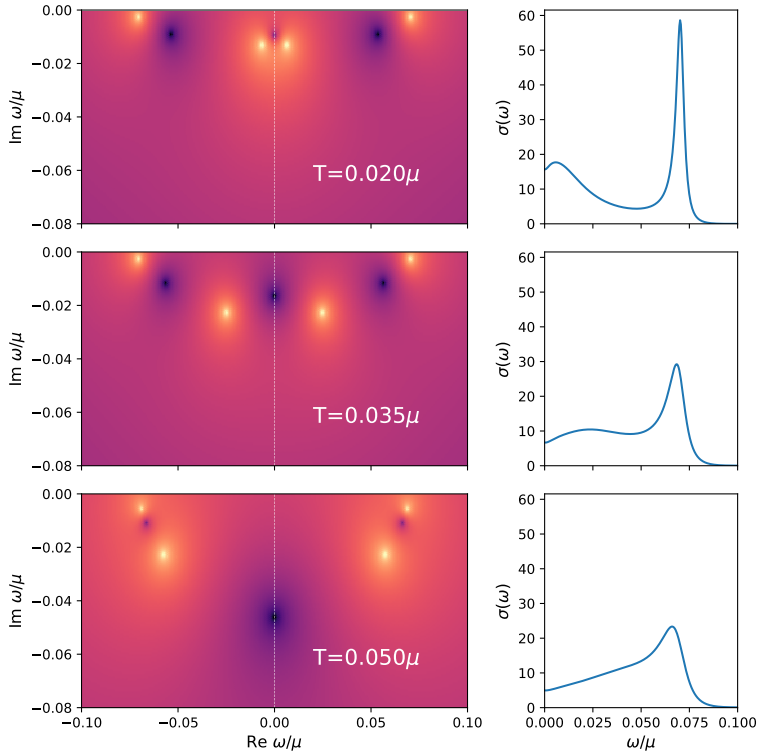


Figure 6.9.: Optical conductivity (right) and the quasiparticle spectra (left) for intermediate lattice strength GR lattices for $A = 1$, $G/\mu = 0.1\mu$ at three different temperatures. Compared to small A the pole collision (see section 6.6.2) has already happened even at lowest $T/\mu = 0.02$. As one increases T the Umklapped sound poles which stay almost fixed at $\text{Re } \omega = \pm c_s G = \pm \frac{1}{\sqrt{2}} G$ (and others not shown) become more important and their dominance in the AC conductivity signals the transition to an incoherent metal regime.

the results as a function of the inverse lattice strength $1/A$ rather than A , one sees that they asymptote to zero as $1/A$; see Fig. 6.12. One also notes that the electrical conductivity does not saturate but turns over when inspected this precisely. However, we will argue that the dissipative process does saturate. Increasing the lattice potential A has two effects, it changes the strength and possibly mechanism of dissipation, but it can also shift degrees of freedom from lower to higher energy and vice versa. In simple Drude language where $\sigma_{DC} = \omega_p^2/\Gamma$, increasing the lattice strength cannot only affect Γ , but also the Drude weight ω_p^2 . The Drude formula doesn't necessarily apply at large A , of course. Nevertheless, to focus on the dissipation we must also account for possible shifts in the weight. Because the total weight of the optical conductivity is protected and conserved, a more appropriate measure of the dissipation is to normalize the measured DC conductivity by

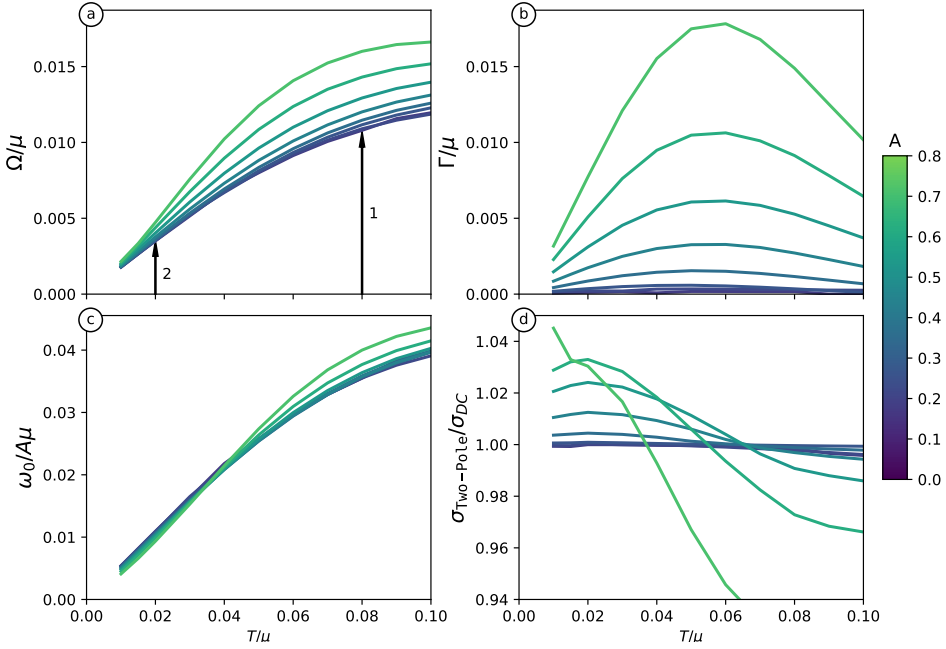


Figure 6.10.: (a-c) The evolution of the phenomenological parameters Γ/μ , Ω/μ , $\omega_0/A\mu$ as present in the “two-coupled-relaxational-current” expression Eq. 6.32 as a function of A and T/μ at $G/\mu = 0.12$ in the iD Gubser-Rocha model. These parameters are extracted from a four-pole fit to the optical conductivity that includes the two lowest-order Umklapped sound peaks which reside at $\text{Re } \omega \approx \pm c_s G$. Both Ω/μ and $\omega_0/A\mu$ show little A -dependence, whereas Γ/μ depends strongly non-linearly on A . In (a), the arrows labelled 1 and 2 point to the temperatures at which the pole collision happens at $A = 0.1$ and $A = 0.2$, respectively. For the stronger lattices, the pole collision has already happened at lower temperatures than we have access to in our numerics. (d) Comparison of $\sigma_{\text{Two-Pole}}$, the conductivity reconstructed from only the “two-coupled-relaxational-current” part of the spectrum in figures to σ_{DC} , the observed DC conductivity. At larger values of A , it becomes clear that one must include more information, such as the Umklapped sound modes, in order to accurately reconstruct the DC conductivity at all temperatures.

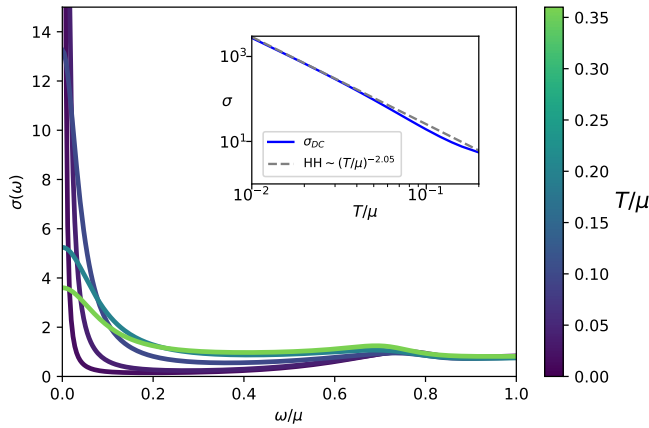


Figure 6.11.: The AC conductivity of the GR model at $G = 1.0\mu$ and lattice strength $A = 1.0$ for a large temperature range. The low ω -response is of the Drude form for all values and no transition to a mid-IR-peak or an incoherent metal is seen in contrast to lattice momenta $G < \mu$. The small rise at $\omega/\mu = \frac{1}{\sqrt{2}} \frac{G}{\mu} = \frac{1}{\sqrt{2}}$ is the Umklapped sound mode which now has barely noticeable height at low temperatures. The inset shows that the DC conductivity obeys leading order Hartnoll-Hofman scaling at low temperature, which is expected to go as $(T/\mu)^{-2.05}$ at low temperatures.

the total weight $\int_0^\Lambda d\omega \sigma(\omega)$ and study the resultant rate $\Gamma_{\text{corrected}}^{-1} = \sigma_{\text{DC}} / \int_0^\Lambda d\omega \sigma(\omega)$. Fig. 6.13 shows both the naive Drude rate $\Gamma_{\text{bare}}^{-1} = \sigma_{\text{DC}} / \omega_p^2$ and the corrected rate. Indeed in terms of the naive Drude rate even at the largest A the saturating behavior in the conductivity is not exact. However, when corrected for a possible spectral shift, the relaxation rate does saturate. Not only does this relaxation rate saturate, as Fig. 6.13 shows, it saturates to a value that is numerically close to the Planckian dissipation rate $\Gamma_{\text{corrected}} \simeq 2\pi / \tau_{\hbar} = 2\pi T$. To understand whether Planckian dissipation is really occurring, we must resort to a different theoretical framework.

6.7.2. An Incoherent Metal Explained with Microscopic Scrambling

How to understand transport in a system where translation invariance is badly broken was discussed in detail by Hartnoll [219], and its connection with Planckian dissipation was set out in a series of papers [225–227, 235, 267] in the context of systems with strong translational disorder. The essence is that in this regime only energy and charge are the conserved currents that survive at long distances. For this section we shall not just focus on the electrical conductivity but on the full thermoelectric transport matrix

$$\begin{pmatrix} \vec{J} \\ \vec{j}_Q \end{pmatrix} = \begin{pmatrix} \sigma & \alpha T \\ \alpha & \bar{\kappa} \end{pmatrix} \begin{pmatrix} \vec{E} \\ \frac{1}{T} \vec{\nabla} T \end{pmatrix} \quad (6.35)$$

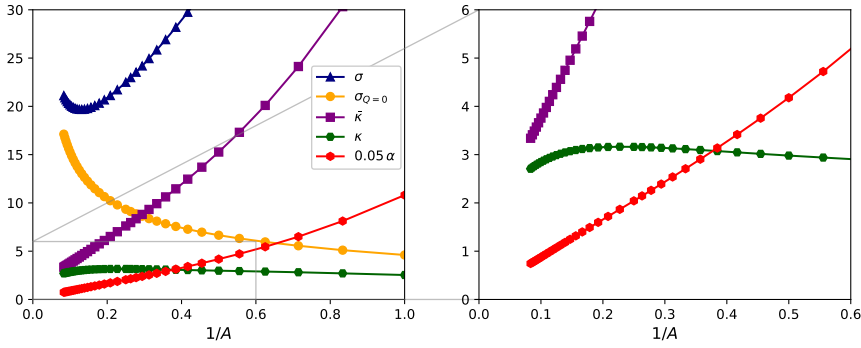


Figure 6.12.: (Left panel) Absence of exact saturation of the conductivities as a function of lattice strength at fixed temperature in the 2D GR model is made quite clear when they are plotted as a function of $1/A$ instead of A . The electrical conductivity σ reaches a minimum and then starts to grow again at larger A , whereas the thermoelectric α and heat conductivity $\bar{\kappa}$ scale as $1/A$ rather than saturate. (Right panel) The open boundary heat conductivity κ at first instances does appear to be independent of the lattice strength A for most of the computed values. However, at the largest A it does show a downturn, asymptoting to $\bar{\kappa}$ which vanishes as $1/A \rightarrow 0$. In this large A regime, these asymptotes $\kappa \rightarrow \bar{\kappa}$ and $\sigma_{Q=0} \rightarrow \sigma$ indicate the increased dominance of the diffusive channel. These results are for the 2D GR lattice with $T = 0.06\mu$, $G = 0.1\sqrt{2}\mu$.

with $j_Q^i = \frac{1}{T}(T^{0i} - \mu J^i)$. Here $\bar{\kappa} = \kappa + \frac{T\alpha^2}{\sigma}$ is the heat conductivity in the absence of electric field, and κ is the heat conductivity in the absence of electric current (open boundary heat conductivity). Fig. 6.1 shows the result for all conductivities for increasing lattice strength into the incoherent regime, both in the Gubser-Rocha ($s_{\text{GR}} \sim T + \dots$) and in the Reissner-Nordström AdS_2 metal ($s_{\text{RN}} \sim c_0 + c_1 T + \dots$). The conductivities are rescaled such that their dominant power-law scaling with T is scaled out. In detail one observes also that the thermoelectric and the heat conductivity conform sharper to the conjectured appropriate temperature scaling as A increases, culminating again in a saturating behavior for large A .

It is tempting to view this scaling of the thermoelectric conductivities as validating that the system is dominated by a single common relaxation time that scales like the entropy at low temperatures, even though it does not apply here as A is large. Single relaxation time Drude theory would suggest that $\sigma = \omega_p^2/\Gamma$, $\alpha = \frac{s}{n}\sigma$, and $\frac{\bar{\kappa}}{T} = \frac{s^2}{n^2}\sigma$. If $\Gamma \sim s(T)$ as naively guessed above, it is consistent with the above observations. As we will now explain, and confirmed with counterexamples in studies of strong translational disorder, this single relaxation time description is not correct.

To extract possible relaxation rates in an incoherent metal with strong translational symmetry breaking, one posits constitutive relations for the two remaining currents and does a hydrodynamic analysis. One finds that the DC conductivities are the zero frequency limit of the dynamics

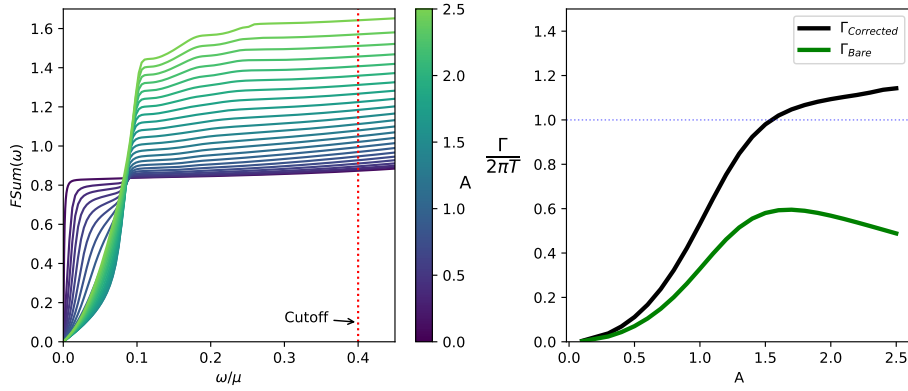


Figure 6.13.: The upper figures show the saturating behavior of the relaxation rate of the conductivity is not exact when inspected closely. However, the integrated optical conductivity $\text{FSum}(\Lambda) = \int_0^\Lambda \sigma(\omega) d\omega$ shows that the spectral weight increases with A . We can account for this effect by normalising the Drude weight to this integrated spectral weight. The resulting corrected relaxation rate $\Gamma_{\text{corrected}}^{-1} \equiv \sigma_{\text{DC}}/\text{FSum}(\Lambda)$ does appear to show a saturating behavior compared to the bare rate $\Gamma_{\text{bare}}^{-1} = \sigma_{\text{DC}}/\omega_p^2$. Furthermore, this rate is remarkably close to the Planckian value of $2\pi T/\mu$. From inspection a cut-off value $\Lambda/\mu = 0.4$ is sufficient to account for all the spectral weight in any Drude or Umklapped sound peaks. These results are taken in the 1D GR model with $T = 0.06\mu$, $G = 0.12\mu$.

of two independent diffusive modes with diffusion constants D_+ and D_- . These are

$$D_+ + D_- = \frac{\kappa}{c_n} + \frac{\sigma}{\chi} + \frac{T\sigma}{c_n} \left(\frac{\alpha}{\sigma} - \left(\frac{\partial s}{\partial n} \right)_T \right)^2$$

$$D_+ D_- = \frac{\kappa}{c_n} \frac{\sigma}{\chi} \quad (6.36)$$

Here $c_n = T \left(\frac{\partial s}{\partial T} \right)_n$ is the specific heat at fixed charge density, $\chi = \left(\frac{\partial n}{\partial \mu} \right)_T$ is the isothermal charge compressibility, and the conductivities σ, κ are both the transport coefficients as well as the DC values. One recognizes a charge diffusion and a heat/energy diffusion mode (the remnant of sound in absence of a nearly conserved momentum), cross coupled through the combination

$g \equiv \frac{T\sigma}{c_n} \left(\frac{\alpha}{\sigma} - \left(\frac{\partial s}{\partial n} \right)_T \right)^2$. If we are to make the case that a single dissipative mechanism dominates, this cross-coupling is important, as in its absence, charge and energy diffusion are clearly independent. Fig. 6.14 shows what the strength of this coupling is numerically. As was shown in [227], this coupling behaves as $g/\sigma \sim T^{(z+d-\theta)/z}$ if the scaling of the homogeneous non-trivial IR fixed point remains valid in the presence of strong translational symmetry breaking. For the GR metal this means $g \sim T$. Compared to $\sigma/\chi \sim T^{-1}$ it is therefore small and can be treated

perturbatively in the low temperature limit.

Solving for σ, κ in the limit where the terms in the cross coupling $\frac{T\alpha^2}{c_n\sigma} \sim T$, $\frac{T\alpha}{c_n} \left(\frac{\partial s}{\partial n}\right) \sim T$ and $\frac{T\chi\sigma}{c_n} \left(\frac{\partial s}{\partial n}\right)_T^2 \sim T$ are small compared to $\sigma \sim T^{-1}$, one finds⁵

$$\begin{aligned} \frac{\sigma}{\chi} &= D_+ \left[1 + \frac{T}{c_n\chi} \frac{\left(\alpha - D_+\chi \left(\frac{\partial s}{\partial n}\right)_T\right)^2}{D_+(D_- - D_+)} \right] \\ \frac{\kappa}{c_n} &= D_- \left[1 - \frac{T}{c_n\chi} \frac{\left(\alpha - D_+\chi \left(\frac{\partial s}{\partial n}\right)_T\right)^2}{D_+(D_- - D_+)} \right] \end{aligned} \quad (6.37)$$

To lowest order in the temperature the electrical and heat conductivity are therefore determined by independent diffusion constants; see Fig. 6.14. The electrical conductivity is determined by $D_+ \sim T^{-1}$ and the heat conductivity by $D_- \sim T$. There is therefore no simultaneous explanation for both conductivities in terms of universal Planckian dissipation. In holographic models with strong translational disorder there are systems where both conductivities are set by Planckian dissipation [225, 226]. This happens when the charge susceptibility is relevant. For irrelevant or marginal charge susceptibility, the electrical conductivity is set by a different dissipative mechanism. The Gubser-Rocha model with strong disorder belongs to this class [235], and so does our strong ionic lattice model with $\chi \sim T^0$.

Despite the existence of two independent dissipative mechanisms, the heat conductivity can be explained from Planckian dissipation. Very strongly coupled systems are similar to weakly coupled dilute classical gases in that their macroscopic transport can be understood from microscopic processes. For weakly coupled dilute gases this is through the Boltzmann equation summing microscopic scattering; for ultrastrongly coupled systems this is through parameters of microscopic scrambling as measured through the out-of-time-ordered correlation function $C(t, x) = \langle W(t, x)V(0)W(t, x)V(0) \rangle_T \sim e^{\lambda(t-x/v_B)}$.⁶ In holographic systems this connection manifests itself in that the OTOC is equivalent to computing the hydrodynamic response function (of longitudinal sound) at imaginary ω and k [162]. The Lyapunov exponent λ and the butterfly velocity v_B can then be read off from a skipped pole in the hydrodynamic dispersion relation

⁵Note that the coupling term $\frac{T\chi}{c_n} \left(\frac{\partial s}{\partial n}\right)_T = \frac{nT}{(\epsilon+P)} - \frac{c_s^2\mu}{\alpha_n s}$ contains the same thermodynamic factor as Γ_d . If the

temperature scaling in the strong lattice is the same as in the homogeneous system, this coupling scales as $\frac{nT}{(\epsilon+P)} -$

$\frac{c_s^2\mu}{\alpha_n s} \sim T$ since $\alpha_n \sim T^{-2}$ as was shown in Appendix 6.E. Numerics confirms that this is the case.

⁶This “ballistic” OTOC expression applies to large N systems such as holographic and SYK systems. The more generic answer is “diffusive” $C(t, x) \sim e^{\lambda(t-x^2/v_B t)}$.

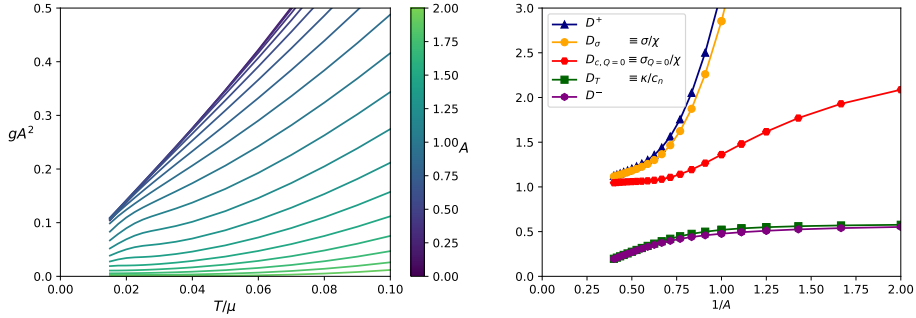


Figure 6.14.: Left: The cross-coupling between the heat and electrical conductivity in the strongly

coherent regime is governed by the combination $g = \frac{T\sigma}{c_n} \left(\frac{\alpha}{\sigma} - \left(\frac{\partial s}{\partial n} \right)^2 \right)$ respectively at low temperatures. Clearly g decreases linear in temperature at low T , but it also decreases with stronger lattice potential A . Right: As a consequence the diffusivities at low T in a strong lattice become independent. Shown are the empirical combinations $D_\sigma \equiv \frac{\sigma}{\chi}$, $D_T = \frac{\kappa}{c_n}$, $D_{\sigma_{Q=0}} = \frac{\sigma_{Q=0}}{\chi}$ as a function of $1/A$ for fixed $T/\mu = 0.05$.

[162]. One finds that in holographic systems λ saturates the Maldacena-Shenker-Stanford unitarity bound $\lambda \leq 2\pi/T$. The butterfly velocity is more sensitive to the theory. On general grounds it scales near (translationally invariant) quantum critical IR fixed points as $v_B^2 \sim T^{2-2/z}$. The fact that both macroscopic transport and the scrambling parameters λ, v_B are encoded in the hydrodynamic response means that they are not unrelated. In particular the thermal diffusivity $D_T = \frac{\kappa}{c_n} = E \frac{v_B^2}{\lambda}$ with $E = \frac{1}{2}$ for AdS_2 $z \rightarrow \infty$ metals in strong disorder [226, 227, 267]. Since the natural units of diffusivity are $v^2\tau$, this is interpreted as Planckian dissipation with $\tau = \frac{1}{\lambda} = \frac{1}{2\pi T}$. The RN metal is a special case. As explained in [267], there the butterfly velocity is controlled by a dangerously irrelevant operator instead of universal scaling. A careful computation reveals that for the RN strange metal $v_B \sim \sqrt{T}$. Combined with Planckian dissipation $\tau = \frac{1}{\lambda} = \frac{1}{2\pi T}$, this explains the observed RN thermal diffusivity $D_- = \frac{\kappa}{c_n} = T^0 \sim v_B^2\tau$.

This result is established and confirmed in the many studies cited above on connecting scrambling to hydrodynamics for weak momentum relaxation or “homogeneous” momentum relaxation (so-called Q-lattices or disorder). We postulate that the same applies in the explicit strong lattice systems studied here. This need not be, for computing the butterfly velocity v_B in a non-translationally invariant system is not straightforward (the Lyapunov exponent on the other hand is universally $\lambda = 2\pi/T$ [268]). At the same time the scaling we observe for strong lattice potentials is the same as that which is observed for strong translational disorder. This is strong evidence in favor of the argument that the same should apply here.

Within the framework of incoherent metals there is no universal explanation of the observed

inverse-in- T scaling of the conductivity for the Gubser-Rocha metal. Its tantalizing behavior $\sigma \sim s(T)^{-1}$ or rather $\sigma \sim \frac{1}{\Gamma_h}$ on the other hand *does* suggest that some type of universality is at work. This is confirmed by the RN results. The obvious conjecture is that $D_- = (v_B^{(c)})^2/\lambda$ where the butterfly velocity $v_B^{(c)}$ for charged objects *differs* from the butterfly velocity for neutral objects. Some evidence that this can be the case is presented in [236–239]. If $v_B^{(c)}$ were independent of temperature, this would explain the observed incoherent metal phenomenology in the large lattice GR and RN metals in terms of a single Planckian relaxation time, but differing scrambling velocities. We leave this for future research.

6.7.3. Saturating Behavior and Planckian Dissipation

The diffusivities in the incoherent regime should be insensitive to the details of translational symmetry breaking. This is what allows them to expose universal dissipative physics. This resulting explanation of universality in terms of microscopic scrambling also makes physical sense: the onset of chaos is controlled by the short-range interactions and is not expected to be influenced significantly by a background lattice. The data we present is obviously dependent on the lattice strength A . For most values of A we are therefore not in the universal regime. However, as A increases to the largest value we can observe in our numerical data, there is a saturating behavior in the electrical conductivity that together with its sharper single power behavior argues strongly that we are close to this universal incoherent limit. Such saturating behavior in the incoherent electrical conductivity at large lattice strength was already noted in [269]. That study focused on the regime where the dimensionless combinations $\frac{\mu}{G} \rightarrow 0$, $\frac{A\mu}{G}$ fixed and large. Here we focus on the regime where both $\frac{\mu}{G}$ and $\frac{A\mu}{G}$ are fixed and large with the latter parametrically larger.

We can use our numerical results to directly check these assertions. Rather than observing the conductivities we do so for the diffusivities

$$D_\sigma = \frac{\sigma}{\chi}, \quad D_T = \frac{\kappa}{c_n}, \quad D_{\sigma_{Q=0}} = \frac{\sigma_{Q=0}}{\chi} \quad (6.38)$$

We have introduced here a charge-without-heat diffusivity $D_{\sigma_{Q=0}} = \frac{\sigma_{Q=0}}{\chi}$ as this is the appropriate counterpart to the heat-without charge open boundary thermal diffusivity $D_T \equiv \kappa/c_n$. Fig. 6.14 shows indeed how the charge diffusivities $D_\sigma, D_{\sigma_{Q=0}}$ not only both saturate, but also become approximately equal. The latter shows indeed that we have entered the incoherent regime. A more detailed depiction of the saturation is given in Fig. 6.15.

We have already shown in the Introduction that the crossover into the incoherent sector can also be seen in the conductivities directly (Fig. 6.2). The open boundary thermal conductivity κ starts to comprise more than 80% of the full heat conductivity. A stronger statement extrapolated from the incoherent metal considerations is that the open boundary heat conductivity κ is rather insensitive to momentum relaxation for any translational symmetry breaking potential irrespective of its strength [227]. According to Fig. (6.12) this is indeed the case in the perturbative small A case. Upon pushing the potential to extremely large values we do observe that some changes in κ start to arise. This is fully in the incoherent regime, where we can equate $\kappa \equiv c_n D_T$ with one of the physical diffusion constants $\kappa = c_n D_-$. This diffusion constant also changes from A -independent to

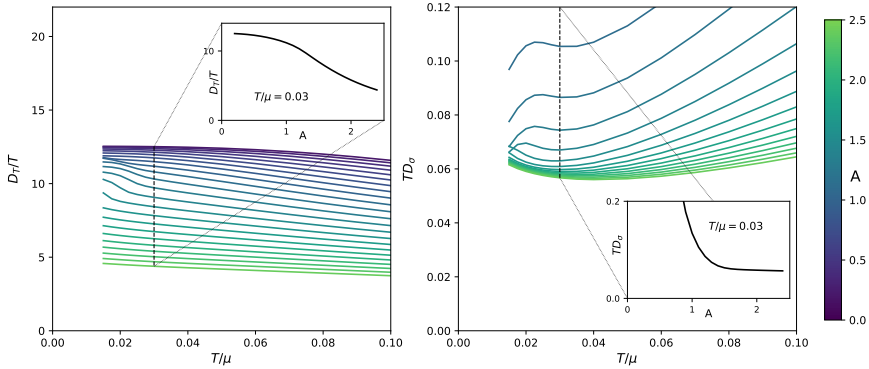


Figure 6.15.: Electrical and thermal diffusivities as a function of T for various A . The T -dependence shows how they become more single-power like at larger A . The A -crosssection shows the saturation for large A for the charge diffusivity, but an increasing A dependence for the thermal diffusivity. These results are in the GR lattice at $G = 0.1\mu$.

slight decaying behavior, explaining the change in behavior in κ . We conclude that at least for D_T our computations confirm the universal nature of the diffusion constants.

6.8. Discussion: Is it Relevant for Condensed Matter Physics?

We started this paper with just presenting the data as these rolled out of the computer. As such these are highly suggestive. We focus in on a holographic strange metal that fulfills minimal conditions that appear to be imposed by experiment: local quantum criticality ($z \rightarrow \infty$) and a Fermi-liquid like thermodynamics in the form of a Sommerfeld entropy ($s \sim T$). We then invoke a lattice potential that may become very strong, again a minimal requirement suggested by experiment. For a wavevector of the potential that is not too large (smaller than the inverse local length) we find a resistivity that is to good approximation linear in temperature for a large range of potential strength. Ramping up the potential the slope of the linear resistivity saturates at a value that is consistent with a Planckian (τ_h) current life time. Although the dynamical range in temperature and potential strength is limited in our computations, we can track the temperature evolution of the optical conductivity in the regime where the saturation is setting in. This temperature evolution is also suggestive with regard to experiment: at low temperature we find a simple Drude response that turns into an incoherent mid IR peak, and this gross change does not imprint on the DC resistivity that stays linear. Taken together, this shines an unusual light on the three problems of principle in strange metal transport: (a) Why is the resistivity linear in temperature down to the lowest temperatures? (b) Why is the empirically extracted current relaxation time so close to the Planckian rate τ_h ? (c) Why does the cross-over from good metal (Drude optical conductivity)

to bad metal (the mid IR peak response) not affect the DC resistivity at all?

The question remains whether the resemblances between numerical observations from this holographic toy model and the complicated reality of the copper oxide electron systems are just a coincidence or whether they reveal a truly universal principle governing transport that supersedes all the differences between them. To get a better understanding, we focused in on both the small- and large lattice potential regimes. We showed that in the perturbative small potential regime the transport behavior can be completely reconstructed on basis of the thermodynamics and transport properties of the unbroken homogeneous system. This is based on hydrodynamical flow behavior in the presence of a weak periodic potential and we discovered a generic principle governing linear response: next to the usual shear drag, a mode coupling emerges with the Umklapped charge diffusion mode. As we increase temperature the coupling between two relaxation modes can account for a second new phenomenon: the two poles can collide and this explains the emerging mid-IR peak in the AC conductivity. Even though the temperature dependence of the DC-resistivity is formally set by the same thermodynamic quantities, the underlying non-trivial IR fixed point constrains these in such a way that the DC resistivity temperature scaling can be independent of the dynamical change in the AC conductivity.

The large lattice potential regime on the other hand is where the resistivity slope saturates. Our numerics indicate that this happens in the “incoherent metal” regime where momentum conservation does not play any role. Accordingly, the temperature dependence of the resistivity should be inversely proportional to the *charge* diffusivity. This charge diffusivity in the incoherent regime $D_- \sim T^{-1}$ should not be compared with the hydrodynamical charge diffusivity for weak or zero momentum relaxation which scales as $D_\rho \sim T$. The *thermal* diffusivity $D_T \sim T$ on the other hand is essentially insensitive to the strength of the lattice potential. It scales similarly for both small and large potential, though only at large potential can it be explained in terms of microscopic chaos anchored in a saturated Lyapunov bound $\Gamma = \lambda = 2\pi T$ having a Planckian magnitude. Although this is presently not well understood this is consistent with the analytical findings in a homogeneous holographic strange metal with momentum relaxation (Q-lattice).

Although this does shed light on various aspects we do not claim a complete understanding of our numerical results. The above suggests that there are quite different forms of physics at work pending the strength of the potential. Nevertheless, we do find that the evolution of the transport quantities is of a strikingly smooth kind. Another striking aspect is the contrast between the GR and RN results in Fig. 6.1: the differences in temperature dependencies appear to be entirely linked to the different temperature dependence of the entropy. The above analysis, where we can expose the different origins in the weak and large lattice potential regime, does make clear that this connection with entropy is almost certainly a coincidence, though we cannot exclude that some yet to be identified greater universality may be at work linking the dissipative properties in the convective and diffusive regimes together where entropy may play a crucial role.

To use this to explain the experimental observations, the critical holographic input is in the form of the current being controlled by “generalized” hydrodynamics (including the incoherent metal) that in turn requires (a) an existence of hydrodynamics up to microscopic length scales shorter than

the lattice spacing, (b) thermodynamical behavior that is anchored in a non-trivial IR fixed point, and (c) a saturation of the chaos bound (with a charge dependent butterfly velocity v_B^{charge}).

In fact, the most critical question is whether experimental strange metal transport is governed by hydrodynamics, and not by the usual quasiparticle transport. In this regard our finding that hydrodynamics provides a most natural explanation for the temperature evolution of the DC and AC charge response is encouraging: it is an elementary mechanism that offers a minimal and simple explanation for this otherwise mysterious affair. However, to prove it one would like to mobilize the mesoscopic transport devices of the kind that have proven successful in this regard observing hydrodynamical flow behavior in graphene (e.g., [270]).

The next issue is, are the hydrodynamical modes surviving down to length scales of order of the microscopic lattice spacing $1/G$? We found this to be a special property of the local quantum critical holographic metals, but is this also at work in the cuprate strange metals? This is far from obvious. Besides the Umklapped charge diffusion mode, we also saw the sharp and prominent Umklapped sound peak in the optical conductivity when the potential becomes sizable. This relates directly to a first discrepancy between our results for the optical conductivity and the experimental results in the cuprates. We find that for the strongest potentials that our numerics can handle, the optical response rather abruptly switches off at frequencies above the umklapped sound peak (Fig. 6.9). In experiment no sound peak is seen, and a power law (branch cut) tail is found instead, extending all the way up to $\mu \simeq 1$ eV [217, 218, 271]. Our holographic results do not shed any light on this matter, although one could imagine that perhaps an umklapped *overdamped* sound channel could conspire to give rise to such a quasi-critical behavior. But the issue is whether the charge diffusion hydro-mode that is responsible for the mid IR peak in holography may survive up to large momenta in the experimental systems. Different from sound, this mode is non-convective and perhaps less sensitive to translational symmetry breaking. Presently we have no answer to this question. It could be interesting to study the optical conductivity of the cuprate metals experimentally at high temperatures. The data in so far available are sketchy and it would be interesting to find out what a systematical and high precision study would reveal regarding for instance the way in which the mid IR peak depends on temperature. Alternatively the sound contribution to the density-density response can be measured directly by EELS [50, 272], with the caveat that sound is promoted to a plasmon in the presence of dynamical electromagnetism. This may be hard, because the plasmon is damped stronger in strange metallic states than ordinary Fermi liquids [273–276]. The results are at this moment inconclusive, and need to still be found consistent with the AC optical conductivity.

Perhaps the most delicate issue relates to the connection with microscopic chaos. The connection with Planckian dissipation requires a saturation of the Maldacena-Shenker-Stanford bound on the Lyapunov exponent of the OTOC $\lambda \leq 2\pi T$. It appears that a necessary condition for this to happen is in the form of *dense many body entanglement*. One may argue that this is the secret of the experimental strange metals: these are born from strongly interacting *fermion* systems at a finite density and it may well be that the concomitant sign problem enforces dense entanglement in the non-Fermi-liquids [223]. But this may not be a sufficient condition. The chaos bound is known to saturate in matrix large N systems at strong coupling with a holographic dual as well as the disorder averaged SYK models. These systems are characterized by dense matrix interactions.

However, the Hubbard models that are the community standard as microscopic point of departure for the cuprate electrons are characterized by local interactions and the associated Hamiltonians correspond with rather sparse matrices. As with regard to the transport properties, the present benchmark is in the form of finite temperature quantum Monte Carlo computations for the resistivity [277]. The temperatures that can be reached are still quite high ($\simeq 1000$ K) but arguably approaching the linear resistivity regime. However, the outcomes are quite different from what we find.

The Hubbard models are of course in their own way toy models, capturing the largest scales in the problem but ignoring a lot of other physics. Could it be that long range interactions arising e.g. from Coulomb interactions and/or phonon mediated interactions are crucial to support the rapid scrambling near the Lyapunov bound given their non-local nature [278]? Could there be a direct relation to SYK physics associated with the observation of spin glass physics [279, 280], with the obvious difficulty that this has only been observed in the spin striped 214 system?

At the least, holography inspires to ask quite unusual questions to experiment: it suggests a physics that is tantalizingly different from the usual Fermi-liquid quasiparticle physics. Eventually, it should be possible by targeted experimentation to reach a verdict. This is not easy: the cuprates have been subjected to unprecedented experimental scrutiny over the last 35 years but on basis of the available information it is still impossible to decide the issue.

An example of this law-of-Murphy that insightful results may be the hardest to obtain experimentally is the thermal transport. So much is clear that the thermal conductivity κ of the GR metal acquires a universal temperature dependence that is up to very high lattice potentials independent of the potential strength. Numerically we observe that $\kappa \sim T^2$. But this is in gross contrast with the thermal conductivity in a Fermi liquid, where $D_T \sim \tau_c$ where $\tau_c \sim 1/T^2$ is the quasiparticle collision time such that $\kappa \sim 1/T$ [281]. There is a large difference of the order T^3 in the temperature dependence of the thermal conductivity between the holographic metal and a Fermi liquid!

This should be the smoking gun but why can this not be used? The reason is that at the high temperatures where the strange metal is realized (> 100 K) the thermal transport is rather completely dominated by the *phonons*. The phonon heat conduction short circuits the heat transport and it is virtually impossible to extract the electronic contributions. The same problem is there for a measurement a charge transport without heat $\sigma_{Q=0}$. Aside from the experimental hurdle of zeroing out heat transport cleanly, the definition of $\sigma_{Q=0} = \sigma - T\alpha^2/\bar{\kappa}$ implicitly refers to the *electronic* component of the heat transport only.

Finally, there is one thermo-electrical transport coefficient that is readily available experimentally: the Seebeck coefficient enumerating the thermopower. This is given by $s = \alpha/\sigma$. According to Fig. 6.1, $\alpha \sim T^0$ and $\sigma \sim 1/T$, and we predict $s \sim T$: although for different reason this is the same temperature dependence generic for a Fermi-liquid (the Mott formula), this is indeed the scaling that has been observed in cuprate strange metals, e.g. [282, 283].

We thank R. Davison, B. Gout  raux, S. Grozdanov, S. Hartnoll and A. Krikun for discussions. This research was supported in part by the Dutch Research Council (NWO) project 680-91-116 (*Planckian Dissipation and Quantum Thermalisation: From Black Hole Answers to Strange Metal*

Questions.), the FOM/NWO program 167 (*Strange Metals*), and by the Dutch Research Council/Ministry of Education. K.G. acknowledges funding from the European Union's Horizon 2020 research and innovation programme under the Marie Skłodowska-Curie grant agreement No 101024967. The numerical computations were carried out on the Dutch national Cartesius and Snellius national supercomputing facilities with the support of the SURF Cooperative as well as on the ALICE-cluster of Leiden University. We are grateful for their help.

6.A. Appendix A: AdS RN and GR Black Holes

We will be interested in perturbations of both Reissner-Nordström and Gubser-Rocha black holes.

6.A.1. Reissner-Nordström

The RN black holes start from the Einstein-Maxwell action

$$S = \int d^4x \sqrt{-g} \left[\frac{L^2}{2\kappa^2} (R - 2\Lambda) - \frac{L^2}{4e^2} F_{\mu\nu} F^{\mu\nu} \right], \quad (6.39)$$

with $2\kappa^2 = e^2 = L^2 = 1$ and $\Lambda = -3$. The equations of motion are

$$\begin{aligned} R_{\mu\nu} - \Lambda g_{\mu\nu} &= \frac{1}{2} \left[F_{\mu\rho} F_{\nu}^{\rho} - \frac{1}{4} g_{\mu\nu} F_{\rho\sigma} F^{\rho\sigma} \right], \\ \nabla_{\mu} F^{\mu\nu} &= 0. \end{aligned} \quad (6.40)$$

These equations admit an electrically charged black hole solution, the AdS-Reissner-Nordström (RN) solution in asymptotically AdS₄ space-time, for which the metric and gauge field are given by⁷

$$\begin{aligned} ds^2 &= g_{\mu\nu} dx^{\mu} dx^{\nu} = \frac{1}{z^2} \left[-f(z) dt^2 + \frac{dz^2}{f(z)} + dx^2 + dy^2 \right], \\ A &= A_t(z) dt, \end{aligned} \quad (6.41)$$

where

$$f(z) = (1 - z) \left(1 + z + z^2 - \frac{\mu^2 z^3}{4} \right), \quad A_t(z) = \mu(1 - z). \quad (6.42)$$

The radial coordinate z can be scaled such that the horizon is located at $z_h = 1$ and the boundary of the space-time is at $z = 0$. The temperature of the black hole can be computed by considering the surface gravity of the horizon, and is given by

$$T_{\text{RN}} = \left| \frac{f'(z_h)}{4\pi} \right| = \frac{12 - \mu^2}{16\pi} \quad (6.43)$$

⁷Sometimes, it is more convenient to make a change of variable $z \rightarrow 1 - (1 - r)^2$ [127].

6.A.2. Einstein-Maxwell-Dilaton

For the dilatonic black holes, we depart from the Einstein-Maxwell-Dilaton action [98, 107]

$$S = \frac{1}{2\kappa^2} \int d^4x \sqrt{-g} \left[R - \frac{Z(\phi)}{4} F_{\mu\nu} F^{\mu\nu} - \frac{1}{2} (\partial_\mu \phi)^2 + V(\phi) \right]. \quad (6.44)$$

The potentials Z, V are given by

$$Z(\phi) = \exp(\phi/\sqrt{3}), \quad V(\phi) = \frac{6}{L^2} \cosh(\phi/\sqrt{3}). \quad (6.45)$$

The cosmological constant is given by $\Lambda = -V(0)/2 = -3$. Setting $2\kappa^2 = L^2 = 1$, the equations of motion for this system are given by

$$\begin{aligned} R_{\mu\nu} &= \frac{Z(\phi)}{2} \left[F_\mu{}^\rho F_{\nu\rho} - \frac{1}{4} g_{\mu\nu} F^2 \right] + \frac{1}{2} \partial_\mu \phi \partial_\nu \phi + \frac{1}{2} g_{\mu\nu} V(\phi), \\ \nabla_\mu [Z(\phi) F^{\mu\nu}] &= 0, \\ \square \phi &= V'(\phi) + \frac{Z'(\phi)}{4} F^2, \end{aligned} \quad (6.46)$$

where we used that on-shell $R = -2V(\phi) + \frac{1}{2}(\partial\phi)^2$. This setup also has an analytic solution which is given by a metric, gauge field and non-trivial scalar ϕ in the form of

$$\begin{aligned} ds^2 &= g_{\mu\nu} dx^\mu dx^\nu = \frac{1}{z^2} \left[-h(z) dt^2 + \frac{1}{h(z)} dz^2 + g(z) (dx^2 + dy^2) \right] \\ A &= \frac{\sqrt{3Qz_h(1+Qz_h)}}{z_h} \frac{(1-z/z_h)}{1+Qz} dt \\ \phi &= \frac{\sqrt{3}}{2} \log(1+Qz) \end{aligned} \quad (6.47)$$

where

$$\begin{aligned} h(z) &= \frac{(1-z/z_h)}{g(z)} \left[1 + (1+3Qz_h) \frac{z}{z_h} + (1+3Qz_h(1+Qz_h)) \left(\frac{z}{z_h} \right)^2 \right], \\ g(z) &= (1+Qz)^{3/2}. \end{aligned} \quad (6.48)$$

The parameter Q encodes the charge of the black hole. The chemical potential is given by $\mu = \sqrt{3Qz_h(1+Qz_h)}/z_h$. The near-horizon form of the potentials in equation (6.44) corresponds to a scaling behavior of $z, -\theta \rightarrow \infty$, also identified by $\gamma, -\delta = 1/\sqrt{3}$ in [102]. The temperature here is given by

$$T_{\text{GR}} = \left| \frac{h'(1)}{4\pi} \right| = \frac{3\sqrt{1+Qz_h}}{4\pi z_h}. \quad (6.49)$$

6.A.3. Lattice Backgrounds

The translational symmetry of the black hole backgrounds is broken by applying a periodic ionic lattice in the boundary field theory through the modulation of the chemical potential [118]. In the gravitational theory, this corresponds to imposing a boundary condition on the gauge field

$$A_t(x, y, z = 0) = \bar{\mu} \left(1 + A_x \cos(G_x x) + A_y \cos(G_y y) \right). \quad (6.50)$$

$A_{x,y}$ parameterize the strength of the lattice, while $G_{x,y}$ are the reciprocal lattice dimensions, respectively. Our computational domain in (x, y) is chosen to always contain a whole number of lattice periods, i.e. $x \sim x + 2\pi n_x/G_x, y \sim y + 2\pi n_y/G_y$ where $n_x, n_y \in \mathbb{Z}$. Throughout this work, we take $G_x = G_y \equiv G$ and $A_x = A_y \equiv A_0/2$ in a 2D lattice and $A_x \equiv A_0, A_y = 0$ for a 1D lattice.

This breaking of translational symmetry influences the solutions dramatically. The additional curvature generated by the periodic lattice means that in principle all the off-diagonal components of the metric as well as all components of the gauge field will become non-trivial.

For RN, the ansatz for the fields is adapted from reference [127]:

$$\begin{aligned} ds^2 &= \frac{1}{z^2} \left(-Q_{tt} f(z) \eta_t^2 + Q_{xx} \eta_x^2 + Q_{yy} \eta_y^2 + \frac{Q_{zz}}{f(z)} \eta_z^2 \right), \\ \eta_t &= dt, \\ \eta_x &= dx + Q_{xy} dy + Q_{xz} dz, \\ \eta_y &= dy + Q_{yz} dz, \\ \eta_z &= dz, \\ A &= \mu(1 - z) A_t dt \end{aligned} \quad (6.51)$$

Our EMD ansatz looks similar and is given by

$$\begin{aligned} ds^2 &= \frac{1}{z^2} \left(-Q_{tt} h(z) \eta_t^2 + g(z) \left(Q_{xx} \eta_x^2 + Q_{yy} \eta_y^2 \right) + \frac{Q_{zz}}{h(z)} \eta_z^2 \right), \\ \eta_t &= dt, \\ \eta_x &= dx + Q_{xy} dy + Q_{xz} dz, \\ \eta_y &= dy + Q_{yz} dz, \\ \eta_z &= dz, \\ A &= \frac{\mu(1 - z)}{1 + Qz} A_t dt, \quad \phi = \frac{3}{2} \log(1 + \varphi Qz). \end{aligned} \quad (6.52)$$

For both types of solutions, we are interested in stationary solutions, and therefore all functions $F = \{Q_{ij}, A_i, \varphi\}$ are functions of (x, y, z) , each periodic in (x, y) with a periodicity of $L_{x,y} = 2\pi n_{x,y}/G_{x,y}$. The equations of motion in equation (6.40) and (6.46) form very

complicated systems of non-linear partial differential equations in three dimensions, which in general cannot be solved analytically. For numerical convenience, the DeTurck trick and another gauge fixing term for the gauge field can be used to turn this set of equations into an elliptic boundary value problem [127–129]. The UV boundary conditions on the radial coordinate come from imposing an asymptotically AdS solution while imposing that the dilaton be a marginal operator with no source, as was highlighted in [99]. The horizon boundary conditions arise from requiring regularity at the horizon, which means that in a series expansion in powers of $(z - 1)$ we can relate each $\partial_z F_i$ to all functions and their tangential derivatives at the horizon,⁸ together with the condition that $Q_{tt}|_{z=1} = Q_{zz}|_{z=1}$.⁹

The boundary value problems are solved using a self-developed software package in C, using the PETSc library [284, 285]. A Newton line-search algorithm employing second- and third order finite difference schemes on rectangular grids is used to find solution to the non-linear problem. The computational grids are either uniformly spaced or have the radial coordinate run over the Chebyshev-Lobatto nodes for increased accuracy near the boundaries of the problem. Typical grid sizes for the simulations run between $N_x \times N_y \times N_z = 40 \times 40 \times 60$ to $80 \times 80 \times 120$. For convergence checks, the vanishing of the norm of the DeTurck vector provides a good measure [129]. Due to the large number of degrees of freedom involved ($O(10^7)$ for the largest lattices) most of the numerical work was done using the ALICE cluster at Leiden University and the Dutch national Cartesius and Snellius supercomputers with the support of SURF Cooperative.

6.A.4. DC Conductivity

The DC conductivity is computed by solving a Stokes flow problem on the black hole horizon [142, 143, 146, 243]. Using a set of time-independent perturbations, one can show that the bulk linear response problem of computing (thermo)electric DC conductivities can be reduced to a linearised version of the Navier-Stokes equations for an auxiliary fluid that lives on a static black hole horizon background. The equations take a similar form for both EMD and RN black holes, and can be written as [142]

$$\begin{aligned} \eta^{(0)} \left(-2\nabla^j \nabla_{(i} v_{j)} + 3v^j \nabla_j \phi^{(0)} \nabla_i \phi^{(0)} \right) - d\chi_{ij}^{(0)} Q^j - F_{ij}^{(0)} J^j = \\ \rho^{(0)} (E_i + \nabla_j w) + T s^{(0)} \left(\zeta_i - \nabla_i \frac{p}{4\pi T} \right) \quad (6.53) \\ \partial_i Q^i = 0, \quad \partial_i J^i = 0. \end{aligned}$$

The superscript (0) indicates that these are background quantities evaluated at the horizon. These are the values we extract from the numerical solutions to the background lattices described above.¹⁰ The Stokes equations (6.53) is then a set of four equations for the four unknown functions v_x, v_y, w, p . The currents Q, J and transport coefficients $\rho^{(0)}, \eta^{(0)}, s^{(0)}, \chi^{(0)}$ can be

⁸If the change of coordinates in footnote 7 is used, this simplifies to $\partial_r F_i = 0 \forall i$, as only even powers of r will appear in the near-horizon expansion. This comes at the cost of accuracy near the horizon.

⁹This ensures a constant temperature across the (corrugated) horizon.

¹⁰For the RN black holes, one should take $\phi = 0, Z(\phi) = 1, V(\phi) = 6$.

written in terms of these four functions, the background horizon quantities and the induced metric on the horizon $h_{ij}^{(0)}$ [142]. E_i, ζ_i source the electric field and thermal gradient, and are taken to be constant over the unit cell. The thermoelectric DC conductivities are then extracted by evaluating

$$\begin{pmatrix} \vec{J} \\ \vec{Q} \end{pmatrix} = \begin{pmatrix} \sigma & \alpha T \\ \bar{\alpha} T & \bar{\kappa} T \end{pmatrix} \begin{pmatrix} \vec{E} \\ \vec{\zeta} \end{pmatrix}, \quad (6.54)$$

where \vec{J}, \vec{Q} are here the spatial averages of the solutions when evaluating equation (6.53). These averaged values do not renormalise when lifted to the boundary to be interpreted in the field theory. As a result, the thermoelectric conductivity matrix defined in equation (6.54) is that of the field theory.

In previous works, e.g. [143], these equations have been used to study simpler systems that do not fully break spatial translational symmetry or break it in a homogeneous way. That simplification allows for a largely analytic treatment of these equations. The systems we are interested in do not permit us such luxuries and therefore we have to solve this coupled linear PDE in two periodic dimensions numerically. For this, we developed a package in Python which can solve coupled (non-)linear partial differential equations for backgrounds as well as perturbations. This package is rather flexible, in that it can make use of both (pseudo)spectral and arbitrary-order finite difference methods to solve the equations. This package will be made available publicly at a later date.

6.B. Appendix B: Semi-local Criticality and an Induced IR Length Scale

Semi-local quantum liquids can be defined by a “self-energy” that is either a power-law in frequency $\Sigma \sim \omega^{2\nu(k)}$ or exponential $\Sigma \sim \exp\left(-\frac{k^z/(z-1)}{\omega^{z-1}}\right)$ with z the dynamical critical exponent. In the limit $z \rightarrow \infty$ the latter reduces to the former [156]. Both ω and k are dimensionless frequencies and momenta in units of the chemical potential μ . As emphasized in [232] the spatial structure of such semi-local quantum liquids is that the spread of local perturbations decays very rapidly and is bounded by an emergent length scale $\xi \propto \mu^{-1}$.

Though the emergence of this semi-local physics is poorly understood from a conventional point of view, its emergence bound is surprisingly clear from a dual holographic perspective. It is a direct consequence of the existence of a maximal distance, $x_{\max} \sim 1/\xi_\mu$ that two light-rays emitted from near the AdS black hole horizon can spread [232]. It implies that a local perturbation in the IR can only originate from/influence a finite spatial region (in the UV variables).

This supplementary section shows how this maximal distance arises. A light-ray parametrized by $X^\mu(\tau)$ follows a null geodesic, i.e.

$$g_{\mu\nu} \dot{X}^\mu \dot{X}^\nu = 0. \quad (6.55)$$

Consider a generic $z = \infty$ metric

$$ds^2 = \left(\frac{r}{R}\right)^{-\frac{2\eta}{d}} \left[-\mu^2 R^2 r^2 dt^2 + \frac{R_2^2}{r^2} dr^2 + \mu^2 R^2 dx_i dx^i \right] \quad (6.56)$$

The parameter $\eta = -\frac{\theta}{z}$ is the remnant of the hyperscaling violation exponent θ in the limit $z \rightarrow \infty$ and $R_2 = R/\sqrt{6}$ is the emergent AdS₂ radius. For a geodesic emanating from the horizon we can use the radial r coordinate as the affine parameter τ , and the physical gauge $X^r = r$. Then solving the geodesic equation $D_\tau \dot{X}^\mu = 0$ subject to the null length constraint, one finds for the motion in the transverse directions

$$X_{i,\pm}(r) = x_i^{(0)} \pm \frac{v_i R_2}{\mu R v} \tan^{-1} \left(\frac{rv}{\sqrt{v_t^2 - r^2 v^2}} \right). \quad (6.57)$$

with $v^2 = \sum_i v_i^2$. Two light-rays starting from the same point $x_i^{(0)}$ one pointing to the left and one to the right therefore arrive at the boundary ($r = \infty$) a distance $2 \frac{v_i}{v} \frac{R_2}{\mu R} \frac{1}{\tan(i)}$ apart.

We are now interested in the intersection of two lightcones $x_{i,+}$ and $x_{i,-}$, which can be found from

$$x_{i,+}(r_0; x^{(0)} = 0) = x_{i,-}(r_0; x^{(0)}) \implies r_0 = \frac{v_t}{v} \sin \left(\frac{\mu R v x_i^{(0)}}{2 v_i R_2} \right). \quad (6.58)$$

After combining (6.57) with (6.58), we find that the maximal allowed distance is

$$x_1^{(\max)} = \frac{R_2}{R\mu} \pi \cos \theta, \quad x_2^{(\max)} = \frac{R_2}{R\mu} \pi \sin \theta. \quad (6.59)$$

where we have chosen the parametrization for the initial velocity components along (x_1, x_2) as $v_1 = v \cos \theta$, $v_2 = v \sin \theta$, where $\theta \in [0, \pi/2]$ is the initial angle, measured with respect to the x_1 -axis.

The relative initial distance between the two geodesics Δs reads

$$\Delta s = \sqrt{x_1^{(\max)2} + x_2^{(\max)2}} = \frac{R_2}{R\mu} \pi, \quad (6.60)$$

which is universal and does not depend on the initial conditions. It coincides with the result presented in [232].

In figure 6.16, we plot the causal structure for two light-rays separated by a certain initial distance. For an initial separation larger than the critical distance, (6.59), both light-rays are not causally connected anymore. To illustrate this, we have chosen as a dialing parameter the external time t . After some computations, we get

$$t(x_i) = -\frac{R_2 v}{\mu R v_t} \cot \left[\frac{\mu R v}{v_i R_2} (x_i - x_i^{(0)}) \right]. \quad (6.61)$$

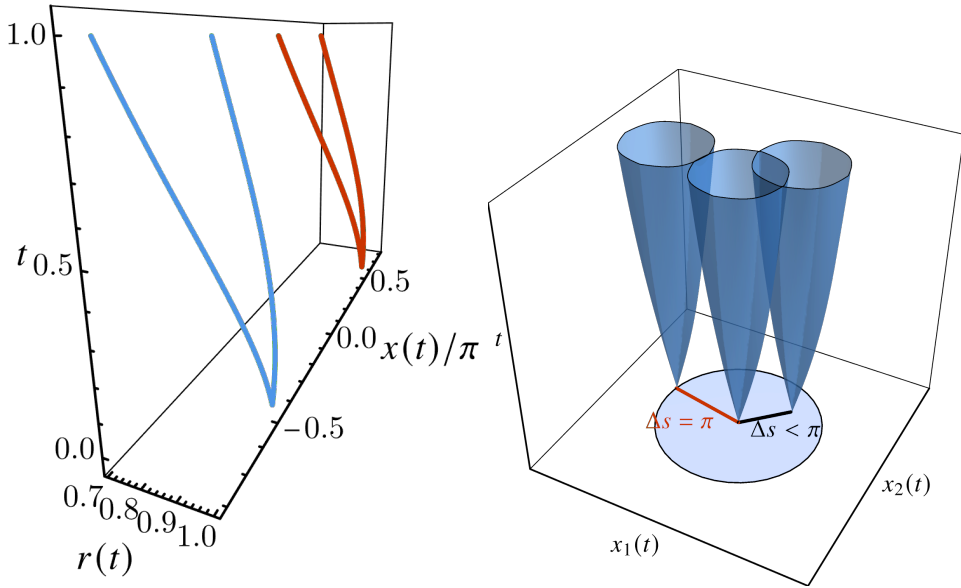


Figure 6.16.: Left figure: Causal structure for two light-rays separated at a relative distance $x_0 = \pi$. The x -axis corresponds to the $x_1(t)$, while the y -axis to the $r(t)$ coordinate. The external time has been taken as the dialing parameter, along the z -axis in the figure. For the present purposes, we have considered no motion along the x_2 direction, and we have also set $R_2 = R = \mu = 1$. Right figure: Causal structures for three light-cones as functions of $(x_1(t), x_2(t))$. The z -axis corresponds to time, for which we have set $t = 1$ as the time that the geodesics reach the boundary. Those geodesics that start at any point within the disk of radius π will be causally connected, while disconnected if otherwise.

which is plotted in the second figure in 6.16. From here, we highlight that any geodesic that starts at an initial relative distance $\Delta s \leq \pi$, will be causally connected, whereas if $\Delta s > \pi$, it will be causally disconnected.

Based on (6.60) and on the fact that the 2-point correlation function $G \sim 1/\xi_m \sim \pi$, we conclude that the maximal correlation distance in Planckian dissipation is related to the existence of this maximal causality distance in geodesic.

6.C. Appendix C: Four-Pole Fitting Formula

The full 4-pole fitting formula that can fit the four poles nearest to the origin in the complex frequency plane is given by the following nine-parameter formula

$$\sigma(\omega) = \sigma_0 + Z \frac{\Omega - i\omega}{(\Omega - i\omega)(\Gamma - i\omega) + \omega_0^2} + \left(\frac{Z_{s,1} + iZ_{s,2}}{\omega - (\omega_{s,1} + i\omega_{s,2})} + \text{time-reversed} \right). \quad (6.62)$$

The weights and positions of the sound poles is constrained by time reversal symmetry, which dictates that

$$\sigma^*(-\omega^*) = \sigma(\omega). \quad (6.63)$$

6.D. Appendix D: Memory Matrix Formalism

The correlation functions of the homogeneous GR and RN fluids are well described by the standard hydrodynamics of relativistic conformal fluids with U(1) charge (see [81]). To compute (6.30), we simply need the correlator $G_{J^t J^t}$ which is given by

$$G_{J^t J^t}(\omega, k) = \frac{\sigma_Q k^2}{D_\rho k^2 - i\omega} - \frac{k^2 \omega_p^2}{\omega^2 + iD_\pi k^2 \omega - c_s^2 k^2}. \quad (6.64)$$

This form quite readily shows how this dynamical response has both a convective part (sound) and a dissipative part. At low frequencies, this correlator can be expanded as

$$G_{J^t J^t}(\omega, k) = \frac{\omega_p^2}{c_s^2} + \frac{\sigma_Q}{D_\rho} + i\omega \left[\frac{\sigma_Q}{D_\rho k^2} + \omega_p^2 \frac{D_\pi}{c_s^4} \right] + \mathcal{O}(\omega^2). \quad (6.65)$$

The leading term is entirely real and will not contribute to the imaginary part. Therefore, we can eventually obtain (6.30) as

$$\Gamma_{\text{mom.rel.}} = \frac{\bar{\mu}^2 A^2}{2(\bar{\epsilon} + \bar{p})D_\rho \alpha_n} + \frac{\bar{\mu}^2 A^2 D_\pi \bar{n}^2}{2c_s^4 (\bar{\epsilon} + \bar{p})^2} G^2 = \Gamma_d + \Gamma_\eta, \quad (6.66)$$

where we recognize the quantities Γ_d, Γ_η introduced in (6.17).

6.E. Appendix E: Scaling of Hydrodynamical Relaxation Rates

Consider an equation of state $P(T, \mu)/\mu^3 = a_0 + a_1(T/\mu)^{\hat{\eta}+1}$ where $\hat{\eta} = (d - \theta)/z$ is the generic effective dimension in the presence of a dynamical critical exponent z and hyperscaling violation exponent θ . This equation of state will be a valid approximation for the low-temperature

regime of the holographic Einstein-Maxwell-Dilaton systems, such as RN and GR. Then, the entropy and charge density one obtains from this pressure are $s/\mu^2 = (\hat{\eta} + 1)a_1(T/\mu)^{\hat{\eta}}$ and $n/\mu^2 = 3a_0 - (\hat{\eta} + 2)a_1(T/\mu)^{\hat{\eta}+1}$. We will now look at the momentum relaxation rate (6.30) for a relativistic charged fluid such that the viscosity saturates the minimal viscosity bound $\eta = s/(4\pi)$ and we will take the EMD T-scaling $\sigma_Q = \hat{\sigma}_Q(T/\mu)^{\hat{\eta}+2}$ [286]. From the integrated first law $\epsilon + P = sT + \mu n$, we find $\epsilon = 2P$ for this choice such that we still have a conformal system and therefore $\zeta = 0$.

The relaxation rate has two contributions, one G -dependent and one G -independent, reminiscent of our result (6.17), which we will by analogy name Γ_η and Γ_d . In the general non-conformal case we have now introduced, these therefore take the form

$$\begin{aligned}\Gamma_\eta/\mu &= A^2(G/\mu)^2 \frac{\pi a_1(\hat{\eta} + 1)}{6a_0} \left(\frac{T}{\mu}\right)^{\hat{\eta}} \frac{\left(1 - \frac{a_1(\hat{\eta}-2)}{3a_0}(T/\mu)^{\hat{\eta}+1}\right)^2}{\left(1 + \frac{a_1}{a_0}(T/\mu)^{\hat{\eta}+1}\right)^3}, \\ \Gamma_d/\mu &= A^2 \frac{a_1^2(\hat{\eta} + 1)^2}{6a_0\hat{\sigma}_Q} \left(\frac{T}{\mu}\right)^{\hat{\eta}} \frac{\left(\hat{\eta} + \frac{a_1(\hat{\eta}-2)}{3a_0}(T/\mu)^{\hat{\eta}+1}\right)^2}{\left(1 + \frac{a_1}{a_0}(T/\mu)^{\hat{\eta}+1}\right)^3}.\end{aligned}\tag{6.67}$$

The leading order of Γ_η can therefore be obtained as

$$\Gamma_\eta/\mu \sim A^2(G/\mu)^2 \frac{\pi a_1(\hat{\eta} + 1)}{6a_0} \left(\frac{T}{\mu}\right)^{\hat{\eta}} \sim A^2(G/\mu)^2 \frac{\pi}{2} \frac{s}{n}.\tag{6.68}$$

This shear drag contribution is therefore entirely determined by the entropy at low temperature. The other contribution, Γ_d , is slightly less straightforward. When $\hat{\eta} > 0$, a similar behavior arises

$$\Gamma_d/\mu \sim A^2 \frac{a_1^2(\hat{\eta} + 1)^2 \hat{\eta}^2}{6a_0\hat{\sigma}_Q} \left(\frac{T}{\mu}\right)^{\hat{\eta}} \sim \frac{A^2}{2n/\mu^2} \left(T \frac{\partial s}{\partial T}\right)^2 \sigma_Q^{-1} \left(\frac{T}{\mu}\right)^2.\tag{6.69}$$

Therefore in this general case, which encompasses the GR case $\hat{\eta} = 1$, Γ_d and Γ_η have the same temperature dependence although Γ_d is more sensible to the susceptibilities like the specific heat $T \frac{\partial s}{\partial T}$ and the hydrodynamic transport coefficient σ_Q . A counterexample of this general rule however arises when $\hat{\eta} = 0$, as it is for the RN black hole for instance, where the leading order of Γ_d vanishes and instead one must expand to second order to have

$$\Gamma_d/\mu \stackrel{\hat{\eta}=0}{\sim} A^2 \frac{a_1^4}{3a_0^3\hat{\sigma}_Q} \left(\frac{T}{\mu}\right)^2.\tag{6.70}$$

Finally, we can explain how this $(T/\mu)^2$ factor in (6.69) arises naturally from the α_n factor introduced in (6.9). To do so, consider the quantity $D_\rho \Gamma_d = A^2 \frac{\bar{\mu}^2}{2(\bar{\epsilon} + \bar{p})\alpha_n}$. We will relax here our assumptions about the equation of state and only assume some Sommerfeld entropy $s = \gamma(\bar{\mu})\bar{T}$

and $n = n_0(\bar{\mu})$ at low temperature. The scaling of $D_\rho \Gamma_d$ is therefore entirely determined by that of α_n^{-1} which can be determined using

$$\begin{aligned} \left(\frac{\partial \bar{n}}{\partial \bar{T}} \right)_{\bar{\mu}} &= \left(\frac{\partial \bar{s}}{\partial \bar{\mu}} \right)_{\bar{T}} \sim \gamma'(\bar{\mu}) \bar{T}, \\ \left(\frac{\partial \bar{n}}{\partial \bar{\mu}} \right)_{\bar{T}} &\sim n'_0(\bar{\mu}), \\ \left(\frac{\partial \bar{\epsilon}}{\partial \bar{T}} \right)_{\bar{\mu}} &= \bar{T} \left(\frac{\partial \bar{s}}{\partial \bar{T}} \right)_{\bar{\mu}} + \bar{\mu} \left(\frac{\partial \bar{n}}{\partial \bar{T}} \right)_{\bar{\mu}} \sim (\gamma(\bar{\mu}) + \bar{\mu} \gamma'(\bar{\mu})) \bar{T}, \\ \left(\frac{\partial \bar{\epsilon}}{\partial \bar{\mu}} \right)_{\bar{T}} &= \bar{T} \left(\frac{\partial \bar{s}}{\partial \bar{\mu}} \right)_{\bar{T}} + \bar{\mu} \left(\frac{\partial \bar{n}}{\partial \bar{\mu}} \right)_{\bar{T}} \sim \bar{\mu} n'_0(\bar{\mu}) + \gamma'(\bar{\mu}) \bar{T}^2. \end{aligned} \quad (6.71)$$

Then, we can plug these relations into Eqs. (6.9) and obtain

$$\alpha_n \sim \frac{\bar{T}^2 (\gamma(\bar{\mu}) + 2\bar{\mu} \gamma'(\bar{\mu})) + \bar{\mu} n'_0(\bar{\mu})}{\bar{T} \left[n'_0(\bar{\mu}) (\gamma(\bar{\mu}) + \bar{\mu} \gamma'(\bar{\mu})) \bar{T} - \gamma'(\bar{\mu}) \bar{T} (\bar{\mu} n'_0(\bar{\mu}) + \gamma'(\bar{\mu}) \bar{T}^2) \right]} \sim \frac{\bar{\mu}}{\bar{T}^2 \gamma(\bar{\mu})}. \quad (6.72)$$

Therefore, given Sommerfeld entropy, we naturally get that $D_\rho \Gamma_d \sim T^2$. Provided then that $D_\rho \sim T$, which is the case for the GR holographic metal, you recover the scaling $\Gamma_d \sim T$.

6.F. Appendix F: Lorentz Oscillator Decoupling

Consider a system of modes coupled to one another in the following way

$$\begin{aligned} \partial_t J_1 + \Gamma_1 J_1 + \gamma_1 J_2 &= E_1, \\ \partial_t J_2 + \Gamma_2 J_2 - \gamma_2 J_1 &= E_2, \end{aligned} \quad (6.73)$$

where $\Gamma_{1,2}$ are relaxation rates for the currents $J_{1,2}$, $E_{1,2}$ are explicit sourcing and $\gamma_{1,2}$ couple the two modes to one another. In matrix notation $\partial_t J_a + M_{ab} J_b = E_a$, this leads to the following evolution matrix

$$M_{\text{LO}} = \begin{pmatrix} \Gamma_1 & \gamma_1 \\ -\gamma_2 & \Gamma_2 \end{pmatrix}. \quad (6.74)$$

We can then solve this dynamic system and obtain, in frequency space,

$$\begin{aligned} J_1(\omega) &= \frac{(\Gamma_2 - i\omega) E_1}{(\Gamma_1 - i\omega)(\Gamma_2 - i\omega) + \gamma_1 \gamma_2}, \\ J_2(\omega) &= \frac{\gamma_2 E_1}{(\Gamma_1 - i\omega)(\Gamma_2 - i\omega) + \gamma_1 \gamma_2}, \end{aligned} \quad (6.75)$$

where we have set $E_2 = 0$ as we are only interested in externally sourcing one of the currents. Critically, we will be interested in a total current J which overlaps with both J_1 and J_2 through

$$J = \sigma_0 E_1 + a J_1 + b J_2 \quad (6.76)$$

where σ_0 is some explicit contribution by the external sourcing. Therefore, the conductivity associated to this current is

$$\sigma = J/E_1 = \sigma_0 + \frac{a(\Gamma_2 - i\omega) + b\gamma_2}{(\Gamma_1 - i\omega)(\Gamma_2 - i\omega) + \gamma_1\gamma_2}. \quad (6.77)$$

This form is very reminiscent of (6.19) with

$$\begin{aligned} Z_{\text{eff}} &= a, \quad \Omega = \Gamma_2 + \frac{b}{a}\gamma_2 \\ \Gamma &= \Gamma_1 - \frac{b}{a}\gamma_2, \quad \omega_0^2 = \gamma_1\gamma_2 - \frac{b}{a}\gamma_2 \left[\Gamma_1 - \Gamma_2 - \frac{b}{a}\gamma_2 \right]. \end{aligned} \quad (6.78)$$

Let us now compare to the matrix M (6.11) describing the dynamical hydrodynamic system in the small lattice expansion. From this system of 4 coupled fields, it is possible to decouple two by taking the large speed of sound limit $c_s \rightarrow \infty^u$ which formally just encodes the assumption that the sound poles live far from the two poles close to origin. While this is a relatively simple limit to illustrate the qualitative behavior of the isolated two pole sector, we must emphasize that this limit will not reproduce quantitatively the mapping (6.20) exactly, and that is because there are higher order effects of the coupling to the sound sector which should be more carefully disentangled. It will be however a helpful illustration of the dynamics of the low frequency sector. The two currents remaining $J_{1,2}$ are then the momentum current density $\delta\pi_x^{(0)}$ and the parity-odd charge density $\delta n^{(S)}$.

The decoupled system then takes the form

$$M = \begin{pmatrix} 0 & AG\bar{\mu}/2 \\ -\frac{AG\bar{\mu}}{(\bar{\epsilon}+\bar{p})\alpha_n} & D_\rho G^2 \end{pmatrix} = \begin{pmatrix} 0 & AG\bar{\mu}/2 \\ -\frac{2D_\rho G\Gamma_d}{A\bar{\mu}} & D_\rho G^2 \end{pmatrix}, \quad (6.79)$$

while the total current of interest is $J = \sigma_Q E_x + \omega_p^2 \delta\pi_x^{(0)} - \frac{\bar{\mu}A}{2} \omega_p^2 D_\rho G \delta n^{(S)}$. Thus, we deduce from this that $Z_{\text{eff}} = \omega_p^2$ while the effective momentum relaxation rates and effective couplings are

$$\begin{aligned} \Omega &= D_\rho G^2 [1 - D_\rho \Gamma_d], \\ \Gamma &= (D_\rho G)^2 \Gamma_d, \\ \omega_0^2 &= D_\rho G^2 \Gamma_d [1 - (D_\rho G)^2 + D_\rho^3 G^2 \Gamma_d]. \end{aligned} \quad (6.80)$$

As expected, there is a discrepancy between Eqs. (6.20) and Eqs. (6.80) which just highlights that the limit $c_s \rightarrow \infty$ should be refined. However, this correctly predicts the leading order in A of every coefficient and gives a very close, qualitative estimate of the corrections at the next order.

^uTo take this limit carefully, one needs to rescale the momentum modes $\delta\epsilon^{(C)}, \delta\pi_x^{(C)}$ by a factor of c_s^2 beforehand.

7. Conclusion

The central theme of this thesis has been the exploration of holographic systems where translational symmetry is explicitly broken in an inhomogeneous manner. In particular, we were interested in systems that have some relevance to condensed matter physics, such as the cuprate strange metals. By solving the Einstein equations for a corrugated black hole in negatively curved space-time, we were able to explore thermodynamical and transport properties of strongly coupled systems where translational symmetry is broken. There have been several results that appear to show similar behaviour to what is observed in physical experiment. But, as we have tried emphasise, the holographic results are not to be interpreted literally, and instead need to be digested carefully in order to properly interpret what holography is telling us.

This is of great importance in chapter 4, which deals with holographic fermions. The spectral function of these fermions can be thought of as an analogue to what is measured in ARPES experiments in the laboratory. We were able show that at weak translational symmetry breaking, the physics of the probe holographic fermions we use is not much different than that of normal fermions undergoing weak potential scattering in a periodic potential. This changes drastically when the lattice strength is raised into the non-perturbative regime. Here instead, we see that the Fermi surface appears to end at a point instead of forming a continuous sheet throughout the $x-y$ plane. The root cause of this turns out to be the proximity of a sheet of poles to a sheet of zeros in the complex frequency-momentum space. This is rather remarkable, as in conventional materials the Fermi surface is typically closed. This phenomenon also appears to be present in ARPES experiments on some cuprates in the pseudogap phase for example.

It is tempting to get excited and take holography as a physical explanation of what is happening in the lab. As we are cautioned, we have to admit that the large- N nature of the dual quantum field theory, the probe status of the fermions and the unidirectional nature of the potential all contribute to our inability to interpret the results of holography in a condensed matter physics setting. The line of zeros that causes the Fermi arc-like phenomenon is also purely holographic in origin, relying on some special range of masses that allow us freedom in the choice of quantization for the bulk fermion. Peering through this is perhaps something interesting; namely, if there is some phenomenon that would cause a line of zeros to come close to the Fermi surface, similar extinction effects might be observed in strongly coupled systems where translational symmetry is strongly broken, e.g. the strange metal. Therefore, purely phenomenologically, holographic fermions could make a useful numerical exploration tool.

Chapter 6 takes a different approach. This chapter shows perhaps the deepest and most high-precision test of the application of holography to condensed matter theory yet. It takes aim simultaneously at the three key mysteries to the cuprate strange metal: the linear-in-temperature resis-

tivity at low temperature, the observed Planckian relaxation rate, and the indifference of the DC conductivity to the good-to-bad-metal transition. The holographic Gubser-Rocha model presents an excellent testing grounds for this. By exploring carefully the thermodynamics and conductivity in the weak lattice regime, we were able to show that hydrodynamical flow can not only be used to reproduce the Drude-like line shape, but also the transition into the ‘bad metal’/Mid-IR peak that is seen in experiments. Intriguingly, even though the peak appears through an effective diffusive-to-propagating crossover of the poles of the Green’s function, we can show that the parameters governing the low-frequency conductivity evolve smoothly and therefore that the DC resistivity cannot be sensitive to this crossover.

The large lattice ‘incoherent metal’ regime shows a completely different story. Here, nothing of our hydrodynamical intuition remains, as momentum conservation is absolutely not present. The slope of the resistivity appears to saturate with increased lattice potential to some value that is of the order of the Planckian scale. The conductivity in this regime can be understood in terms of the thermal and charge diffusivities. The first of these is rather insensitive to the translational symmetry breaking, showing a universal temperature scaling which can be understood from quantum chaos and rapid scrambling in the black hole, but it disappears as the lattice becomes increasingly strong. On the other hand the charge diffusivity saturates, but it evades such a clear understanding as the thermal diffusivity.

Again, we must ask ourselves, what do these black holes actually tell us about the physical experiment, and where does it fall short? First of all, there are also significant discrepancies. The Umklapped sound peak, which is observed to be the peak responsible for a significant fraction of the large-lattice conductivity, is not seen in experiment. Likewise, quantum critical power law tails seen in experiment are not reproduced directly here. However, both of these discrepancies can be understood, and one can reasonably pose conditions under which these phenomena might match.

What remains underneath then is that the real, number one claim that we can draw from these results is that holography is arguing for a fundamentally different kind of physics than that of the Fermi liquid to be governing the strange metal phase. Is it possible that it is hydrodynamics that governs the physics of the strange metal, and is that rooted in the densely many-body entangled nature of the fermions? There are some ways of exploring this in experiment, but with the currently available data it is not possible to make a conclusive decision either way.

It is my hope that the works presented in this thesis have made a sufficiently strong case that the holographic lattice offers a highly intriguing and suggestive view of condensed matter physics. What is more, the interest on the experimental side into holographic claims seems to be increasing. One can think here of recent data suggesting $z \rightarrow \infty$ scaling, and perhaps the soonest revolution will come from the new mesoscopic devices that can potentially be used to detect hydrodynamic behaviour in strongly coupled electronic systems. If the coin falls the right way, the AdS/CFT correspondence will finally be truly cemented as a tool for studying condensed matter physics, in particular in systems where strong correlations and dense entanglement are present. The holographic lattices will then have yet another part to play, and hopefully this work can be of use for future generations of physicists.

List of Publications

- F. Balm, A. Krikun, A. Romero-Bermúdez, K. Schalm, and J. Zaanen, *Isolated Zeros Destroy Fermi Surface in Holographic Models with a Lattice*, J. High Energ. Phys. 2020, 151 (2020).[148]
- J. Zaanen, F. Balm, and A. Beekman, *Crystal Gravity*, SciPost Physics 13, 039 (2022).[287]
- N. Chagnet, F. Balm, and K. Schalm, *Proper Quantization of the Gubser-Rocha Einstein-Maxwell-Dilaton Model Reveals an Exactly Marginal Operator*, preprint arXiv:2209.13951.[99]
- F. Balm, N. Chagnet, S. Arend, J. Aretz, K. Grosvenor, M. Janse, O. Moors, J. Post, V. Ohanesjan, D. Rodriguez-Fernandez, K. Schalm and J. Zaanen. *T-linear resistivity, optical conductivity and Planckian transport for a holographic local quantum critical metal in a periodic potential*, preprint arXiv:2211.05492, prepared for submission to Physical Review X.[213]
- N. Chagnet, F. Balm, K. Schalm and J. Zaanen, *Umklapp Hydrodynamics*, to appear (2023).

Bibliography

- ¹P. Drude, “Zur Elektronentheorie der Metalle”, *Annalen der Physik* **306**, 566–613 (1900).
- ²J. J. Thomson, “Cathode Rays”, *Philosophical Magazine* **44**, 293–316 (1897).
- ³N. W. Ashcroft and N. D. Mermin, *Solid State Physics*, 1st edition (Cengage Learning, New York, Jan. 2, 1976), 848 pp.
- ⁴R. Franz and G. Wiedemann, “Ueber die Wärme-Leitungsfähigkeit der Metalle”, *Annalen der Physik* **165**, 497–531 (1853).
- ⁵M. Peskin and D. Schroeder, *An Introduction to Quantum Field Theory* (Westview Press, 1995).
- ⁶H. Goldstein, C. Poole, and J. Safko, *Classical Mechanics*, 3rd edition (Pearson, San Francisco Munich, June 15, 2001), 664 pp.
- ⁷L. Landau, “The Theory of Phase Transitions”, *Nature* **138**, 840–841 (1936).
- ⁸J. Goldstone, A. Salam, and S. Weinberg, “Broken Symmetries”, *Phys. Rev.* **127**, 965–970 (1962).
- ⁹C. P. Burgess, “Goldstone and Pseudo-Goldstone Bosons in Nuclear, Particle and Condensed Matter Physics”, *Physics Reports* **330**, 193–261 (2000).
- ¹⁰H. K. Onnes, “Further Experiments with Liquid Helium. D. On the Change of the Electrical Resistance of Pure Metals at very low Temperatures, etc. V. The Disappearance of the resistance of mercury”, in *Through Measurement to Knowledge: The Selected Papers of Heike Kamerlingh Onnes 1853–1926*, edited by H. K. Onnes, K. Gavroglu, and Y. Goudaroulis, *Boston Studies in the Philosophy of Science* (Springer Netherlands, Dordrecht, 1991), pp. 264–266.
- ¹¹J. G. Bednorz and K. A. Müller, “Possible high T_c superconductivity in the BaLaCuO system”, *Z. Physik B - Condensed Matter* **64**, 189–193 (1986).
- ¹²H. Maeda, Y. Tanaka, M. Fukutomi, and T. Asano, “A New High-T_c Oxide Superconductor without a Rare Earth Element”, *Jpn. J. Appl. Phys.* **27**, L209 (1988).
- ¹³M. K. Wu, J. R. Ashburn, C. J. Torng, P. H. Hor, R. L. Meng, L. Gao, Z. J. Huang, Y. Q. Wang, and C. W. Chu, “Superconductivity at 93 K in a new mixed-phase Y-Ba-Cu-O compound system at ambient pressure”, *Phys. Rev. Lett.* **58**, 908–910 (1987).
- ¹⁴C. W. Chu, P. H. Hor, R. L. Meng, L. Gao, Z. J. Huang, and a. Y. Q. Wang, “Evidence for superconductivity above 40 K in the La-Ba-Cu-O compound system”, *Phys. Rev. Lett.* **58**, 405–407 (1987).
- ¹⁵L. Gao, Y. Y. Xue, F. Chen, Q. Xiong, R. L. Meng, D. Ramirez, C. W. Chu, J. H. Eggert, and H. K. Mao, “Superconductivity up to 164 K in HgBa₂Ca_{m-1}Cu_mO_{2m+2+δ} (m=1, 2, and 3) under quasihydrostatic pressures”, *Phys. Rev. B* **50**, 4260–4263 (1994).

- ¹⁶J. Bardeen, L. N. Cooper, and J. R. Schrieffer, “Theory of Superconductivity”, *Phys. Rev.* **108**, 1175–1204 (1957).
- ¹⁷M. Tinkham, *Introduction to Superconductivity: Second Edition*, Second edition (Dover Publications, Mineola, NY, June 14, 2004), 480 pp.
- ¹⁸C. Kittel, *Quantum Theory of Solids*, 2nd edition (Wiley, New York, Jan. 16, 1991), 528 pp.
- ¹⁹F. Marsiglio, “Eliashberg theory: A short review”, *Annals of Physics, Eliashberg Theory at 60: Strong-coupling Superconductivity and Beyond* **417**, 168102 (2020).
- ²⁰G. W. Webb, F. Marsiglio, and J. E. Hirsch, “Superconductivity in the elements, alloys and simple compounds”, *Physica C: Superconductivity and its Applications, Superconducting Materials: Conventional, Unconventional and Undetermined* **514**, 17–27 (2015).
- ²¹G. R. Stewart, “Unconventional superconductivity”, *Advances in Physics* **66**, 75–196 (2017).
- ²²D. J. Scalapino, “The case for $d_{x^2 - y^2}$ pairing in the cuprate superconductors”, *Physics Reports* **250**, 329–365 (1995).
- ²³J. M. Bok, J. J. Bae, H.-Y. Choi, C. M. Varma, W. Zhang, J. He, Y. Zhang, L. Yu, and X. J. Zhou, “Quantitative determination of pairing interactions for high-temperature superconductivity in cuprates”, *Science Advances*, 10.1126/sciadv.1501329 (2016).
- ²⁴A. Garg, M. Randeria, and N. Trivedi, “Strong correlations make high-temperature superconductors robust against disorder”, *Nature Phys* **4**, 762–765 (2008).
- ²⁵W. L. McMillan, “Transition Temperature of Strong-Coupled Superconductors”, *Phys. Rev.* **167**, 331–344 (1968).
- ²⁶P. W. Anderson, “The Resonating Valence Bond State in La_2CuO_4 and Superconductivity”, *Science*, 10.1126/science.235.4793.1196 (1987).
- ²⁷X. Zhou, W.-S. Lee, M. Imada, N. Trivedi, P. Phillips, H.-Y. Kee, P. Törmä, and M. Eremets, “High-temperature superconductivity”, *Nat Rev Phys* **3**, 462–465 (2021).
- ²⁸C. W. Chu, L. Z. Deng, and B. Lv, “Hole-doped cuprate high temperature superconductors”, *Physica C: Superconductivity and its Applications, Superconducting Materials: Conventional, Unconventional and Undetermined* **514**, 290–313 (2015).
- ²⁹M. Imada, A. Fujimori, and Y. Tokura, “Metal-insulator transitions”, *Rev. Mod. Phys.* **70**, 1039–1263 (1998).
- ³⁰R. L. Greene, P. R. Mandal, N. R. Poniatowski, and T. Sarkar, “The Strange Metal State of the Electron-Doped Cuprates”, *Annu. Rev. Condens. Matter Phys.* **11**, 213–229 (2020).
- ³¹J. Friedel, “The high- T_c superconductors: a conservative view”, *J. Phys.: Condens. Matter* **1**, 7757–7794 (1989).
- ³²T. M. Rice, K.-Y. Yang, and F. C. Zhang, “A phenomenological theory of the anomalous pseudogap phase in underdoped cuprates”, *Rep. Prog. Phys.* **75**, 016502 (2011).
- ³³W. W. Warren, R. E. Walstedt, G. F. Brennert, R. J. Cava, R. Tycko, R. F. Bell, and G. Dabbagh, “Cu spin dynamics and superconducting precursor effects in planes above T_c in $\text{YBa}_2\text{Cu}_3\text{O}_{6.7}$ ”, *Phys. Rev. Lett.* **62**, 1193–1196 (1989).

- ³⁴T. Wu, H. Mayaffre, S. Krämer, M. Horvatić, C. Berthier, W. N. Hardy, R. Liang, D. A. Bonn, and M.-H. Julien, “Magnetic-field-induced charge-stripe order in the high-temperature superconductor $\text{YBa}_2\text{Cu}_3\text{O}_y$ ”, *Nature* **477**, 191–194 (2011).
- ³⁵N. Barišić, M. K. Chan, Y. Li, G. Yu, X. Zhao, M. Dressel, A. Smontara, and M. Greven, “Universal sheet resistance and revised phase diagram of the cuprate high-temperature superconductors”, *PNAS* **110**, 12235–12240 (2013).
- ³⁶N. E. Hussey, H. Gordon-Moys, J. Kokalj, and R. H. McKenzie, “Generic strange-metal behaviour of overdoped cuprates”, *J. Phys.: Conf. Ser.* **449**, 012004 (2013).
- ³⁷N. E. Hussey, “Phenomenology of the normal state in-plane transport properties of high-Tccuprates”, *J. Phys.: Condens. Matter* **20**, 123201 (2008).
- ³⁸A. Legros, S. Benhabib, W. Tabis, F. Laliberté, M. Dion, M. Lizaire, B. Vignolle, D. Vignolles, H. Raffy, Z. Z. Li, P. Auban-Senzier, N. Doiron-Leyraud, P. Fournier, D. Colson, L. Taillefer, and C. Proust, “Universal T-linear resistivity and Planckian dissipation in overdoped cuprates”, *Nature Phys* **15**, 142–147 (2019).
- ³⁹S. Martin, A. T. Fiory, R. M. Fleming, L. F. Schneemeyer, and J. V. Waszczak, “Normal-state transport properties of $\text{Bi}_{2+x}\text{Sr}_{2-y}\text{CuO}_{6+\delta}$ crystals”, *Phys. Rev. B* **41**, 846–849 (1990).
- ⁴⁰C. K. Subramaniam, C. V. N. Rao, A. B. Kaiser, H. J. Trodahl, A. Mawdsley, N. E. Flower, and J. L. Tallon, “Thermopower and resistivity of La-doped thallium 1201 and bismuth 2204 superconductors”, *Supercond. Sci. Technol.* **7**, 30–35 (1994).
- ⁴¹E. M. Lifshitz and L. Pitaevskii, *Statistical Physics: Theory of the Condensed State (Course of Theoretical Physics Vol. 9)*, Revised Edition, Vol. 9 (Butterworth-Heinemann, Jan. 15, 1980).
- ⁴²N. E. Hussey, K. Takenaka, and H. Takagi, “Universality of the Mott–Ioffe–Regel limit in metals”, *Philosophical Magazine* **84**, 2847–2864 (2004).
- ⁴³B. Keimer, S. A. Kivelson, M. R. Norman, S. Uchida, and J. Zaanen, “From quantum matter to high-temperature superconductivity in copper oxides”, *Nature* **518**, 179–186 (2015).
- ⁴⁴T. R. Chien, Z. Z. Wang, and N. P. Ong, “Effect of zn impurities on the normal-state hall angle in single-crystal $\text{YBa}_2\text{Cu}_{3-x}\text{Zn}_x\text{O}_{7-\delta}$ ”, *Phys. Rev. Lett.* **67**, 2088–2091 (1991).
- ⁴⁵U. Chatterjee, D. Ai, J. Zhao, S. Rosenkranz, A. Kaminski, H. Raffy, Z. Li, K. Kadowaki, M. Randeria, M. R. Norman, and J. C. Campuzano, “Electronic phase diagram of high-temperature copper oxide superconductors”, *Proceedings of the National Academy of Sciences* **108**, 9346–9349 (2011).
- ⁴⁶L. Chen, D. T. Lowder, E. Bakali, A. M. Andrews, W. Schrenk, M. Waas, R. Svagera, G. Eguchi, L. Prochaska, Q. Si, S. Paschen, and D. Natelson, *Shot noise indicates the lack of quasiparticles in a strange metal*, (June 1, 2022) <http://arxiv.org/abs/2206.00673> (visited on 11/06/2022), preprint.
- ⁴⁷I. M. Vishik, W. S. Lee, R.-H. He, M. Hashimoto, Z. Hussain, T. P. Devereaux, and Z.-X. Shen, “ARPES studies of cuprate Fermiology: superconductivity, pseudogap and quasiparticle dynamics”, *New J. Phys.* **12**, 105008 (2010).
- ⁴⁸S. Sachdev, *Quantum Phase Transitions*, 2nd edition (Cambridge University Press, Cambridge ; New York, May 9, 2011), 516 pp.

- ⁴⁹S.-D. Chen, M. Hashimoto, Y. He, D. Song, K.-J. Xu, J.-F. He, T. P. Devereaux, H. Eisaki, D.-H. Lu, J. Zaanen, and Z.-X. Shen, “Incoherent strange metal sharply bounded by a critical doping in Bi₂Te₂”, *Science* **366**, 1099–1102 (2019).
- ⁵⁰M. Mitrano, A. A. Husain, S. Vig, A. Kogar, M. S. Rak, S. I. Rubeck, J. Schmalian, B. Uchoa, J. Schneeloch, R. Zhong, G. D. Gu, and P. Abbamonte, “Anomalous density fluctuations in a strange metal”, *PNAS* **115**, 5392–5396 (2018).
- ⁵¹J. Zaanen, “Why the temperature is high”, *Nature* **430**, 512–513 (2004).
- ⁵²J. Zaanen, “Planckian dissipation, minimal viscosity and the transport in cuprate strange metals”, *SciPost Phys.* **6**, 061 (2019).
- ⁵³D. J. Scalapino, “Numerical Studies of the 2D Hubbard Model”, Oct. 25, 2006.
- ⁵⁴U. Schollwoeck, “The density-matrix renormalization group”, *Rev. Mod. Phys.* **77**, 259–315 (2005).
- ⁵⁵R. Orús, “Tensor networks for complex quantum systems”, *Nat Rev Phys* **1**, 538–550 (2019).
- ⁵⁶Y.-F. Jiang, J. Zaanen, T. P. Devereaux, and H.-C. Jiang, “Ground state phase diagram of the doped Hubbard model on the four-leg cylinder”, *Phys. Rev. Research* **2**, 033073 (2020).
- ⁵⁷L. Susskind, “The World as a Hologram”, *Journal of Mathematical Physics* **36**, 6377–6396 (1995).
- ⁵⁸G. ’t Hooft, “Dimensional Reduction in Quantum Gravity”, Mar. 20, 2009.
- ⁵⁹J. M. Maldacena, “The Large N Limit of Superconformal Field Theories and Supergravity”, *International Journal of Theoretical Physics* **38**, 1113–1133 (1999).
- ⁶⁰O. Aharony, S. S. Gubser, J. Maldacena, H. Ooguri, and Y. Oz, “Large N Field Theories, String Theory and Gravity”, *Physics Reports* **323**, 183–386 (2000).
- ⁶¹J. Zaanen, Y. Liu, Y.-W. Sun, and K. Schalm, *Holographic Duality in Condensed Matter Physics* (Cambridge University Press, Cambridge, 2015).
- ⁶²M. Ammon and J. Erdmenger, *Gauge/Gravity Duality: Foundations and Applications* (Cambridge University Press, Cambridge, 2015).
- ⁶³H. Nastase, *String Theory Methods for Condensed Matter Physics* (Cambridge University Press, Cambridge, 2017).
- ⁶⁴Blumenhagen, *Introduction to Conformal Field Theory*, 2009th edition (Springer, Dordrecht ; New York, July 31, 2009), 280 pp.
- ⁶⁵M. Henningson and K. Skenderis, “The Holographic Weyl anomaly”, *J. High Energy Phys.* **1998**, 023–023 (1998).
- ⁶⁶O. Aharony, O. Bergman, D. L. Jafferis, and J. Maldacena, “N=6 superconformal Chern-Simons-matter theories, M2-branes and their gravity duals”, *J. High Energy Phys.* **2008**, 091–091 (2008).
- ⁶⁷S. S. Gubser, I. R. Klebanov, and A. M. Polyakov, “Gauge Theory Correlators from Non-Critical String Theory”, *Physics Letters B* **428**, 105–114 (1998).

- ⁶⁸K. G. Wilson, “The renormalization group: Critical phenomena and the Kondo problem”, *Reviews of Modern Physics* **47**, 773–840 (1975).
- ⁶⁹M. Gell-Mann and F. E. Low, “Quantum Electrodynamics at Small Distances”, *Physical Review* **95**, 1300–1312 (1954).
- ⁷⁰G. Evenbly and G. Vidal, *Entanglement renormalization in free bosonic systems: real-space versus momentum-space renormalization group transforms*, (Mar. 5, 2010) <http://arxiv.org/abs/0801.2449> (visited on 10/30/2022), preprint.
- ⁷¹S. A. Hartnoll, A. Lucas, and S. Sachdev, *Holographic quantum matter*, (Mar. 20, 2018) <http://arxiv.org/abs/1612.07324> (visited on 10/26/2022), preprint.
- ⁷²M. Baggioli, “A Practical Mini-Course on Applied Holography”, 2019.
- ⁷³G. B. Arfken and H. J. Weber, *Mathematical Methods for Physicists, 6th Edition*, 6th edition (Academic Press, Boston, July 5, 2005), 1200 pp.
- ⁷⁴I. R. Klebanov and E. Witten, “AdS/CFT Correspondence and Symmetry Breaking”, June 3, 1999.
- ⁷⁵M. Bianchi, D. Z. Freedman, and K. Skenderis, “Holographic renormalization”, *Nuclear Physics B* **631**, 159–194 (2002).
- ⁷⁶J. D. Bekenstein, “Black holes and the second law”, *Lett. Nuovo Cimento* **4**, 737–740 (1972).
- ⁷⁷S. W. Hawking, “Particle creation by black holes”, *Communications in Mathematical Physics* **43**, 199–220 (1975).
- ⁷⁸C. Misner, K. Thorne, and J. A. Wheeler, *Gravitation* (2017).
- ⁷⁹T. Andrade, A. Krikun, K. Schalm, and J. Zaanen, “Doping the holographic Mott insulator”, *Nature Physics* **14**, 1049 (2018).
- ⁸⁰G. T. Horowitz and V. E. Hubeny, “Quasinormal Modes of AdS Black Holes and the Approach to Thermal Equilibrium”, *Phys. Rev. D* **62**, 024027 (2000).
- ⁸¹P. Kovtun, “Lectures on hydrodynamic fluctuations in relativistic theories”, *J. Phys. A: Math. Theor.* **45**, 473001 (2012).
- ⁸²J. de Boer, J. Hartong, E. Have, N. A. Obers, and W. Sybesma, “Non-Boost Invariant Fluid Dynamics”, *SciPost Phys.* **9**, 018 (2020).
- ⁸³M. Rangamani, “Gravity & Hydrodynamics: Lectures on the fluid-gravity correspondence”, *Class. Quantum Grav.* **26**, 224003 (2009).
- ⁸⁴V. E. Hubeny, S. Minwalla, and M. Rangamani, “The fluid/gravity correspondence”, July 28, 2011.
- ⁸⁵P. Kovtun, D. T. Son, and A. O. Starinets, “Viscosity in Strongly Interacting Quantum Field Theories from Black Hole Physics”, *Phys. Rev. Lett.* **94**, 111601 (2005).
- ⁸⁶P. Kovtun, D. T. Son, and A. O. Starinets, “Holography and hydrodynamics: diffusion on stretched horizons”, *J. High Energy Phys.* **2003**, 064–064 (2003).
- ⁸⁷E. V. Shuryak, “What RHIC Experiments and Theory tell us about Properties of Quark-Gluon Plasma?”, *Nuclear Physics A* **750**, 64–83 (2005).

- ⁸⁸A. Altland and B. D. Simons, *Condensed Matter Field Theory*, 2nd ed. (Cambridge University Press, Cambridge, 2010).
- ⁸⁹K. S. Novoselov, A. K. Geim, S. V. Morozov, D. Jiang, Y. Zhang, S. V. Dubonos, I. V. Grigorieva, and A. A. Firsov, “Electric Field Effect in Atomically Thin Carbon Films”, *Science*, **10** . 1126/ science.1102896 (2004).
- ⁹⁰C. P. Herzog, P. Kovtun, S. Sachdev, and D. T. Son, “Quantum critical transport, duality, and M-theory”, *Phys. Rev. D* **75**, 085020 (2007).
- ⁹¹J. P. Gauntlett and O. Varela, “Consistent Kaluza-Klein Reductions for General Supersymmetric AdS Solutions”, *Phys. Rev. D* **76**, 126007 (2007).
- ⁹²S. M. Carroll, *Spacetime and Geometry: An Introduction to General Relativity* (Addison-Wesley, San Francisco, Sept. 1, 2003), 750 pp.
- ⁹³T. Faulkner, H. Liu, J. McGreevy, and D. Vegh, “Emergent quantum criticality, Fermi surfaces, and AdS₂”, *Phys. Rev. D* **83**, 125002 (2011).
- ⁹⁴I. Papadimitriou and K. Skenderis, “Thermodynamics of Asymptotically Locally AdS Space-times”, *J. High Energy Phys.* **2005**, 004–004 (2005).
- ⁹⁵A. Rex and C. B. P. Finn, *Finn’s Thermal Physics*, 3rd edition (CRC Press, Boca Raton, FL, Apr. 7, 2017), 386 pp.
- ⁹⁶A. Donos and J. P. Gauntlett, “On the thermodynamics of periodic AdS black branes”, *J. High Energ. Phys.* **2013**, 38 (2013).
- ⁹⁷C. Y. Chang, P. M. Hui, and K. W. Yu, “Zero-temperature entropy of fully frustrated generalized Sierpiński gaskets”, *Physics Letters A* **172**, 219–223 (1993).
- ⁹⁸S. S. Gubser and F. D. Rocha, “Peculiar properties of a charged dilatonic black hole in AdS₅”, *Phys. Rev. D* **81**, 046001 (2010).
- ⁹⁹N. Chagnet, F. Balm, and K. Schalm, *Proper quantization of the Gubser-Rocha Einstein-Maxwell-Dilaton model reveals an exactly marginal operator*, (Sept. 30, 2022) [http : //arxiv.org/abs/2209.13951](http://arxiv.org/abs/2209.13951) (visited on 10/25/2022), preprint.
- ¹⁰⁰V. Balasubramanian and P. Kraus, “A Stress Tensor for Anti-de Sitter Gravity”, *Communications in Mathematical Physics* **208**, 413–428 (1999).
- ¹⁰¹E. Kiritsis and J. Ren, “On holographic insulators and supersolids”, *J. High Energ. Phys.* **2015**, 168 (2015).
- ¹⁰²C. Charmousis, B. Goutéraux, B. Soo Kim, E. Kiritsis, and R. Meyer, “Effective holographic theories for low-temperature condensed matter systems”, *J. High Energ. Phys.* **2010**, 151 (2010).
- ¹⁰³D. S. Fisher, “Scaling and critical slowing down in random-field Ising systems”, *Phys. Rev. Lett.* **56**, 416–419 (1986).
- ¹⁰⁴X. Dong, S. Harrison, S. Kachru, G. Torroba, and H. Wang, “Aspects of holography for theories with hyperscaling violation”, May 28, 2012.
- ¹⁰⁵B. S. Kim, “Hyperscaling violation : a unified frame for effective holographic theories”, *J. High Energ. Phys.* **2012**, 61 (2012).

- ¹⁰⁶R. A. Davison, K. Schalm, and J. Zaanen, “Holographic duality and the resistivity of strange metals”, *Phys. Rev. B* **89**, 245116 (2014).
- ¹⁰⁷Y. Ling, C. Niu, J.-P. Wu, and Z.-Y. Xian, “Holographic Lattice in Einstein-Maxwell-Dilaton Gravity”, *J. High Energ. Phys.* **2013**, 6 (2013).
- ¹⁰⁸B. S. Kim, “Holographic renormalization of Einstein-Maxwell-Dilaton theories”, *J. High Energ. Phys.* **2016**, 44 (2016).
- ¹⁰⁹E. Mauri and H. T. C. Stoof, *Coulomb drag between two strange metals*, (July 21, 2022) <http://arxiv.org/abs/2103.05652> (visited on 10/29/2022), preprint.
- ¹¹⁰M. Blake and D. Tong, “Universal resistivity from holographic massive gravity”, *Phys. Rev. D* **88**, 106004 (2013).
- ¹¹¹M. Blake, D. Tong, and D. Vegh, “Holographic Lattices Give the Graviton a Mass”, *Phys. Rev. Lett.* **112**, 071602 (2014).
- ¹¹²R. A. Davison, “Momentum relaxation in holographic massive gravity”, *Phys. Rev. D* **88**, 086003 (2013).
- ¹¹³I. U. of Crystallography, *International Tables for Crystallography* ().
- ¹¹⁴A. Donos and J. P. Gauntlett, “Holographic Q-lattices”, *J. High Energ. Phys.* **2014**, 40 (2014).
- ¹¹⁵A. Bagrov, N. Kaplis, A. Krikun, K. Schalm, and J. Zaanen, “Holographic fermions at strong translational symmetry breaking: a Bianchi-VII case study”, *J. High Energ. Phys.* **2016**, 57 (2016).
- ¹¹⁶Y. Ling, P. Liu, C. Niu, J.-P. Wu, and Z.-Y. Xian, “Holographic Superconductor on Q-lattice”, *J. High Energ. Phys.* **2015**, 59 (2015).
- ¹¹⁷M. Baggioli, K.-Y. Kim, L. Li, and W.-J. Li, “Holographic Axion Model: a simple gravitational tool for quantum matter”, *Sci. China Phys. Mech. Astron.* **64**, 270001 (2021).
- ¹¹⁸G. T. Horowitz, J. E. Santos, and D. Tong, “Optical conductivity with holographic lattices”, *J. High Energ. Phys.* **2012**, 168 (2012).
- ¹¹⁹B. Withers, “Holographic checkerboards”, *J. High Energ. Phys.* **2014**, 102 (2014).
- ¹²⁰G. T. Horowitz, J. E. Santos, and D. Tong, “Further evidence for lattice-induced scaling”, *J. High Energ. Phys.* **2012**, 102 (2012).
- ¹²¹A. Donos and J. P. Gauntlett, “Holographic striped phases”, *J. High Energ. Phys.* **2011**, 140 (2011).
- ¹²²A. Donos, J. P. Gauntlett, J. Sonner, and B. Withers, “Competing orders in M-theory: superfluids, stripes and metamagnetism”, *J. High Energ. Phys.* **2013**, 108 (2013).
- ¹²³A. Donos and J. P. Gauntlett, “Holographic charge density waves”, *Phys. Rev. D* **87**, 126008 (2013).
- ¹²⁴S. A. Hartnoll and D. M. Hofman, “Locally critical umklapp scattering and holography”, *Phys. Rev. Lett.* **108**, 241601 (2012).
- ¹²⁵D. Das, “TIME DEPENDENT HOLOGRAPHY”, *Theses and Dissertations–Physics and Astronomy* (2014).

- ¹²⁶A. Donos, “Striped phases from holography”, J. High Energ. Phys. **2013**, 59 (2013).
- ¹²⁷A. Donos and J. P. Gauntlett, “Minimally packed phases in holography”, J. High Energ. Phys. **2016**, 148 (2016).
- ¹²⁸M. Headrick, S. Kitchen, and T. Wiseman, “A new approach to static numerical relativity, and its application to Kaluza-Klein black holes”, Class. Quantum Grav. **27**, 035002 (2010).
- ¹²⁹A. Adam, S. Kitchen, and T. Wiseman, “A numerical approach to finding general stationary vacuum black holes”, Class. Quantum Grav. **29**, 165002 (2012).
- ¹³⁰D. M. DeTurck, “Deforming metrics in the direction of their Ricci tensors”, Journal of Differential Geometry **18**, 157–162 (1983).
- ¹³¹C. P. Herzog, *Holographic Superconductors*, <http://insti.physics.sunysb.edu/~cphertzog/superconductor/index.html>.
- ¹³²S. A. Hartnoll, “Lectures on holographic methods for condensed matter physics”, Class. Quantum Grav. **26**, 224002 (2009).
- ¹³³H. Kramers, “La diffusion de la lumière par les atomes”, in, Vol. 2 (1927), pp. 545–557.
- ¹³⁴R. d. L. Kronig, “On the Theory of Dispersion of X-Rays”, J. Opt. Soc. Am., JOSA **12**, 547–557 (1926).
- ¹³⁵M. Edalati, J. I. Jottar, and R. G. Leigh, “Shear Modes, Criticality and Extremal Black Holes”, J. High Energ. Phys. **2010**, 75 (2010).
- ¹³⁶M. Rangamani, M. Rozali, and D. Smyth, “Spatial modulation and conductivities in effective holographic theories”, J. High Energ. Phys. **2015**, 24 (2015).
- ¹³⁷H. Kodama and A. Ishibashi, “Master equations for perturbations of generalised static black holes with charge in higher dimensions”, Progress of Theoretical Physics **111**, 29–73 (2004).
- ¹³⁸D. K. Brattan and S. A. Gentle, “Shear channel correlators from hot charged black holes”, J. High Energ. Phys. **2011**, 82 (2011).
- ¹³⁹R. A. Davison and B. Goutéraux, “Dissecting holographic conductivities”, J. High Energ. Phys. **2015**, 90 (2015).
- ¹⁴⁰A. Donos and J. P. Gauntlett, “The thermoelectric properties of inhomogeneous holographic lattices”, J. High Energ. Phys. **2015**, 35 (2015).
- ¹⁴¹A. Donos, J. P. Gauntlett, T. Griffin, and L. Melgar, “DC Conductivity and Higher Derivative Gravity”, Class. Quantum Grav. **34**, 135015 (2017).
- ¹⁴²A. Donos, J. P. Gauntlett, T. Griffin, and L. Melgar, “DC conductivity of magnetised holographic matter”, J. High Energ. Phys. **2016**, 113 (2016).
- ¹⁴³A. Donos, J. P. Gauntlett, T. Griffin, N. Lohitsiri, and L. Melgar, “Holographic DC conductivity and Onsager relations”, J. High Energ. Phys. **2017**, 6 (2017).
- ¹⁴⁴A. Donos, J. P. Gauntlett, T. Griffin, and V. Zogas, “Incoherent transport for phases that spontaneously break translations”, J. High Energ. Phys. **2018**, 53 (2018).
- ¹⁴⁵A. Donos and J. P. Gauntlett, “Navier-Stokes equations on black hole horizons and DC thermoelectric conductivity”, Phys. Rev. D **92**, 121901 (2015).

- ¹⁴⁶E. Banks, A. Donos, and J. P. Gauntlett, “Thermoelectric DC conductivities and Stokes flows on black hole horizons”, *J. High Energ. Phys.* **2015**, 103 (2015).
- ¹⁴⁷A. Krikun, *Numerical Solution of the Boundary Value Problems for Partial Differential Equations. Crash course for holographer*, (Jan. 4, 2018) <http://arxiv.org/abs/1801.01483> (visited on 02/13/2022), preprint.
- ¹⁴⁸F. Balm, A. Krikun, A. Romero-Bermúdez, K. Schalm, and J. Zaanen, “Isolated zeros destroy Fermi surface in holographic models with a lattice”, *J. High Energ. Phys.* **2020**, 151 (2020).
- ¹⁴⁹F. Balm, *FlorisBalm/holographic-lattice-codes*, Feb. 13, 2022.
- ¹⁵⁰F. Balm, *Holographic Lattice Codes*, Apr. 1, 2022.
- ¹⁵¹A. G. Loeser, Z.-X. Shen, D. S. Dessau, D. S. Marshall, C. H. Park, P. Fournier, and A. Kapitulnik, “Excitation Gap in the Normal State of Underdoped $\text{Bi}_2\text{Sr}_2\text{CaCu}_2\text{O}_{8+d}$ ”, *Science*, 10.1126/science.273.5273.325 (1996).
- ¹⁵²K. M. Shen, F. Ronning, D. H. Lu, F. Baumberger, N. J. C. Ingle, W. S. Lee, W. Meevasana, Y. Kohsaka, M. Azuma, M. Takano, H. Takagi, and Z.-X. Shen, “Nodal Quasiparticles and Antinodal Charge Ordering in $\text{Ca}_{2-x}\text{Na}_x\text{CuO}_2\text{Cl}_2$ ”, *Science*, 10.1126/science.1103627 (2005).
- ¹⁵³X. J. Zhou, T. Yoshida, D.-H. Lee, W. L. Yang, V. Brouet, F. Zhou, W. X. Ti, J. W. Xiong, Z. X. Zhao, T. Sasagawa, T. Kakeshita, H. Eisaki, S. Uchida, A. Fujimori, Z. Hussain, and Z.-X. Shen, “Dichotomy between nodal and antinodal quasiparticles in underdoped $(\text{La}_{2-x}\text{Sr}_x)\text{CuO}_4$ superconductors”, *Phys. Rev. Lett.* **92**, 187001 (2004).
- ¹⁵⁴T. Yoshida, X. J. Zhou, K. Tanaka, W. L. Yang, Z. Hussain, Z.-X. Shen, A. Fujimori, S. Sahrakorpi, M. Lindroos, R. S. Markiewicz, A. Bansil, S. Komiyama, Y. Ando, H. Eisaki, T. Kakeshita, and S. Uchida, “Systematic doping evolution of the underlying fermi surface of $\text{La}_{2-x}\text{Sr}_x\text{CuO}_4$ ”, *Phys. Rev. B* **74**, 224510 (2006).
- ¹⁵⁵M. Čubrović, J. Zaanen, and K. Schalm, “String Theory, Quantum Phase Transitions, and the Emergent Fermi Liquid”, *Science* (2009).
- ¹⁵⁶T. Faulkner, N. Iqbal, H. Liu, J. McGreevy, and D. Vegh, “Holographic non-Fermi liquid fixed points”, *Phil. Trans. R. Soc. A.* **369**, 1640–1669 (2011).
- ¹⁵⁷Y. Liu, K. Schalm, Y.-W. Sun, and J. Zaanen, “Lattice potentials and fermions in holographic non Fermi-liquids: hybridizing local quantum criticality”, *J. High Energ. Phys.* **2012**, 36 (2012).
- ¹⁵⁸S. Cremonini, L. Li, and J. Ren, “Holographic fermions in striped phases”, *J. High Energ. Phys.* **2018**, 80 (2018).
- ¹⁵⁹Y. Ling, C. Niu, J.-P. Wu, Z.-Y. Xian, and H. Zhang, “Holographic fermionic liquid with lattices”, *J. High Energ. Phys.* **2013**, 45 (2013).
- ¹⁶⁰S. Cremonini, L. Li, and J. Ren, “Spectral weight suppression and Fermi arc-like features with strong holographic lattices”, *J. High Energ. Phys.* **2019**, 14 (2019).
- ¹⁶¹O. DeWolfe, O. Henriksson, and C. Rosen, “Fermi surface behavior in the ABJM M2-brane theory”, *Phys. Rev. D* **91**, 126017 (2015).

- ¹⁶²S. Grozdanov, K. Schalm, and V. Scopelliti, “Black Hole Scrambling from Hydrodynamics”, *Phys. Rev. Lett.* **120**, 231601 (2018).
- ¹⁶³M. Blake, H. Lee, and H. Liu, “A quantum hydrodynamical description for scrambling and many-body chaos”, *J. High Energ. Phys.* **2018**, 127 (2018).
- ¹⁶⁴M. Blake, R. A. Davison, S. Grozdanov, and H. Liu, “Many-body chaos and energy dynamics in holography”, *J. High Energ. Phys.* **2018**, 35 (2018).
- ¹⁶⁵S. Grozdanov, “On the connection between hydrodynamics and quantum chaos in holographic theories with stringy corrections”, *J. High Energ. Phys.* **2019**, 48 (2019).
- ¹⁶⁶M. Blake, R. A. Davison, and D. Vegh, “Horizon constraints on holographic Green’s functions”, Apr. 29, 2019.
- ¹⁶⁷N. Ceplak, K. Ramdial, and D. Vegh, “Fermionic pole-skipping in holography”, *J. High Energ. Phys.* **2020**, 203 (2020).
- ¹⁶⁸M. Edalati, R. G. Leigh, K. W. Lo, and P. W. Phillips, “Dynamical gap and cupratelike physics from holography”, *Phys. Rev. D* **83**, 046012 (2011).
- ¹⁶⁹G. Vanacore and P. W. Phillips, “Minding the gap in holographic models of interacting fermions”, *Physical Review D* **90**, 044022 (2014).
- ¹⁷⁰J. Alsup, E. Papantonopoulos, G. Siopsis, and K. Yeter, “Duality between zeroes and poles in holographic systems with massless fermions and a dipole coupling”, *Phys. Rev. D* **90**, 126013 (2014).
- ¹⁷¹Y. Seo, G. Song, Y.-H. Qi, and S.-J. Sin, “Mott transition with holographic spectral function”, *J. High Energ. Phys.* **2018**, 77 (2018).
- ¹⁷²S. Chakrabarti, D. Maity, and W. Wahlang, “Probing the holographic Fermi arc with scalar field: numerical and analytical study”, *J. High Energ. Phys.* **2019**, 37 (2019).
- ¹⁷³N. Gnedilov, A. Krikun, K. Schalm, and J. Zaanen, “Isolated zeros in the spectral function as signature of a quantum continuum”, *Phys. Rev. B* **99**, 165149 (2019).
- ¹⁷⁴P. Phillips, *Mottness*, (Feb. 14, 2007) <http://arxiv.org/abs/cond-mat/0702348> (visited on 10/26/2022), preprint.
- ¹⁷⁵T. D. Stanescu, P. Phillips, and T.-P. Choy, “Theory of the Luttinger surface in doped Mott insulators”, *Phys. Rev. B* **75**, 104503 (2007).
- ¹⁷⁶M. Imada, Y. Yamaji, S. Sakai, and Y. Motome, “Theory of pseudogap and superconductivity in doped Mott insulators”, *Ann. Phys.* **523**, 629–637 (2011).
- ¹⁷⁷K. B. Dave, P. W. Phillips, and C. L. Kane, “Absence of Luttinger’s Theorem due to Zeros in the Single-Particle Green Function”, 10.1103/PhysRevLett.110.090403 (2012).
- ¹⁷⁸G. E. Volovik, “Exotic Lifshitz transitions in topological materials”, *Phys.-Usp.* **61**, 89 (2018).
- ¹⁷⁹I. Dzyaloshinskii, “Some consequences of the Luttinger theorem: The Luttinger surfaces in non-Fermi liquids and Mott insulators”, *Phys. Rev. B* **68**, 085113 (2003).
- ¹⁸⁰N. Iqbal and H. Liu, “Real-time response in AdS/CFT with application to spinors”, *Fortschr. Phys.* **57**, 367–384 (2009).

- ¹⁸¹M. Cubrovic, Y. Liu, K. Schalm, Y.-W. Sun, and J. Zaanen, “Spectral probes of the holographic Fermi groundstate: dialing between the electron star and AdS Dirac hair”, *Phys. Rev. D* **84**, 086002 (2011).
- ¹⁸²R. Contino and A. Pomarol, “Holography for fermions”, *J. High Energy Phys.* **2004**, 058–058 (2004).
- ¹⁸³J. N. Laia and D. Tong, “Flowing Between Fermionic Fixed Points”, *J. High Energ. Phys.* **2011**, 131 (2011).
- ¹⁸⁴N. Iqbal, H. Liu, and M. Mezei, “Lectures on holographic non-Fermi liquids and quantum phase transitions”, *String Theory and Its Applications*, 707–815 (2011).
- ¹⁸⁵T. Faulkner and J. Polchinski, “Semi-Holographic Fermi Liquids”, *J. High Energ. Phys.* **2011**, 12 (2011).
- ¹⁸⁶F. Benini, C. P. Herzog, R. Rahman, and A. Yarom, “Gauge gravity duality for d-wave superconductors: prospects and challenges”, *J. High Energ. Phys.* **2010**, 137 (2010).
- ¹⁸⁷F. Benini, C. P. Herzog, and A. Yarom, “Holographic Fermi arcs and a d-wave gap”, *Physics Letters B* **701**, 626–629 (2011).
- ¹⁸⁸H. Liu, J. McGreevy, and D. Vegh, “Non-Fermi liquids from holography”, *Phys. Rev. D* **83**, 065029 (2011).
- ¹⁸⁹A. Krikun, “Holographic discommensurations”, *J. High Energ. Phys.* **2018**, 30 (2018).
- ¹⁹⁰T. Andrade and A. Krikun, “Commensurate lock-in in holographic non-homogeneous lattices”, *J. High Energ. Phys.* **2017**, 168 (2017).
- ¹⁹¹T. Wiseman, “Numerical construction of static and stationary black holes”, July 27, 2011.
- ¹⁹²Y. Ling, P. Liu, C. Niu, J.-P. Wu, and Z.-Y. Xian, “Holographic fermionic system with dipole coupling on Q-lattice”, *J. High Energ. Phys.* **2014**, 149 (2014).
- ¹⁹³A. Iliasov, A. A. Bagrov, M. I. Katsnelson, and A. Krikun, “Anisotropic destruction of the Fermi surface in inhomogeneous holographic lattices”, *J. High Energ. Phys.* **2020**, 65 (2020).
- ¹⁹⁴K. Skenderis, “Lecture notes on holographic renormalization”, *Class. Quantum Grav.* **19**, 5849–5876 (2002).
- ¹⁹⁵J. P. Boyd, *Chebyshev and Fourier Spectral Methods: Second Revised Edition* (Courier Corporation, Dec. 3, 2001), 690 pp.
- ¹⁹⁶L. N. Trefethen, *Spectral Methods in MATLAB*, Software, Environments and Tools (Society for Industrial and Applied Mathematics, Jan. 1, 2000), 179 pp.
- ¹⁹⁷P. Virtanen, R. Gommers, T. E. Oliphant, M. Haberland, T. Reddy, D. Cournapeau, E. Burovski, P. Peterson, W. Weckesser, J. Bright, S. J. van der Walt, M. Brett, J. Wilson, K. J. Millman, N. Mayorov, A. R. J. Nelson, E. Jones, R. Kern, E. Larson, C. J. Carey, Í. Polat, Y. Feng, E. W. Moore, J. VanderPlas, D. Laxalde, J. Perktold, R. Cimrman, I. Henriksen, E. A. Quintero, C. R. Harris, A. M. Archibald, A. H. Ribeiro, F. Pedregosa, and P. van Mulbregt, “SciPy 1.0: fundamental algorithms for scientific computing in Python”, *Nat Methods* **17**, 261–272 (2020).

- ¹⁹⁸X. S. Li, “An overview of SuperLU: Algorithms, implementation, and user interface”, *ACM Trans. Math. Softw.* **31**, 302–325 (2005).
- ¹⁹⁹I. Wolfram Research, *Mathematica*, Version 13.0 (Wolfram Research, Inc., Champaign, Illinois, 2021).
- ²⁰⁰B. Goutéraux and E. Kiritsis, “Generalized holographic quantum criticality at finite density”, *J. High Energ. Phys.* **2011**, 36 (2011).
- ²⁰¹L. Huijse, S. Sachdev, and B. Swingle, “Hidden Fermi surfaces in compressible states of gauge-gravity duality”, *Phys. Rev. B* **85**, 035121 (2012).
- ²⁰²Q. Si, S. Rabello, K. Ingersent, and J. L. Smith, “Locally critical quantum phase transitions in strongly correlated metals”, *Nature* **413**, 804–808 (2001).
- ²⁰³K. Goldstein, S. Kachru, S. Prakash, and S. P. Trivedi, “Holography of Charged Dilaton Black Holes”, *J. High Energ. Phys.* **2010**, 78 (2010).
- ²⁰⁴M. M. Caldarelli, A. Christodoulou, I. Papadimitriou, and K. Skenderis, “Phases of planar AdS black holes with axionic charge”, *J. High Energ. Phys.* **2017**, 1 (2017).
- ²⁰⁵E. Witten, *Multi-Trace Operators, Boundary Conditions, And AdS/CFT Correspondence*, (Jan. 4, 2002) <http://arxiv.org/abs/hep-th/0112258> (visited on 09/22/2022), preprint.
- ²⁰⁶W. Mück, “An improved correspondence formula for AdS/CFT with multi-trace operators”, *Physics Letters B* **531**, 301–304 (2002).
- ²⁰⁷L. Li, “On thermodynamics of AdS black holes with scalar hair”, *Physics Letters B* **815**, 136123 (2021).
- ²⁰⁸I. Papadimitriou, “Multi-Trace Deformations in AdS/CFT: Exploring the Vacuum Structure of the Deformed CFT”, *J. High Energy Phys.* **2007**, 075–075 (2007).
- ²⁰⁹L. Vecchi, “Multitrace deformations, Gamow states, and Stability of AdS/CFT”, *J. High Energ. Phys.* **2011**, 56 (2011).
- ²¹⁰A. Bernamonti and B. Craps, “D-brane potentials from multi-trace deformations in AdS/CFT”, *J. High Energy Phys.* **2009**, 112 (2009).
- ²¹¹J. Ren, “Analytic solutions of neutral hyperbolic black holes with scalar hair”, *Phys. Rev. D* **106**, 086023 (2022).
- ²¹²E. Dyer and K. Hinterbichler, “Boundary terms, variational principles, and higher derivative modified gravity”, *Phys. Rev. D* **79**, 024028 (2009).
- ²¹³F. Balm, N. Chagnet, S. Arend, J. Aretz, K. Grosvenor, M. Janse, O. Moors, J. Post, V. Ohanesjan, D. Rodriguez-Fernandez, K. Schalm, and J. Zaanen, *T-linear resistivity, optical conductivity and Planckian transport for a holographic local quantum critical metal in a periodic potential*, (Nov. 10, 2022) <http://arxiv.org/abs/2211.05492> (visited on 11/16/2022), preprint.
- ²¹⁴P. W. Phillips, N. E. Hussey, and P. Abbamonte, “Stranger than metals”, *Science* **377**, eabh4273 (2022).
- ²¹⁵R. T. Collins, Z. Schlesinger, F. Holtzberg, P. Chaudhari, and C. Feild, “Reflectivity and conductivity of $\text{YBa}_2\text{Cu}_3\text{O}_7$ ”, *Phys. Rev. B* **39**, 6571–6574 (1989).

- ²¹⁶J. Orenstein, G. A. Thomas, A. J. Millis, S. L. Cooper, D. H. Rapkine, T. Timusk, L. F. Schneemeyer, and J. V. Waszczak, “Frequency- and temperature-dependent conductivity in $\text{YBa}_2\text{Cu}_3\text{O}_{6+x}$ crystals”, *Phys. Rev. B* **42**, 6342–6362 (1990).
- ²¹⁷D. van der Marel, H. J. A. Molegraaf, J. Zaanen, Z. Nussinov, F. Carbone, A. Damascelli, H. Eisaki, M. Greven, P. H. Kes, and M. Li, “Quantum critical behaviour in a high- T_c superconductor”, *Nature* **425**, 271–274 (2003).
- ²¹⁸E. van Heumen, X. Feng, S. Cassanelli, L. Neubrand, L. de Jager, M. Berben, Y. Huang, T. Kondo, T. Takeuchi, and J. Zaanen, “Strange metal electrodynamics across the phase diagram of $\text{Bi}_{2-x}\text{Pb}_x\text{Sr}_{2-y}\text{La}_y\text{CuO}_{6+\delta}$ cuprates”, *Phys. Rev. B* **106**, 054515 (2022).
- ²¹⁹S. A. Hartnoll, “Theory of universal incoherent metallic transport”, *Nature Phys* **11**, 54–61 (2015).
- ²²⁰J. A. N. Bruin, H. Sakai, R. S. Perry, and A. P. Mackenzie, “Similarity of Scattering Rates in Metals Showing T-Linear Resistivity”, *Science* **339**, 804–807 (2013).
- ²²¹L. Delacrétaz, B. Goutéraux, S. Hartnoll, and A. Karlsson, “Bad Metals from Fluctuating Density Waves”, *SciPost Physics* **3**, 025 (2017).
- ²²²L. D’Alessio, Y. Kafri, A. Polkovnikov, and M. Rigol, “From quantum chaos and eigenstate thermalization to statistical mechanics and thermodynamics”, *Advances in Physics* **65**, 239–362 (2016).
- ²²³J. Zaanen, “Lectures on quantum supreme matter”, Dec. 26, 2021.
- ²²⁴S. Chakravarty, B. I. Halperin, and D. R. Nelson, “Two-dimensional quantum Heisenberg antiferromagnet at low temperatures”, *Phys. Rev. B* **39**, 2344–2371 (1989).
- ²²⁵M. Blake, “Universal Charge Diffusion and the Butterfly Effect in Holographic Theories”, *Phys. Rev. Lett.* **117**, 091601 (2016).
- ²²⁶M. Blake, “Universal diffusion in incoherent black holes”, *Phys. Rev. D* **94**, 086014 (2016).
- ²²⁷M. Blake, R. A. Davison, and S. Sachdev, “Thermal diffusivity and chaos in metals without quasiparticles”, *Phys. Rev. D* **96**, 106008 (2017).
- ²²⁸C. Murthy, A. Pandey, I. Esterlis, and S. A. Kivelson, *A stability bound on the T-linear resistivity of conventional metals*, (Dec. 13, 2021) <http://arxiv.org/abs/2112.06966> (visited on 09/22/2022), preprint.
- ²²⁹J. Zaanen, G. A. Sawatzky, and J. W. Allen, “Band gaps and electronic structure of transition-metal compounds”, *Phys. Rev. Lett.* **55**, 418–421 (1985).
- ²³⁰P. A. Lee, N. Nagaosa, and X.-G. Wen, “Doping a Mott insulator: Physics of high-temperature superconductivity”, *Rev. Mod. Phys.* **78**, 17–85 (2006).
- ²³¹J. P. Gauntlett, J. Sonner, and T. Wiseman, “Quantum criticality and holographic superconductors in M-theory”, *J. High Energ. Phys.* **2010**, 60 (2010).
- ²³²N. Iqbal, H. Liu, and M. Mezei, “Semi-local quantum liquids”, *J. High Energ. Phys.* **2012**, 86 (2012).
- ²³³S. A. Hartnoll and D. M. Hofman, “Locally Critical Resistivities from Umklapp Scattering”, *Phys. Rev. Lett.* **108**, 241601 (2012).

- ²³⁴L. V. Delacrétaz, B. Goutéraux, and V. Ziogas, “Damping of Pseudo-Goldstone Fields”, *Phys. Rev. Lett.* **128**, 141601 (2022).
- ²³⁵C. Niu and K.-Y. Kim, “Diffusion and butterfly velocity at finite density”, *J. High Energ. Phys.* **2017**, 30 (2017).
- ²³⁶D. S. Ageev and I. Y. Arefeva, “When things stop falling, chaos is suppressed”, *J. High Energ. Phys.* **2019**, 100 (2019).
- ²³⁷N. Sorokhaibam, “Phase transition and chaos in charged SYK model”, *J. High Energ. Phys.* **2020**, 55 (2020).
- ²³⁸P. Colangelo, F. De Fazio, and N. Losacco, “Chaos in a $Q\bar{Q}$ system at finite temperature and baryon density”, *Phys. Rev. D* **102**, 074016 (2020).
- ²³⁹X. Chen, Y. Gu, and A. Lucas, “Many-body quantum dynamics slows down at low density”, *SciPost Physics* **9**, 071 (2020).
- ²⁴⁰C. M. Varma, P. B. Littlewood, S. Schmitt-Rink, E. Abrahams, and A. E. Ruckenstein, “Phenomenology of the normal state of Cu-O high-temperature superconductors”, *Phys. Rev. Lett.* **63**, 1996–1999 (1989).
- ²⁴¹C. M. Varma, “Colloquium: Linear in temperature resistivity and associated mysteries including high temperature superconductivity”, *Rev. Mod. Phys.* **92**, 031001 (2020).
- ²⁴²J. W. Loram, K. A. Mirza, J. M. Wade, J. R. Cooper, and W. Y. Liang, “The electronic specific heat of cuprate superconductors”, *Physica C: Superconductivity* **235–240**, 134–137 (1994).
- ²⁴³A. Donos and J. P. Gauntlett, “Thermoelectric DC conductivities from black hole horizons”, *J. High Energ. Phys.* **2014**, 81 (2014).
- ²⁴⁴S. A. Hartnoll, R. Mahajan, M. Punk, and S. Sachdev, “Transport near the Ising-nematic quantum critical point of metals in two dimensions”, *Phys. Rev. B* **89**, 155130 (2014).
- ²⁴⁵A. Lucas, S. Sachdev, and K. Schalm, “Scale-invariant hyperscaling-violating holographic theories and the resistivity of strange metals with random-field disorder”, *Phys. Rev. D* **89**, 066018 (2014).
- ²⁴⁶J. Erdmenger, B. Herwerth, S. Klug, R. Meyer, and K. Schalm, “S-wave superconductivity in anisotropic holographic insulators”, *J. High Energ. Phys.* **2015**, 94 (2015).
- ²⁴⁷A. Lucas, “Conductivity of a strange metal: from holography to memory functions”, *J. High Energ. Phys.* **2015**, 71 (2015).
- ²⁴⁸A. Lucas, “Hydrodynamic transport in strongly coupled disordered quantum field theories”, *New J. Phys.* **17**, 113007 (2015).
- ²⁴⁹A. Lucas, J. Crossno, K. C. Fong, P. Kim, and S. Sachdev, “Transport in inhomogeneous quantum critical fluids and in the Dirac fluid in graphene”, *Phys. Rev. B* **93**, 075426 (2016).
- ²⁵⁰A. Donos, J. P. Gauntlett, and V. Ziogas, “Diffusion in inhomogeneous media”, *Phys. Rev. D* **96**, 125003 (2017).
- ²⁵¹N. Chagnet, F. Balm, K. Schalm, and J. Zaanen, “Umklapp Hydrodynamics”, To Appear (2022).

- ²⁵²L. V. Delacrétaz, B. Goutéraux, S. A. Hartnoll, and A. Karlsson, “Theory of hydrodynamic transport in fluctuating electronic charge density wave states”, *Phys. Rev. B* **96**, 195128 (2017).
- ²⁵³A. Amoretti, D. Areán, B. Goutéraux, and D. Musso, “Dc Resistivity of Quantum Critical, Charge Density Wave States from Gauge-Gravity Duality”, *Phys. Rev. Lett.* **120**, 171603 (2018).
- ²⁵⁴A. Amoretti, D. Areán, B. Goutéraux, and D. Musso, “Universal Relaxation in a Holographic Metallic Density Wave Phase”, *Phys. Rev. Lett.* **123**, 211602 (2019).
- ²⁵⁵B. Goutéraux and E. Mefford, “Normal Charge Densities in Quantum Critical Superfluids”, *Phys. Rev. Lett.* **124**, 161604 (2020).
- ²⁵⁶B. Goutéraux and E. Mefford, “Non-vanishing zero-temperature normal density in holographic superfluids”, *J. High Energy. Phys.* **2020**, 91 (2020).
- ²⁵⁷J. Armas and A. Jain, “Hydrodynamics for charge density waves and their holographic duals”, *Phys. Rev. D* **101**, 121901 (2020).
- ²⁵⁸J. Armas, A. Jain, and R. Lier, *Approximate symmetries, pseudo-Goldstones, and the second law of thermodynamics*, (Mar. 30, 2022) <http://arxiv.org/abs/2112.14373> (visited on 10/25/2022), preprint.
- ²⁵⁹D. Areán, R. A. Davison, B. Goutéraux, and K. Suzuki, “Hydrodynamic diffusion and its breakdown near AdS₂ quantum critical points”, *Phys. Rev. X* **11**, 031024 (2021).
- ²⁶⁰M. P. Heller, A. Serantes, M. Spalinski, V. Svensson, and B. Withers, “Convergence of hydrodynamic modes: insights from kinetic theory and holography”, *SciPost Physics* **10**, 123 (2021).
- ²⁶¹N. Wu, M. Baggioli, and W.-J. Li, “On the universality of AdS₂ diffusion bounds and the breakdown of linearized hydrodynamics”, *J. High Energy. Phys.* **2021**, 14 (2021).
- ²⁶²H.-S. Jeong, K.-Y. Kim, and Y.-W. Sun, “The breakdown of magneto-hydrodynamics near AdS₂ fixed point and energy diffusion bound”, *J. High Energy. Phys.* **2022**, 6 (2022).
- ²⁶³Y. Liu and X.-M. Wu, “Breakdown of hydrodynamics from holographic pole collision”, *J. High Energy. Phys.* **2022**, 155 (2022).
- ²⁶⁴R. J. Anantua, S. A. Hartnoll, V. L. Martin, and D. M. Ramirez, “The Pauli exclusion principle at strong coupling: Holographic matter and momentum space”, *J. High Energy. Phys.* **2013**, 104 (2013).
- ²⁶⁵R. A. Davison and A. Parnachev, “Hydrodynamics of cold holographic matter”, *J. High Energy. Phys.* **2013**, 100 (2013).
- ²⁶⁶D. Forster, *Hydrodynamic Fluctuations, Broken Symmetry, and Correlation Functions* (CRC Press, Boca Raton, May 23, 2019), 352 pp.
- ²⁶⁷M. Blake and A. Donos, “Diffusion and chaos from near AdS₂ horizons”, *J. High Energy. Phys.* **2017**, 13 (2017).
- ²⁶⁸J. Maldacena, S. H. Shenker, and D. Stanford, “A bound on chaos”, *J. High Energy. Phys.* **2016**, 106 (2016).
- ²⁶⁹P. Chesler, A. Lucas, and S. Sachdev, “Conformal field theories in a periodic potential: results from holography and field theory”, *Phys. Rev. D* **89**, 026005 (2014).

- ²⁷⁰J. A. Sulpizio, L. Ella, A. Rozen, J. Birkbeck, D. J. Perello, D. Dutta, M. Ben-Shalom, T. Taniguchi, K. Watanabe, T. Holder, R. Queiroz, A. Principi, A. Stern, T. Scaffidi, A. K. Geim, and S. Ilani, “Visualizing Poiseuille flow of hydrodynamic electrons”, *Nature* **576**, 75–79 (2019).
- ²⁷¹B. Michon, C. Berthod, C. W. Rischau, A. Ataie, L. Chen, S. Komiya, S. Ono, L. Taillefer, D. van der Marel, and A. Georges, *Planckian behavior of cuprate superconductors: Reconciling the scaling of optical conductivity with resistivity and specific heat*, (May 9, 2022) <http://arxiv.org/abs/2205.04030> (visited on 10/28/2022), preprint.
- ²⁷²A. A. Husain, M. Mitrano, M. S. Rak, S. Rubeck, B. Uchoa, K. March, C. Dwyer, J. Schneeloch, R. Zhong, G. D. Gu, and P. Abbamonte, “Crossover of Charge Fluctuations across the Strange Metal Phase Diagram”, *Phys. Rev. X* **9**, 041062 (2019).
- ²⁷³U. Gran, M. Tornsö, and T. Zingg, “Holographic plasmons”, *J. High Energ. Phys.* **2018**, 176 (2018).
- ²⁷⁴E. Mauri and H. T. C. Stoof, “Screening of Coulomb interactions in holography”, *J. High Energ. Phys.* **2019**, 35 (2019).
- ²⁷⁵A. Romero-Bermúdez, A. Krikun, K. Schalm, and J. Zaanen, “Anomalous attenuation of plasmons in strange metals and holography”, *Phys. Rev. B* **99**, 235149 (2019).
- ²⁷⁶T. Andrade, A. Krikun, and A. Romero-Bermúdez, “Charge density response and fake plasmons in holographic models with strong translation symmetry breaking”, *J. High Energ. Phys.* **2019**, 159 (2019).
- ²⁷⁷E. W. Huang, R. Sheppard, B. Moritz, and T. P. Devereaux, “Strange metallicity in the doped Hubbard model”, *Science* **366**, 987–990 (2019).
- ²⁷⁸S. Xu and B. Swingle, *Scrambling Dynamics and Out-of-Time Ordered Correlators in Quantum Many-Body Systems: a Tutorial*, (Mar. 1, 2022) <http://arxiv.org/abs/2202.07060> (visited on 11/07/2022), preprint.
- ²⁷⁹N. Tsuji and P. Werner, “Out-of-time-ordered correlators of the Hubbard model: Sachdev-Ye-Kitaev strange metal in the spin-freezing crossover region”, *Phys. Rev. B* **99**, 115132 (2019).
- ²⁸⁰M. Christos, D. G. Joshi, S. Sachdev, and M. Tikhonovskaya, “Critical metallic phase in the overdoped random t-J model”, *Proceedings of the National Academy of Sciences* **119**, e2206921119 (2022).
- ²⁸¹A. A. Abrikosov and I. M. Khalatnikov, “The theory of a fermi liquid (the properties of liquid ^3He at low temperatures)”, *Rep. Prog. Phys.* **22**, 329 (1959).
- ²⁸²C. Collignon, A. Ataie, A. Gourgout, S. Badoux, M. Lizaire, A. Legros, S. Licciardello, S. Wiedmann, J.-Q. Yan, J.-S. Zhou, Q. Ma, B. D. Gaulin, N. Doiron-Leyraud, and L. Taillefer, “Thermopower across the phase diagram of the cuprate $\text{La}_{1.6-x}\text{Nd}_{0.4}\text{Sr}_x\text{CuO}_4$: signatures of the pseudogap and charge density wave phases”, *Phys. Rev. B* **103**, 155102 (2021).
- ²⁸³A. Gourgout, G. Grissonnanche, F. Laliberté, A. Ataie, L. Chen, S. Verret, J.-S. Zhou, J. Mravlje, A. Georges, N. Doiron-Leyraud, and L. Taillefer, “Seebeck Coefficient in a Cuprate Superconductor: Particle-Hole Asymmetry in the Strange Metal Phase and Fermi Surface Transformation in the Pseudogap Phase”, *Phys. Rev. X* **12**, 011037 (2022).

- ²⁸⁴S. Balay, W. D. Gropp, L. C. McInnes, and B. F. Smith, “Efficient Management of Parallelism in Object-Oriented Numerical Software Libraries”, in *Modern Software Tools for Scientific Computing*, edited by E. Arge, A. M. Bruaset, and H. P. Langtangen (Birkhäuser, Boston, MA, 1997), pp. 163–202.
- ²⁸⁵S. Balay, *PETSc/TAO Users Manual* 3.16, 2021.
- ²⁸⁶R. A. Davison, B. Goutéraux, and S. A. Hartnoll, “Incoherent transport in clean quantum critical metals”, *J. High Energ. Phys.* **2015**, 112 (2015).
- ²⁸⁷J. Zaanen, F. Balm, and A. Beekman, “Crystal gravity”, *SciPost Physics* **13**, 039 (2022).

Summary

Progress and discoveries in the physical sciences can often come from unexpected places. For several decades now, a part of the theoretical physics community has been faced with a conundrum: certain superconducting compounds, the so-called cuprate strange metals, display characteristics that cannot be explained with the theoretical models that we have available to us. The most striking of this is the electrical resistivity of these metals. This increases linearly with temperature over a very wide range of temperature, from far below freezing to far above boiling temperatures. This is at odds with conventional wisdom regarding metallic compounds, which would for example predict quadratic scaling at low temperatures. This is only one of many observations.

The reason for our limited understanding of the phenomena of the strange metal has several root causes. For one, the mathematical tools we have at our disposal only work well if the electrons in this material are not strongly influenced by either each other or the underlying crystal structure of the material. In the strange metal, both of these conditions are violated. Computers are also of no great help: while our classical computers are great at dealing with classical data, encoded in 1's and 0s, they are spectacularly unsuited to deal with problems where quantum mechanics plays an important role. In the future quantum computers might be able to shed light on these problems, but the technology is simply not there yet.

It may appear we are stuck. However, from the unlikely realm of string theory comes a surprise: the holographic duality. Here string theory is not used as a model of the finest structure of the universe. Instead, it was found that there exists a remarkable duality between the structure of the mathematical equations that describe strongly interacting quantum systems, similar to the strange metal mentioned above, and the theory of General Relativity. The details of this are intricate, but it offers us an olive branch: we are able to translate the original problem that we could not solve, into a problem of General Relativity, one involving black holes and negatively curved space times. Solving this problem is still hard, but no longer impossible. Unfortunately we are not able to model precisely those physical systems of interest, and must always use some proxy that can never be realised in the laboratory. However, thorough investigation of the results can still give rise to universal answers that cannot be arrived at through any other known means.

In this thesis, the duality was investigated with high precision. In particular, we focused on what effects we observe when we try to also pull the crystal structure of the metals through the duality. We looked at several observables such as resistivity and conductivity, but also spectral functions of fermions in the presence of such a lattice. This is a technically difficult thing to accomplish, and we have developed new codes to solve these black hole problems to high accuracy using supercomputers. The main difficulty here comes from the complexity of Einstein's equations, that get monstrously large when a crystal lattice is included.

After several years of hard work, ironing out all bugs and problems in the code, we were able to use this setup to great effect. Chapter 4 for example shows that the effect of the crystal lattice can lead to very similar behaviour as is found in photoemission experiments. However, the duality is only a phenomenological tool: we show that we can reproduce a similar looking effect, but we have gained no greater insight into what might cause these effects in the real materials in the lab.

The heart of this thesis is formed by Chapter 6. In this chapter, we take a different approach to the duality. Here we treat our supercomputer codes truly like an experiment, and we try to see if we can, in the language of the duality, find explanations or suggestions for the observed mysteries in the strange metal. We are able to see and explain many of the phenomena of the strange metal in our framework. Above all, what we find is that holography appears to argue for there to be a fundamentally different physical principle to be on the foreground when it comes to the strange metal. Rather than electrons zooming around in metals, we should think instead in a truly quantum (supreme) manner: all intuition we have from our everyday life should go out of the window, and instead we should be concerned with the most exotic quantum physics.

While the data is extremely suggestive of this, the jury is still out on this one. The viewpoints of holography are highly unconventional in the condensed matter physics community, and often dismissed out of hand. We propose certain measurements that could potentially be done that can shed more light on the veracity of our statements, but these experiments may be many years away still. On the other hand, with a recent uptake in attention from the community at large, perhaps the time is ripe for the holographic duality to become another common tool in the toolbox of theoretical physics.

Samenvatting

Ontdekkingen die de wetenschap vooruit brengen komen vaak uit onverwachte hoek zetten. Theoretici die zich met gecondenseerde materie bezig houden staan al lange tijd voor een dilemma: bepaalde supergeleidende materialen, de zogeheten ‘cuprate strange metals’, zijn tot nu toe nog niet goed begrepen. Deze strange metals hebben bepaalde karakteristieke eigenschappen, bijvoorbeeld een weerstand die rechtvenredig met de temperatuur oploopt, zowel bij hoge als bij lage temperaturen. In andere metalen zou dit kwadratisch moeten zijn bij lage temperatuur, en het is niet begrepen waarom dit afwijkt. Dit is slechts een van vele observaties die niet verklaard zijn.

De redenen voor het gebrek aan begrip zijn uiteenlopend. Vanuit een wiskundig oogpunt speelt de grote sterkte van de wisselwerking tussen electronen in de strange metals een belangrijke rol. De vergelijkingen die de electronische sector zouden beschrijven zijn niet direct op te lossen. Wanneer deze wisselwerking echter zwak is, is het met bepaalde goed beheersbare benaderingen mogelijk om toch een berekening uit te kunnen voeren. In de strange metals is dit niet het geval. Een andere benadering zou kunnen zijn om het metaal direct met computers te proberen te simuleren. Dit gaat echter catastrofaal fout: de simpele structuur van data in onze computers, die alleen de waardes 1 en 0 aan kunnen nemen, zorgt ervoor dat dit onmogelijk is. Kwantumcomputers bieden hier wellicht uitkomst, maar deze zijn nog lang niet in een dusdanig ver gevorderd stadium dat ze voor dit probleem nuttig zouden kunnen zijn.

De verrassing komt nu uit de hoek van de snaartheorie. Rond de millenniumwisseling kwam daar naar voren dat er een merkwaardige dualiteit bestaat tussen twee verschillende theorieën die op het eerste gezicht niets met elkaar te maken zouden moeten hebben: de holografische dualiteit. Het blijkt namelijk dat de wiskundige structuur een supersymmetrische veldentheorie die niets van zwaartekracht afweet, precies dezelfde wiskundige structuur heeft als een snaartheorie met een extra ruimtedimensie, waar zwaartekracht wel een rol speelt. Dit is een erg diepgaand onderwerp waar vele tienduizenden artikelen over geschreven zijn, maar wij zijn geïnteresseerd in één specifieke realisatie hiervan, waar we niet met snaartheorie maar alleen met Algemene Relativiteitstheorie (AR) te maken hebben. Met behulp van de dualiteit kunnen we dit vertalen naar een veldentheorie, waar sterke wisselwerkingen en kwantumverstrengeling de hoofdrol hebben. Op deze manier ruilen we een onmogelijk op te lossen probleem in voor een moeilijk probleem, AR is namelijk niet bepaald makkelijk op te lossen. Er zijn ook enkele kanttekeningen die geplaatst moeten worden bij de resultaten die wij krijgen: de dualiteit is niet erg gebruiksvriendelijk, en de veldentheorie die de dualiteit beschrijft is nogal ver verwijderd van de veldentheorie die in de strange metal echt gerealiseerd wordt. Desalniettemin is het nog steeds mogelijk om bepaalde algemene waarheden te ontdekken op deze manier.

Om wat specifieker te zijn ontfermt dit proefschrift zich voornamelijk over de vraag wat er gebeurt als we de effecten van een kristalrooster na proberen te bootsen aan de kant van de AR. De niet-lineaire eigenschappen van de AR produceren enorm ingewikkelde vergelijkingen, waarvoor wij speciale computerprogramma's moesten schrijven om met behulp van de nationale supercomputers berekeningen uit te kunnen voeren. De resultaten van deze berekeningen vormen de data die dit proefschrift gebruikt worden. Hoofdstuk 4 laat zien hoe het mogelijk is om bepaalde spectraalfuncties die in fotoemissie-experimenten waargenomen worden, namelijk de zogeheten Fermi Arcs, na te bootsen. Door de hierboven genoemde kanttekeningen is het echter niet mogelijk hieruit op te maken wat het mechanisme is dat deze Fermi arcs veroorzaakt.

Het magnum opus van dit proefschrift is hoofdstuk 6. Door de data van de supercomputer te behandelen als experimentele data hebben wij geprobeerd of het mogelijk is om aan de hand van de dualiteit suggesties kunnen geven over wat er zich daadwerkelijk in de strange metals afspeelt. Wonderbaarlijk genoeg bleek het niet alleen mogelijk, maar zelfs natuurlijk om veel van de in experiment waargenomen verschijnselen na te bootsen. De conclusie die wij hieruit kunnen trekken is dat de holografische dualiteit laat zien dat er waarschijnlijk een compleet ander soort natuurkunde van belang is dan men zou verwachten in de strange metal. Dit betekent dat men de notie van elektronen die zich voortbewegen in een metaal los moet laten, en in plaats daarvan moet denken in termen waar kwantumeffecten en kwantumverstrengeling oppermachtig zijn. Dit staat haaks op de gewone denkwijzen in de theorieën van gecondenseerde materie, en zal daarom ook niet makkelijk op het bredere publiek overslaan.

Ook is het zo dat het onderzoek dat in dit proefschrift aan bod komt op zichzelf verre van genoeg is om hierover een finaal oordeel te vellen. Zoals in hoofdstuk 6 ook aan bod komt hebben wij wel voorstellen voor enkele experimenten die bijzonder gevoelig zouden moeten zijn voor de aan- of afwezigheid van deze nieuwe fysica. Samen met de recente groei in aandacht van de holografische dualiteit is de tijd misschien rijp voor holografie om de boel echt op te schudden in de wereld van de theoretische natuurkunde. Hopelijk dragen de resultaten en onderzoeken van dit proefschrift bij aan een soortgelijke revolutie.

Curriculum Vitae

I was born on August 3, 1994 in Utrecht, the Netherlands. I completed my secondary education at the Gemeentelijk Gymnasium in Hilversum in 2012, on a Nature and Technology profile along with the research project ‘Algae as Biofuel’, which I graduated Summa cum Laude.

That same year of 2012, I left for Scotland, where I studied Theoretical Physics at the University of Edinburgh. I graduated with a Masters of Physics in 2017, on the thesis ‘Exploring the ρ -resonance in Lattice QCD’ under prof.dr. Luigi Del Debbio. Over these five years, I won the class medal for Theoretical and/or Mathematical Physics four times, and I was awarded several scholarships and grants: the Neil Arnott Scholarship, the Donald Fraser Bursary and the Brodie Memorial Prize, and two Summer Research Internship grants for 2015 and 2016.

In September of 2017 I started as a PhD student under prof.dr. Jan Zaanen and prof.dr. Koenraad Schalm at the Lorentz Institute for Theoretical Physics, part of the Leiden Institute of Physics of Leiden University. Alongside the research presented in this thesis I have attended several schools during this time such as the DRSTP Schools in High Energy and Condensed Matter Physics, both in Delft (NL), the MANEP Winter School in Saas-Fee (CH) and the Gapless Fermions International school in Dresden (DE). I have also presented work at several conferences and workshops, among others Physics@Veldhoven (NL) and the 2020 Strange Metal Workshop in Leiden (NL). I have attended several others, such as RDSCQM Nordita, Stockholm (SE), the Amsterdam String Summer workshop (NL), Bringing Holography to the Lab in Leiden (NL) and SCES 2022 in Amsterdam(NL).

As of November 1, 2022, I have started working as a Quantitative Analyst/Credit Risk Modeller for ABN AMRO in Amsterdam.

Acknowledgements

There are many people who have played a vital role in helping me get to the point of completion of this thesis, and it would be remiss not to thank them in detail. First of all Jan Zaanen and Koenraad Schalm, who have throughout my years as a PhD student taught me, advised me, mentored me but also pushed me to become the researcher that I am today. I would like to thank Sasha Krikun, for introducing me to the numerical methods for holographic lattices and mentoring me in that aspect during his time as a postdoc at the Lorentz Institute. Nicolas Chagnet has put in great effort to help finish the second and third papers presented in this thesis in a timely fashion. I hope he will be able to build further on these efforts.

I also want to thank the rest of the Quantum Matter group and the Lorentz Institute, including my office mate Vladimir Ohanesjan, Aleksandar Bukva, David Rodríguez Fernández, Kevin Grosvenor, Aravindh Swaminathan Shankar, Tereza Vakhtel, Vincenzo Scopelliti, Aurelio Romero-Bermúdez, Philippe Sabella-Garnier and many many others, for making it my time as a PhD student at Leiden University a great one.

I would also like to thank the support staff, the secretariat and IT of the Lorentz Institute and LION for all their help over the years, and Leiden University as a whole for being host to my endeavours these past years. I would also like to thank the NWO Strange Metal program for the funding that allowed me to do the research in this thesis, and surfSARA for the personal grants to use the Cartesius and Snellius supercomputers, without which many of the discoveries in this thesis could not have been made.

My parents and sister, thank you for supporting me, as I made my first steps into physics when I left the country at 18 years old to go study abroad in Scotland.

And from the bottom of my heart, I am eternally grateful to my wife. You have supported me and our family as a whole from the very start of my PhD. I could never have done this without you, you have always been there when I needed you most. And finally my son, whose arrival provided me with the drive and motivation to finish this doctorate.